

CHARACTERIZATION OF THE DYNAMIC PERFORMANCE OF MACHINE
SPINDLES

by

Vasishta Ganguly

A dissertation submitted to the faculty of
The University of North Carolina at Charlotte
in partial fulfillment of the requirements
for the degree of Doctor of Philosophy in
Mechanical Engineering

Charlotte

2014

Approved by:

Dr. Tony Schmitz

Dr. Stuart Smith

Dr. John Ziegert

Dr. Ertunga Ozelkan

Dr. Angela Davies

ABSTRACT

VASISHTA GANGULY. Characterization of the dynamic performance of machine spindles. (Under the direction of Dr. TONY SCHMITZ)

Machine spindle dynamics and (axis of rotation) error motions may vary as a function of spindle speed due to gyroscopic effects, changes in bearing preload, centrifugal forces, and thermal effects. It is necessary to characterize these changes in order to fully define the spindle's performance. In this research, two different aspects of spindle performance are considered: a) spindle dynamics; and b) spindle error (SE) motions. The objective is to simultaneously measure the (potential) changes in both the error motions and dynamic response with spindle speed.

This work is motivated by the influence of spindle performance on machining operations. Machining instability (chatter) leads to poor surface finish, high rejection rates, rapid tool wear, and, potentially, spindle damage. Stable machining conditions may be identified using well-known milling process models. To do so, the dynamics of the tool-holder-spindle-machine assembly as reflected at the tool tip is required. Here, the dynamics of an artifact-spindle-machine combination are measured at the tip of a standard artifact when the spindle is rotating. Tests are conducted at different spindle speeds to capture the speed-dependent changes in the spindle dynamics. Receptance coupling substructure analysis (RCSA) is then applied to predict the tool point response for arbitrary tool-holder combination in the same spindle. RCSA is used to first decouple the artifact dynamics from the measured artifact-spindle-machine assembly dynamics (to isolate the spindle contributions) and then analytically couple the dynamics of a modeled tool-holder to the spindle-machine in order to predict the tool point frequency response

function (FRF). A speed-dependent milling stability lobe diagram, which graphically depicts the allowable axial depth of cut as a function of spindle speed, is obtained by identifying the changes in tool point dynamics with spindle speed.

Spindle error motions, which describe the variable position and orientation of the spindle axis as a function of the rotation angle, can affect machined surface quality. Non-contact sensors (such as capacitance gages) may be used to measure the SE motions while the spindle is rotating. A multi-probe error separation method is used to accurately isolate the SE motions and the artifact form error. Tests are repeated at different spindle speeds to examine the associated effects. Together, the identification of the speed-dependent SE motions and tool point FRF will enable an improved capability to predict the milling performance for a given tool-holder-spindle-machine combination.

In this research, the speed-dependent spindle dynamics and the SE motions for three different Haas TM1 machine spindles were studied. At a spindle speed of 3800 rpm, the critical stable axial depth of cut predicted using the stationary tool point FRFs was 6 mm while that predicted using the speed-dependent FRFs was 10 mm. Stable machining was observed at an axial depth of cut of 9 mm at a spindle speed of 3800 rpm. The results showed that incorporating the changing dynamics of the spindle in machining stability models improved the ability to predict chatter. Further, the dynamics and error motions of an NSK HES-500 high speed spindle were also measured.

DEDICATION

To my parents.

ACKNOWLEDGEMENTS

I would like to thank my academic advisor, Dr. Tony Schmitz, for mentoring me throughout my graduate experience and for allowing me the academic freedom to explore research areas of my own personal interest, for which I am extremely grateful.

I am very grateful to my committee members, Dr. John Ziegert, Dr. Stuart Smith, Dr. Ertunga Ozelkan, and Dr. Angela Davies, for their guidance and advice.

I would like to thank my colleagues at the Center for Precision Metrology (CPM) at the University of North Carolina at Charlotte and at the Machine Tool Research Center (MTRC) at the University of Florida for all the assistance and fruitful debate.

I would like to thank my parents, sister, and friends for their continuous support and encouragement.

TABLE OF CONTENTS

| | |
|--|-----|
| LIST OF FIGURES | xii |
| LIST OF TABLES | xii |
| CHAPTER 1: INTRODUCTION | 1 |
| 1.1 High-speed Machining | 1 |
| 1.2 Machining Stability | 2 |
| 1.3 Effects of Spindle Speed on Spindle Dynamics | 4 |
| 1.4 Receptance Coupling Substructure Analysis | 8 |
| 1.5 Spindle Error Motions | 10 |
| 1.6 Research Objectives and Scope | 12 |
| CHAPTER 2: EXPERIMENTAL SETUP – DESIGN AND CALIBRATION | 14 |
| 2.1 Time Domain Simulation of Impact Dynamics | 14 |
| 2.1.1 Influence of Hammer Mass and Stiffness | 20 |
| 2.1.2 Influence of Target Mass and Stiffness | 24 |
| 2.1.3 Influence of Hammer Mass on Multiple Degree of Freedom Targets | 26 |
| 2.2 Experimental Setup Description | 31 |
| 2.2.1 Setup 1: High Mass Excitation Hammer | 31 |
| 2.2.2 Setup 2: Low Mass Excitation Hammer | 33 |
| 2.2.3 Setup 3: Measurement of SE motions of High Speed Spindle | 38 |
| 2.3 Phase Correction Algorithm | 39 |
| 2.3.1 Experimental Setup to Measure Amplifier-induced Phase Lag | 40 |
| 2.3.2 Correction for Phase Lag | 42 |

| | |
|--|------|
| | viii |
| CHAPTER 3: DATA ANALYSIS | 44 |
| 3.1 Dynamic Response of Machine Spindle | 44 |
| 3.1.1 Filtering Synchronous SE Motions and Artifact Form Error | 44 |
| 3.1.2 Windowing | 48 |
| 3.1.3 Impact Synchronous Time Domain Averaging | 50 |
| 3.1.4 Frequency Response Function | 52 |
| 3.1.5 Frequency Response Function from Velocity Measurements | 54 |
| 3.2 Multi-probe Error Separation | 56 |
| 3.2.1 SE Motions using Velocity Data | 65 |
| 3.2.2 Uncertainty Evaluation | 66 |
| 3.2.2.1 Variance in Synchronous SE Motions | 66 |
| 3.2.2.2 Influence of Sampling Rate on SE Motion Measurements | 67 |
| 3.2.3 SE Motion Validation | 69 |
| CHAPTER 4: EXPERIMENTAL RESULTS | 71 |
| 4.1 Haas1 CNC Vertical Machining Center Studies | 71 |
| 4.1.1 Speed-dependent Dynamics | 71 |
| 4.1.1.1 Standard Cylindrical Artifact | 71 |
| 4.1.1.2 Solid Carbide Blank | 75 |
| 4.1.2 SE Motions for Haas1 | 78 |
| 4.1.2.1 Artifact Form Error | 78 |
| 4.1.2.2 Synchronous SE Motions | 78 |
| 4.1.2.3 Asynchronous SE Motions | 81 |
| 4.1.2.4 Frequency Content of SE Motions | 83 |

| | | |
|------------|---|-----|
| | ix | |
| 4.2 | NSK HES-500 HIGH SPEED SPINDLE | 90 |
| 4.2.1 | Speed-dependent Spindle Dynamics | 90 |
| 4.2.2 | SE Motions for NSK HES-500 High Speed Spindle | 92 |
| 4.2.2.1 | Artifact Form Error | 93 |
| 4.2.2.2 | Synchronous SE Motions | 94 |
| 4.2.2.3 | Asynchronous SE motions | 96 |
| 4.2.2.4 | Frequency Content of SE Motions | 98 |
| CHAPTER 5: | RECEPTANCE COUPLING SUBSTRUCTURE ANALYSIS | 105 |
| 5.1 | RCSA Background | 106 |
| 5.2 | Simplex Based Nelder-Mead Optimization | 113 |
| 5.2.1 | Step 1: Individual Mode Identification | 113 |
| 5.2.2 | Step 2: Optimization for Individual Modes | 115 |
| 5.2.2.1 | Step 2.1: Determining Frequency Range | 115 |
| 5.2.2.2 | Step 2.2: Optimization for Each Individual Mode | 117 |
| 5.2.3 | Step 3: Floating modes | 118 |
| 5.2.4 | Step 4: Optimization for All Modes | 120 |
| 5.2.4.1 | Mode Deletion | 121 |
| 5.2.5 | Step 4: Mapping from Modal to Equivalent EB Beam Parameters | 122 |
| 5.3 | Equivalent Diameter Model of Fluted Endmill | 124 |
| 5.4 | Experimental Results | 126 |
| CHAPTER 6: | MACHINING STABILITY | 132 |
| 6.1 | Speed-dependent Cutting Force Coefficients | 132 |
| 6.2 | Tool Tip FRF | 133 |

| | |
|--|-----|
| | x |
| 6.2.1 Standard Cylindrical Artifact | 134 |
| 6.2.2 Solid Carbide Blank | 135 |
| 6.3 Speed-Dependent Stability Lobe Diagram | 137 |
| 6.4 Machining Stability Trials | 138 |
| CHAPTER 7: CONCLUSIONS AND FUTURE WORK | 143 |
| 7.1 Conclusions | 143 |
| 7.2 Future Work | 145 |
| REFERENCES | 147 |
| APPENDIX A: FRF Measurements | 153 |
| A.1: Speed-Dependent FRF : Haas2 | 153 |
| A.1.1: Standard Cylindrical Artifact | 153 |
| A.1.2: Solid Carbide Blank | 154 |
| A.2: Speed-Dependent FRF : Haas3 | 155 |
| A.2.1: Standard Cylindrical Artifact | 155 |
| A.2.2: Solid Carbide Blank | 156 |
| APPENDIX B: SE MOTION MEASUREMENTS | 157 |
| B.1: SE Measurements : Haas2 | 157 |
| B.1.1: Synchronous SE Motions | 157 |
| B.1.2: Asynchronous SE Motions | 163 |
| B.2: SE Measurements : Haas3 | 168 |
| B.2.1: Synchronous SE Motions | 168 |
| B.2.2: Asynchronous SE Motions | 174 |

| | |
|------------------------------|-----|
| | xi |
| APPENDIX C: RCSA COMPARISONS | 179 |
| C.1: RCSA Comparison : Haas2 | 179 |
| C.2: RCSA Comparison : Haas3 | 180 |

LIST OF FIGURES

| | | |
|--------------|---|----|
| FIGURE 1.1: | Stability lobe diagram: (x) unstable, (o) stable. | 3 |
| FIGURE 2.1: | Schematic representation of hammer and target interaction. | 15 |
| FIGURE 2.2: | Plot of hammer position, X_h , tool position, X_t , and elastic deformation at interface, δ_c . | 18 |
| FIGURE 2.3: | Contact force at the point of impact. | 18 |
| FIGURE 2.4: | Excited bandwidth (left); Impulse time (right). | 20 |
| FIGURE 2.5: | Response magnitude: frequency domain (left); time domain (right). | 20 |
| FIGURE 2.6: | Excited bandwidth (top), impulse time (middle), and response magnitude (m) as a function of hammer mass, M_h , and hammer stiffness, K_h . | 22 |
| FIGURE 2.7: | Influence of hammer mass, M_h , on impulse time and excited bandwidth for a constant hammer stiffness $K_h = 500$ N/m. | 23 |
| FIGURE 2.8: | Normalized hammer position, $X_h - X_{t0}$, normalized toll position, $X_t - X_{t0}$, and contact deformation, δ_c , for different values of hammer mass, M_h . $K_h = 500$ N/m. | 24 |
| FIGURE 2.9: | Excited bandwidth (top), impulse time (middle), and response magnitude (m) as a function of target mass, M_t , and target stiffness, K_t . | 25 |
| FIGURE 2.10: | Influence of target stiffness, M_h , on impulse time and excited bandwidth for a constant target mass $M_t = 0.01$ kg. | 26 |
| FIGURE 2.11: | Influence of hammer mass, M_h , on measured response for Target 1 in the presence of sensor noise. Response magnitude (left column); impulse force (middle column); FRF (right column). | 29 |
| FIGURE 2.12: | Influence of hammer mass, M_h , on measured response for Target 2 in the presence of sensor noise. Response magnitude (left column); impulse force (middle column); FRF (right column). | 30 |
| FIGURE 2.13: | 3D Solidworks model of three targets. | 31 |

| | |
|--|----|
| FIGURE 2.14: Schematic representation of experimental setup 1. | 36 |
| FIGURE 2.15: Schematic representation of experimental setup 2. | 37 |
| FIGURE 2.16: Setup used to measure SE motions of NSH HES – 500 high speed spindle. | 39 |
| FIGURE 2.17: Schematic setup of experimental setup to measure amplifier induced phase lag. | 41 |
| FIGURE 2.18: Measured phase lag as a function of oscillation frequency (CG – capacitance gage). | 42 |
| FIGURE 2.19: Comparison of FRF obtained using capacitance gage and accelerometer. | 43 |
| FIGURE 3.1: Tachometer signal. | 45 |
| FIGURE 3.2: Displacement measurement for single impulse load. | 45 |
| FIGURE 3.3: Once-per-revolution SE motion and artifact form error. | 47 |
| FIGURE 3.4: Plot of the measured response and the once-per-revolution fit. | 47 |
| FIGURE 3.5: Extracted direct response measurement. | 48 |
| FIGURE 3.6: Impulse and response window. Magnified time axis (right). | 49 |
| FIGURE 3.7: Effect of response window on displacement data. Magnified displacement axis (right). | 50 |
| FIGURE 3.8: Effect of impulse window on force data. Magnified force axis (right). | 50 |
| FIGURE 3.9: Impact synchronized time average of impulse force. | 51 |
| FIGURE 3.10: Impact synchronized time average of direct response data. | 52 |
| FIGURE 3.11: FFT of response (left) and impulse (right) signals. | 52 |
| FIGURE 3.12: Real (top) and imaginary (bottom) parts of the estimated FRF. | 54 |
| FIGURE 3.13: Coherence measured at 1000 rpm (left) and 1500 rpm (right): Haas1, y – direction. | 54 |
| FIGURE 3.14: Measured velocity response: time domain (left), frequency domain | 55 |

(right).

| | |
|--|----|
| FIGURE 3.15: FRF estimated using velocity response data. | 55 |
| FIGURE 3.16: Schematic of setup for multi-probe error separation. | 57 |
| FIGURE 3.17: Displacement signal for a single revolution at 1000 rpm. 0 deg (top left), 99.84 deg (top right), 202.5 deg (bottom). | 58 |
| FIGURE 3.18: Combined displacement signal M . | 59 |
| FIGURE 3.19: Fourier coefficients of combined measurement signal: real part F_k (left) and imaginary part G_k (right). | 60 |
| FIGURE 3.20: Fourier coefficients of constructed artifact form error: real part A_k (left) and imaginary part B_k (right). | 61 |
| FIGURE 3.21: Polar plot of artifact form error. | 62 |
| FIGURE 3.22: Polar plot of SE motions: total SE (left), synchronous SE (middle), asynchronous SE (right). | 63 |
| FIGURE 3.23: Polar plot of standard deviation of asynchronous spindle errors measured along the fixed sensitive y-direction on Haas1. | 63 |
| FIGURE 3.24: Polar plot of synchronous SE motions: fixed sensitive x- (left), fixed sensitive y- (middle), rotating sensitive (right). | 64 |
| FIGURE 3.25: FFT of synchronous SE motions: fixed sensitive x- (left), fixed sensitive y- (middle), rotating sensitive (right). | 65 |
| FIGURE 3.26: FFT of synchronous SE motions: fixed sensitive x- (left), fixed sensitive y- (middle), rotating sensitive (right). | 65 |
| FIGURE 3.27: Velocity (left), integrated displacement (middle), and high pass filtered displacement (right) derived from LDV output. | 66 |
| FIGURE 3.28: Superimposed form errors (left) and synchronous SE motions (right) for ten averages. | 67 |
| FIGURE 3.29: Mean and $\pm 3 \sigma$ standard deviation curves for form error (left) and synchronous SE (right). | 67 |
| FIGURE 3.30: Delay in detecting spindle 0° orientation. | 69 |
| FIGURE 3.31: Measured synchronous SE motions at the two different cross- | 70 |

sections.

| | |
|---|----|
| FIGURE 3.32: Form error of the artifact at the two different cross-sections. | 70 |
| FIGURE 4.1: Standard cylindrical artifact FRF: x-direction. | 73 |
| FIGURE 4.2: Standard cylindrical artifact FRF: x-direction (magnified view). | 73 |
| FIGURE 4.3: Changes in magnitude and frequency of two most compliant modes: cylindrical artifact FRF measurement, x-direction. | 73 |
| FIGURE 4.4: Standard cylindrical artifact FRF: y-direction. | 74 |
| FIGURE 4.5: Standard cylindrical artifact FRF: y-direction (magnified view). | 74 |
| FIGURE 4.6: Changes in magnitude and frequency of two most compliant modes: cylindrical artifact FRF measurement, y-direction. | 74 |
| FIGURE 4.7: Solid carbide blank FRF: x-direction. | 76 |
| FIGURE 4.8: Solid carbide blank FRF: x-direction (magnified view). | 76 |
| FIGURE 4.9: Changes in magnitude and frequency of two most compliant modes: solid carbide | 76 |
| FIGURE 4.10: Solid carbide blank FRF: y-direction. | 77 |
| FIGURE 4.11: Solid carbide blank FRF: y-direction. (magnified view). | 77 |
| FIGURE 4.12: Changes in magnitude and frequency of two most compliant modes: solid carbide | 77 |
| FIGURE 4.13: Comparison of artifact form error measured at different spindle speeds. | 78 |
| FIGURE 4.14: Synchronous SE motion: fixed sensitive x-direction (left); fixed sensitive y-direction (middle); rotating sensitive direction (right). Spindle speeds: 500 rpm, 1000 rpm, 1500 rpm, 2000 rpm. | 79 |
| FIGURE 4.15: Synchronous SE motion: fixed sensitive x-direction (left); fixed sensitive y-direction (middle); rotating sensitive direction (right). Spindle speeds: 2500 rpm, 3000 rpm, 3500 rpm, 4000 rpm. | 80 |
| FIGURE 4.16: Peak-to-valley estimate of synchronous SE motions. | 81 |
| FIGURE 4.17: 1σ standard deviation of asynchronous SE motion: fixed sensitive | 82 |

x-direction (top); fixed sensitive y-direction (middle); rotating sensitive direction (bottom).

| | |
|--|----|
| FIGURE 4.18: Maximum 1σ standard deviation of asynchronous SE motion. | 83 |
| FIGURE 4.19: Magnitude of FFT of synchronous SE in fixed-sensitive x-direction. | 84 |
| FIGURE 4.20: Magnitude of FFT of synchronous SE in fixed-sensitive y-direction. | 85 |
| FIGURE 4.21: Magnitude of FFT of synchronous SE in rotating sensitive direction. | 86 |
| FIGURE 4.22: Magnitude of FFT of asynchronous SE in fixed-sensitive x-direction. | 87 |
| FIGURE 4.23: Magnitude of FFT of asynchronous SE in fixed-sensitive y-direction. | 88 |
| FIGURE 4.24: Magnitude of FFT of asynchronous SE in rotating sensitive direction. | 89 |
| FIGURE 4.25: Speed-dependent FRF measurements on high speed spindle: x-direction. | 91 |
| FIGURE 4.26: Changes in magnitude and frequency of two most compliant modes: x-direction. | 91 |
| FIGURE 4.27: Speed-dependent FRF measurements on high speed spindle: y-direction. | 92 |
| FIGURE 4.28: Changes in magnitude and frequency of two most compliant modes: y-direction. | 92 |
| FIGURE 4.29: Comparison of artifact form error measured at different spindle speeds. | 93 |
| FIGURE 4.30: Peak-to-valley estimate of synchronous SE motions. | 94 |
| FIGURE 4.31: Synchronous SE: fixed sensitive x-direction (top), fixed sensitive y-direction (middle), rotating sensitive direction (bottom). | 95 |
| FIGURE 4.32: Maximum 1σ standard deviation of asynchronous SE motion. | 96 |
| FIGURE 4.33: 1σ standard deviation of asynchronous SE motion: fixed sensitive | 97 |

| | | |
|--------------|--|-----|
| | x-direction (top); fixed sensitive y-direction (middle); rotating sensitive direction (bottom). | |
| FIGURE 4.34: | Magnitude of FFT of synchronous SE in fixed-sensitive x-direction. | 99 |
| FIGURE 4.35: | Magnitude of FFT of synchronous SE in fixed-sensitive y-direction. | 100 |
| FIGURE 4.36: | Magnitude of FFT of synchronous SE in rotating-sensitive direction. | 101 |
| FIGURE 4.37: | Magnitude of FFT of asynchronous SE in fixed-sensitive x-direction. | 102 |
| FIGURE 4.38: | Magnitude of FFT of asynchronous SE in fixed-sensitive y-direction. | 103 |
| FIGURE 4.39: | Magnitude of FFT of asynchronous SE in rotating-sensitive direction. | 104 |
| FIGURE 5.1: | Schematic of the RCSA components. | 108 |
| FIGURE 5.2: | Optimization flow chart. | 112 |
| FIGURE 5.3: | Measured direct FRF (H_{11}^m) with selected modes (crosses). | 114 |
| FIGURE 5.4: | The effect of H_{sens} on peak identification ($H_{sens} = 1$: circles ; $H_{sens} = 20$: cross). | 114 |
| FIGURE 5.5: | Selection of frequency range. Influence of constraints a) and c). | 117 |
| FIGURE 5.6: | Selection of frequency range. Influence of constraint b). | 117 |
| FIGURE 5.7: | Optimal fit at different steps of the individual mode optimization process for mode at 2254 Hz. | 118 |
| FIGURE 5.8: | Identification of three modes with the largest absolute value of the imaginary part. The floating modes were distributed around these modes. | 119 |
| FIGURE 5.9: | Optimization for individual mode with contributions of other modes taken into account. | 121 |
| FIGURE 5.10: | Comparison between optimized fit and experimental measurement. The fit for all 20 iterations are superimposed on the | 122 |

same plot.

| | |
|---|-----|
| FIGURE 5.11: Comparison of fit and measured H_{11} direct FRF measured at tip of the spindle artifact. | 123 |
| FIGURE 5.12: Individual H_{11}^j FRFs for the individual fixed-free EB beams. | 123 |
| FIGURE 5.13: Simulated L_{11} and N_{11} (left) and P_{11} (right) receptances at the tip of the artifact. | 124 |
| FIGURE 5.14: Solidworks model of fluted end mill. | 125 |
| FIGURE 5.15: Modal analysis of endmill performed in ANSYS. First bending mode. | 126 |
| FIGURE 5.16: Equivalent diameter depiction of the fluted section. | 126 |
| FIGURE 5.17: Models of the spindle artifact, blank-holder, and tool-holder assembly. | 127 |
| FIGURE 5.18: Comparison between predicted and measured tool tip FRF: x-direction. | 130 |
| FIGURE 5.19: Comparison between predicted and measured tool tip FRF: y-direction. | 131 |
| FIGURE 6.1: Speed-dependent specific cutting force coefficient, K_s (left), and cutting force angle, β (right). | 133 |
| FIGURE 6.2: Tool tip FRF estimated using standard cylindrical artifact FRF measurements: x-direction. | 134 |
| FIGURE 6.3: Tool tip FRF estimated using standard cylindrical artifact FRF measurements: y-direction. | 135 |
| FIGURE 6.4: Tool tip FRF estimated using solid carbide blank FRF measurements: x – direction. | 136 |
| FIGURE 6.5: Tool tip FRF estimated using solid carbide blank FRF measurements: y – direction. | 136 |
| FIGURE 6.6: Magnitude of interpolated speed-dependent tool tip FRF: x-direction (left), y-direction (right). | 137 |
| FIGURE 6.7: Speed-dependent stability lobe diagram comparison. | 138 |

| | | |
|--------------|--|-----|
| FIGURE 6.8: | Experimental setup for machining stability trials. | 139 |
| FIGURE 6.9: | Machining stability trials: blue star indicates stable cut; red cross indicates unstable cut. | 140 |
| FIGURE 6.10: | Magnitude of $ A(f) $ at the different combinations of b_{lim} and Ω . | 142 |
| FIGURE A.1: | Standard cylindrical artifact FRF (Haas2): x-direction. | 153 |
| FIGURE A.2: | Standard cylindrical artifact FRF (Haas2): y-direction. | 153 |
| FIGURE A.3: | Solid carbide blank FRF (Haas2): x-direction. | 154 |
| FIGURE A.4: | Solid carbide blank FRF (Haas2): y-direction. | 154 |
| FIGURE A.5: | Standard cylindrical artifact FRF (Haas3): x-direction. | 155 |
| FIGURE A.6: | Standard cylindrical artifact FRF (Haas3): y-direction. | 155 |
| FIGURE A.7: | Solid carbide blank FRF (Haas3): x-direction. | 156 |
| FIGURE A.8: | Solid carbide blank FRF (Haas3): y-direction. | 156 |
| FIGURE B.1: | Peak-to-valley estimate of synchronous SE motions. | 157 |
| FIGURE B.2: | Synchronous SE motion: fixed sensitive x-direction (left); fixed sensitive y-direction (middle); rotating sensitive direction (right). Spindle speeds: 500 rpm, 1000 rpm, 1500 rpm, 2000 rpm. | 158 |
| FIGURE B.3: | Synchronous SE motion: fixed sensitive x-direction (left); fixed sensitive y-direction (middle); rotating sensitive direction (right). Spindle speeds: 2500 rpm, 3000 rpm, 3500 rpm, 4000 rpm. | 159 |
| FIGURE B.4: | Magnitude of FFT of synchronous SE in fixed sensitive x-direction. | 160 |
| FIGURE B.5: | Magnitude of FFT of synchronous SE in fixed sensitive y-direction. | 161 |
| FIGURE B.6: | Magnitude of FFT of synchronous SE in rotating-sensitive direction. | 162 |
| FIGURE B.7: | Maximum 1σ standard deviation of asynchronous SE motion. | 163 |
| FIGURE B.8: | 1σ standard deviation of asynchronous SE motion: fixed sensitive x-direction (top); fixed sensitive y-direction (middle); rotating | 164 |

| | | |
|--------------|---|-----|
| | sensitive direction (bottom). | |
| FIGURE B.9: | Magnitude of FFT of asynchronous SE in fixed sensitive x-direction. | 165 |
| FIGURE B.10: | Magnitude of FFT of asynchronous SE in fixed sensitive y-direction. | 166 |
| FIGURE B.11: | Magnitude of FFT of asynchronous SE in rotating sensitive direction. | 167 |
| FIGURE B.12: | Peak-to-valley estimate of synchronous SE motions. | 168 |
| FIGURE B.13: | Synchronous SE motion: fixed sensitive x-direction (left); fixed sensitive y-direction (middle); rotating sensitive direction (right). Spindle speeds: 500 rpm, 1000 rpm, 1500 rpm, 2000 rpm. | 169 |
| FIGURE B.14: | Synchronous SE motion: fixed sensitive x-direction (left); fixed sensitive y-direction (middle); rotating sensitive direction (right). Spindle speeds: 500 rpm, 1000 rpm, 1500 rpm, 2000 rpm. | 170 |
| FIGURE B.15: | Magnitude of FFT of synchronous SE in fixed sensitive x-direction. | 171 |
| FIGURE B.16: | Magnitude of FFT of synchronous SE in fixed sensitive y-direction. | 172 |
| FIGURE B.17: | Magnitude of FFT of synchronous SE in rotating sensitive direction. | 173 |
| FIGURE B.18: | Maximum 1σ standard deviation of asynchronous SE motion. | 174 |
| FIGURE B.19: | 1σ standard deviation of asynchronous SE motion: fixed sensitive x-direction (top); fixed sensitive y-direction (middle); rotating sensitive direction (bottom). | 175 |
| FIGURE B.20: | Magnitude of FFT of asynchronous SE in fixed sensitive x-direction. | 176 |
| FIGURE B.21: | Magnitude of FFT of asynchronous SE in fixed sensitive y-direction. | 177 |
| FIGURE B.22: | Magnitude of FFT of asynchronous SE in rotating-sensitive direction. | 178 |
| FIGURE C. 1: | Comparison between predicted and measured tool tip FRF: x- | 179 |

direction.

FIGURE C. 2: Comparison between predicted and measured tool tip FRF: y- 179
direction.

FIGURE C. 3: Comparison between predicted and measured tool tip FRF: x- 180
direction.

FIGURE C. 4: Comparison between predicted and measured tool tip FRF: y- 180
direction.

LIST OF TABLES

| | |
|---|-----|
| TABLE 2.1: Modal parameters for multiple degree of freedom targets. | 27 |
| TABLE 5.1: Section geometries. All dimensions are in mm. | 128 |
| TABLE 5.2: Material properties | 129 |

CHAPTER 1: INTRODUCTION

1.1 High-speed Machining

Milling is a subtractive manufacturing process, where a rotating tool with defined cutting edges is fed into the workpiece to remove material. Milling finds extensive application in the aerospace and automotive industries, where complex components are often manufactured from single billets of stock material via material removal. Over the last few decades, improvements in rotary bearing and drive technology and performance has led to the development of high-speed machine spindles, capable of speeds over 20,000 rpm, while delivering power in excess of tens of kW. Higher spindle speeds and increased power enable larger material removal rates (MRR) and increased productivity. The MRR, which depends on the depth of cut, is limited by the dynamics of the system. Under certain machining conditions, the dynamics of the process become unstable. Instability, or self-excited vibration, in machining is commonly referred to as chatter. Drawbacks of chatter include:

- poor machined surface quality
- excessive noise
- high part rejection rates
- potential damage to the machine spindle
- higher power consumption
- reduced tool life.

1.2 Machining Stability

In milling operations, material is removed by feeding a rotating cutting tool into the workpiece. The cutting forces during the machining operation depend on the instantaneous chip thickness. Since the tool is not rigid, the cutting forces lead to tool vibration. These vibrations are imprinted on the machined surface as a wavy profile. As the tool rotates, the wavy surface produced by one cutting edge is removed by the next. This is called regeneration of waviness. Therefore, the instantaneous chip thickness depends both on the current state of vibration, as well as on the wavy surface left behind by the previous cutting edge. This introduces a “memory”, or time delay, into the system dynamics [1]. If the instantaneous tool deflection is in phase with the wavy surface produced by the previous cutting edge, then, although the tool is vibrating, the cutting forces depend only on the tool geometry and selected machining parameters and the process is more likely to be stable. However, if the instantaneous tool deflection is out of phase with the previously generated wavy surface, it leads to a variable chip thickness which influences the cutting forces and, subsequently, the tool vibrations. Again, the tool vibrations influence the chip thickness. This introduces a feedback mechanism, which may result in self-excited vibration, referred to as chatter, depending on the depth of cut.

Over the last 50 years, significant effort has gone in developing models to identify machining stability limits that enable pre-process identification of chatter free machining conditions. A stability lobe diagram (SLD), which plots the spindle speed on the abscissa and the axial depth of cut on the ordinate, is used to identify the stability limits. Pioneering work to develop the SLD is described in papers by Tlustý [2], Tobias [3] and Merritt [4]. In 1995, Altintas and Budak [5] proposed a zeroth order approximation of a

Fourier series expansion of the cutting forces to derive an analytical expression for the SLD. The model provided accurate results for milling operations with high radial immersion and/or a large number of cutting edges. Insperger and Stepan [6] used a semi-discretization (SD) method to solve the delayed differential equations to predict chatter. Sims *et al.* [7] employed the SD approach to predict chatter for variable pitch and variable helix angle milling operations. Quintana *et al.* [8] proposed an experimental method to develop a SLD, without the measurement of the tool point dynamics or the cutting force coefficients. Slotting operations were performed on a wedge shaped workpiece and the depth at which chatter occurred was estimated as the stability limit. The process was repeated for different spindle speeds to develop a complete SLD.

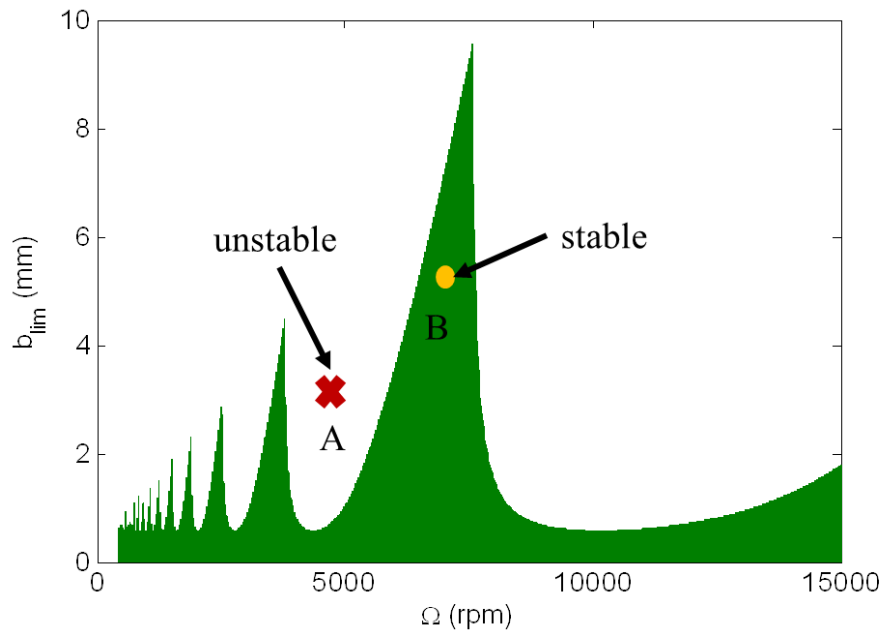


Figure 1.1: Stability lobe diagram: (x) unstable, (o) stable.

In industrial environments, operators often employ conservative machining parameters to avoid chatter, leading to reduced productivity. The ability to predict stable machining parameters (spindle speed and axial depth of cut combinations), enables

machine operators to identify the most favorable machining conditions and maximize productivity. Often, stable machining conditions may be realized by increasing the operating spindle speed, which also increases the MRR and productivity. Figure 1.1 shows an example SLD, where b_{lim} is the limiting axial depth of cut and Ω is the spindle speed. By changing the machining conditions from A to B, the process becomes stable. The spindle speed and permissible axial depth of cut also increase, thereby increasing the MRR.

In order to develop a SLD, the following system and process parameters must be known:

- 1) tool point frequency response function (FRF) in two orthogonal directions perpendicular to the tool axis
- 2) cutting force coefficients (CFCs)
- 3) radial immersion or step-over distance
- 4) number of cutting edges on the tool.

The radial immersion and the number of cutting edges are operator defined. The CFCs relate the instantaneous chip area to the cutting forces. The CFCs depend on the workpiece material and the tool geometry and may be identified experimentally for a particular tool-workpiece combination. The tool point FRF depends on the machine-spindle-holder-tool dynamics. The tool point FRF may be measured by modal testing or predicted.

1.3 Effects of Spindle Speed on Spindle Dynamics

Typically, the tool point FRF used in stability analysis is measured when the spindle is stationary. However, the dynamics of a machine spindle may change with spindle

speed due to centrifugal effects, gyroscopic effects, changes in bearing preload, and thermal effects. The changes in the tool point dynamics with spindle speed must be considered to accurately estimate the stability boundary.

With the development of faster and more powerful machine spindles, substantial research effort has focused on developing spindle models that include speed-dependent thermal and structural effects. These models provide machine tool designers with a useful tool for optimizing spindle designs. For example, Jorgensen [9, 10] and Shin [10] developed a finite element (FE) model for a machine spindle system which coupled the non-linear bearing model with the Timoshenko beam FE spindle model.

The spindle drive motor and friction in rolling contact bearings are significant heat sources in machine spindles. The temperature increase during spindle operation leads to dimensional changes in spindle components. These dimensional changes may affect the bearing preload and subsequently, the spindle dynamics. Bossmanns and Tu [11] proposed a power flow model which predicted the thermal distribution for the entire motorized spindle assembly and included the thermal effects of the drive motor and friction in the angular contact bearings. Lin *et al.* [12] proposed an integrated thermo-mechanical-dynamic model, which integrated the thermal model with the bearing model and the spindle FE model. They observed that, for a constant preload, the system stiffness is reduced due to the centrifugal effects of the spindle shaft. The paper identified the effects of spindle speed on bearing preload and changes in natural frequencies of the system, but did not illustrate the FRF. Li and Shin [13] examined the effect of bearing configuration on speed-dependent spindle dynamics.

Cao and Altintas [14-16] also developed a FE model to identify spindle dynamics. The spindle shaft was modeled using the Timoshenko beam FE model and the bearing was described using Jones' theory. Thermal effects were not incorporated in the spindle model. The model coupled the dynamics of the spindle-holder-tool assembly with the measured dynamics of the milling machine without the spindle. The model also predicted the time domain response of the spindle to cutting forces using incremental FE methods. Holkup *et al.* [17] developed a thermo-mechanical model using FE modeling in ANSYS to examine both transient and steady-state spindle speed-dependent thermal effects on bearing preload.

Movahhedy and Mosaddegh [18] used Timoshenko beam theory to show that gyroscopic effects lower the critical depth of cut, especially at high speeds. Gagnol *et al.* [19] proposed a model-based speed-dependent SLD where the speed-dependent spindle dynamics were estimated using a FE model. A global readjustment procedure was employed to tune the material and damping properties of the spindle model to match the modeled FRF with the measured FRF. Later, Gagnol *et al.* [20] proposed a three dimensional speed-dependent SLD which also accounted for the workpiece dynamics. When machining thin walled sections, for example, the workpiece dynamics become relevant to chatter prediction. More recently, Cao *et al.* [21] also used a FE model to model the spindle assembly and studied the effects of centrifugal and gyroscopic effects on the tool point FRF. It was suggested that, while the gyroscopic effects have minimal influence on the tool point FRF, the centrifugal forces lower the stiffness of the spindle system. None of the models described here account for thermal effects on the spindle dynamics.

Often, the bearing preload of machine spindles is deliberately changed with spindle speed to compensate for speed-dependent structural and thermally induced changes. Changes in bearing preload influence the spindle dynamics. Alfares and Elsharkawy [22] examined the effects of axial preload on grinding machine dynamics and found that increased preload resulted in higher spindle stiffness and natural frequencies. Ozturk *et al.* [23] examined the effects of bearing preload on spindle dynamics for a Starrag Heckert ZT-1000 CNC machining center. The results showed an increase in the natural frequencies with bearing preload. Smith *et al.* [24] examined the effect of drawbar force on spindle dynamics and found that the drawbar force influences both the damping and the natural frequencies of the spindle system.

Models used to simulate spindle behavior require knowledge of the spindle design and construction, bearing stiffness, and drawbar force, which are typically not available to machine tool users. Furthermore, the damping characteristics used in models are not easily predicted and must generally be determined experimentally. Models are more useful in spindle design optimization to identify trends, rather than as tools to accurately predict the tool point FRF necessary for chatter prediction. Previously, Cheng *et al.* [25] performed rotating FRF measurements to measure the speed-dependent spindle dynamics.

This research expands on Cheng's preliminary work. Here, the dynamic response of an artifact clamped in the machine spindle was measured during rotation using impact testing. Tests were conducted at different spindle speeds. A setup was designed to impart an impulse force to the rotating artifact and the dynamic response was measured using

non-contact sensors. A phase correction algorithm was also developed to correct for amplifier-induced, frequency dependent phase lags in the FRF measurement.

1.4 Receptance Coupling Substructure Analysis

In industrial settings, a variety of different tool-tool holder combinations are used in machining processes. It can be prohibitively expensive and time consuming to measure the tool point FRF for each tool- holder combination individually. Receptance Coupling Substructure Analysis (RCSA) is an analytical technique used to couple/de-couple the receptances (or frequency response functions, FRFs) of different components for a structural assembly. The difficult-to-model machine-spindle sub-assembly receptances are measured and archived for each machine spindle. The receptances of the tool- holder sub-assembly are modeled. RCSA may then be used to couple the tool- holder sub-assembly receptances with the machine-spindle sub-assembly receptances to obtain the tool tip FRF for the machine-spindle-holder-tool assembly. RCSA has been shown to significantly reduce the experimental effort required in predicting tool point FRFs for a variety of tool holder-tool combinations. The SLD may then be developed.

Schmitz [26-28] first introduced the application of RCSA to predict tool tip receptances in machining applications. The model considered the translational receptances. Park *et al.* [29] expanded Schmitz's model to include both translational and rotary degrees of freedom and found improved agreement between simulated and predicted receptances. Duncan and Schmitz [30] introduced the three component RCSA method where the spindle-holder-tool assembly was divided into three components. The measured spindle receptances were coupled with the modeled holder and tool receptances using RCSA. Later, Duncan *et al.* [31] used RCSA to show that the dynamic absorber

effect may be exploited in machining operations to increase the critical stability limit by adjusting the tool length. Erturk *et al.* [32] used Timoshenko beam theory to develop a FE model for the spindle-holder-tool assembly using RCSA to couple the different sections of the subassembly. The influence of the bearing was also considered. Schmitz [33] also developed and experimentally verified the RCSA model for torsional and axial frequency response prediction.

The receptances of the tool and tool holder are modeled using FE methods here. Timoshenko beam theory includes rotary inertia and shear deformation effects [34]. Timoshenko beam FE models accurately predict the receptances for both low and high aspect ratio beams. Yokohama [35] proposed the mass and stiffness matrices for a stationary Timoshenko beam. Nelson [36] upgraded the model for a spinning beam to account for rotary inertia, gyroscopic effects, and damping. Later, Greenhill *et al.* [37] upgraded Nelson's rotating Timoshenko beam model to account for conical beam elements. Hutchinson [38] proposed a model to identify shear coefficients to be used in Timoshenko beam theory for a number of different beam cross-sections. Other investigators have used spectral-Tchebychev methods [39-41] and equivalent beam diameter methods [42, 43] to model the fluted portion of end mills, which have helical, variable cross-sections.

Kumar and Schmitz [44] used a sum of equivalent fixed-free Euler-Bernoulli (EB) beams to fit the measured displacement-to-force spindle receptance (measured using a simple artifact inserted in the spindle under test). The displacement-to-moment, force-to-rotation, and rotation-to-moment receptances were then identified using the parameters of the fitted EB beams. This method was shown to improve RCSA predictions with less

experimental effort. This fitting procedure was manually completed mode-by-mode. Ganguly and Schmitz [45] developed a particle swarm optimization (PSO) method to automate the identification of the EB beam parameters. The PSO was specifically tailored to be robust enough to handle a variety of different FRFs. Here, the optimization algorithm is upgraded to make it faster and more reliable. The PSO algorithm was replaced with a number of constrained simplex based Nelder-Mead [46-49] optimization subroutines, which was found to improve optimization performance.

In order to accurately predict assembly receptances using RCSA, translational and rotational connection stiffnesses and damping parameters at the assembly interfaces must be considered. Schmitz *et al.* [50] developed a FE method to estimate the connection parameters for a shrink fit tool holder. Erturk *et al.* [51] conducted an effect analysis using a FE model to show that the natural frequency of the tool mode was most effected by the translational connection stiffness, while the magnitude of the tool mode depends on the translational contact damping at the tool holder-tool interface. Ozsahin *et al.* [52] proposed a closed form solution to identify contact parameters for a spindle-holder-tool assembly based on experimental data. Wang *et al.* [53] proposed a particle swarm optimization method to optimize for the connection parameters.

1.5 Spindle Error Motions

Spindle error (SE) motions quantify the “wandering” of the spindle axis as a function of the rotation angle. Characterizing the SE motions provides a quantitative estimate of a machine spindle’s quality. As noted previously, spindle speed has been shown to have a significant effect on spindle dynamics. Here, the effects of spindle speed on SE motions were studied.

SE motion measurements are complicated by the necessity to accurately isolate the errors in the motion of the spindle axis from artifact form errors. Evans *et al.* [54] surveyed the different reversal techniques and provided an overview of methods used to isolate instrument errors from part errors. Donaldson [55] proposed a ball reversal technique for isolating SE motions from the ball errors. Gredja *et al.* [56] improved upon the implementation of the Donaldson ball reversal technique by incorporating a precision rotary table. The rotary table was used in the reversal process, eliminating any errors which may occur due to handling and fixturing of setup components. All reversal techniques required more than one measurement to isolate SE motions from artifact form error. Whitehouse [57] first suggested the use of multiple displacement sensors, strategically positioned around the spindle to measure the SE motions in a single setup without the need to perform any reversal. Marsh *et al.* [58] employed the multi-probe error separation method to identify the SE motions of high precision spindles and identified the optimal angular orientations for the multiple sensors. The multi-probe error separation method can identify both the SE motions and the artifact form errors from one measurement. The multi-step error separation technique [58], operates on a similar mathematical basis as the multi-probe error separation method, but requires multiple measurements to accurately isolate SE motions and artifact form errors. Marsh *et al.* [59] performed a comparative study of the reversal and multi-probe methods and found them to be comparable.

In this study, a setup was built to simultaneously measure the SE motions, the artifact form error, and the dynamic response of the spindle at the artifact tip. Typically, in SE motion measurements a precision ground sphere with negligible form error is used as the

artifact. However, in this study, the standard cylindrical artifact used in RCSA was used. Therefore, the artifact form errors cannot be ignored and must be captured with each measurement. Consequently, a multi-probe error separation method was used here. In this study, the SE motions were measured over the entire range of spindle speeds. The results showed a significant influence of spindle speed on SE motions.

1.6 Research Objectives and Scope

The objective of the research was to experimentally characterize the effects of spindle speed on spindle performance. An experimental setup was designed, constructed, and calibrated to apply a selectable impulse force and measure the dynamic response while the spindle is rotating. The SE motions were also measured simultaneously using a three-probe error separation method. The speed-dependent changes in the tool point FRF were used to develop an interpolated speed-dependent SLD that provides an accurate estimation of the machining stability boundary. A robust optimization procedure was developed to identify equivalent fixed-free EB beam parameters for each mode of the displacement-to-force spindle receptance. Identifying the EB beam parameters reduced the experimental effort required and improved the quality of predictions in RCSA. The changes in the SE motions were also measured to quantitatively assess the quality of a machine spindle over its entire speed range. In this study, the speed-dependent dynamics and SE motions of three different, yet nominally identical Haas TM1 vertical machining centers were measured. Further tests were also performed on an NSK HES-500 high speed spindle.

The dissertation is structured as follows. In chapter 2, a time domain simulation of the contact dynamics and the influence of the dynamic properties of the hammer and target

on the measured FRF are described. The design and construction of the test setup is also discussed. The data analysis procedure is discussed in chapter 3. The experimental measurements are reported in chapter 4. The equivalent fixed-free Euler Bernoulli optimization algorithm and the RCSA technique are described in chapter 5. The speed-dependent stability lobe diagrams and results from experimental chatter trials are reported in chapter 6. Chapter 7 provides conclusions and discussion of the research effort.

CHAPTER 2: EXPERIMENTAL SETUP – DESIGN AND CALIBRATION

The dynamic response of the machine spindle may be measured by modal testing. In modal testing, a known force, $F(t)$, is imparted to the structure and the response, $X(t)$, is measured using an appropriate sensor. For example, the input force may be a hammer impact and the response may be recorded using a displacement sensor. The FRF of the structure may be estimated from [60],

$$H(\omega) = \frac{X(\omega)}{F(\omega)}, \quad (2.1)$$

where $X(\omega)$ and $F(\omega)$ are the fast Fourier transforms (FFT) of the response and force signals, respectively.

2.1 Time Domain Simulation of Impact Dynamics

In order to measure the dynamics of the spindle, it is necessary to impart an impulse force which excites the entire bandwidth of interest. The impulse force and excited bandwidth depend on the dynamics of the hammer, the dynamics of the target, as well as on the geometries and the material properties of the two colliding interfaces. In this section, a time domain simulation to evaluate the influence of the hammer and target dynamics on the excited bandwidth and response is discussed.

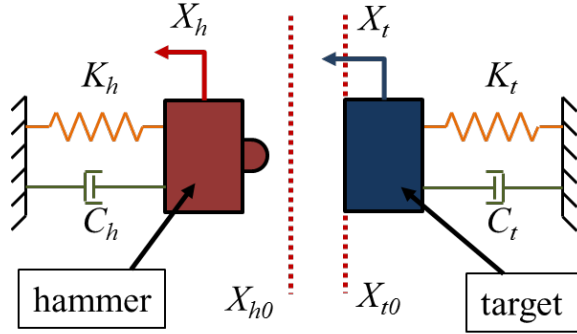


Figure 2.1: Schematic representation of hammer and target interaction.

In order to predict the impulse forces, excited bandwidth and target response levels, an analytical model was developed to simulate the interaction of the hammer and the target. Figure 2.1 shows a schematic representation of the lumped parameter model used to describe the impulse hammer and target. As shown in Figure 2.1, X_h , K_h , M_h , and C_h represent the position, spring constant, mass, and viscous damping coefficient for the hammer. Similarly, X_t , K_t , M_t , and C_t represent the position, spring constant, mass, and viscous damping coefficient for the target. X_{h0} and X_{t0} represent the resting positions of the hammer and the target, respectively. The point of contact, X_{t0} , was kept to the right of the resting position of the hammer, X_{h0} . This ensures a restoring force exerted by the hammer spring, K_h , at the point of contact which pulls the hammer away from the target. To cause an impact the hammer was retracted away from the target and released. The initial position of the hammer at release was defined as X_{hi} . The initial velocity and acceleration of both the hammer and target were set to zero.

At each step, i , in the time domain simulation, the equations of motion of the hammer and target were evaluated. They were defined as,

$$M_h \ddot{X}_h^i + C_h \dot{X}_h^{i-1} + K_h X_h^{i-1} = F_c^i \quad \text{and} \quad M_t \ddot{X}_t^i + C_t \dot{X}_t^{i-1} + K_t X_t^{i-1} = -F_c^i \quad (2.2)$$

respectively. Here, F_c^i , represents the contact force due to the collision between the hammer and the target. Rearranging the terms in Eq. (2.2), the accelerations at the current simulation time step were evaluated as,

$$\ddot{X}_h^i = \frac{F_c^i - C_h \dot{X}_h^{i-1} - K_h X_h^{i-1}}{M_h} \text{ and } \ddot{X}_t^i = \frac{-F_c^i - C_t \dot{X}_t^{i-1} - K_t X_t^{i-1}}{M_t}. \quad (2.3)$$

When X_h^{i-1} was greater than X_t^{i-1} , there was no contact between the two bodies, and F_c^i was set to zero. However, when X_h^{i-1} was less than X_t^{i-1} , it implied that the two bodies were in contact with each other. The difference $X_t^{i-1} - X_h^{i-1}$ was defined as δ_c^i and represents the sum of the deformations of the two colliding bodies in the region of contact. Under these conditions, the contact force was defined using sphere-sphere Hertzian contact theory [61-65]. The contact force including hysteresis damping was expressed as [61, 63],

$$F_c^i = K (\delta_c^i)^{1.5} \left(1 + \frac{3(1-e^2)}{4} \frac{\dot{\delta}_c^i}{V_i} \right), \quad (2.4)$$

where V_i is the velocity at the point of impact and e is the coefficient of restitution. K was defined as,

$$K = \frac{4}{3(k_1 + k_2)} \left\{ \frac{r_1 r_2}{r_1 + r_2} \right\}^{1/2}. \quad (2.5)$$

Here, r_1 and r_2 represent the radii of the two colliding bodies. The k_1 and k_2 terms depend upon the material properties and were defined as,

$$k_1 = \frac{1-\nu_1^2}{E_1} \text{ and } k_2 = \frac{1-\nu_2^2}{E_2} \quad (2.6)$$

respectively. Here, E_1 and E_2 denote the elastic modulus, while ν_1 and ν_2 represent the Poisson's ratio. Other contact interactions such as plane-cylinder, sphere-cylinder, or sphere-plane may also be used depending upon the geometries of the colliding bodies.

Once the contact force, F_c^i , was estimated, the accelerations of the two bodies were calculated using Eq. (2.3). Then, the velocities and positions for the hammer and target at the current simulation step, i , were evaluated using numerical Euler integration:

$$\begin{aligned}\dot{X}_h^i &= \dot{X}_h^{i-1} + \ddot{X}_h^i \cdot \delta t \quad \text{and} \quad \dot{X}_t^i = \dot{X}_t^{i-1} + \ddot{X}_t^i \cdot \delta t, \\ X_h^i &= X_h^{i-1} + \dot{X}_h^i \cdot \delta t \quad \text{and} \quad X_t^i = X_t^{i-1} + \dot{X}_t^i \cdot \delta t,\end{aligned}\tag{2.7}$$

where δt represents the integration time step. Note that both the hammer and the target may be modelled as multiple degree of freedom systems.

To demonstrate the simulation, an example is provided here. The mass, M_h , and stiffness, K_h , of the hammer were 0.01 kg and 100 N/m, respectively. The mass, M_t , and stiffness, K_t , of the target were 0.1 kg and 1×10^7 N/m, respectively. The initial retracted position of the hammer, X_{hi} , was 10 mm. The point of contact, X_{t0} , was -3 mm. The contact forces were estimated assuming the two colliding bodies to be steel spheres with Young's modulus = 200 GPa and Poisson's ratio = 0.29. The radii of the two spheres, r_1 and r_2 , were set as 6.35 mm and 1 mm respectively. The coefficient of restitution was assumed to be 0.95. Note that these contact parameters and initial conditions were maintained constant throughout this study. Figure 2.2 shows a plot of the normalized hammer position, $X_h - X_{t0}$, the tool position, $X_t - X_{t0}$, and the deformation in the region of contact δ_c . The magnified views of the positions are shown on the right which captures the interaction between the two colliding bodies. Figure 2.3 shows a plot of the contact force.

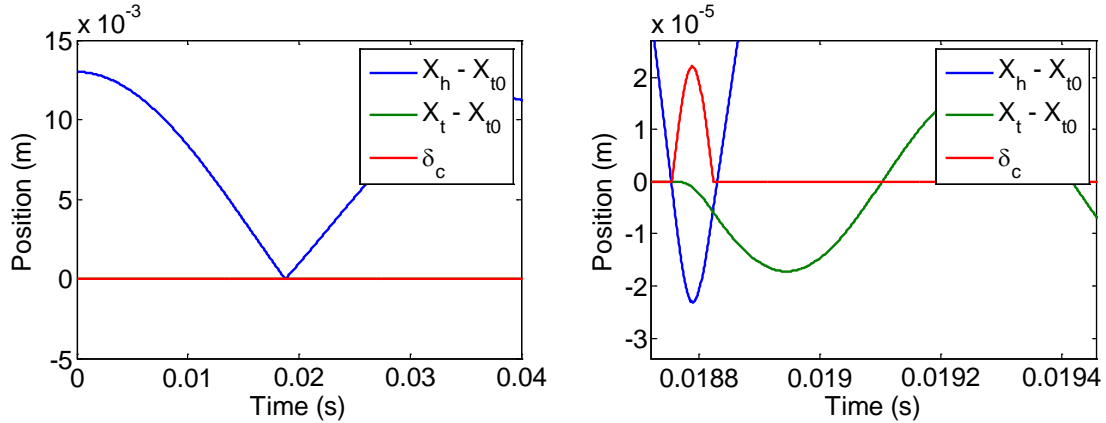


Figure 2.2: Plot of hammer position, X_h , tool position, X_t , and elastic deformation at interface, δ_c .

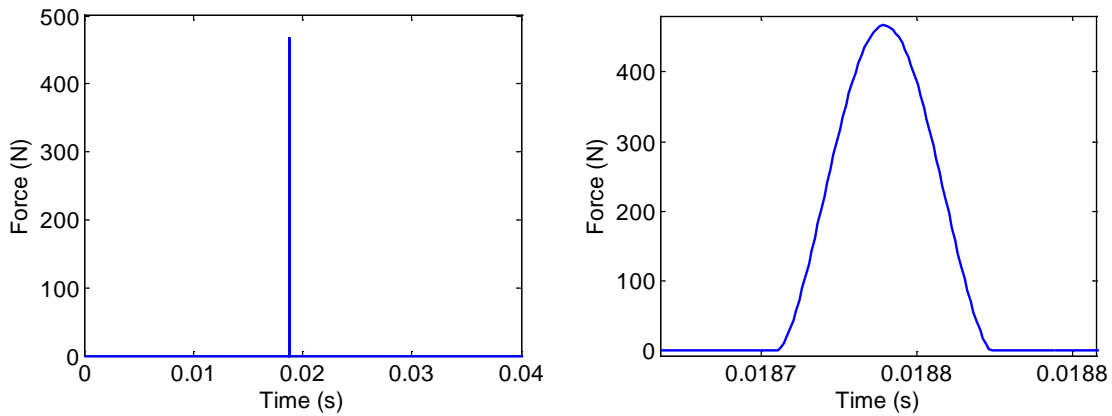


Figure 2.3: Contact force at the point of impact.

In the following section, the influence of the dynamic properties of the hammer and target on the excited bandwidth and response magnitude is examined. First, three terms are defined here.

- (i) Excited bandwidth: The excited bandwidth was defined as the frequency where the normalized amplitude of contact force spectrum represented in the frequency domain first falls below -10 dB. Figure 2.4 (left) shows a plot of the force signal in the frequency domain. The excited bandwidth is shown.

- (ii) Impulse time: The impulse time was defined as the duration between the time at which the hammer first makes contact with the target to the time at which the hammer last touches the target. Figure 2.4 (right) shows a plot of the impulse profile. The defined impulse time is clearly indicated.
- (iii) Response magnitude: The response magnitude was defined as the magnitude of the displacement of the target, expressed in the frequency domain, evaluated at the natural frequency of the target. Figure 2.5 (left) shows a plot of the target displacement in the frequency domain. Figure 2.5 (right) shows the target displacement in the time domain. Note that the target displacement is offset by the contact point X_{t0} . The damping of the hammer, C_h , and the target, C_t , was assumed to be zero. The response magnitude provides an indication of the amplitude of the response. In the presence of sensor noise, it is essential for the applied input impulse to elicit sufficient output target displacement so as to accurately measure the response. This is particularly critical in measuring rotating FRFs as the response is further corrupted by the error motions of the rotating spindle. Therefore, the response magnitude is used as an indicator of the expected target displacement.

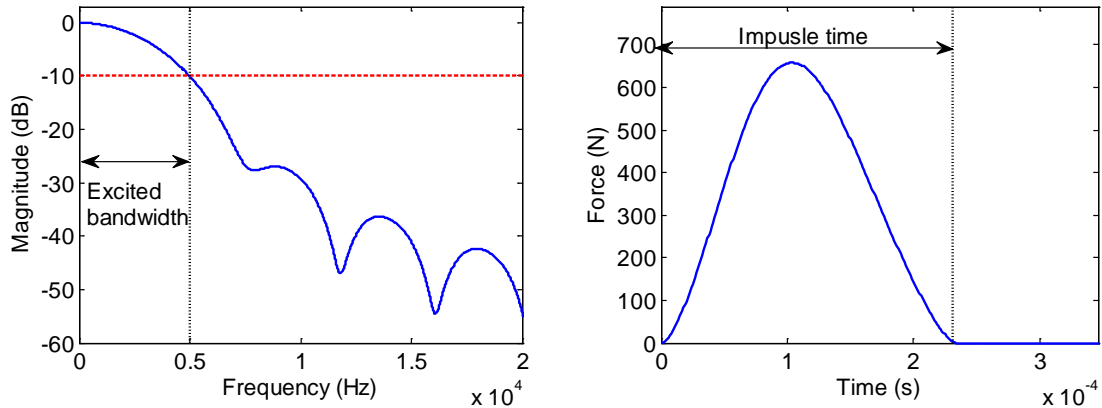


Figure 2.4: Excited bandwidth (left); Impulse time (right).

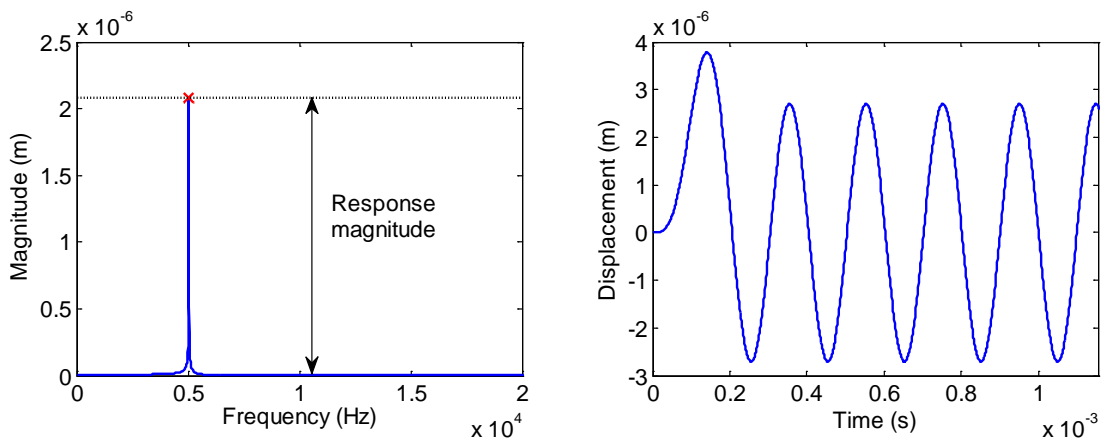


Figure 2.5: Response magnitude: frequency domain (left); time domain (right).

2.1.1 Influence of Hammer Mass and Stiffness

In this section the influence of the hammer mass, M_h , and stiffness, K_h , on excited bandwidth, impulse time and response magnitude is discussed. Here, the mass, M_t , and stiffness, K_t , of the target were kept constant at 0.1 kg and 5×10^7 N/m, respectively. The time domain simulation was performed for a wide range of M_h and K_h values. Figure 2.6 (top), (middle), and (bottom) shows the excited bandwidth, the impulse time and the response magnitude, respectively. The excited bandwidth was found to be the highest at low values of M_h . It was observed that as M_h increased, the excited bandwidth decreased and impulse time increased. A sharp increase in impulse time was observed at around $M_h = 0.05$ kg. As M_h was increased through 0.05 kg, the impulse time increases drastically

from around 0.13 ms to around 0.27 ms. An increase in impulse time was accompanied by a decrease in excited bandwidth. The natural frequency of the target in this simulation was 3558 Hz. This corresponds to an oscillation period of approximately 0.28 ms. Therefore, when the impulse time approached half the period of the target's natural frequency (0.14 ms), a drastic increase in the impulse time was observed.

The plot of the response magnitude (Figure 2.6 bottom) shows that at very low values for M_h the response magnitude was low. Also, at high values of M_h the impulse time increases and the magnitude of the output response decreases. An optimal value of the response magnitude was observed at $M_h = 0.0525$ kg and $K_h = 1000$ N/m.

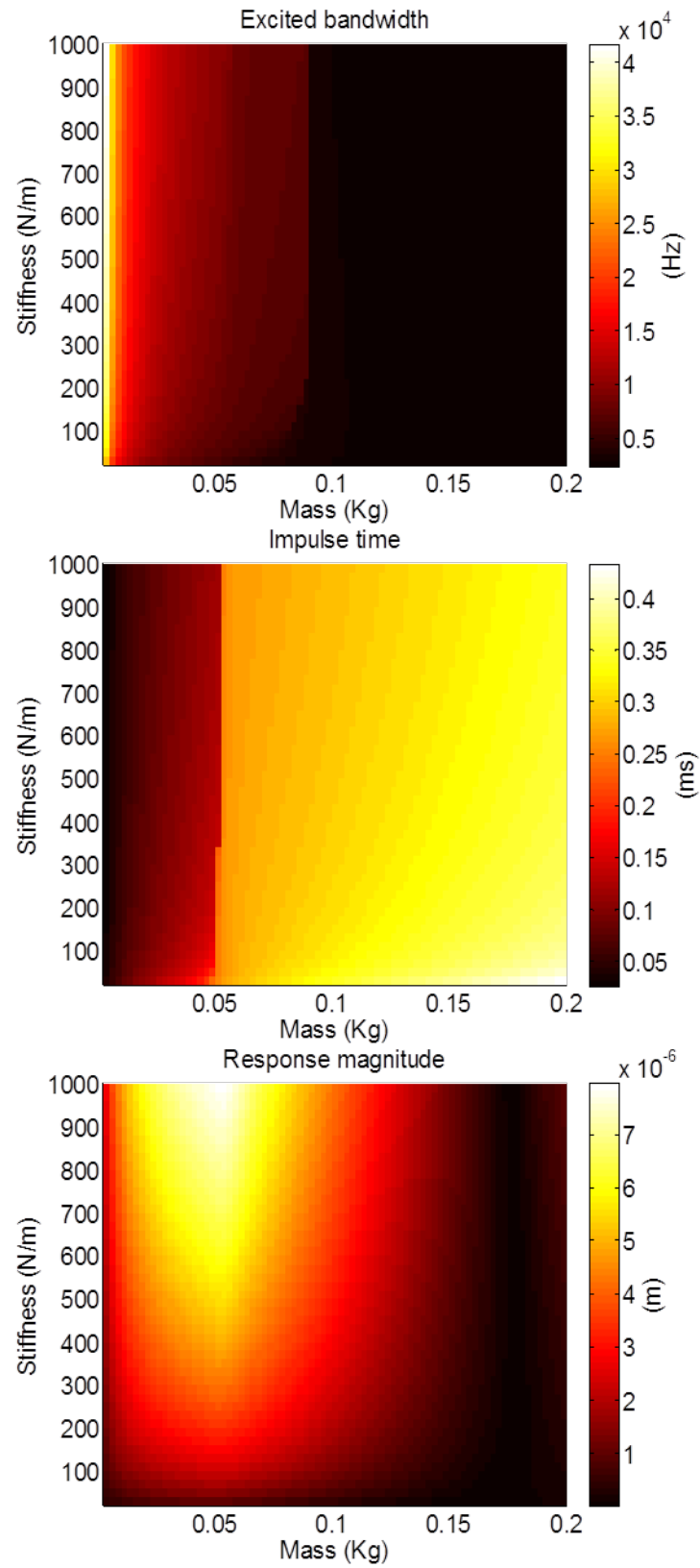


Figure 2.6: Excited bandwidth (top), impulse time (middle), and response magnitude (m) as a function of hammer mass, M_h , and hammer stiffness, K_h .

Figure 2.7 shows a plot of the force impulse in the time and frequency domains (right). K_h was kept constant at 500 N/m and M_h was increased from 0.03 kg to 0.07 kg. As M_h increases beyond 0.05 kg, a second peak appears in the impulse force profile resulting in an increase in the impulse time and the subsequent decrease in excited bandwidth.

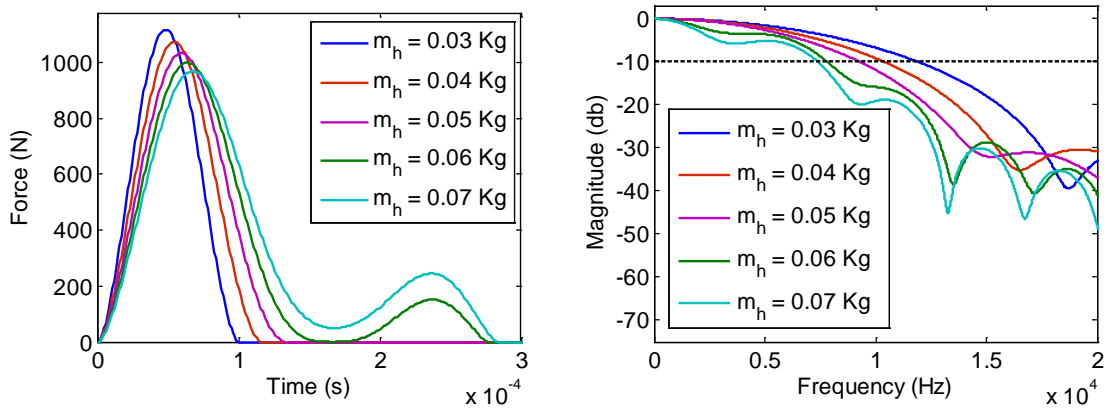


Figure 2.7: Influence of hammer mass, M_h , on impulse time and excited bandwidth for a constant hammer stiffness $K_h = 500$ N/m.

Figure 2.8 shows the normalized hammer position, $X_h - X_{t0}$, the target position, $X_t - X_{t0}$, and the deformation in the region of contact δ_c . As M_h increases, the hammer stays in contact with the target for a longer period of time. It was also observed that as M_h increased, the resulting extended contact time is due to the continuation of contact even after the target has reversed direction and is moving in the same direction as the hammer. Therefore, under these conditions, the hammer takes a longer period to leave the target resulting in a higher impulse time and subsequently a lower excited bandwidth.

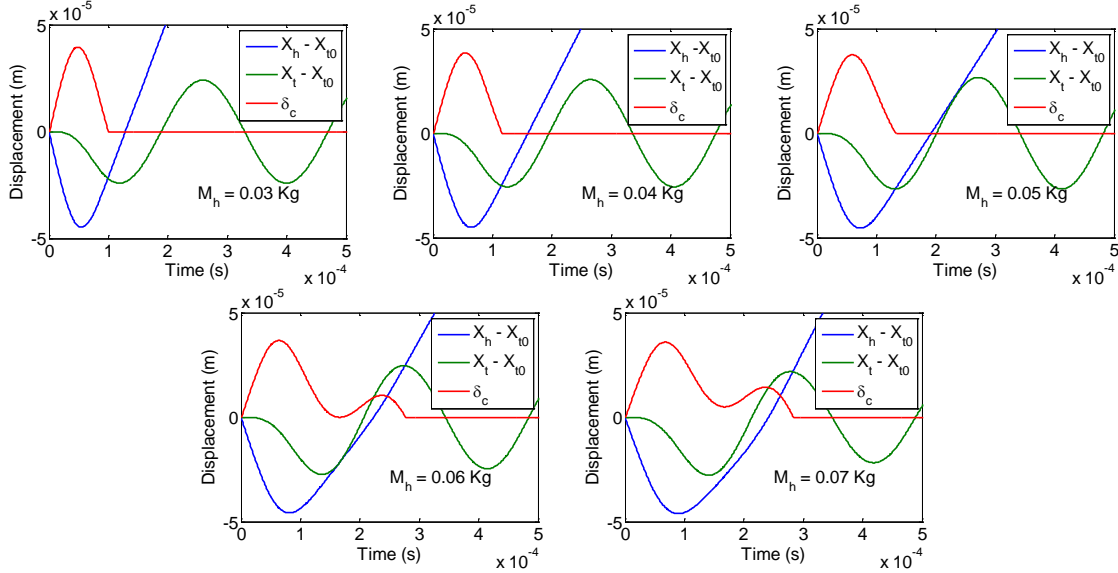


Figure 2.8: Normalized hammer position, $X_h - X_{t0}$, normalized toll position, $X_t - X_{t0}$, and contact deformation, δ_c , for different values of hammer mass, M_h . $K_h = 500$ N/m.

2.1.2 Influence of Target Mass and Stiffness

In this section the influence of the target mass, M_t , and stiffness, K_t , on excited bandwidth, impulse time and response magnitude is studied. Here, the mass, M_h , and stiffness, K_h , of the hammer were maintained constant at 0.1 kg and 200 N/m respectively. The time domain simulation was performed for a range of M_t and K_t values. Figure 2.9 (top), (middle), and (bottom) shows the excited bandwidth, the impulse time and the response magnitude, respectively. It was observed that for 93% of the combinations of K_t and M_t , the excited bandwidth was above 5000 Hz and for 99 % of the combinations of K_t and M_t , the impulse time was below 0.3 ms. However, for a few combinations at low M_t and K_t values, it was observed that the impulse time and excited bandwidth deteriorates. Under these conditions, as described earlier, the hammer maintains contact with the flexible target for an extended time period, which reduces the excited bandwidth.

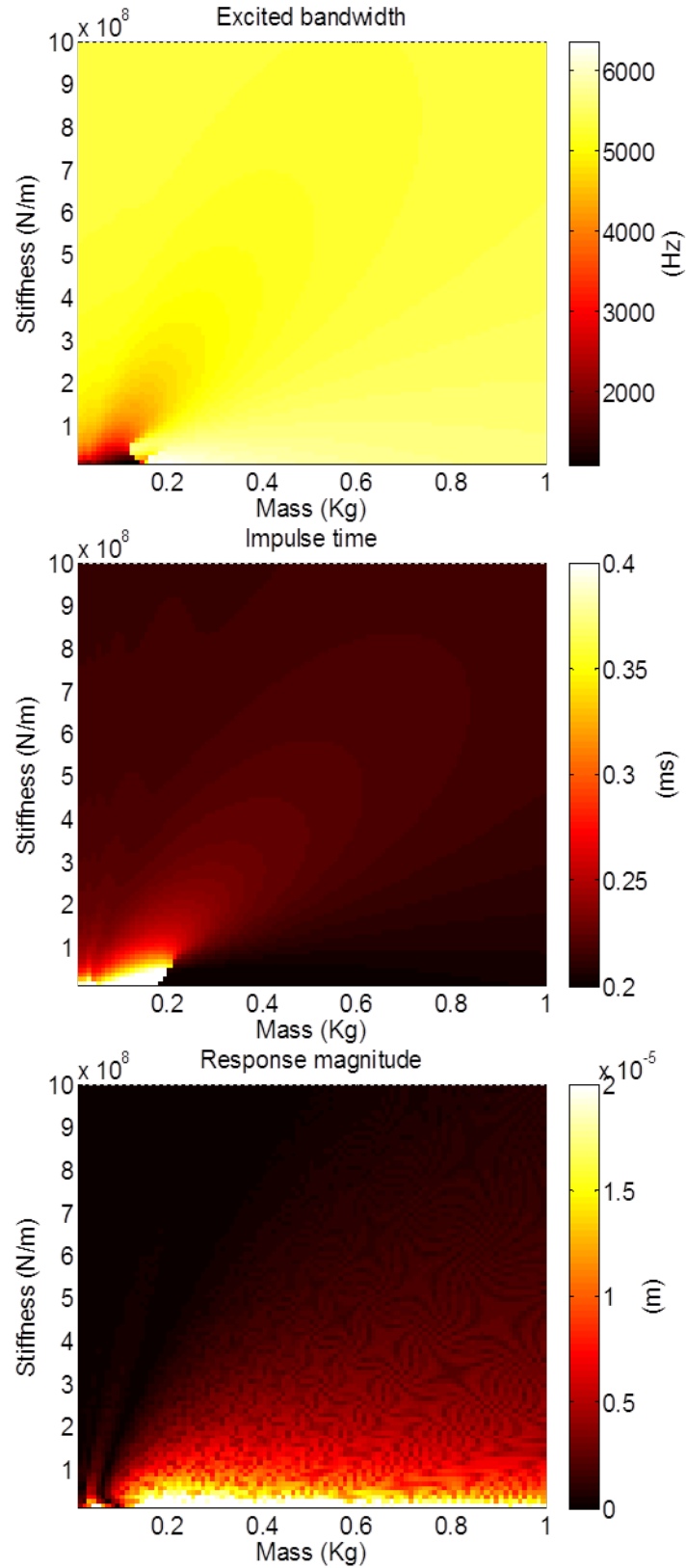


Figure 2.9: Excited bandwidth (top), impulse time (middle), and response magnitude (m) as a function of target mass, M_t , and target stiffness, K_t .

As expected, the response magnitude was found to be higher for low K_t and high M_t combinations. These combinations of target properties have low natural frequencies which are excited by the impulse hammer. As the natural frequency of the target increases (low M_t and high K_t), the excited bandwidth and the response magnitude reduce.

Figure 2.10 shows a plot of the impulse force in the time (left) and frequency (right) domains. The mass of the target, M_t , was kept constant at 0.01 kg and the stiffness was increased. At lower stiffness values, the hammer stays in contact with the target for a longer period of time, which results in higher impulse time and, subsequently, a decrease in excited bandwidth.

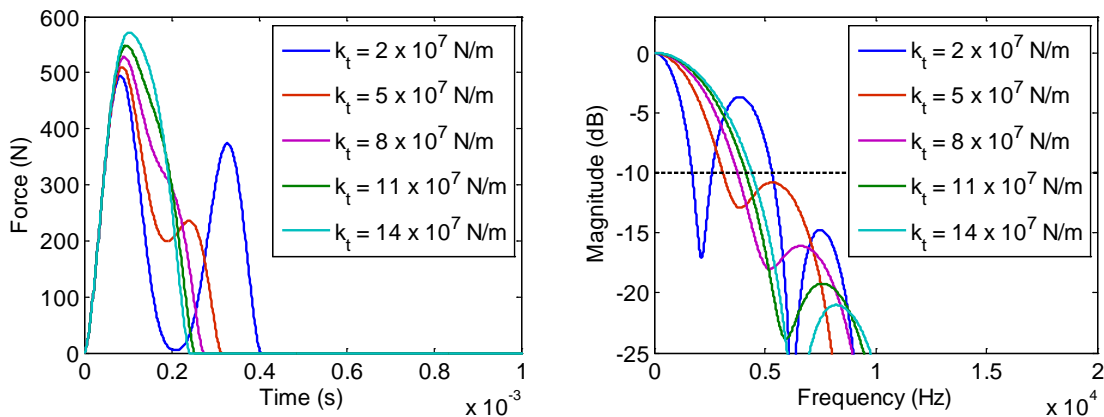


Figure 2.10: Influence of target stiffness, M_h , on impulse time and excited bandwidth for a constant target mass $M_t = 0.01$ kg.

2.1.3 Influence of Hammer Mass on Multiple Degree of Freedom Targets

In this section the influence of the hammer mass on two different multiple degree of freedom targets was explored. Each target is modelled using 10 modes. It must be noted that the mass, stiffness, and damping properties of the multiple degrees of freedom are defined in the modal parameter space. The modal parameters for the two targets are defined in Table 2.1.

Table 2.1: Modal parameters for multiple degree of freedom targets.

| Mode | Target 1 | | | Target 2 | | |
|------|--------------|--------------------------------|-------------------------------|--------------|--------------------------------|-------------------------------|
| | Mass (kg) | Stiffness $\times 10^6$ N/m | Damping $\times 10^3$ Ns/m | Mass (kg) | Stiffness $\times 10^6$ N/m | Damping $\times 10^3$ Ns/m |
| 1 | 2.56 | 76.90 | 1.11 | 0.06 | 11.90 | 0.08 |
| 2 | 1.94 | 78.96 | 1.04 | 0.60 | 30.71 | 0.41 |
| 3 | 6.25 | 69.35 | 7.50 | 4.31 | 157.60 | 1.35 |
| 4 | 125.99 | 813.04 | 27.07 | 0.54 | 36.40 | 0.59 |
| 5 | 14.97 | 234.46 | 9.09 | 7.10 | 103.74 | 3.90 |
| 6 | 125.80 | 547.60 | 39.60 | 0.27 | 101.09 | 0.29 |
| 7 | 1.32 | 278.99 | 3.85 | 0.17 | 149.96 | 0.23 |
| 8 | 2.13 | 1016.30 | 3.82 | 0.22 | 328.74 | 0.21 |
| 9 | 19.26 | 2177.73 | 55.61 | 1.05 | 342.52 | 1.39 |
| 10 | 3.97 | 4781.16 | 7.29 | 0.54 | 1488.68 | 0.99 |

The hammer was modelled as a single degree of freedom mass with a stiffness, K_h , of 100 N/m. As before, the initial position of the hammer, X_{h0} , at the point of release was 10 mm and the point of contact of the hammer with the target, X_{t0} , was -3 mm. At the end of the time domain simulation, a randomly distributed noise with standard deviation of 25 nm was added to the response signal in order to simulate sensor noise. The simulation was repeated for three values of M_h : 0.001 kg, 0.01 kg, and 0.1 kg. Figure 2.11 shows the response (left column), impulse (middle column) and frequency response (right column) plotted in the frequency domain for target 1. Each row in the plot corresponds to a different M_h ; $M_h = 0.001$ kg (top row), $M_h = 0.01$ kg (middle row), and $M_h = 0.1$ kg

(bottom row). Figure 2.12 shows the same for target 2. It should be noted that the maximum amplitude of the FRF for target 1 is around 20% that of target 2.

It was found that when $M_h = 0.001$ kg, the response magnitude was the lowest and the excited bandwidth was the highest. Therefore, although the hammer impulse excites the entire bandwidth of interest, the magnitude of the response is low and therefore susceptible to sensor noise. This is reflected in the FRF. As M_h is increased, the response magnitude increases and the excited bandwidth decreases. At $M_h = 0.1$ kg, low noise was observed in the FRF below 4000 Hz, while the impulse excitation is low above 8000 Hz resulting in increased FRF noise. A similar trend was also observed for the simulations performed on target 2. At $M_h = 0.001$ kg, the excited bandwidth is high, but the impulse response is low leading to high noise in the FRF over the entire bandwidth. As M_h increases, the FRF noise at low frequencies decrease, while the high frequency content of the FRF becomes more susceptible to sensor noise as the excited bandwidth decreases.

In summary, it was shown that the measurement of the target FRF depends upon both the dynamics of the impulse hammer and the target which is being measured. In this study, FRF measurements were performed on three targets: a cylindrical spindle artifact, a half inch diameter carbide blank clamped in a shrink fit holder, and a half inch diameter carbide square end mill tool clamped in a shrink fit holder. To accommodate the varying dynamics of the different targets, two different setups were designed and built with different hammer dynamic properties. The two setups are described in more detail in the following section.

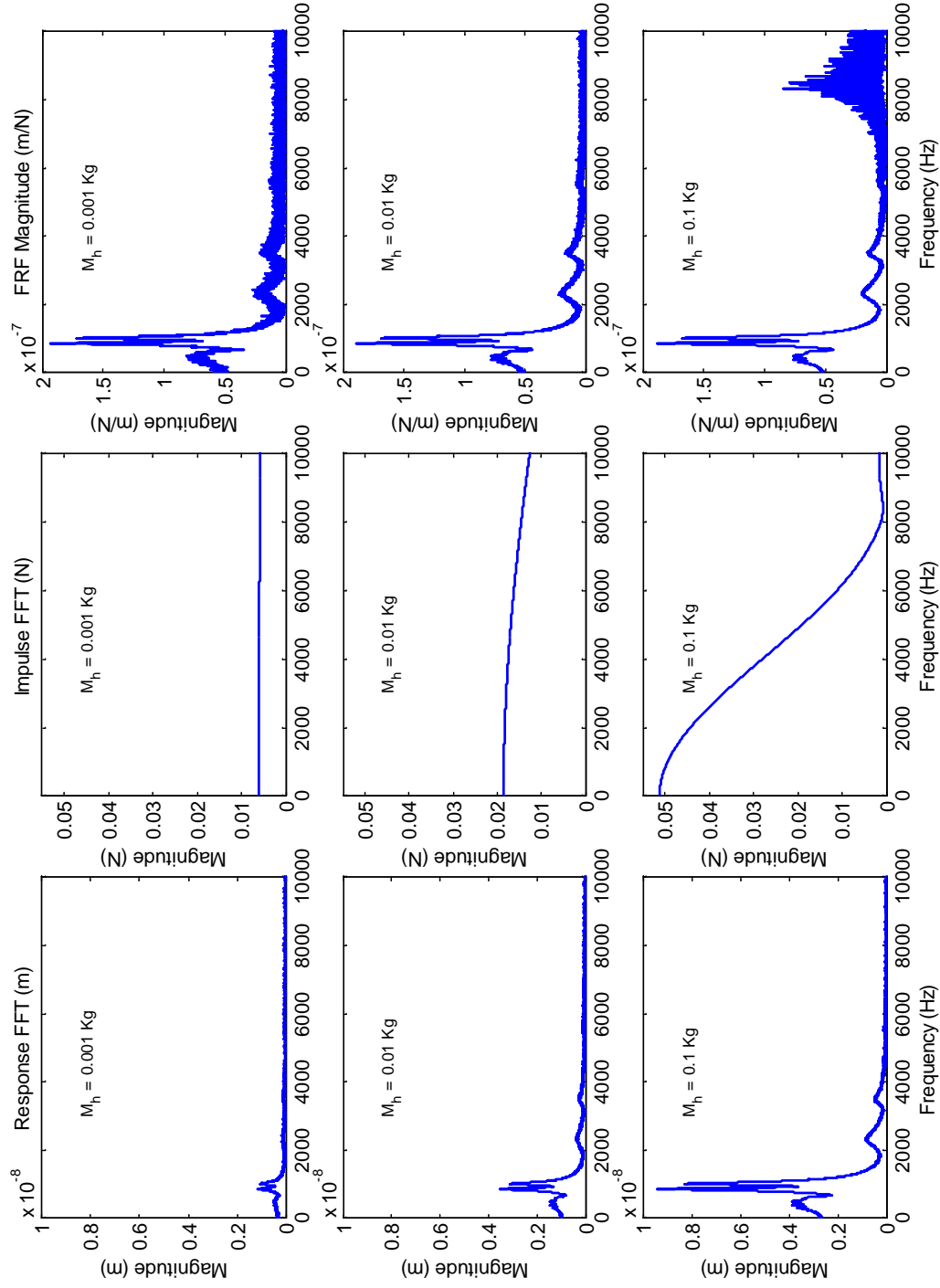


Figure 2.11: Influence of hammer mass, M_h , on measured response for Target 1 in the presence of sensor noise. Response magnitude (left column); impulse force (middle column); FRF (right column).

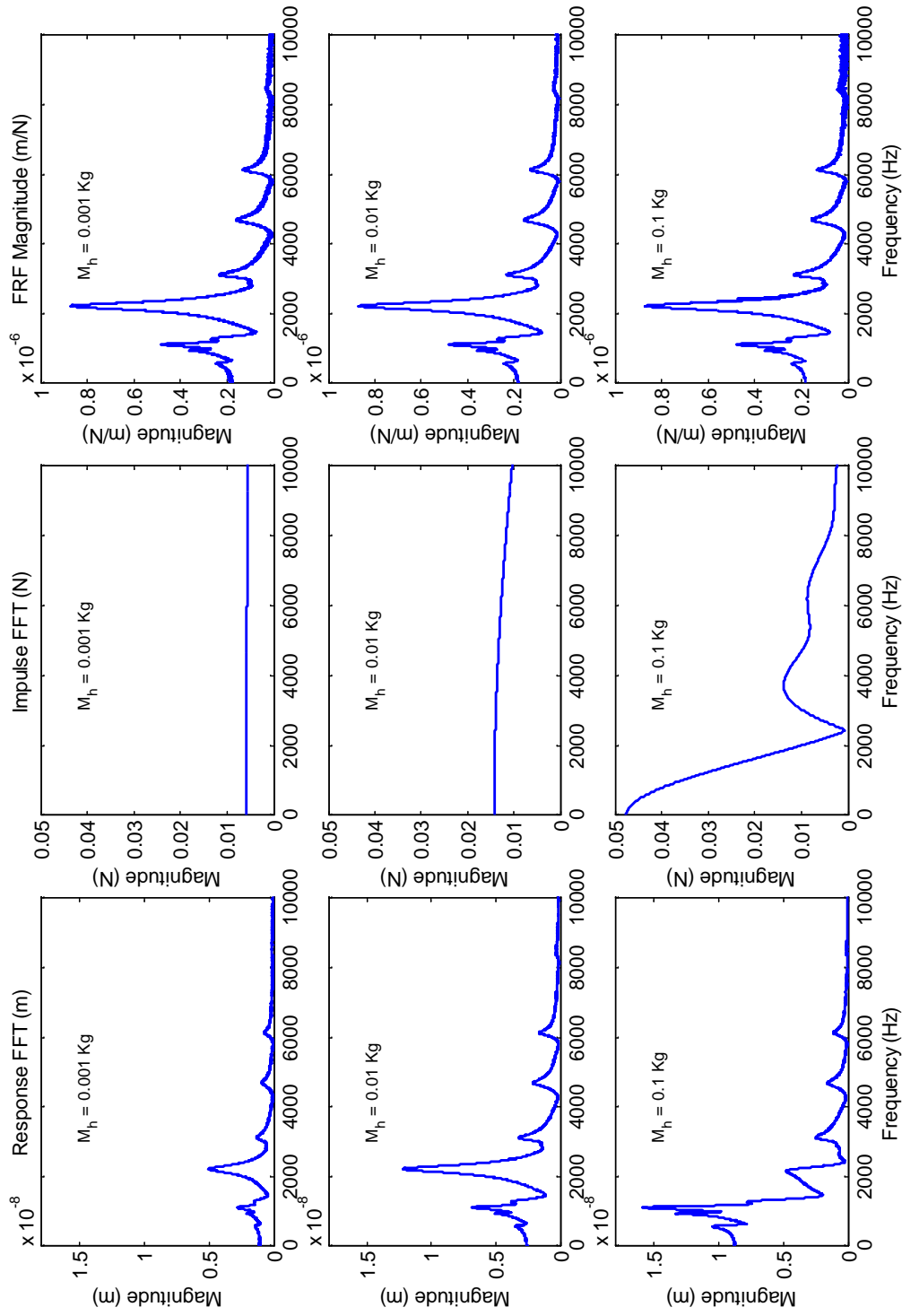


Figure 2.12: Influence of hammer mass, M_h , on measured response for Target 2 in the presence of sensor noise. Response magnitude (left column); impulse force (middle column); FRF (right column).

2.2 Experimental Setup Description

Modal testing was performed on three targets: (1) a cylindrical spindle artifact; (2) a half inch diameter solid carbide cylindrical blank clamped in a shrink fit tool holder, and (3) a half inch diameter square endmill clamped in a shrink fit tool holder. Figure 2.13 shows 3D Solidworks models of the three targets. As demonstrated in the previous section, the noise in the measured FRF depends on the excited bandwidth and response magnitudes. In turn, these parameters depend on the dynamics of the hammer and the target. To accommodate the different dynamics, two different hammer setups were designed and constructed.

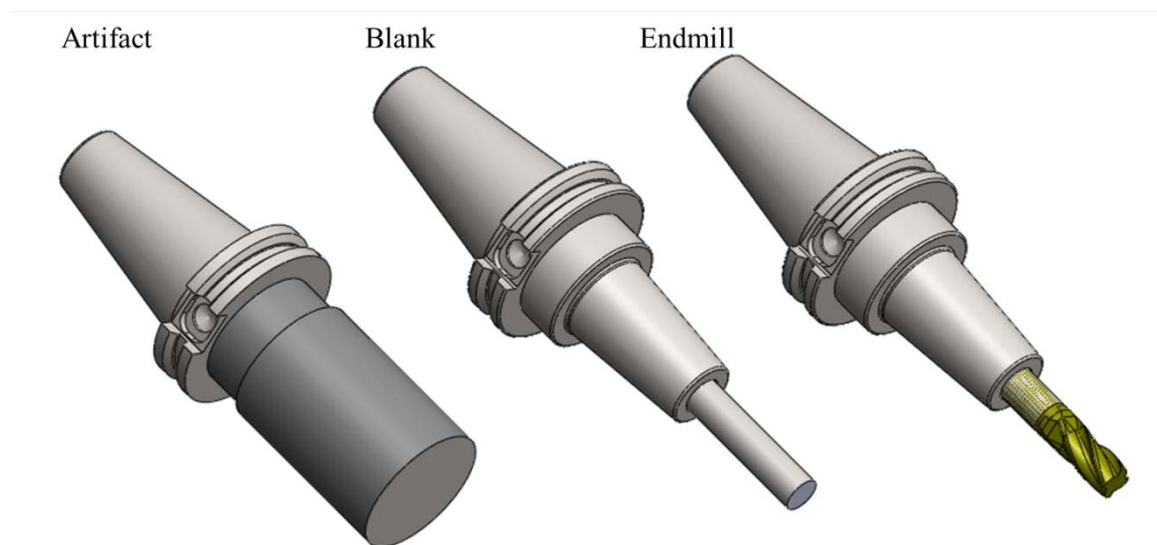


Figure 2.13: 3D Solidworks model of three targets.

2.2.1 Setup 1: High Mass Excitation Hammer

The first setup was designed to measure the dynamics of a standard artifact mounted in the machine spindle at different spindle speeds; see Figure 2.14. A standard cylindrical artifact was mounted in the machine spindle and the FRF at the free end of the artifact was measured. A sub-assembly consisting of a three-axis force dynamometer (Kistler 9252A), an impact tip, and the sensor mount was attached to the carriage of a linear

bearing. A three-axis force dynamometer was selected to measure the normal impulse forces as well as any frictional forces that may arise due to impacting the rotating artifact. A three-channel Kistler 5010B dual mode charge amplifier was used to convert the charge output from the force dynamometer to a voltage signal. This sub-assembly formed the oscillating impact hammer, which translated along the linear bearing and imparted an impulse force to the artifact. The impact hammer, mounted on the carriage of the linear bearing, was spring loaded. The mass of the impulse hammer was 0.21 kg and the stiffness of the spring was estimated to be 200 N/m at the resting position. Note that in this setup the spring constant along the direction of motion of the impulse hammer is nonlinear and depends upon the position of the impulse hammer. Nonlinear spring constants may be accommodated in the time domain simulation.

A 12 V DC electromagnet mounted on a linear motion stage (Zaber Technologies A-LSQ075B-E01) captured and pulled the impact hammer away from the spindle axis. The electromagnet voltage was controlled by a variable voltage DC power supply (Extech Instruments – 382200). When the spring load exceeded the electromagnetic force, the hammer was released. The restoring spring force caused the hammer to impact the artifact. The position of the artifact axis relative to the equilibrium position of the hammer was tuned to avoid multiple impacts. After each strike, the direction of the linear stage was reversed and the stage was moved towards the hammer until it was recaptured by the electromagnet. Dynamic response data was collected for a number of impulses and averaged. The electromagnetic force was controlled by the supply voltage. This provided a control for the retracted length before the striker was released, which, in turn, controlled

the impulse force. A calibration was performed to find the relationship between the supply voltage and the retracted distance before release.

The response of the structure was recorded using a non-contact displacement measuring sensor. In this setup, capacitance gages (Lion Precision C5D) were used to measure the response. The capacitance gage signals were converted to analog voltage outputs by a three-channel Lion Precision Elite Series CPL-290 amplifier. The capacitance gages were mounted in a capacitance gage nest. The nest was mounted on a micrometer-controlled linear stage to position the sensors with respect to the artifact axis. Because the response was measured when the spindle was rotating, the measured response data was corrupted by out-of-roundness form errors of the artifact, as well as any SE motions. To accurately isolate the structural response data, the artifact form errors and spindle axis error motions needed to be identified and extracted. To do so, a multi-probe error separation technique was employed [58]. In this method, three displacement measuring sensors, positioned at strategically selected angular locations around the artifact are used to simultaneously measure both the artifact form errors and the SE motions. The performance of the algorithm is sensitive to the angular orientations of the three displacement measurement sensors. Therefore, the angles selected for the three gages were 0° , 99.84° , and 202.5° . The algorithm to extract the form error and SE motions from the three displacement measurement signals is discussed in section 3.2.

2.2.2 Setup 2: Low Mass Excitation Hammer

To measure the dynamics of the half inch diameter carbide blank, the hammer mass of setup 1 was found to be too high. This resulted in multiple impulse hits and lower excited bandwidths. Therefore, a secondary setup was designed; see Figure 2.15. In this

setup, a PCB086E80 force sensor was mounted on the oscillating part of a parallelogram leaf spring flexure. The flexure was manufactured from Delrin[®] acetal resin. This material was chosen for its easy machinability, good impact resistance, fatigue properties and low Young's modulus compared to metals. The mass of the oscillating part was found to be 0.01 kg and the spring stiffness of the flexure was 623 N/m. The linear motion stage and DC electromagnet were used to retract the oscillating part and trigger the impulse. A laser Doppler vibrometer (Polytec OFV – 534 laser head with OFV-5000 controller), or LDV, was used to measure the response of the structure. The OFV-5000 controller provides an output voltage proportional to the change in velocity of the target. The SE motions and blank form errors were not identified with this setup. However, the once per revolution content of the displacement signal due to these errors were removed from the response signal as described in Section 3.1.

In both setups, a laser tachometer (Terahertz Technologies Limited LT-880) was used to measure the spindle speed and identify the spindle orientation. The tachometer signal served as an indicator to synchronize the angular position of the artifact with the displacement signals measured by the capacitance gages. The angular orientation of the spindle was required to accurately estimate the SE motions and the artifact form errors, which were, in turn, required to extract the dynamic response data from the displacement measurement signals. The tachometer also tracked any variations in the nominally constant spindle speed.

In this study, a National Instruments (NI) data acquisition system (two 16-bit NI 9215 analog input modules mounted in a NI 9417c compact DAQ chassis) was used to collect data. To estimate FRFs over a wide bandwidth, data was collected at a high sampling rate

(100 kHz). The NI DAQ card and the linear motion stage were controlled by a laptop using MATLAB to coordinate the impact and the data collection.

In this study, measurements were performed on three nominally identical Haas TM1 CNC vertical machining centers as well as the NSK HES-500 high speed spindle. Henceforth, in this document, the three Haas machines are referred to as Haas1, Haas2, and Haas3.

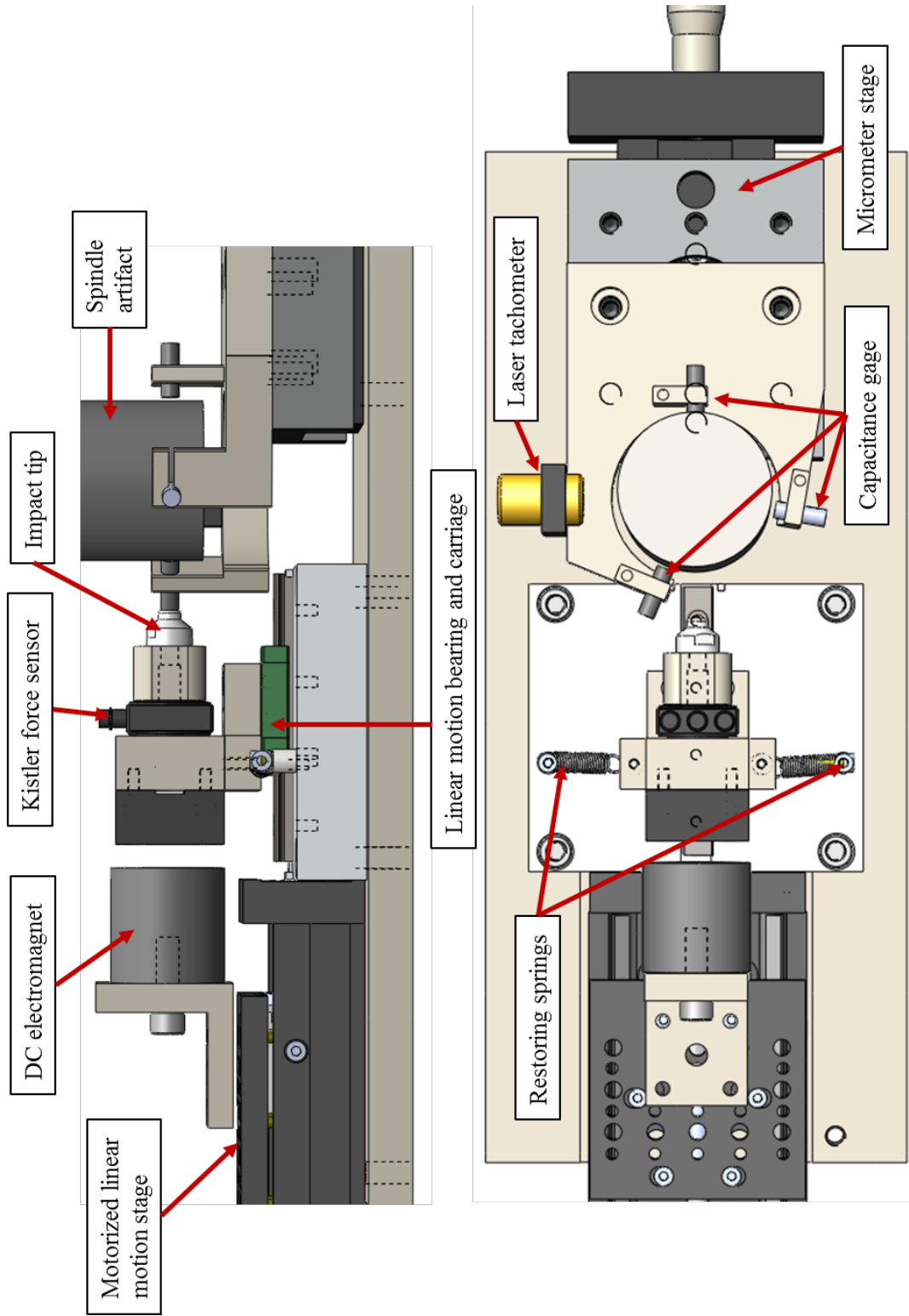


Figure 2.14: Schematic representation of experimental setup 1.

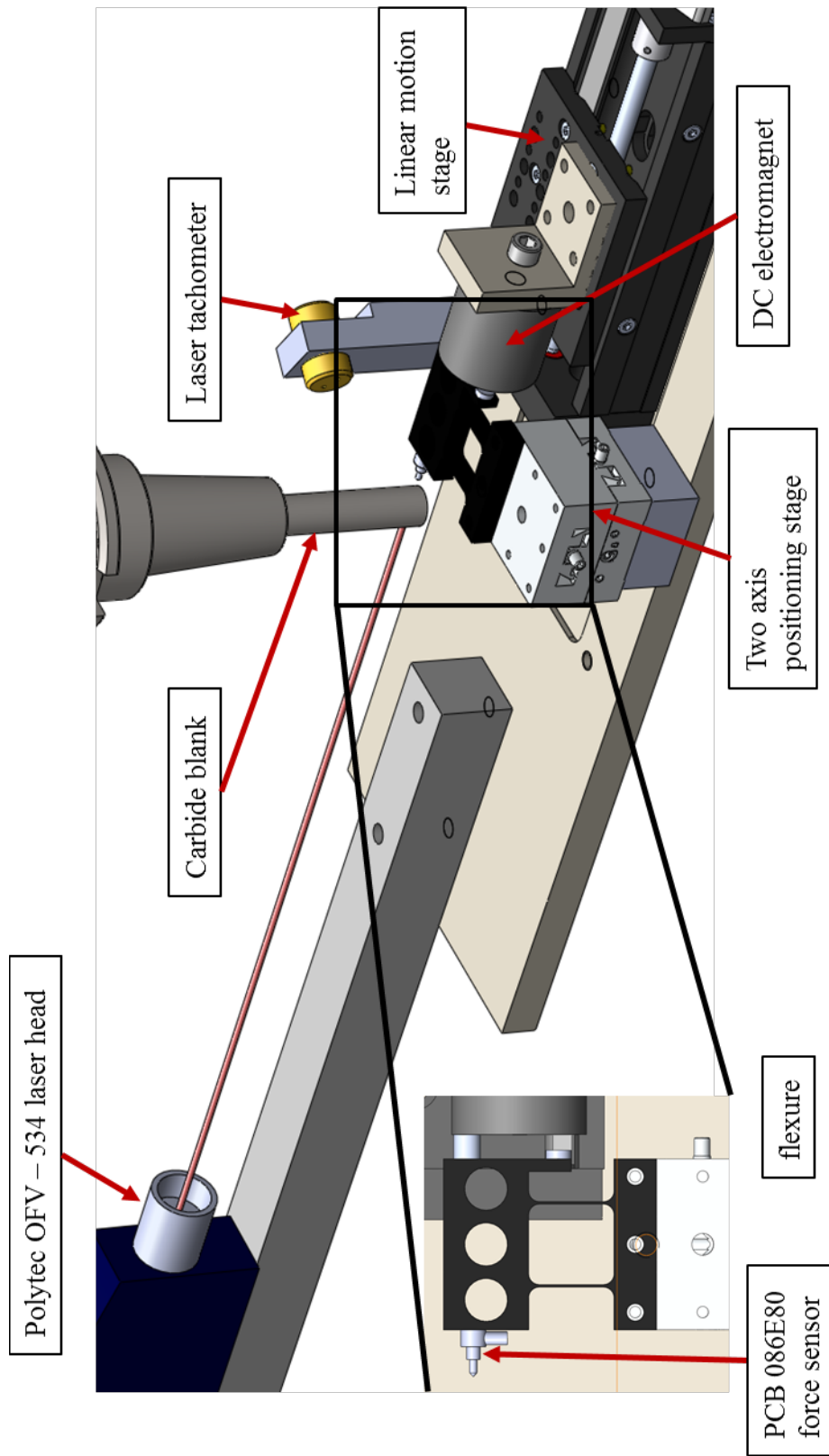


Figure 2.15: Schematic representation of experimental setup 2.

2.2.3 Setup 3: Measurement of SE motions of High Speed Spindle

To measure the SE error motions of the high speed NSK HES-500 spindle, the LDV was used as the motion sensor. The high speed spindle has a maximum collet size of 3.175 mm. In this study, a 3.175 mm carbide blank was used as the target to measure the SE motions of the high speed spindle. The LDV has a significantly smaller measurement area (40 μm diameter at a stand-off distance of 300 mm) than the capacitance gage probe (2 mm diameter) and was therefore chosen for this measurement. Figure 2.16 shows a picture of the setup. The LDV was mounted on a rotary table. The axis of the rotary table was aligned with the axis of the high speed spindle. As it was not possible to collect the displacements at all three angles, as required by the multi-probe error separation method, simultaneously, the measurement for each angle was performed independently. First, the measurements were performed with the LDV aligned with the x-axis of the machine. Then, the rotary table was commanded to rotate to the next desired angle (99.84°) and the measurements were repeated for the entire desired range of spindle speeds. Finally, measurements were performed at the third angle (202.5°). The laser tachometer was fixed to the machine table and did not rotate with the LDV. The tachometer signal was used to synchronize the three independently measured displacements at the three angles. The form error of the blank and the SE motions were then calculated using the multi-probe error separation technique discussed in section 3.2.

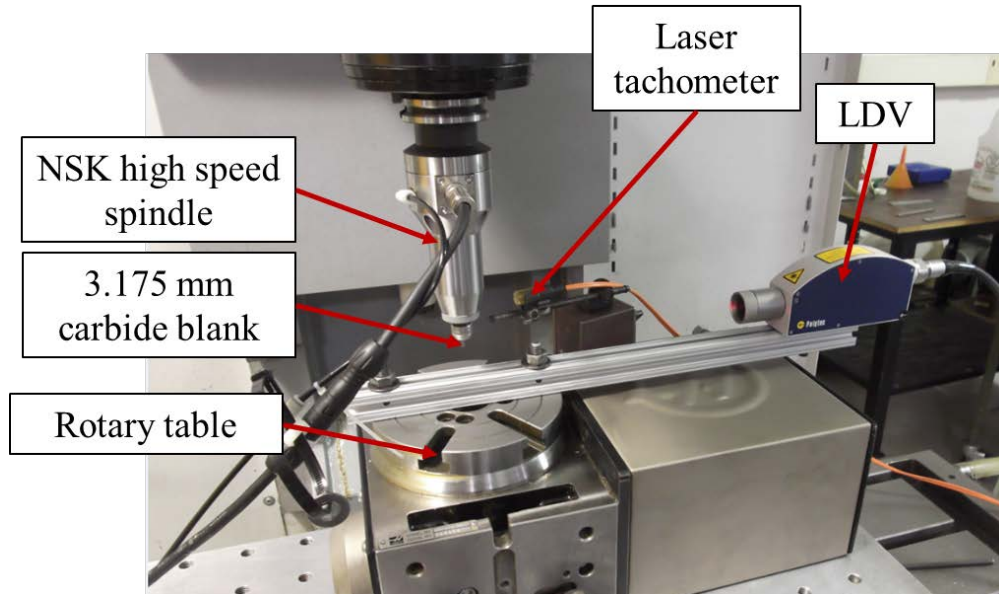


Figure 2.16: Setup used to measure SE motions of NSH HES – 500 high speed spindle.

2.3 Phase Correction Algorithm

In this study, two different non-contact displacement measuring sensors were used to measure the dynamic response. In both cases, an amplifier is used to convert the change in target displacement/velocity into a proportional change in motion-dependent output voltage. Depending on its design, the amplifier can induce a time delay in the measurement signal, i.e., there is a small time delay between the input displacement/velocity of the target and the output voltage from the amplifier. This time delay translates into a frequency-dependent phase shift in the frequency domain. This phase shift is critical when measuring the dynamic response of a structural system because the complex FRF characterizes both the magnitude and phase (or real and imaginary parts) of the structure's response to the force input.

In modal testing [60], an impulse is often used to excite the structure and a linear transducer is used to measure the response. For these impact tests, two signals are measured: the impulsive force and the vibration response. Any lack of synchronization in

the time domain acquisition of the two signals results in a frequency-dependent phase error in the FRF. However, knowledge of the time delay may be used to correct the FRF. In this research, tests were conducted to measure the frequency-dependent phase lag for both the capacitance gage system and LDV system and a frequency domain technique is proposed to correct the FRF for the phase lag. The method was also validated using an FRF measurement of an artifact mounted in a milling machine spindle.

2.3.1 Experimental Setup to Measure Amplifier-induced Phase Lag

The amplifier-induced phase lag was evaluated by measuring the phase shift between a “known” accelerometer and the capacitance gage/LDV system. The target was oscillated using a modal shaker (TIRAvib 51075) capable of generating oscillations up to 5000 Hz. A function generator (Hewlett Packard 33120A) was used to drive the shaker at the desired fixed frequency. The target motion was measured using a low-mass accelerometer (PCB 352C23), a capacitance gage sensor (Lion Precision C23 B), and the LDV (Polytec OFV-534). The capacitance gage signal was amplified using a Lion Precision CPL 290 Elite series amplifier. The amplifier bandwidth was set to 15 kHz. The LDV signal was amplified using the Polytec OFV-5000 controller. The time delay of the OFV-5000 controller is sensitive to the range and low pass filter settings. In this research, measurements were performed with the controller range at 50 mm/s/V and the low pass filter set at 20 kHz. Data was acquired at 100 kHz using a NI 9215 data acquisition card mounted in a NI 9174 CompactDAQ chassis. Figure 2.17 shows a schematic representation of the measurement setup. The amplifier induced phase error, ϕ_{disp} (deg), between the sinusoidal acceleration and displacement signals, a and x , with frequency, f , may be calculated using,

$$\phi_{disp}(f) = \cos^{-1}\left(\frac{x \cdot a}{|x||a|}\right) - 180 \quad (2.8)$$

The amplifier induced phase error, ϕ_{vel} (deg), between the sinusoidal acceleration and velocity signals, a and v , with frequency, f , may be calculated using,

$$\phi_{vel}(f) = 90 - \cos^{-1}\left(\frac{v \cdot a}{|v||a|}\right) \quad (2.9)$$

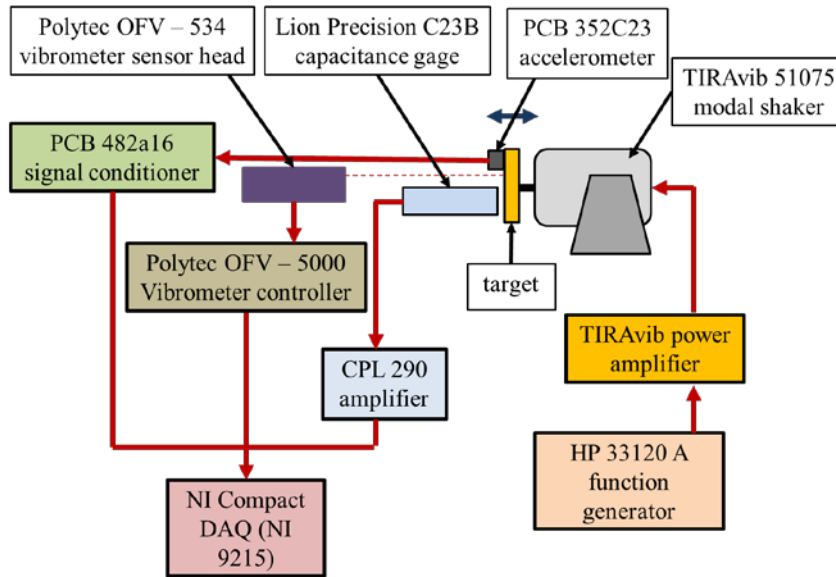


Figure 2.17: Schematic setup of experimental setup to measure amplifier induced phase lag.

Measurements were conducted over a frequency range of 100 Hz to 5000 Hz. The measured data was digitally filtered using a 3rd order band pass filter with a bandwidth of 100 Hz centered at the oscillation frequency. Figure 2.18 shows the measured phase lag as a function of the oscillation frequency. Within the measured bandwidth, the phase lag for the capacitance gage system changed linearly with respect to the oscillating frequency at a rate of -13.84 deg/kHz. For the LDV system, the rate of change of phase lag was found to be -10.27 deg/kHz. Both these values were consistent with the manufacturer-

reported values [66, 67]. Scatter from the line in the 1000 Hz to 2000 Hz range was attributed to the rotary modes of vibration of the target.

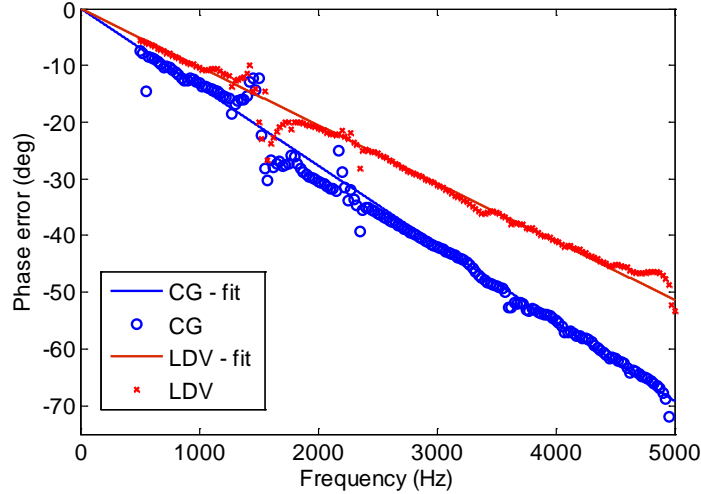


Figure 2.18: Measured phase lag as a function of oscillation frequency (CG – capacitance gage).

2.3.2 Correction for Phase Lag

FRF tests were performed on an artifact mounted in the spindle of a Haas TM-1 CNC vertical machining center. A modally tuned hammer (PCB 086C04) was used to impart an impulse force on the artifact and the response was measured using both a capacitance gage (Lion Precision C5D) and an accelerometer (PCB 352C23). The data was acquired at 100 kHz using the NI data acquisition device. For any FRF, the measured frequency-dependent phase difference between the input force and the output response is,

$$\phi_{meas}(\omega) = \tan^{-1} \left[\frac{Im(FRF(\omega))}{Re(FRF(\omega))} \right] \quad (2.10)$$

where Re indicates the real part and Im indicates the imaginary part of the complex FRF.

The phase difference is corrected to account for the amplifier induced phase lag using,

$$\phi(\omega)_{cor} = \phi(\omega)_{meas} - \Delta\theta \cdot \omega, \quad (2.11)$$

where $\Delta\theta$ is the rate of change of phase lag with frequency (the slope of the line in Figure 2.18). The corrected Re and Im parts of the FRF may then be computed as [68],

$$Re(FRF)_{cor} = |FRF| \cos(\phi(\omega)_{cor}), \text{ and} \quad (2.12)$$

$$Im(FRF)_{cor} = |FRF| \sin(\phi(\omega)_{cor}),$$

where $|FRF|$ is the FRF magnitude, which is not affected by the amplifier-induced phase lag. Figure 2.19 shows the measured and corrected FRFs obtained using the capacitance gage. Notice that the uncorrected capacitance gage measurement deviates from the accelerometer FRF at higher frequencies, while the corrected capacitance gage FRF aligns closely with the accelerometer result.

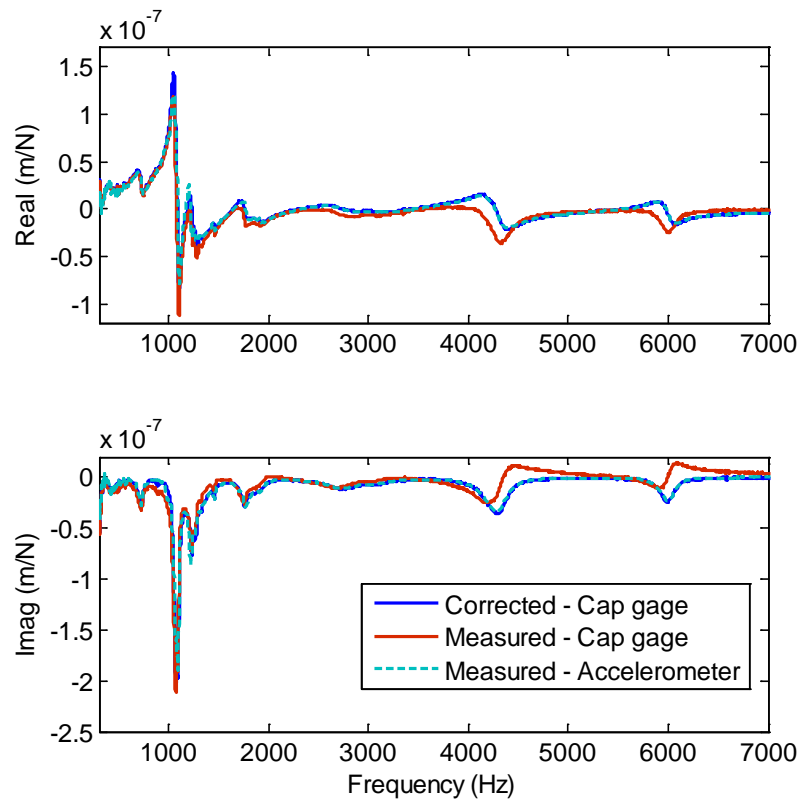


Figure 2.19: Comparison of FRF obtained using capacitance gage and accelerometer.

CHAPTER 3: DATA ANALYSIS

In this study, the dynamic response of a standard artifact mounted in the machine spindle was measured while the spindle was rotating. The out-of-roundness form errors and the SE motions compose part of the displacement measurement and must be extracted to accurately identify the machine spindle dynamics. The dynamics of a machine spindle are known to change as a function of spindle speed due to centrifugal effects, gyroscopic effects, and changes in bearing preload. The objective of the study is to measure these changes in spindle dynamics. Simultaneously, the SE motions were also measured to track any changes with spindle speed. The multi-probe error separation method was used to identify the SE motions and out-of-roundness form errors for the standard artifact. In this chapter, the data collection and analysis steps are presented.

3.1 Dynamic Response of Machine Spindle

3.1.1 Filtering Synchronous SE Motions and Artifact Form Error

A laser tachometer was used to provide a once-per-revolution index which related the angular orientation of the machine spindle to the displacement and force signals. Figure 3.1 shows a plot of the tachometer signal. Note that in this section, all the data used to demonstrate the data analysis procedure was collected with the setup oriented along the y-direction of the machine with the spindle rotating at 1000 rpm. The falling edge of the tachometer signal was selected as the beginning of each revolution ($\theta = 0$).

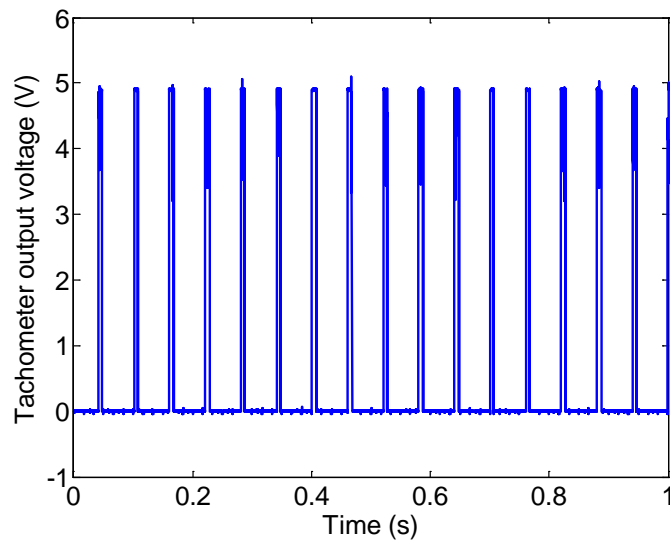


Figure 3.1: Tachometer signal.

Figure 3.2 shows the displacement measurements for a single impulse load. Apart from the fundamental mode displacement signal, the SE motions and form errors in the nominally cylindrical artifact corrupt the response data. Therefore, it is necessary to eliminate the once-per-revolution data from the displacement signals to obtain the dynamic response.

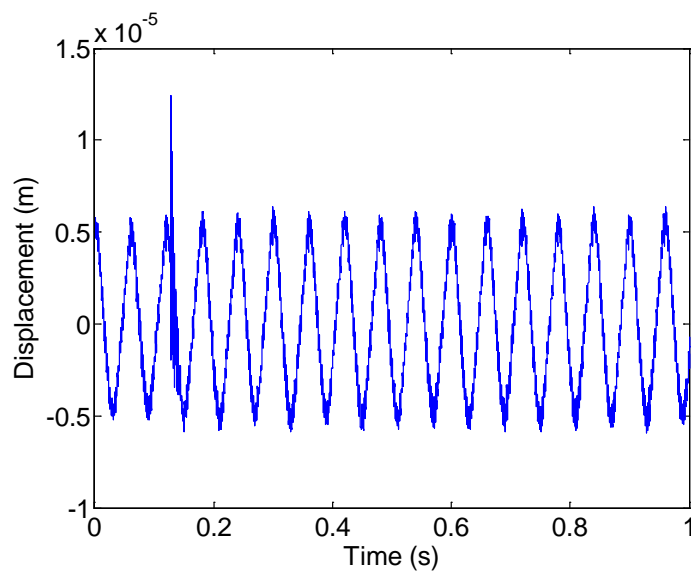


Figure 3.2: Displacement measurement for single impulse load.

The once-per-revolution displacement signal is estimated by averaging the displacement signals for a number of rotations. Note that the average is obtained from a part of the signal which does not include the dynamic response data. The tachometer provides an index which was used as a reference to identify the start point of each revolution of the spindle. The spindle speed may vary marginally leading to a different number of measured points for each rotation because the data was collected at a constant sampling rate. In order to obtain the once-per-revolution displacement at the same angular orientations for each revolution, the data for each rotation was mapped onto an angular orientation vector using piece-wise interpolation [69]. Once an average was obtained for a few revolutions, the once-per-revolution errors were mapped back to the original time vector and subtracted from the displacement signal to isolate the dynamic response. Figure 3.3 shows the averaged once-per-revolution errors obtained for the direct response signal. It should be noted that the averaged once-per-revolution errors only represents the synchronous error motions along the x- or y- fixed-sensitive direction in which the displacement sensor is oriented. Asynchronous error motions, which are not consistent for each rotation of the spindle, cannot be captured and continue to form part of the response data.

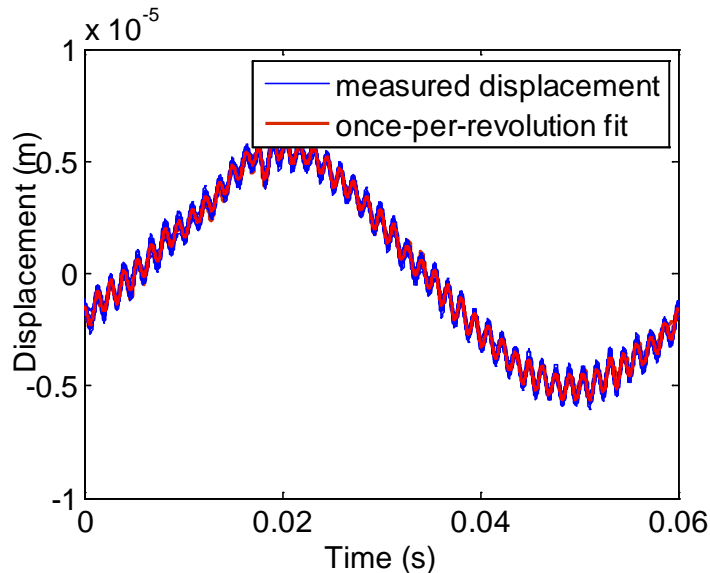


Figure 3.3: Once-per-revolution SE motion and artifact form error.

Figure 3.4 shows the measured response data as well as the once-per-revolution fit.

The direct response data, obtained by subtracting the fit, is shown in Figure 3.5.

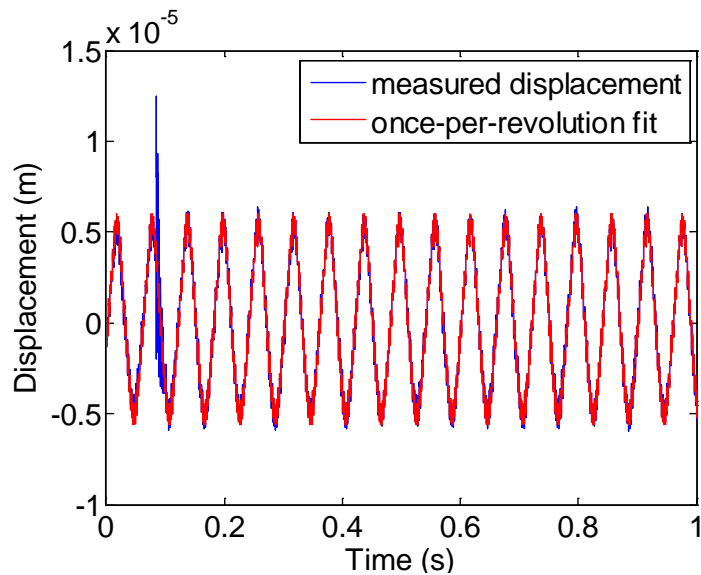


Figure 3.4: Plot of the measured response and the once-per-revolution fit.

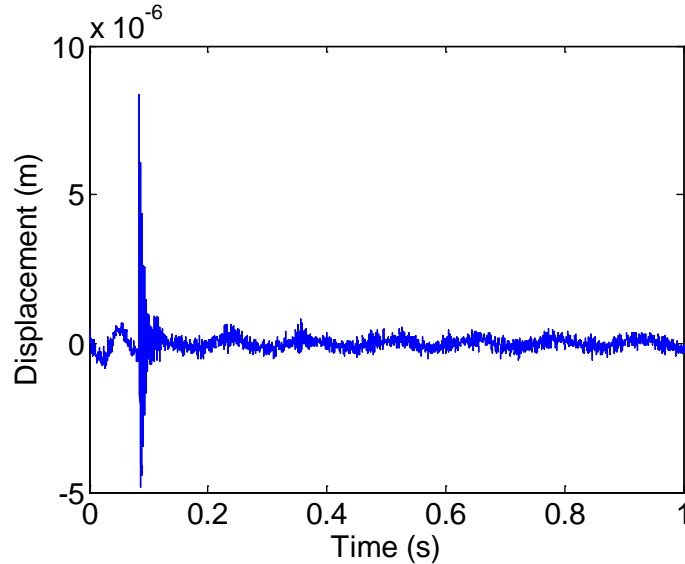


Figure 3.5: Extracted direct response measurement.

3.1.2 Windowing

The dynamic response of the structure is estimated as the complex ratio of the discrete fast Fourier transforms (FFT), $X(\omega)$ and $F(\omega)$, of the response displacement, $x(t)$, and the input impulse force, $F(t)$, respectively; see Eq. 3.1. The FFT only predicts accurate values of the magnitude and phase of a sinusoidal signal if there are an integer number of cycles within the finite sampling time. Incomplete cycles within the sampling time result in the appearance of spectral content at frequencies surrounding the true sinusoidal frequency of the time domain signal. Energy is said to have “leaked” into the neighboring frequencies [60]. Leakage is an artifact that arises from the data analysis and is not a true representation of the input signal in the frequency domain. Leakage may be reduced by applying windows to the impulse and response data [60]. Windowing involves the imposition of a known profile on the time domain signals. A rectangular window was applied to the impulse signal while an exponentially decaying window was applied to the transient vibrations of the response. Figure 3.6 shows both the rectangular

impulse window and the exponential response window. In Figure 3.6 (right), the time axis is magnified to provide a better representation of the rectangular window.

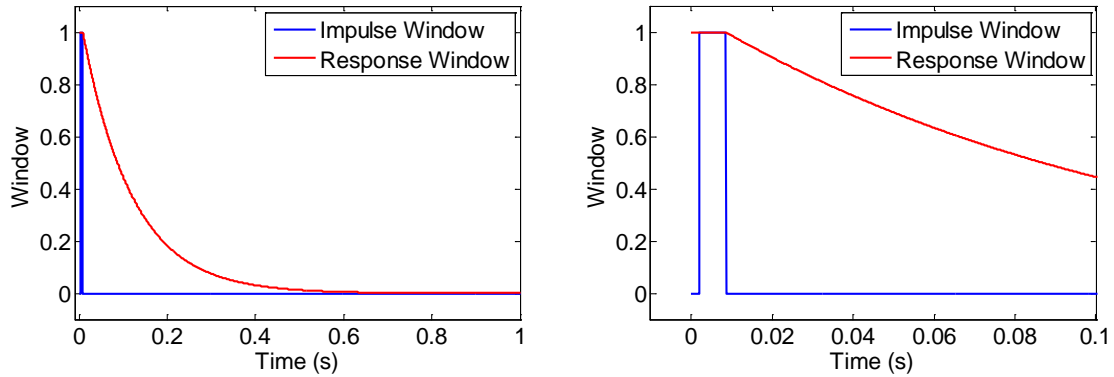


Figure 3.6: Impulse and response window. Magnified time axis (right).

Figure 3.7 shows the effect of the exponentially decaying window on the response data. In Figure 3.7 (right), the vertical scale is expanded. The plot clearly shows that at the beginning of the response, where much of the important information is, the window has little effect on the data while after 0.1 s the response data is quickly suppressed. Therefore, the effects of the asynchronous SE motions are also reduced by applying an exponential window. Figure 3.8 shows the effect of the rectangular impulse window on impulse force data. The vertical scale is magnified in Figure 3.8 (right). The plot shows that the force data picked up due to the oscillations of the impact hammer after impulse are eliminated from the impulse force signal by applying the rectangular window. The width of the rectangular impulse window is 6.5 ms and the time constant of the exponential response window is 0.113. Note that for the exponential window, decay begins only at the end of the rectangular impulse window. These values are consistent with those used in commercially available instrumentation (MetalMax©) used for predicting the dynamic response of structures. In effect, applied windows also serve the purpose of zero padding. Zero padding consists of extending the force and response

signals with zeros. Zero padding improves the frequency domain resolution of the FRF. Zero padding serves the same purpose in the frequency domain that interpolation does in the time domain [60].

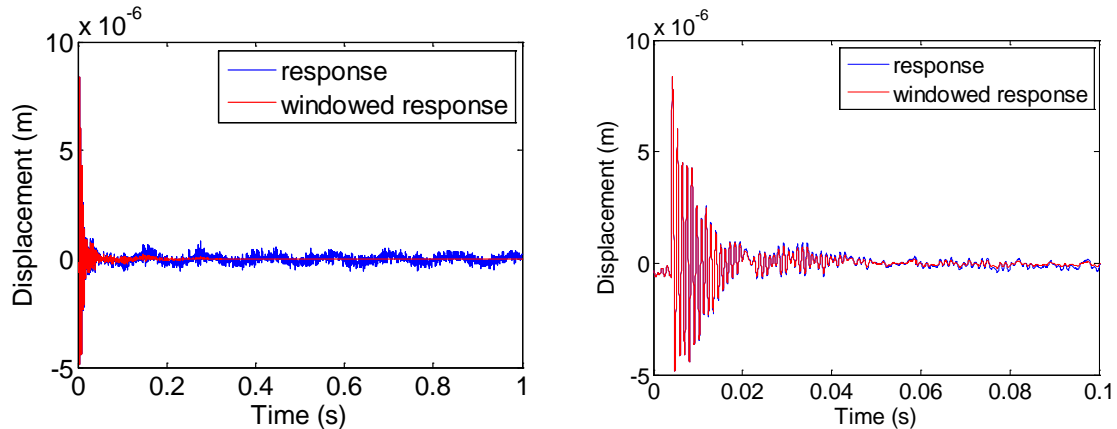


Figure 3.7: Effect of response window on displacement data. Magnified displacement axis (right).

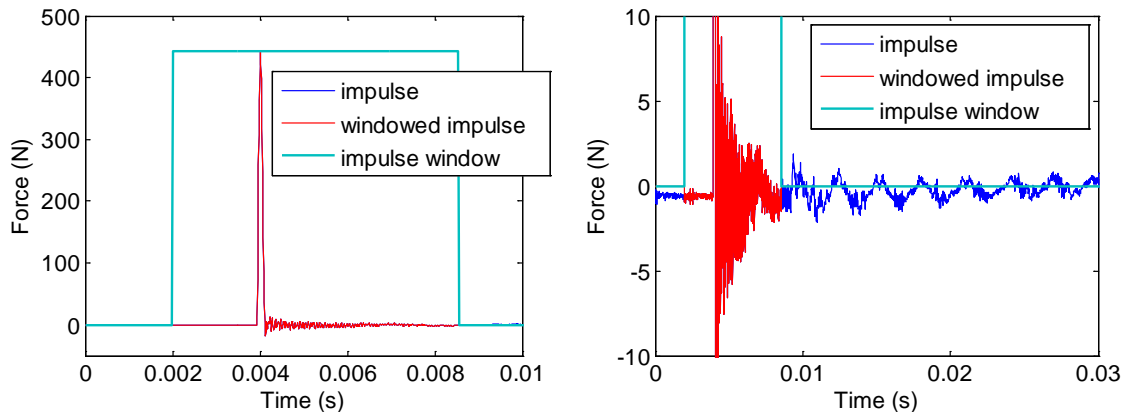


Figure 3.8: Effect of impulse window on force data. Magnified force axis (right).

3.1.3 Impact Synchronous Time Domain Averaging

To improve the fidelity of the FRF measurement, a number of measurements were averaged. Typically, averaging is performed in the frequency domain [60]. However, frequency domain averaging does not reduce the noise level of the measurement. For the rotating FRF measurements, an impact synchronous time domain averaging was performed [70]. Here, the different impulse force and response displacement

measurements were averaged in the time domain. The different measurements were synchronized so that the maximum value of the impact force occurs at the same time in the analysis. In this study, 20 measurements were averaged to obtain the mean impulse force and response displacement data. Figure 3.9 shows a plot of the different impulse forces and the average impulse force in the time domain. Figure 3.10 shows a plot of the direct response displacements and its average. By averaging in the time domain, the effect of the asynchronous SE motions was reduced.

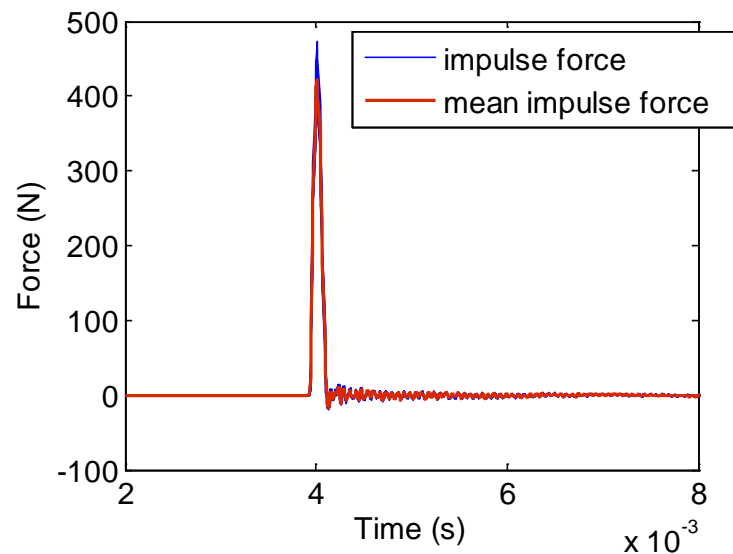


Figure 3.9: Impact synchronized time average of impulse force.

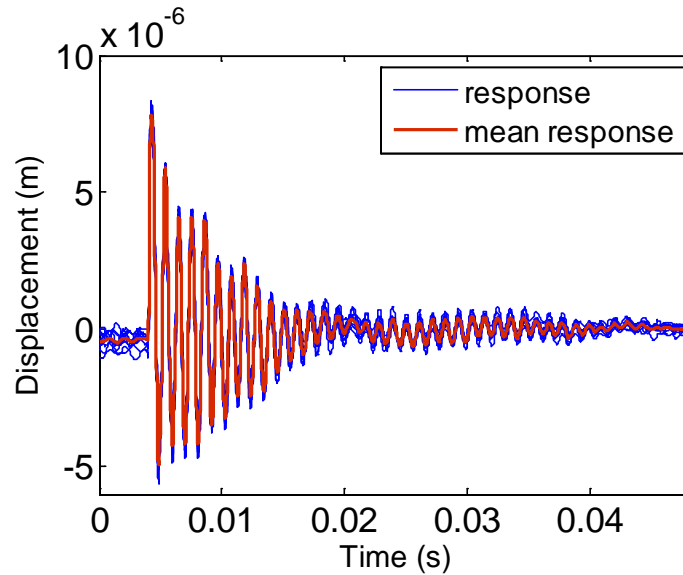


Figure 3.10: Impact synchronized time average of direct response data.

3.1.4 Frequency Response Function

Once the force and response data were processed in the time domain, the discrete fast Fourier transforms (FFT) of the averaged time domain response and force signals were calculate. Figure 3.11 shows the FFT of the response (left) and impulse signals (right).

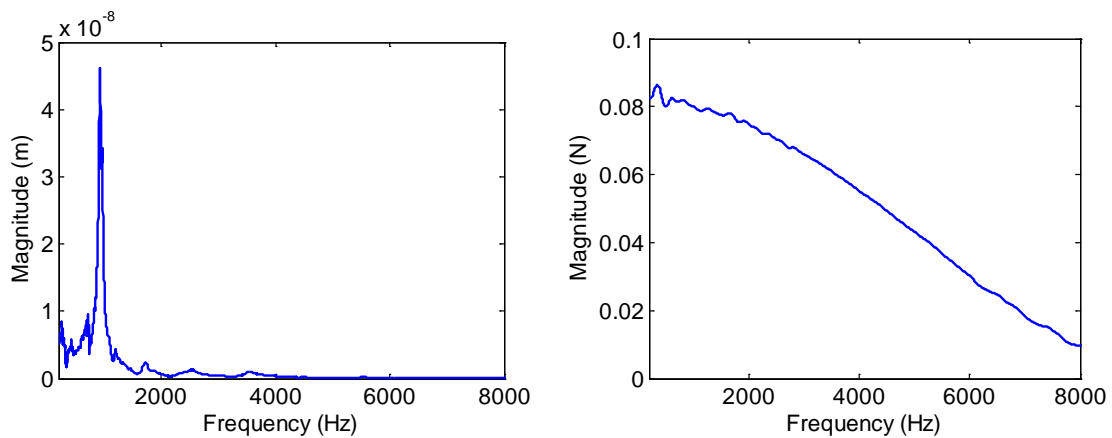


Figure 3.11: FFT of response (left) and impulse (right) signals.

The FRF of the artifact tip mounted in the machine spindle was estimated using Eq.(2.1). It is repeated here for completeness.

$$H(\omega) = \frac{X(\omega)}{F(\omega)} \quad (3.1)$$

where $X(\omega)$ and $F(\omega)$ are the fast Fourier transforms (FFT) of the response signal, $x(t)$, and force signal, $F(t)$, respectively. The coherence provides an estimate of the reliability of the FRF prediction. The coherence is defined as [60],

$$Coherence = \frac{|S_{xf}|^2}{S_{xx}S_{ff}} \quad (3.2)$$

where S_{xf} is the cross power spectral density function for a force signal f , and displacement signal x ; S_{ff} is the direct power spectral density function for a force signal f , and S_{xx} is the direct power spectral density function for a displacement signal x . The coherence should be less than or equal to 1. Ideally, the coherence is 1 over the entire measurement bandwidth. Figure 3.12 shows a plot of the estimated FRF. The coherence is plotted in Figure 3.13. A sharp drop in coherence was found at around 730 Hz. At this frequency, a significant increase in synchronous SE motions was observed (see Figure 3.25). This showed that, although the synchronous error components and the artifact form errors were eliminated from the response while calculating the FRF as shown in the previous steps, high synchronous error motions may still influence the measured FRF. Figure 3.13 shows a plot of the coherence for a FRF measured at 1500 rpm. At this spindle speed the synchronous error motions at 730 Hz is low at the coherence of the FRF is close to 1 for the entire bandwidth on interest.

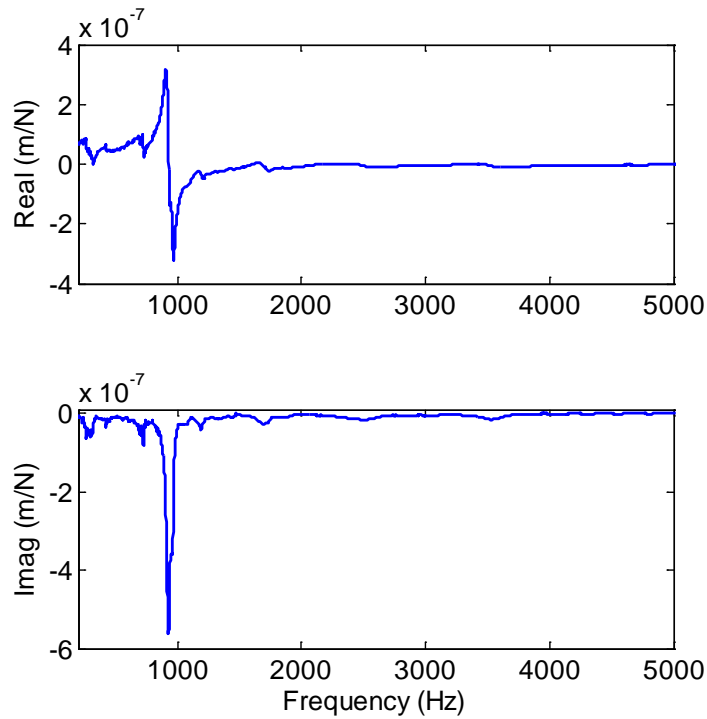


Figure 3.12: Real (top) and imaginary (bottom) parts of the estimated FRF.

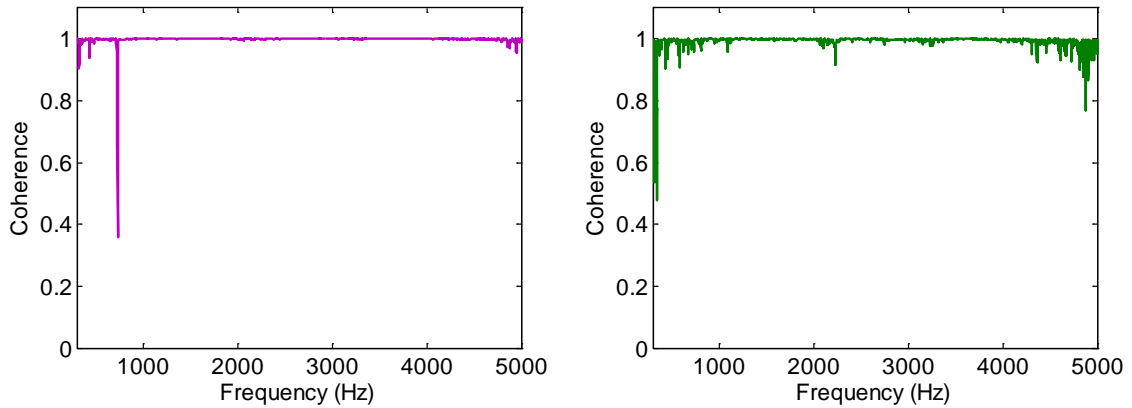


Figure 3.13: Coherence measured at 1000 rpm (left) and 1500 rpm (right): Haas1, y – direction.

3.1.5 Frequency Response Function from Velocity Measurements

The LDV produces an output voltage proportional to a change in velocity. In order to estimate the FRF using velocity data, Eq (3.3) is used.

$$H(\omega) = \frac{1}{i\omega} \frac{V(\omega)}{F(\omega)}, \quad (3.3)$$

where $V(\omega)$ and $F(\omega)$ represent the FFTs of the velocity response and force signals respectively, ω is the frequency in rad/s. The once-per-revolution error elimination method used was the same as described earlier except with the velocity signal rather than a displacement signal. Figure 3.14 shows the measured velocity response in the time (left) and frequency (right) domains. The FRF is plotted in Figure 3.15. The velocity-to-force response was integrated in the frequency domain to obtain the displacement-to-force FRF.

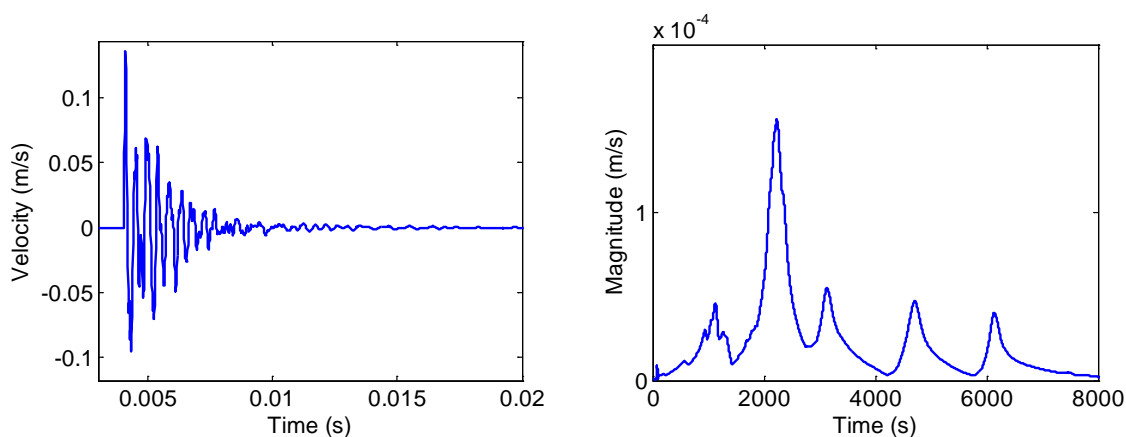


Figure 3.14: Measured velocity response: time domain (left), frequency domain (right).

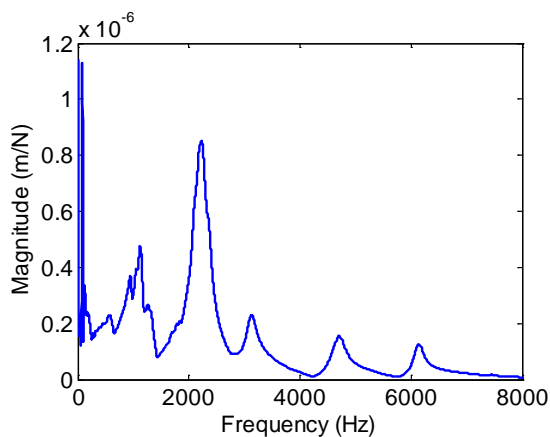


Figure 3.15: FRF estimated using velocity response data.

3.2 Multi-probe Error Separation

In this study, the response of an artifact mounted in the machine spindle was measured as the spindle rotates. The position of the axis of the machine spindle is known to deviate from its ideal location as the spindle rotates. These deviations of the position of the spindle axis are known as spindle error motions. The magnitude of the error motions serves as a metric of the quality of the machine spindle. These errors may be dependent on the spindle speed. At different spindle speeds, different modes of the machine spindle structural assembly may be excited. Also, the errors may be affected by changes in centrifugal forces, gyroscopic effects, and spindle bearing preload which are all known to change with spindle speed. Therefore, it was necessary to characterize the SE motions for the entire range of spindle speeds.

SE motions can be estimated by measuring the displacement of a precision ground spherical target mounted in the machine spindle along two orthogonal directions normal to the spindle axis. The out-of-roundness of the sphere leads to errors in the characterization of SE motions. The out-of-roundness of the target sphere may be accounted for using reversal methods [54, 55, 58, 59]. However, reversal techniques require more than one measurement. In this study, an imperfect cylindrical artifact, suitable for measuring the spindle's dynamic response, was used as the target to measure both the SE motions and the spindle dynamics. Also, the artifact cylindrical profile is subject to change considering it is constantly subjected to impact loads. Therefore, to accurately extract the dynamic response data from the displacement measurement, it was necessary to accurately identify the out-of-roundness form errors in the artifact as well as the SE motions. In this study a multi-probe error separation approach was implemented

[58]. In this method, three displacement measuring sensors positioned at different angular orientations around the spindle axis are used to measure the displacement of the artifact mounted in the machine spindle as it rotates. The error separation approach and data analysis method is described here.

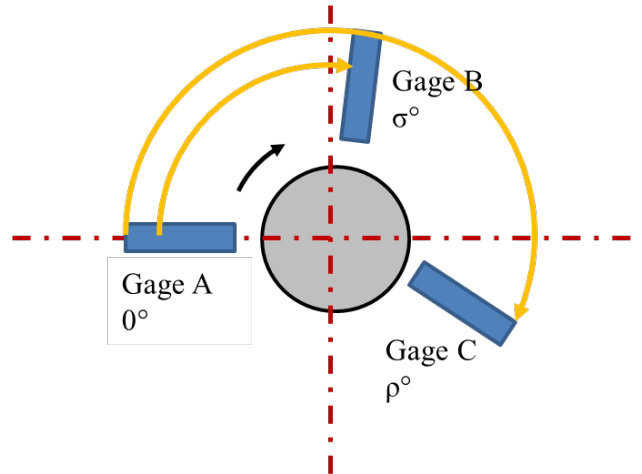


Figure 3.16: Schematic of setup for multi-probe error separation.

The three displacement capacitance gages are labeled as A, B, and C in Figure 3.16. The three displacement measurement signals are,

$$m_A(\theta) = R(\theta) + x(\theta), \quad (3.4)$$

$$m_B(\theta) = R(\theta - \sigma) + x(\theta)\cos\sigma + y(\theta)\sin\sigma, \text{ and}$$

$$m_C(\theta) = R(\theta - \rho) + x(\theta)\cos\rho + y(\theta)\sin\rho,$$

where θ is the angular orientation of the machine spindle, σ is the angular orientation of gage B (99.84°), and ρ is the angular orientation of gage C (202.5°). $R(\theta)$, $x(\theta)$, and $y(\theta)$ are the artifact out-of-roundness form errors and SE motions in the x- and y-directions, respectively, as a function of spindle angular orientation, θ . Figure 3.17 shows the displacement measurements from the three sensors. To demonstrate the process, the data

collected at 1000 rpm on Haas1 is used with the setup oriented along the machine y-direction.

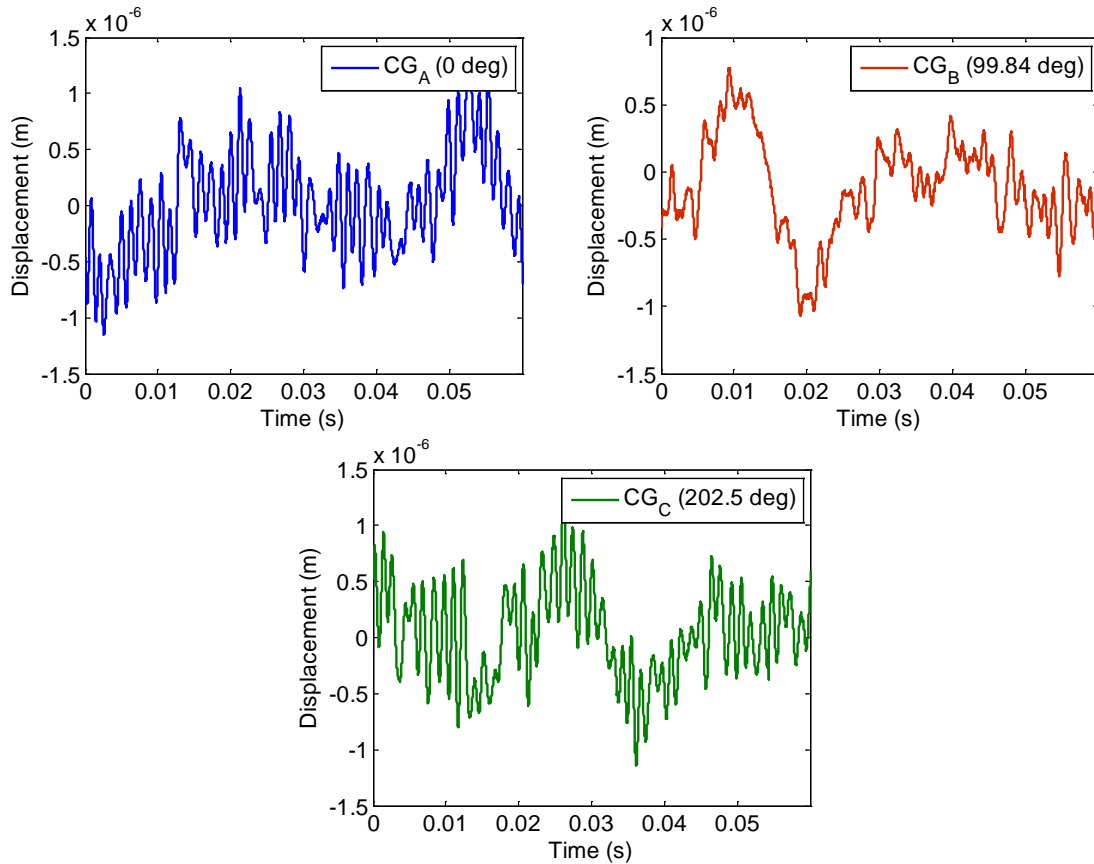


Figure 3.17: Displacement signal for a single revolution at 1000 rpm. 0 deg (top left), 99.84 deg (top right), 202.5 deg (bottom).

The three measurement signals are manipulated to eliminate the contributions of the error motions, $x(\theta)$ and $y(\theta)$. Figure 3.18 shows the combined signal.

$$M(\theta) = m_A(\theta) + a \cdot m_B(\theta) + b \cdot m_C(\theta). \quad (3.5)$$

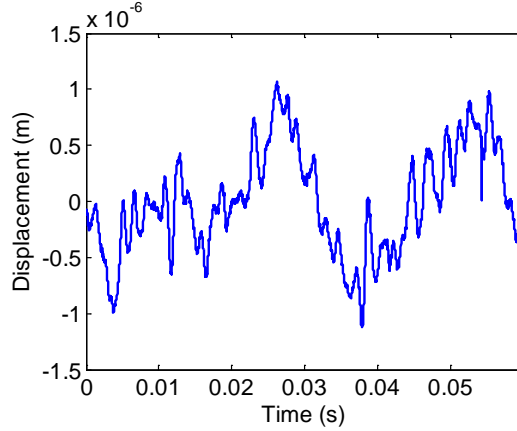


Figure 3.18: Combined displacement signal M .

Upon substitution from Eq. (3.4),

$$M(\theta) = R(\theta) + aR(\theta - \sigma) + bR(\theta - \rho) + x(\theta)(1 + a \cdot \cos \sigma + b \cdot \sin \rho) + y(\theta)(a \cdot \sin \sigma + b \cdot \cos \rho). \quad (3.6)$$

The values of a and b are selected so that the contributions of $x(\theta)$ and $y(\theta)$ towards $M(\theta)$ are eliminated.

$$0 = (1 + a \cdot \cos \sigma + b \cdot \sin \rho) \quad (3.7)$$

$$0 = (a \cdot \sin \sigma + b \cdot \cos \rho)$$

Solving Eq. (3.7) simultaneously gives,

$$a = \frac{\sin \rho}{\sin(\sigma - \rho)}, \text{ and} \quad (3.8)$$

$$b = \frac{-\sin \sigma}{\sin(\sigma - \rho)}.$$

The out-of-roundness form error predictions must maintain continuity at 0° and 360° . Therefore, the out-of-roundness errors are defined in terms of undulations per revolution (UPR). UPR corresponds to the number of complete sinusoidal cycles in the form profile of the artifact. The total out-of-roundness error can be expressed as the sum of individual contributions from the different UPRs. The out-of-roundness errors of a circular artifact

may be expressed as the sum of a Fourier series. The coefficients of the Fourier series terms relate to the magnitude and phase (relative to spindle orientation) of the corresponding UPR. Therefore, the out-of-roundness form errors of the artifact may be expressed as,

$$R(\theta) = \sum_{k=1}^{\infty} A_k \cos k\theta + B_k \sin k\theta \quad (3.9)$$

where k is the number of UPR. Substituting Eq. (3.6) into Eq. (3.9), expanding, and grouping the like terms gives,

$$\begin{aligned} M(\theta) = & \sum_{k=1}^{\infty} A_k (1 + a \cdot \cos k\sigma + b \cdot \sin k\rho) \cos k\theta + \sum_{k=1}^{\infty} A_k (a \cdot \sin \sigma + b \cdot \cos \rho) \sin k\theta \\ & + \sum_{k=1}^{\infty} B_k (1 + a \cdot \cos k\sigma + b \cdot \sin k\rho) \sin k\theta - \sum_{k=1}^{\infty} B_k (a \cdot \sin \sigma + b \cdot \cos \rho) \cos k\theta. \end{aligned} \quad (3.10)$$

$M(\theta)$ may also be expressed as the sum of a Fourier series,

$$M(\theta) = \sum_{k=1}^{\infty} F_k \cos k\theta + G_k \sin k\theta \quad (3.11)$$

The coefficients F_k and G_k can be evaluated from the FFT of $M(\theta)$. Figure 3.19 shows a plot of F_k and G_k , plotted as a function of UPR.

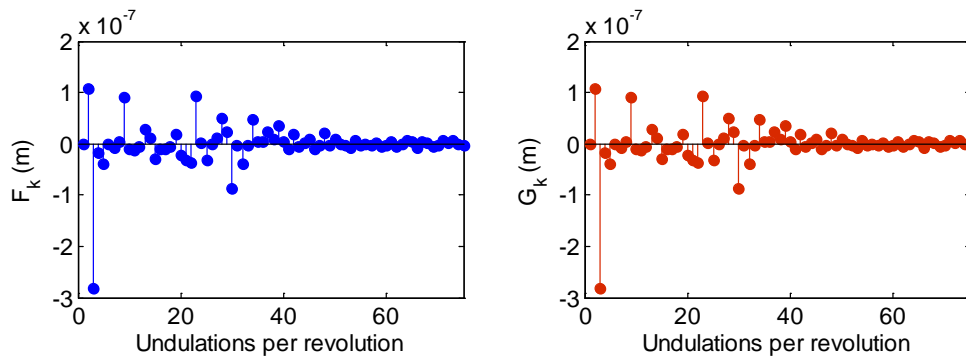


Figure 3.19: Fourier coefficients of combined measurement signal: real part F_k (left) and imaginary part G_k (right).

The Fourier coefficients of the out-of-roundness form errors of the artifact, A_k and B_k , may then be evaluated as,

$$\begin{Bmatrix} A_k \\ B_k \end{Bmatrix} = \begin{bmatrix} \alpha_k & -\beta_k \\ \beta_k & \alpha_k \end{bmatrix}^{-1} \begin{Bmatrix} F_k \\ G_k \end{Bmatrix}, \quad (3.12)$$

where $\alpha_k = (1 + a \cdot \cos k\sigma + b \cdot \sin k\rho)$ and $\beta_k = (a \cdot \sin \sigma + b \cdot \cos \rho)$. Figure 3.20 shows the Fourier coefficients of the artifact form error, A_k and B_k , plotted as a function of UPR. The artifact form error may then be reconstructed using Eq. (3.9). Figure 3.21 shows a polar plot of the artifact form error as a function of theta.

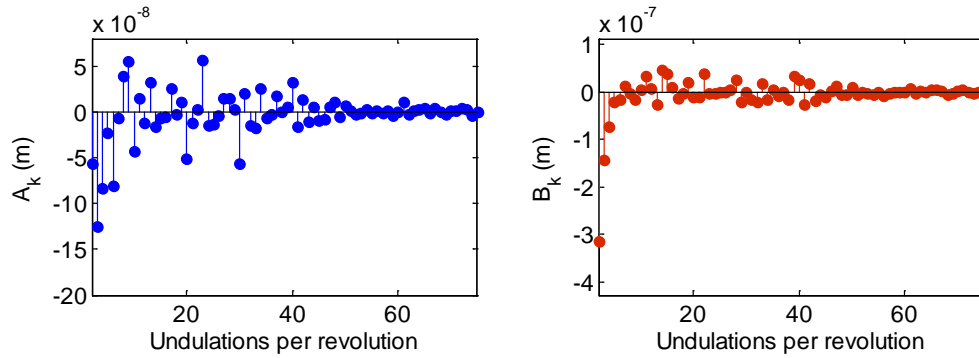


Figure 3.20: Fourier coefficients of constructed artifact form error: real part A_k (left) and imaginary part B_k (right).

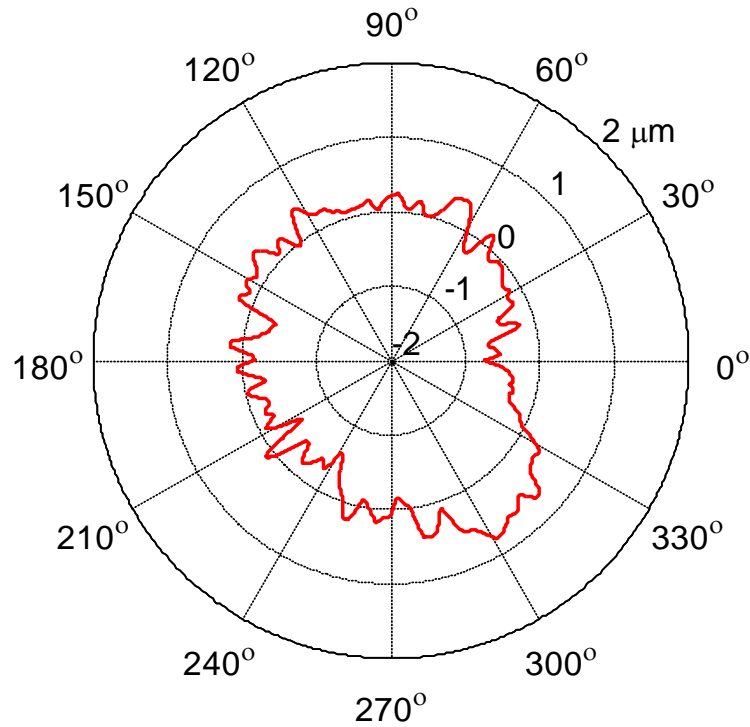


Figure 3.21: Polar plot of artifact form error.

Once the form errors of the artifact are evaluated, the SE motions along the measurement direction may be estimated as,

$$x(\theta) = R(\theta) - m_A(\theta). \quad (3.13)$$

The synchronous SE motions correspond to the component of the error which is consistent for each revolution of the spindle. The synchronous error motions may be obtained by averaging the total SE motions for a number of rotations. In the averaging process, the asynchronous component of the error is eliminated. The asynchronous component of the SE motion is calculated by subtracting the synchronous part from the total error. Figure 3.22 (left) shows the total SE as a function of spindle orientation in the fixed sensitive y-direction. The synchronous component is shown in Figure 3.22 (middle) and the asynchronous component is shown in Figure 3.22 (right). The magnitude of the synchronous SE is defined as the difference between the maximum and minimum value

for any polar orientation, i.e., the difference between two solid circles as shown in Figure 3.22 (middle). The magnitude of the asynchronous SE is also defined similarly.

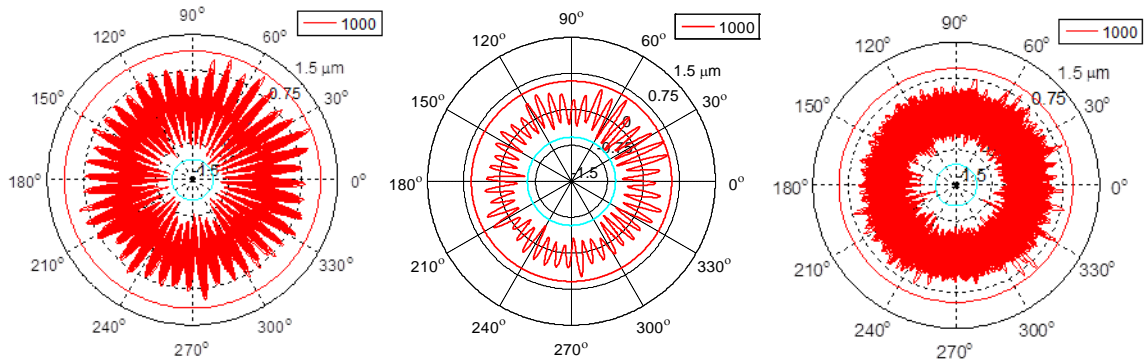


Figure 3.22: Polar plot of SE motions: total SE (left), synchronous SE (middle), asynchronous SE (right).

The asynchronous error standard deviation is a polar plot of the standard deviation of the asynchronous error at each angular orientation taken for a number of rotations. Figure 3.23 shows a polar plot of the standard deviation in the asynchronous SE as a function of θ . Notice the change in scale.

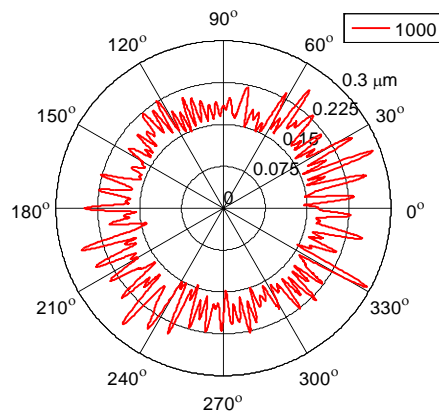


Figure 3.23: Polar plot of standard deviation of asynchronous SE motions measured along the fixed sensitive y-direction on Haas1.

The fixed sensitive x-direction errors were measured when the setup was oriented along the machine x-axis and the y-direction errors were measured with the setup oriented along the machine y-axis. Then the two fixed sensitive x- and y-direction SE

motions were combined to produce a rotating sensitive direction SE motions. The rotating-sensitive direction error, $r(\theta)$, is,

$$r(\theta) = x(\theta)\cos(\theta) + y(\theta)\sin(\theta). \quad (3.14)$$

Figure 3.24 shows the synchronous SE motions measured in the fixed sensitive x- and y-directions as well as in the rotating sensitive direction. The results plotted here were measured on Haas1 at a spindle speed of 1000 rpm.

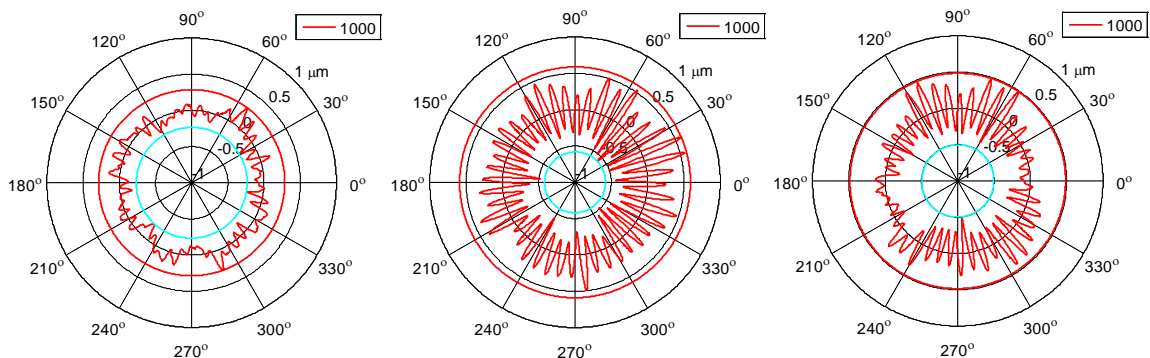


Figure 3.24: Polar plot of synchronous SE motions: fixed sensitive x- (left), fixed sensitive y- (middle), rotating sensitive (right).

A fast Fourier transform (FFT) of the SE motions provides an estimate of the frequency content. The FFT was computed separately for the synchronous and asynchronous SE motions. For the plots of FFT of the synchronous SE motions, the horizontal axis was normalized by the spindle speed to represent ‘undulations per revolution’. Figure 3.25 shows the magnitudes of the FFT of the synchronous SE motions in the fixed-sensitive x- (left) and y-directions (middle) as well as in the rotating-sensitive direction (right) measured at a spindle speed of 1000 rpm. It is evident from the plots that the synchronous errors occur at the harmonics of spindle speed as expected. There is a sharp peak at 44 cycles per revolution in the synchronous error in the fixed-sensitive y-direction.

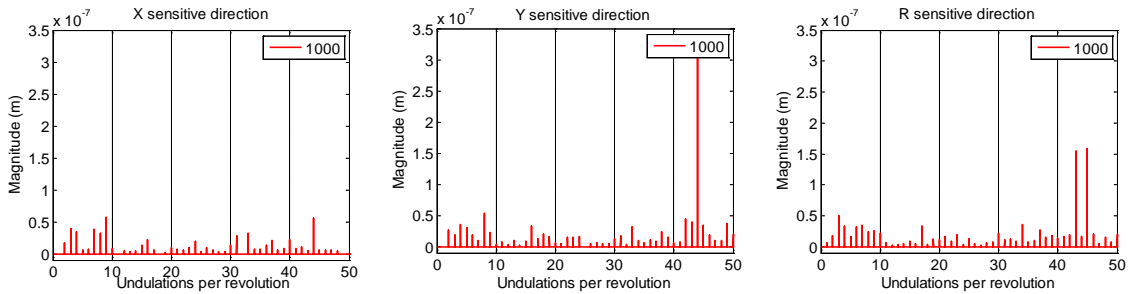


Figure 3.25: FFT of synchronous SE motions: fixed sensitive x- (left), fixed sensitive y- (middle), rotating sensitive (right).

The FFT of the asynchronous SE motions may also be evaluated. Figure 3.26 shows a plot of the magnitude of the FFT of the asynchronous SE motions in the fixed sensitive x- (left), the fixed sensitive y- (middle), and the rotating sensitive (right) directions. In the case of the asynchronous SE motions, the horizontal axis represents frequency. It was observed from the plot of FFT in the fixed sensitive y-direction that there is an increase in errors at around 730 Hz. This frequency corresponds to 44 UPRs at 1000 rpm. It was shown in Figure 3.25 that a peak in the fixed sensitive y-direction SE motions occurs at 44 UPRs.

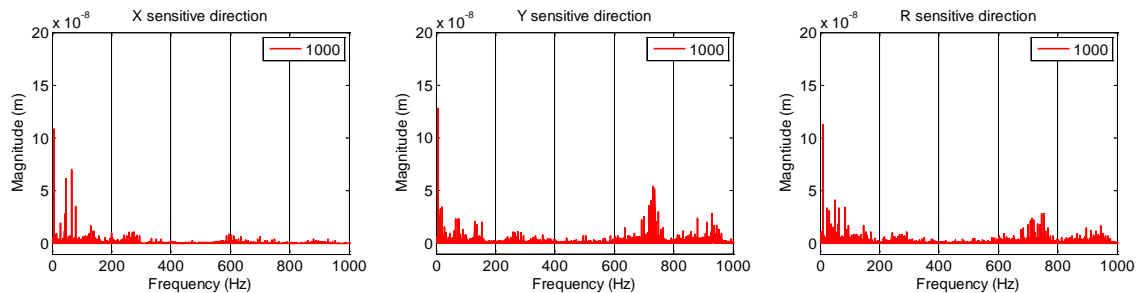


Figure 3.26: FFT of asynchronous SE motions: fixed sensitive x- (left), fixed sensitive y- (middle), rotating sensitive (right).

3.2.1 SE Motions using Velocity Data

To measure the SE motions of the high speed NSK HES-500 spindle the LDV was used. The LDV produces an output voltage proportional to the change in target velocity. To convert the output velocity into a displacement, trapezoidal integration was used (*cumtrapz* command in MATLAB). To eliminate the low frequency integration errors,

the integrated displacement was processed through a high pass 3rd order Butterworth filter. The cut-off frequency was set at half the spindle speed. The measured velocity (left), the integrated displacement (middle), and the high pass filtered displacement (right) are shown in Figure 3.27.

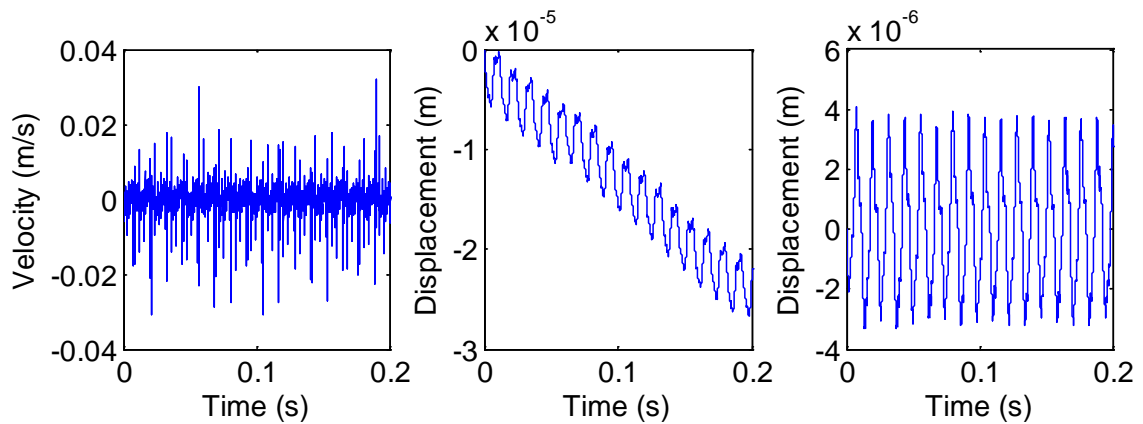


Figure 3.27: Velocity (left), integrated displacement (middle), and high pass filtered displacement (right) derived from LDV output.

3.2.2 Uncertainty Evaluation

3.2.2.1 Variance in Synchronous SE Motions

In this study, to measure the SE motions of the three Haas TM1 CNC machines, data was collected for 200 revolutions at eight different spindle speeds between 500 rpm and 4000 rpm in increments of 500 rpm. The collected data was segmented into ten sections of 20 revolutions each and the SE motions and form errors were calculated for each section. Figure 3.28 (left) shows a polar plot of the form errors and estimated synchronous SE motions (right) for each of the ten segments. The data plotted here was collected on Haas1 at a spindle speed of 2000 rpm with the setup oriented along the machine y-direction. From this plot, an estimate of the variance of the synchronous SE motions was evaluated for each angular orientation. Figure 3.29 shows the mean synchronous SE motion evaluated by averaging the ten measurements. The encompassing

curves represent the $\pm 3 \sigma$ lines, where σ represents the standard deviation. Note that a different standard deviation was calculated for each angular orientation. The mean standard deviation was also calculated. The mean standard deviation for the form measurement was 6.3 nm, while that for the synchronous SE motions was 63 nm.

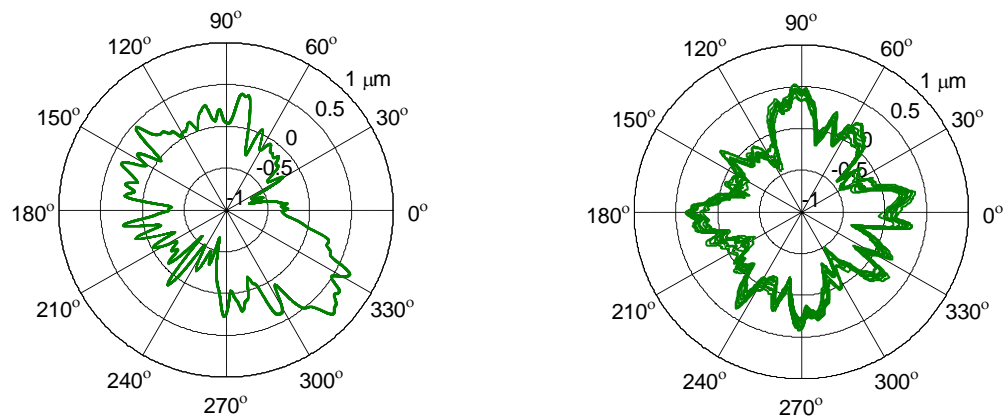


Figure 3.28: Superimposed form errors (left) and synchronous SE motions (right) for ten averages.

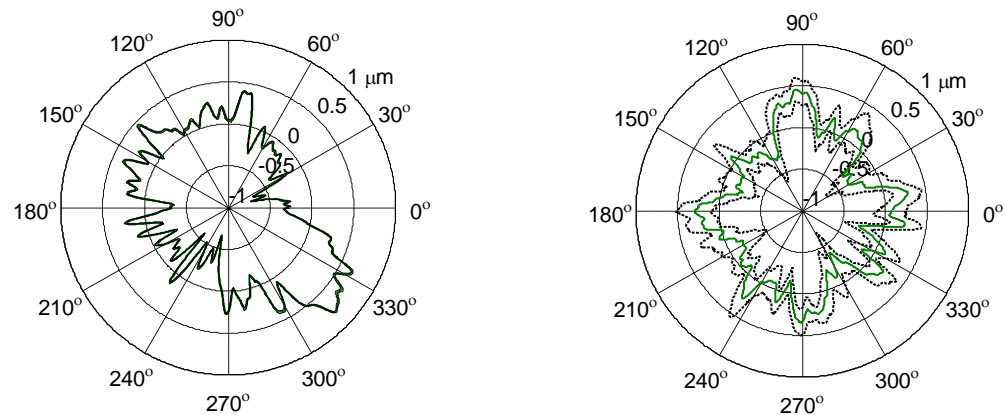


Figure 3.29: Mean and $\pm 3 \sigma$ standard deviation curves for form error (left) and synchronous SE (right).

3.2.2.2 Influence of Sampling Rate on SE Motion Measurements

In this study, a NI 9215 DAQ card mounted in a NI 9417 CompactDAQ chassis was used to acquire analog data. The maximum sampling capability of the data acquisition system was 100 kHz. At high spindle speeds, the sampling rate can provide constraints on

the accuracy of SE measurements. In this section, the influence of sampling rate on SE motion measurements is discussed.

In order to make accurate estimations of SE motions over a wide range of UPRs, a large number of data points per revolution are required. At high spindle speeds, the number of data points acquired per rotation decreases for a fixed sampling rate and the ability to estimate the magnitude of the higher UPRs is compromised. For example, for a measurement performed at 50,000 rpm with a sampling rate of 100,000 Hz, 120 data points are collected for each rotation of the spindle. This corresponds to an angular resolution of one data point every three degrees of rotation. This sets the Nyquist limit at 60 UPRs (half the number of data points per revolution). Any SE motions or artifact form errors which may be present at a spatial frequency higher than 60 UPRs cannot be measured. The Nyquist limit in UPRs may be estimated as,

$$Nyquist = \frac{30 \cdot SR}{\Omega} , \quad (3.15)$$

where SR is the sampling rate (Hz) and Ω is the spindle speed (rpm). Furthermore, when the Nyquist limit is low, the presence of frequency content above the Nyquist cut-off frequency results in aliasing unless analog filters are applied.

Furthermore, in order to evaluate SE motions, data is collected for a number of rotations and averaged. A laser tachometer is used to synchronize the angular orientation of the spindle with the displacement signal. The tachometer signal provides a reference to indicate the 0° orientation. The measurement data is then mapped from the time domain onto a corresponding angular orientation vector. However, the tachometer signal, acquired using the data acquisition system, collects data at discrete time intervals. This may result in a delay in observing the actual 0° orientation of the spindle. Figure 3.30

provides an illustration where the falling edge of the tachometer signal, which indicates the 0° orientation, is observed only after a delay $\delta\theta$. This delay results in mapping errors when the displacement signal is mapped onto the angular orientation. As the number of samples collected per rotation decreases, the standard deviation of the error $\delta\theta$ increases, resulting in larger errors in the estimated form and SE motions.

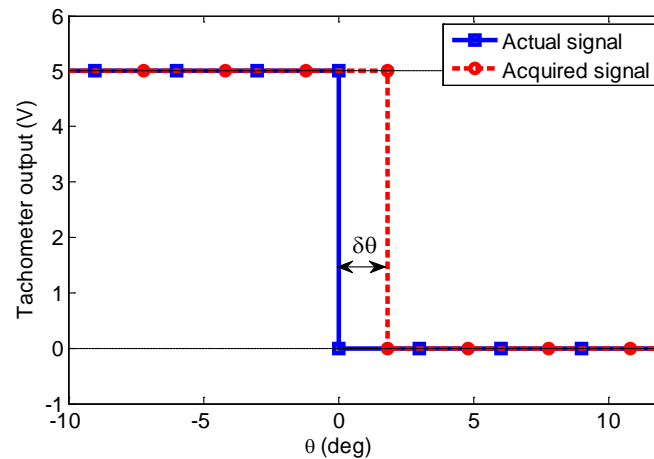


Figure 3.30: Delay in detecting spindle 0° orientation.

3.2.3 SE Motion Validation

In order to validate the SE motion measurements, the SE motions were measured for a different artifact cross section with different form errors. The estimated synchronous SE motions were then compared. Figure 3.31 shows a comparison of the synchronous error motions measured at two different sections of the artifact in the fixed sensitive y -direction measured at 1000 rpm on Haas1. Both the error profiles were within the $\pm 3\sigma$ curves. The artifact form at the two sections is plotted in Figure 3.32.

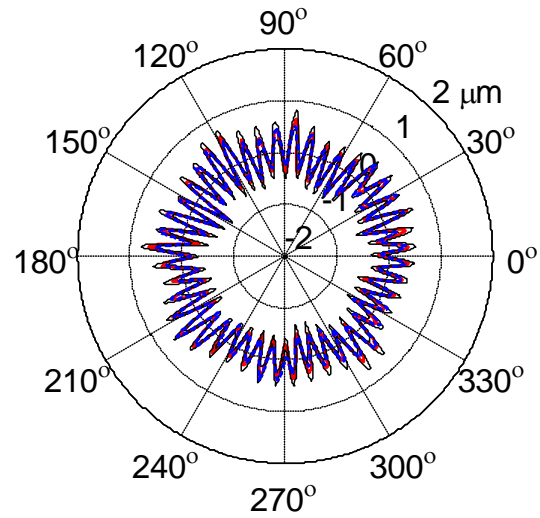


Figure 3.31: Measured synchronous SE motions at the two different cross-sections.

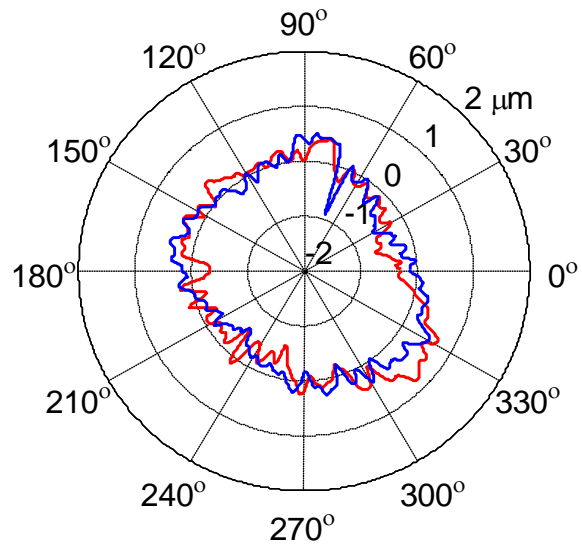


Figure 3.32: Form error of the artifact at the two different cross-sections.

CHAPTER 4: EXPERIMENTAL RESULTS

In this study, speed-dependent structural dynamics and SE motion tests were performed on three nominally identically Haas TM1 CNC vertical machining centers and an NSK HES-500 high speed spindle. In this section, the experimental results for Haas1 and the high speed spindle are presented. The experimental results of Haas2 and Haas3 are presented in Appendix A and Appendix B.

4.1 Haas1 CNC Vertical Machining Center Studies

4.1.1 Speed-dependent Dynamics

In this study, rotating FRF tests were performed on two different targets: 1) the standard cylindrical artifact, and 2) a half inch diameter solid carbide blank mounted in a shrink fit tool holder. Tests were performed over a spindle speed range of 0 to 4000 rpm in increments of 500 rpm.

4.1.1.1 Standard Cylindrical Artifact

The FRF measurements on the standard cylindrical artifact were measured using setup 1 described previously. Figure 4.1 shows a plot of the magnitude of the FRF measured along the machine x-direction. Two distinct modes were observed at 881 Hz and 1043 Hz. Figure 4.2 shows a magnified view of the FRF around the two most compliant modes. Spindle speed was found to have a significant effect on the measured FRF.

The variation of the magnitude and frequency of the two largest peaks in the FRF were tracked as a function of spindle speed. Figure 4.3 shows a plot of the changes in magnitude and natural frequency of the two modes at 881 Hz and 1043 Hz. Note that the two frequencies used to identify the modes were as observed in the FRF measured at 0 rpm. The vertical axis of the plots in Figure 4.3 only denotes the changes in magnitude and frequency. After an initial increase up to 1000 rpm, the magnitude of the FRF was found to decrease with an increase in spindle speed suggesting an increase in stiffness at higher spindle speeds.

Figure 4.4 shows a plot of the magnitude of the FRF measured along the machine y-direction. The magnified view of the FRF is shown in Figure 4.5. As seen, the portion of the FRF between 900 Hz and 1000 Hz consists of two modes which interact with each other. The magnitude of the mode at 961 Hz was found to increase with spindle speed up to 2000 rpm following which it decreases to less than its original magnitude. Once again, a stiffening effect is observed with spindle speed. Also, note that the magnitude of the FRF measured along the machine y-direction is around three times as high as the magnitude measured in the machine x-direction. This suggests that the machine is stiffer along the x-direction.

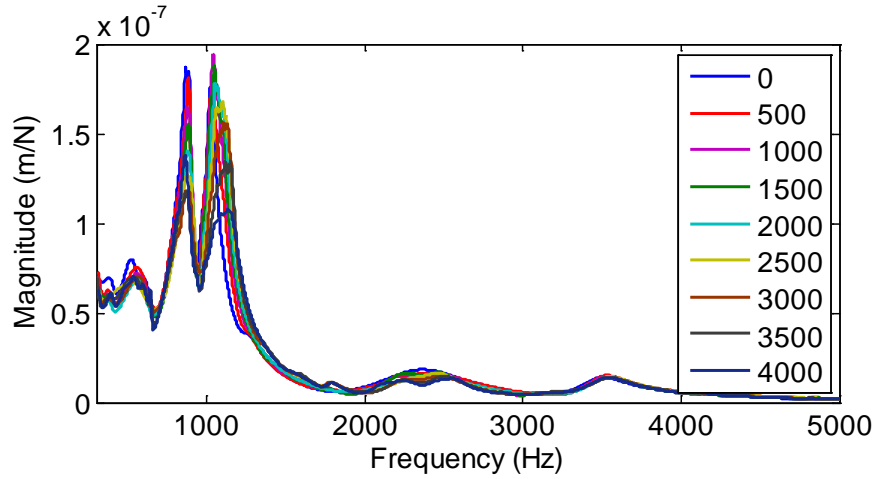


Figure 4.1: Standard cylindrical artifact FRF: x-direction.

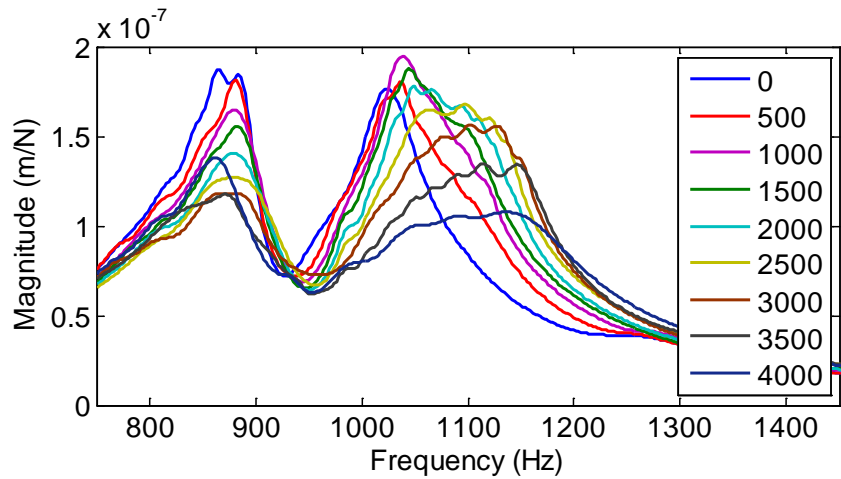


Figure 4.2: Standard cylindrical artifact FRF: x-direction (magnified view).

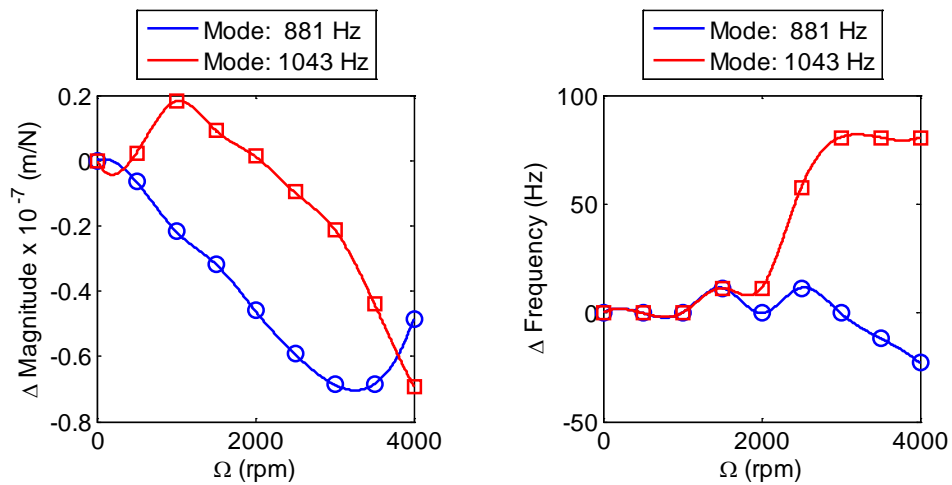


Figure 4.3: Changes in magnitude and frequency of two most compliant modes: cylindrical artifact FRF measurement, x-direction.

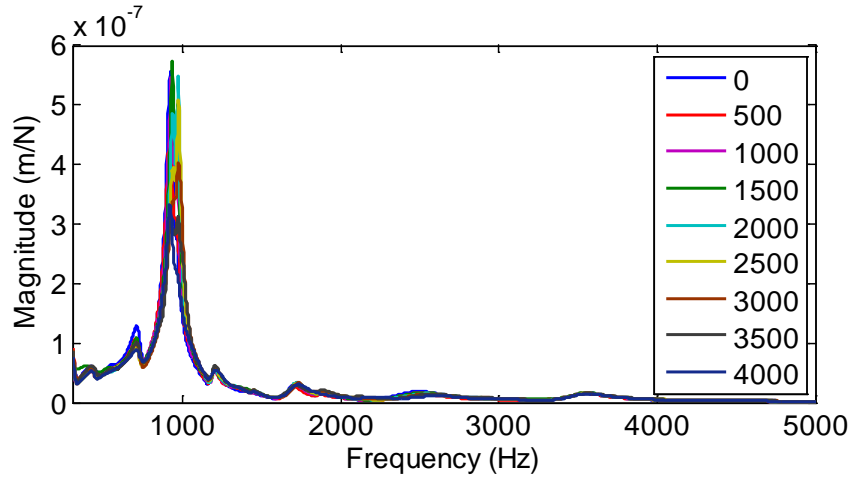


Figure 4.4: Standard cylindrical artifact FRF: y-direction.

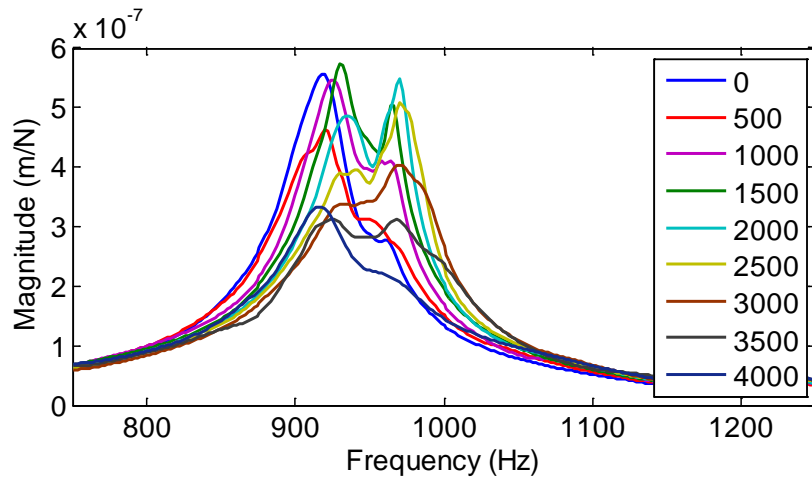


Figure 4.5: Standard cylindrical artifact FRF: y-direction (magnified view).

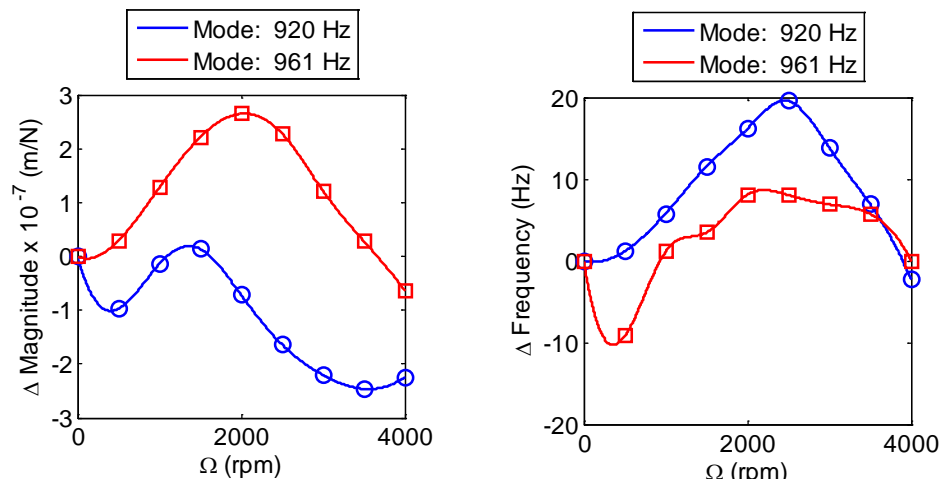


Figure 4.6: Changes in magnitude and frequency of two most compliant modes: cylindrical artifact FRF measurement, y-direction.

4.1.1.2 Solid Carbide Blank

The FRF measurements on the solid carbide blank were performed using setup 2. Figure 4.7 shows the magnitude of the FRF measured along the machine x-direction. The magnified view is plotted in Figure 4.8. Once again, the spindle speed was found to have a strong influence on the measured FRF.

The magnitude of the FRF for the mode at 1127 Hz was found to increase up to a spindle speed of 1500 rpm following which it decreases to approximately its original magnitude. Also, the frequency of the mode at 1127 Hz was found to steadily increase to approximately 1339 Hz. Figure 4.9 tracks the changes in the two most compliant modes of the FRF.

Figure 4.10 shows a plot of the magnitude of the FRF measured along the machine y-direction. Once again, a stiffening effect was observed with increase in spindle speed.

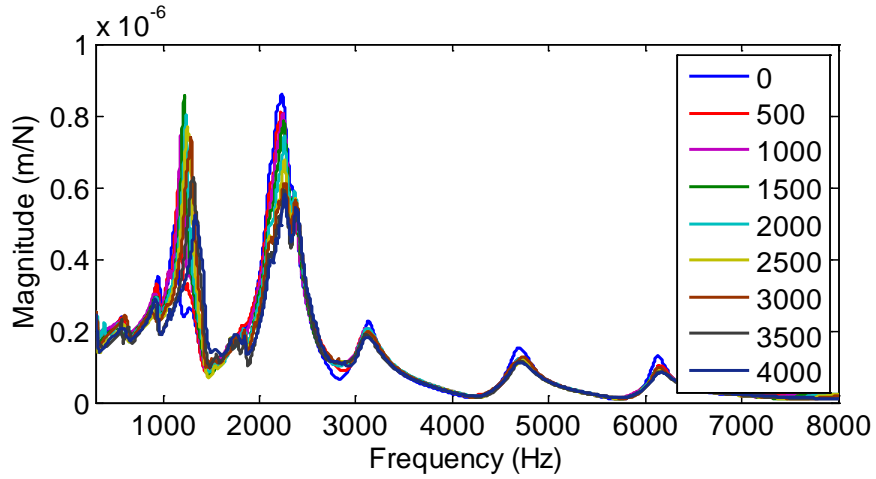


Figure 4.7: Solid carbide blank FRF: x-direction.

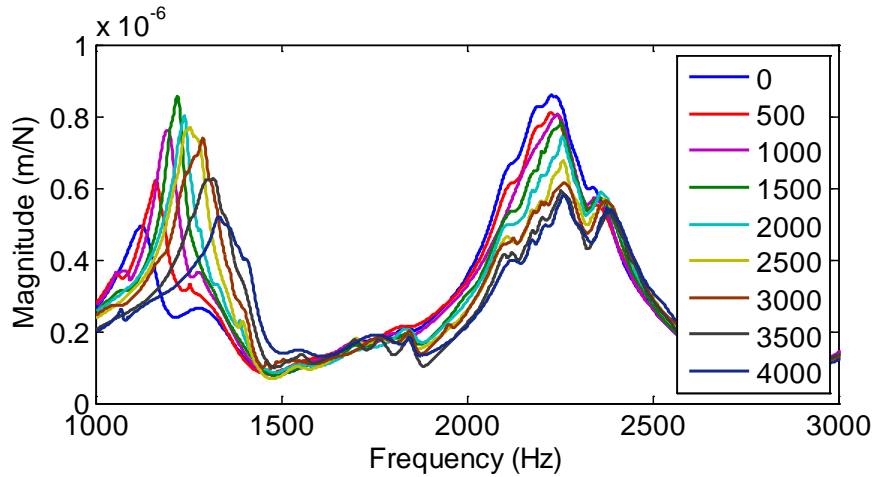


Figure 4.8: Solid carbide blank FRF: x-direction (magnified view).

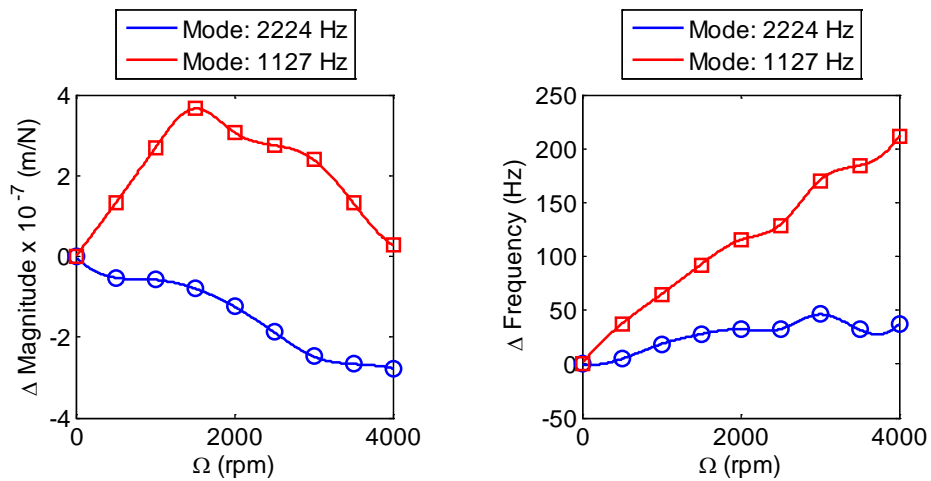


Figure 4.9: Changes in magnitude and frequency of two most compliant modes: solid carbide blank FRF measurement, x-direction.

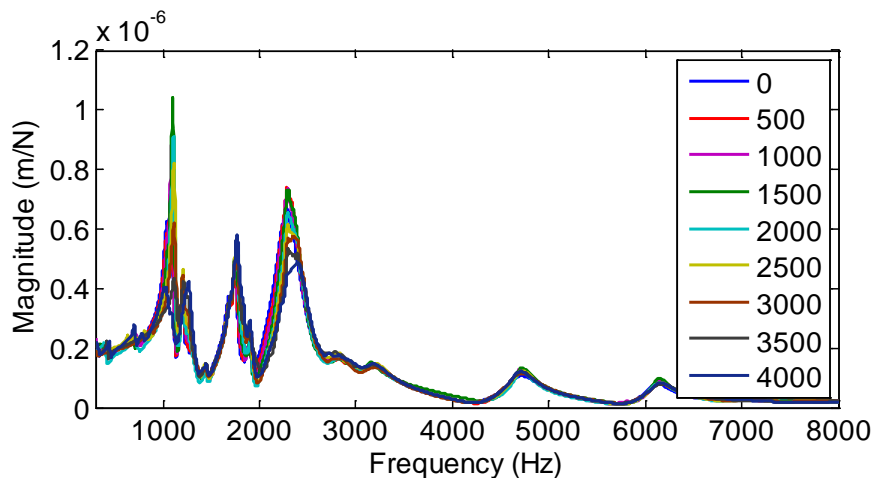


Figure 4.10: Solid carbide blank FRF: y-direction.

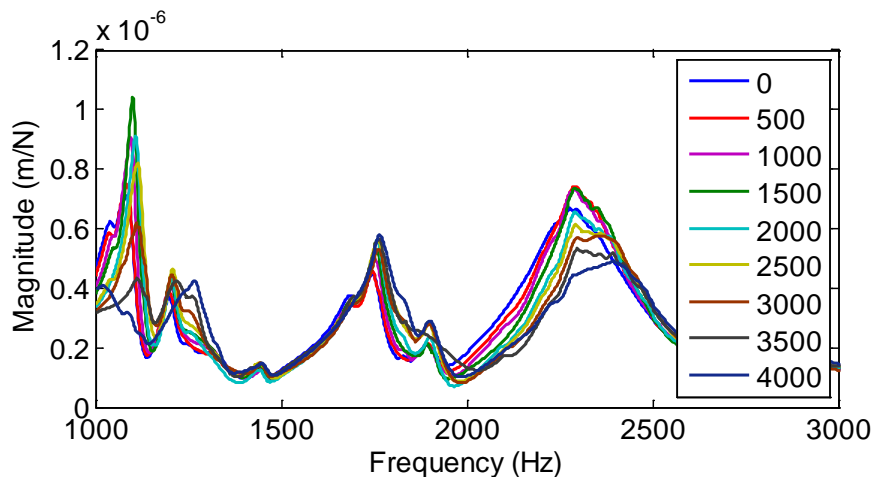


Figure 4.11: Solid carbide blank FRF: y-direction. (magnified view).

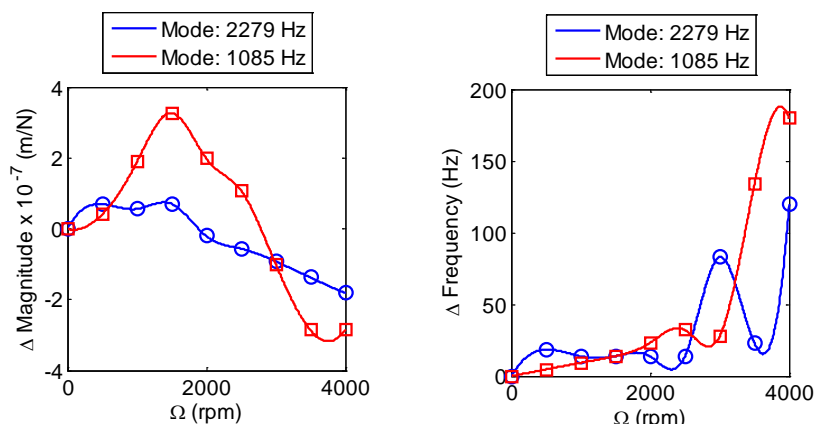


Figure 4.12: Changes in magnitude and frequency of two most compliant modes: solid carbide blank FRF measurement, y-direction.

4.1.2 SE Motions for Haas1

4.1.2.1 Artifact Form Error

Figure 4.13 shows a plot of the artifact form error measured at eight different spindle speeds superimposed on each other. The artifact form error measured at different spindle speeds was found to match closely. That maximum deviation in form error between the eight predictions was found to be 73 nm.

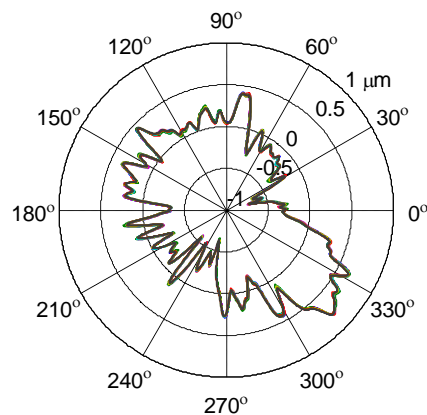


Figure 4.13: Comparison of artifact form error measured at different spindle speeds.

4.1.2.2 Synchronous SE Motions

Figure 4.14 and Figure 4.15 show polar plots of the synchronous SE motions in the fixed sensitive x-direction (left column), fixed sensitive y-direction (middle column), and rotating sensitive direction (right column). The encompassing lines represent the $\pm 2 \sigma$ standard deviations, evaluated as discussed in section 3.2.2.1. The highest synchronous SE motions were observed at 1000 rpm in the fixed sensitive y-direction.

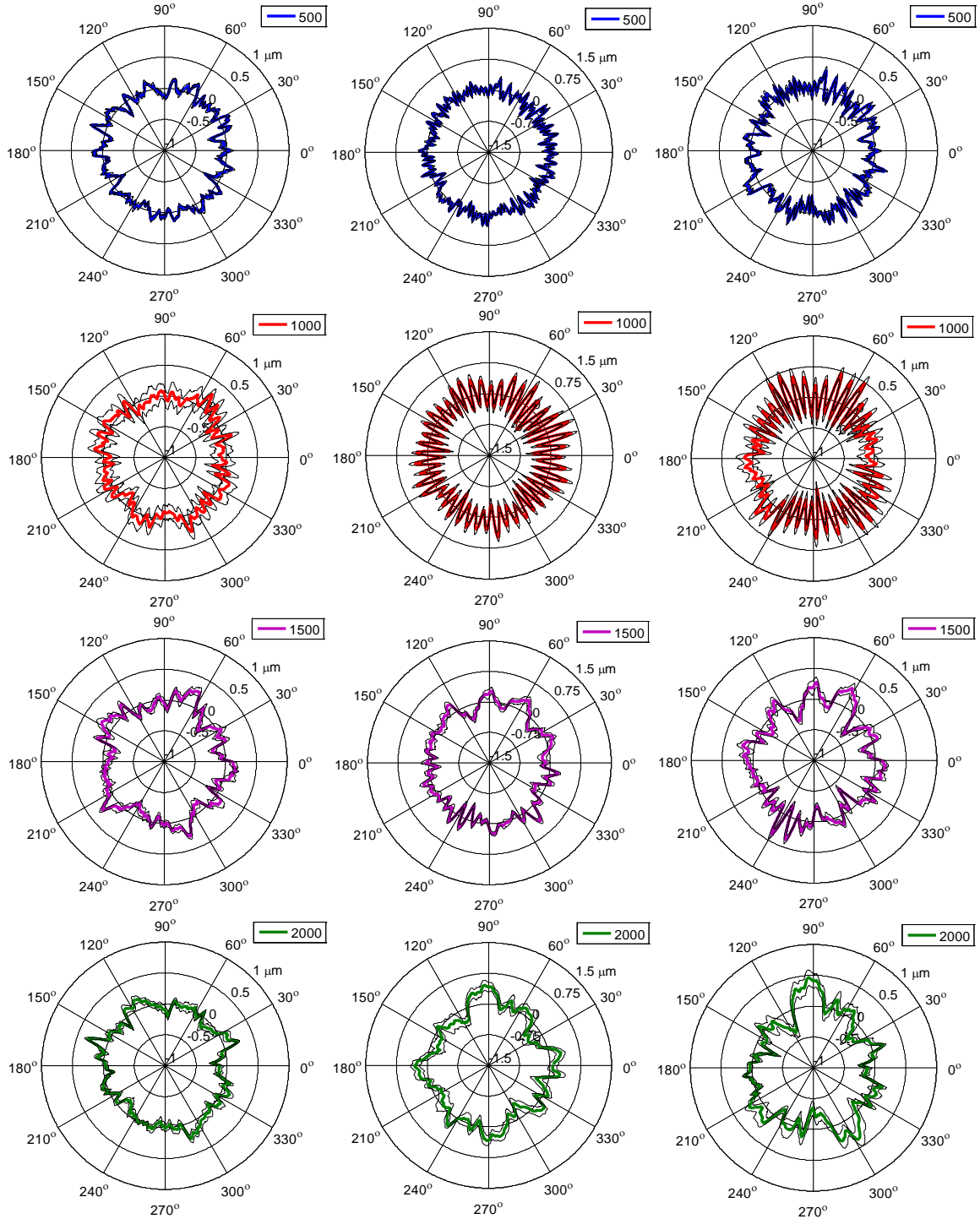


Figure 4.14: Synchronous SE motion: fixed sensitive x-direction (left); fixed sensitive y-direction (middle); rotating sensitive direction (right). Spindle speeds: 500 rpm, 1000 rpm, 1500 rpm, 2000 rpm.

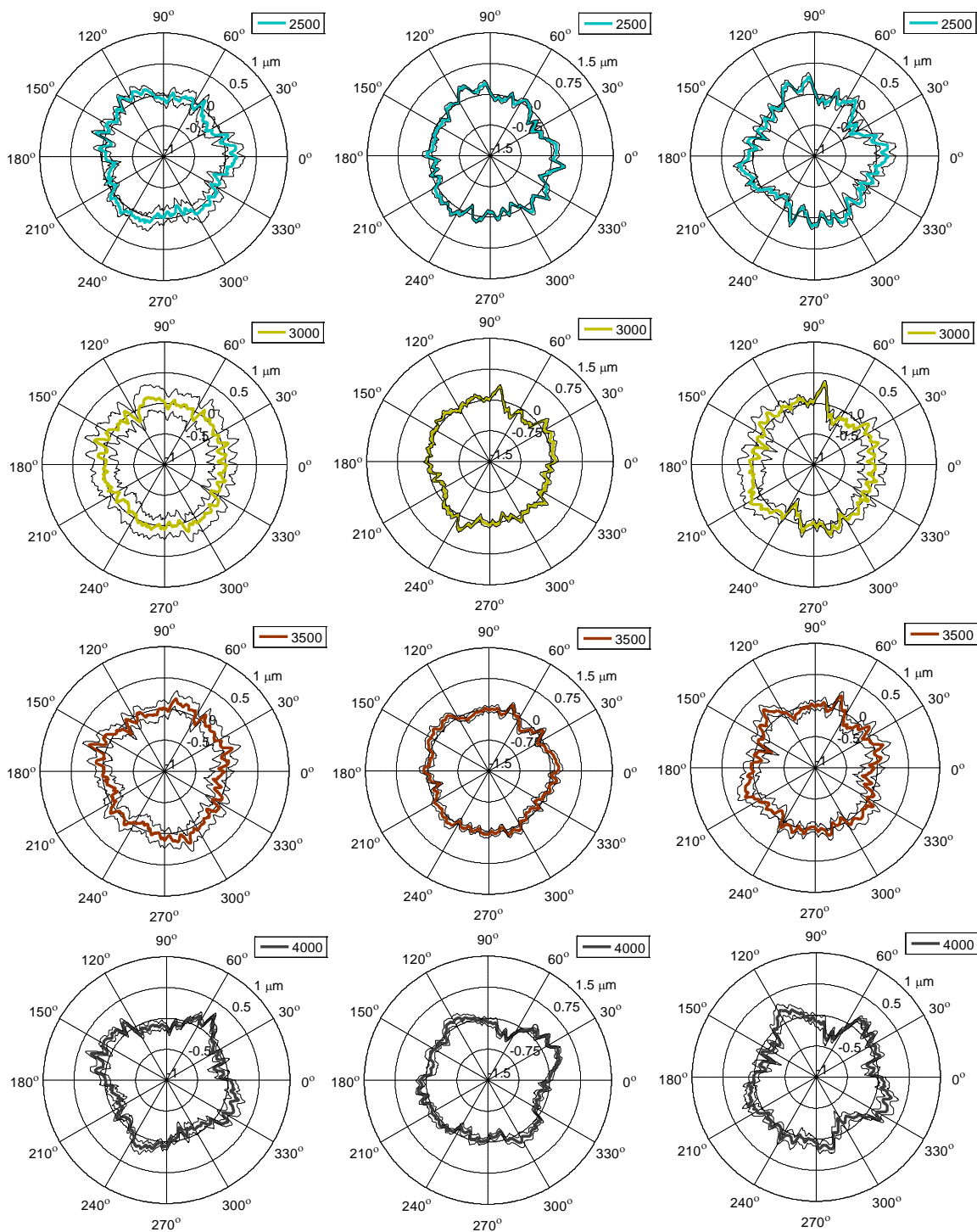


Figure 4.15: Synchronous SE motion: fixed sensitive x-direction (left); fixed sensitive y-direction (middle); rotating sensitive direction (right). Spindle speeds: 2500 rpm, 3000 rpm, 3500 rpm, 4000 rpm.

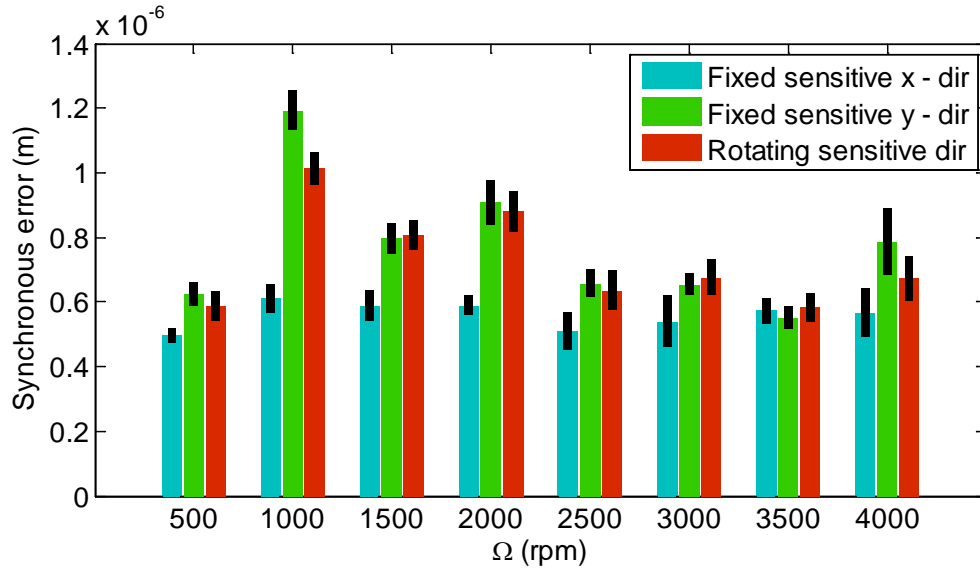


Figure 4.16: Peak-to-valley estimate of synchronous SE motions.

Figure 4.16 shows a plot of the peak-to-valley magnitude of the synchronous error motions as defined in section 3.2. The error bars indicate the $\pm 1 \sigma$ deviations in peak-to-valley magnitude. The maximum error was observed in the fixed sensitive y-direction at 1000 rpm.

4.1.2.3 Asynchronous SE Motions

Figure 4.17 shows a polar plot of the 1σ standard deviations of the asynchronous SE motions as a function of spindle orientation in the fixed sensitive x-direction (top), fixed sensitive y-direction (middle), and rotating sensitive direction (bottom). The maximum values of the 1σ standard deviations are plotted in Figure 4.18. The magnitude of the asynchronous error was found to be maximum at the highest speed in the fixed sensitive y-direction and the rotating sensitive direction. However, in the fixed sensitive x-direction, the asynchronous error magnitude was highest at 3000 rpm.

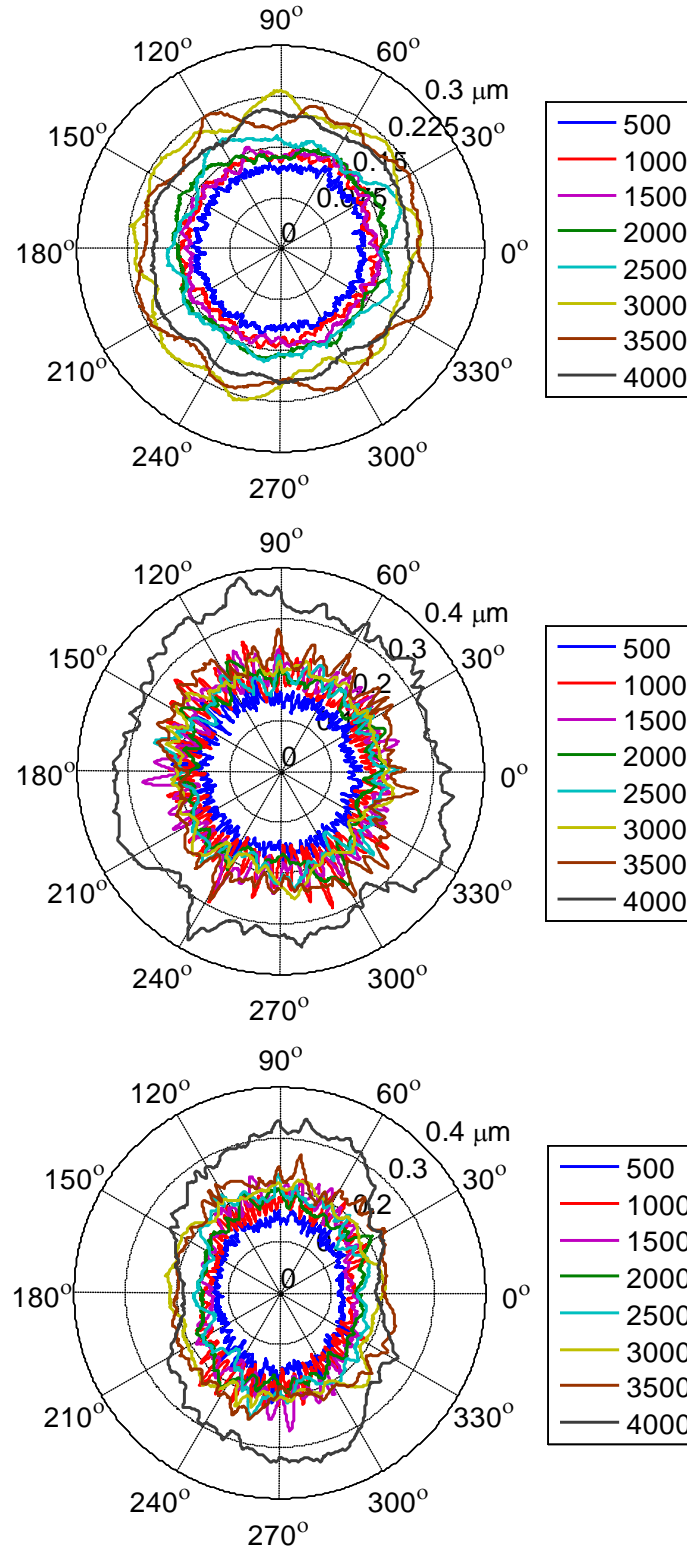


Figure 4.17: 1σ standard deviation of asynchronous SE motion: fixed sensitive x-direction (top); fixed sensitive y-direction (middle); rotating sensitive direction (bottom).

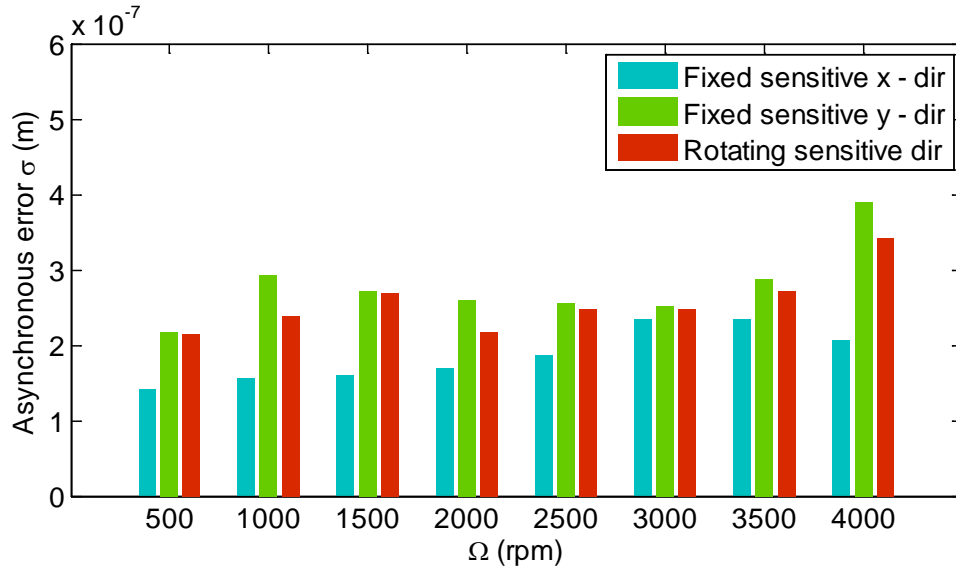


Figure 4.18: Maximum 1σ standard deviation of asynchronous SE motion.

4.1.2.4 Frequency Content of SE Motions

Figure 4.19 to Figure 4.21 show the frequency content of the synchronous SE motions in the fixed sensitive x-direction, fixed sensitive y-direction, and the rotating sensitive direction respectively. The horizontal axis is normalized by the spindle speed to denote undulations per revolution (UPR). There is a sharp peak at 44 UPRs in the fixed sensitive y-direction. This peak corresponds to a synchronous error which repeats 44 times every revolution. This is also evident in Figure 4.14. In the rotating sensitive direction, two peaks were observed at 43 and 45 UPRs.

Figure 4.22 to Figure 4.24 show the frequency content of the asynchronous SE motions in the fixed sensitive x-direction, fixed sensitive y-direction and the rotating sensitive direction respectively. In this case the horizontal axis represents frequency. An increase in asynchronous error content was observed at 730 Hz in the fixed sensitive y-direction (Figure 4.23) at 1000 rpm. This frequency corresponds to 44 UPRs at 1000 rpm at which there is also an increase in synchronous error motions. Also, poor coherence was observed in the measured FRF at 730 Hz as previously observed (Figure 3.13).

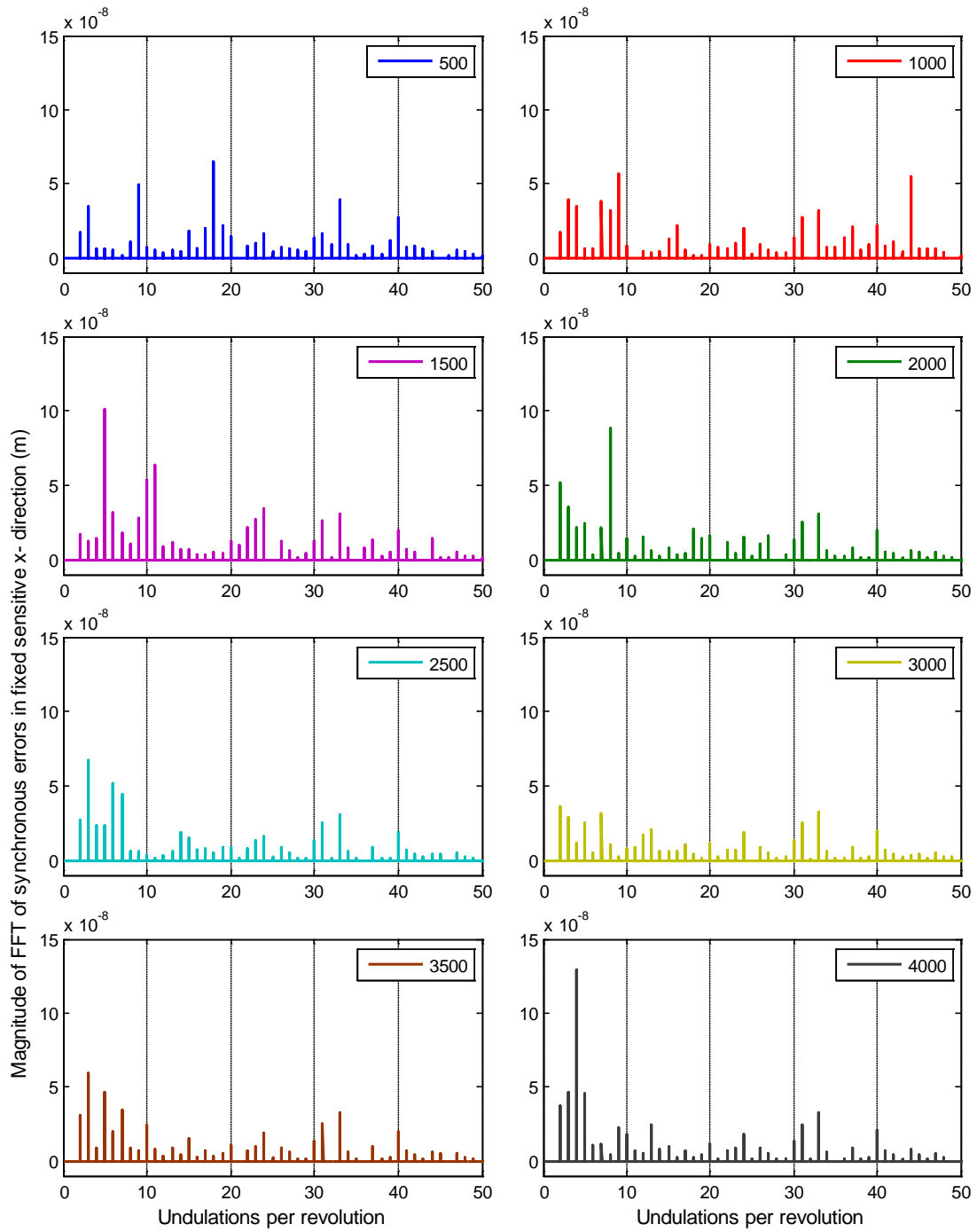


Figure 4.19: Magnitude of FFT of synchronous SE in fixed-sensitive x-direction.

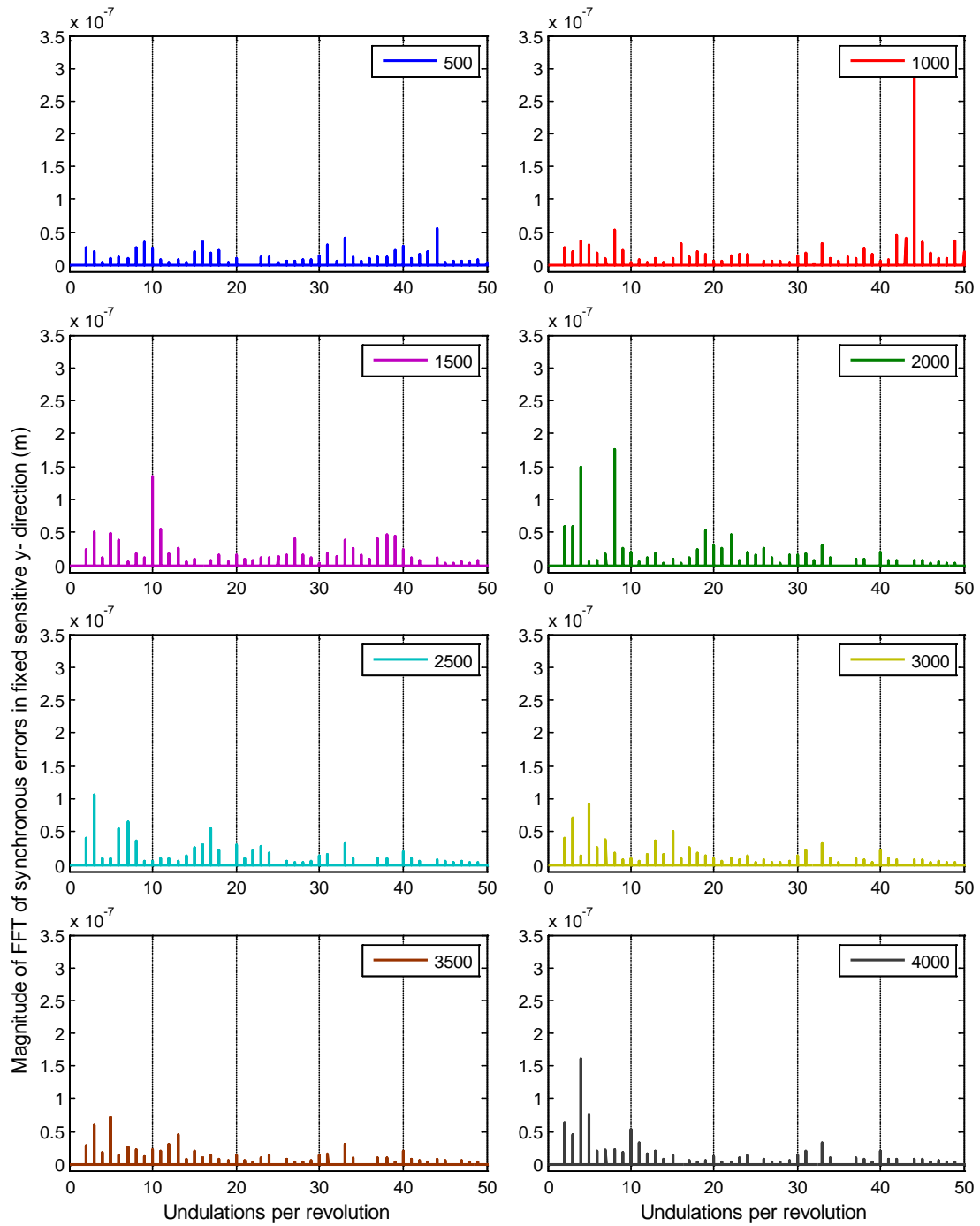


Figure 4.20: Magnitude of FFT of synchronous SE in fixed-sensitive y-direction.

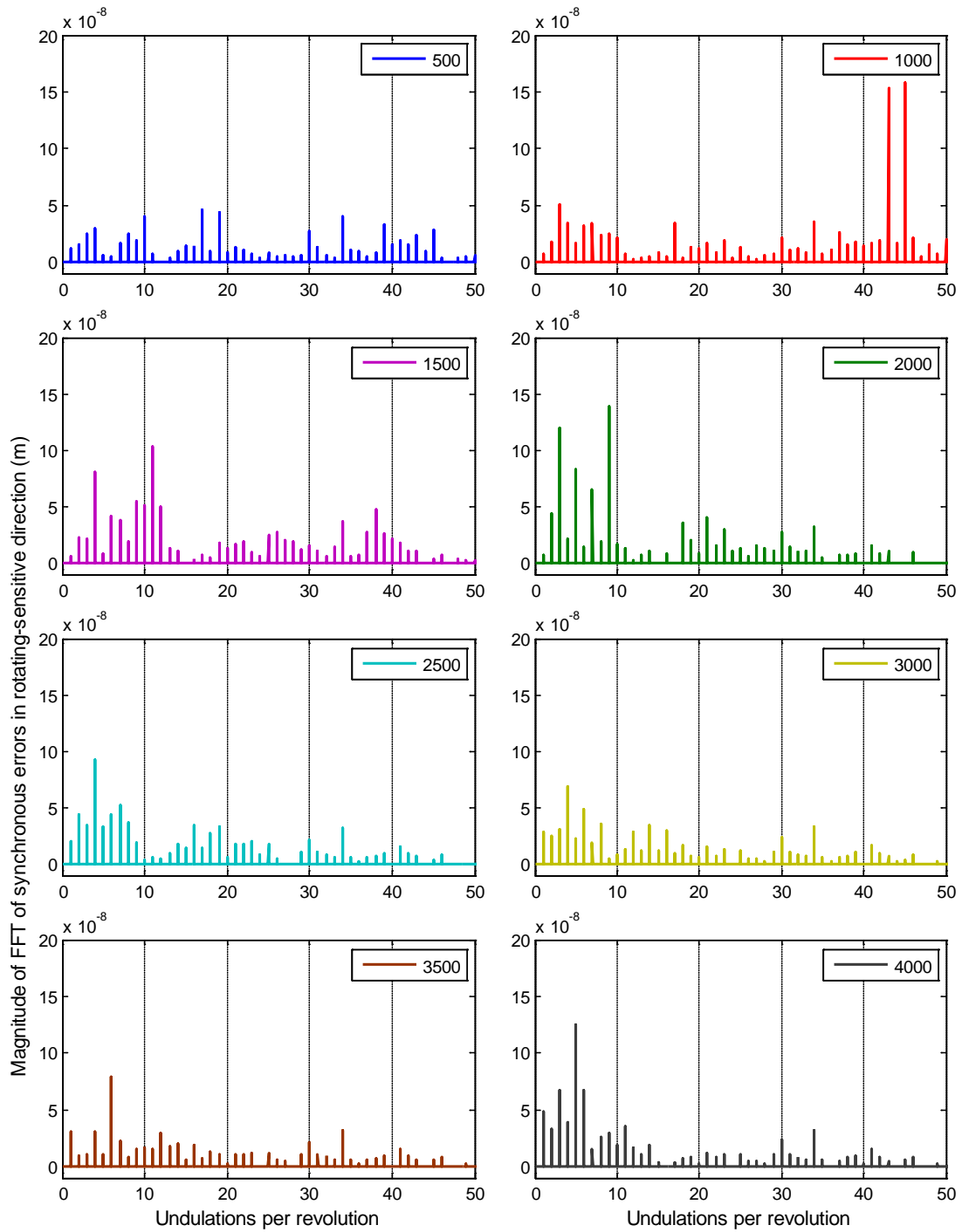


Figure 4.21: Magnitude of FFT of synchronous SE in rotating sensitive direction.

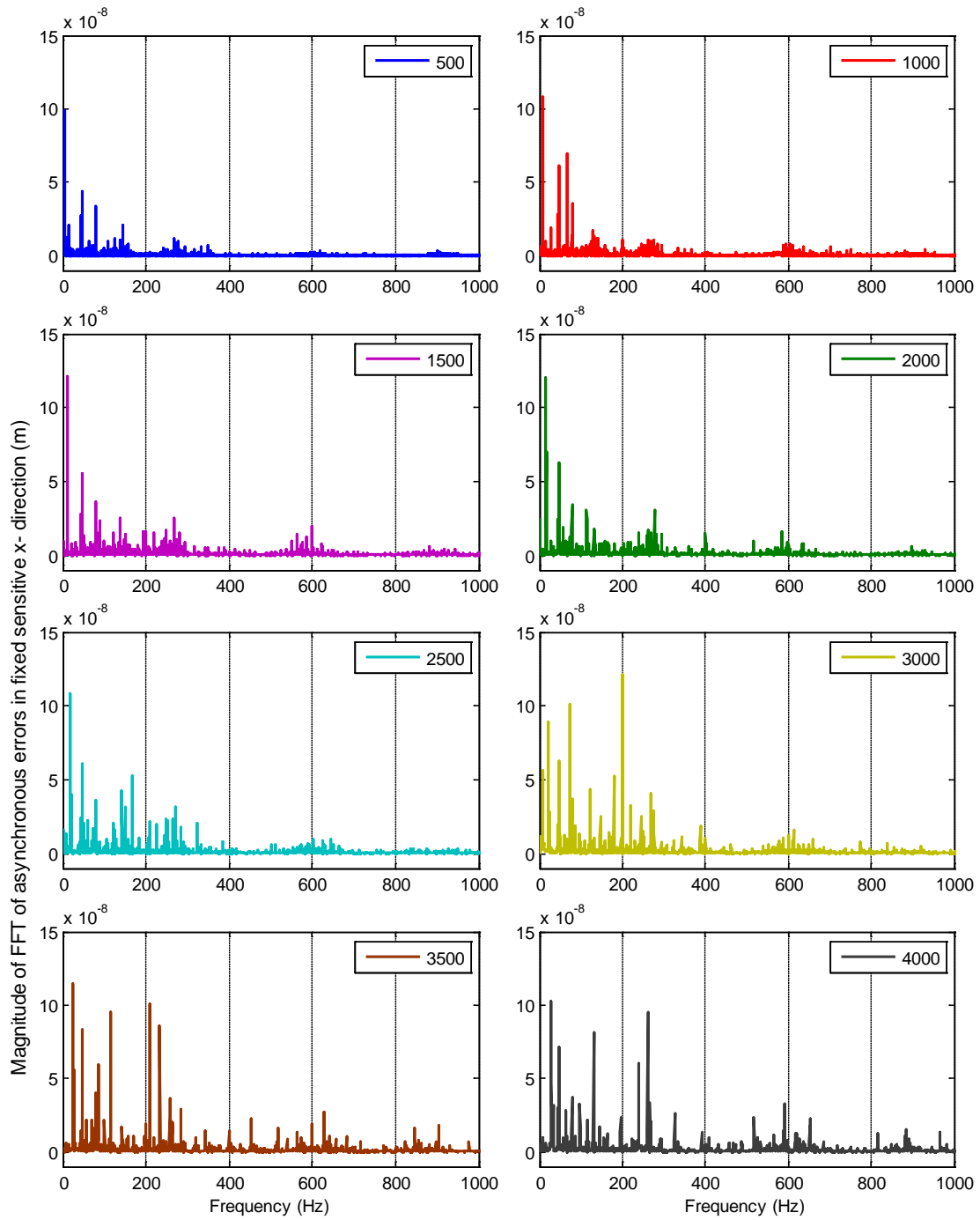


Figure 4.22: Magnitude of FFT of asynchronous SE in fixed-sensitive x-direction.

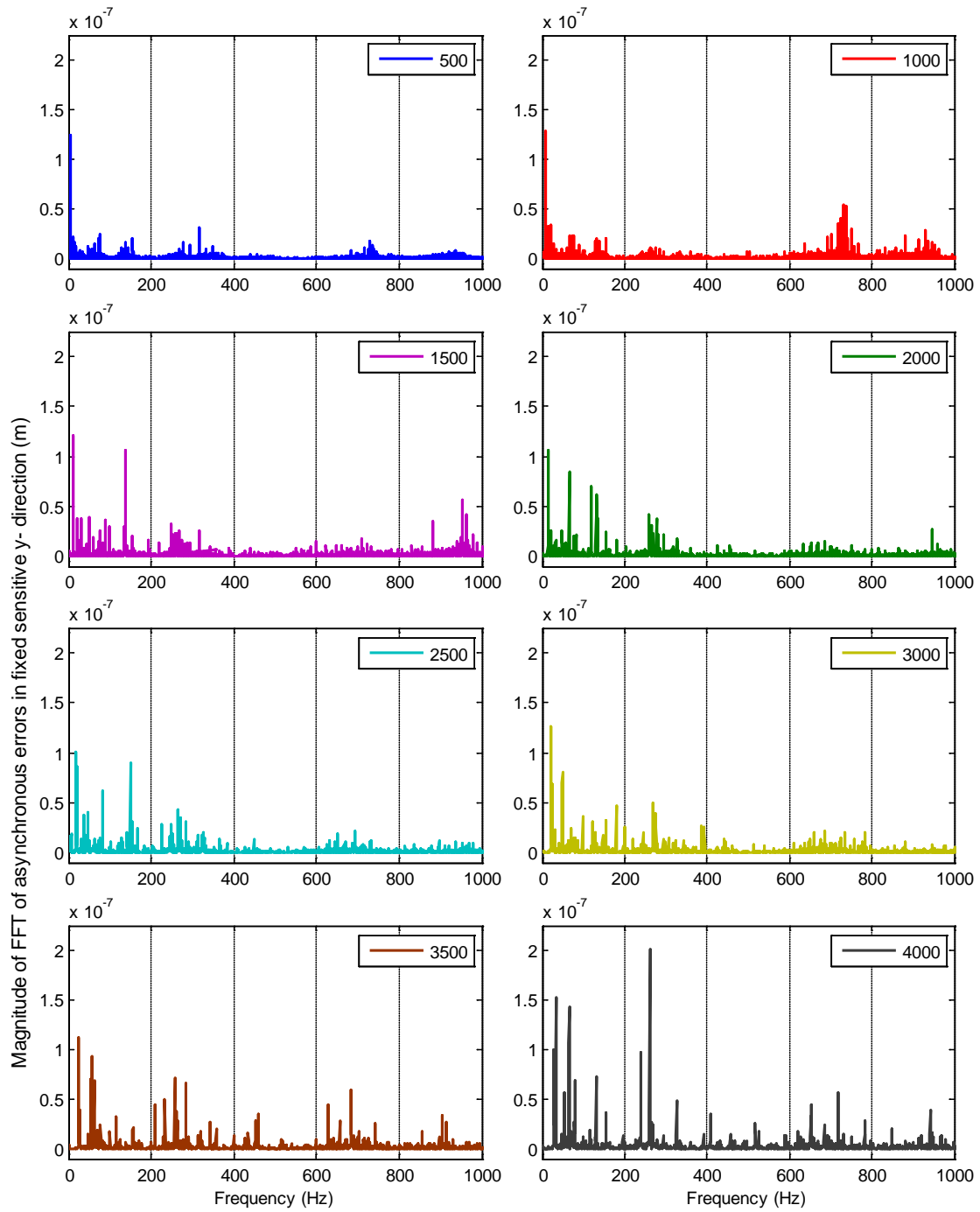


Figure 4.23: Magnitude of FFT of asynchronous SE in fixed-sensitive y-direction.

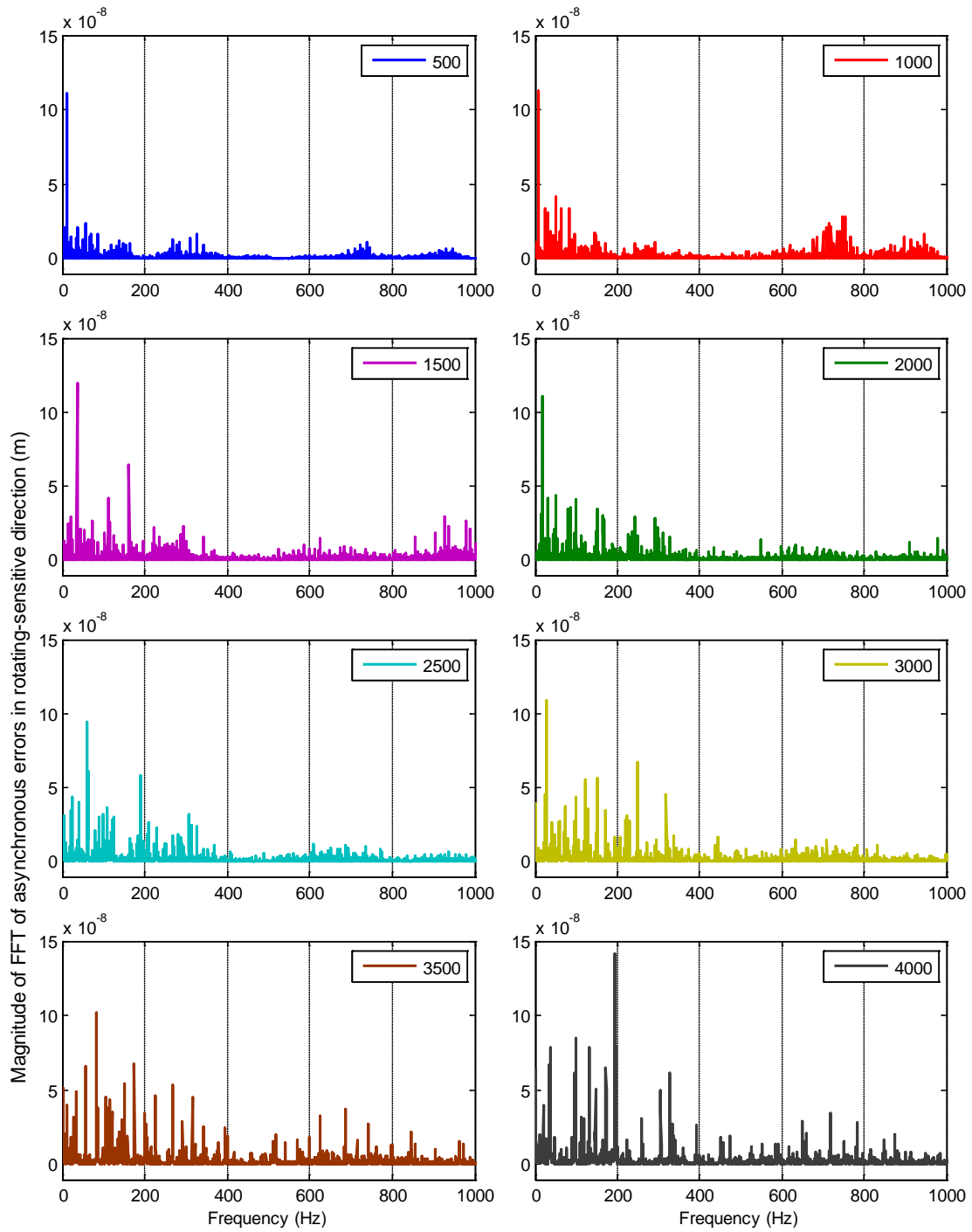


Figure 4.24: Magnitude of FFT of asynchronous SE in rotating sensitive direction.

4.2 NSK HES-500 HIGH SPEED SPINDLE

4.2.1 Speed-dependent Spindle Dynamics

The NSK HES-500 high speed spindle has a maximum permissible spindle speed of 50 krpm. In this study, dynamics measurements were performed between 0 rpm to 50 krpm in increments of 5 krpm. The high speed spindle was mounted in the Haas1 spindle using a CAT-40 connection. A solid carbide blank (3.175 mm diameter) was mounted in the high speed spindle. The stick-out length of the carbide blank from the collet face was 5 mm. Both the structural dynamics, and SE motion measurements were performed with the carbide blank as the target. The structural dynamics measurements were performed using setup 2.

Figure 4.25 shows a plot of the magnitude of the FRF measured along the machine x-direction. Firstly, it was observed that the stationary condition (0 rpm) FRF was significantly different than the rotating FRFs. Figure 4.26 tracks the changes in stiffness and natural frequencies of the two most compliant modes in the FRF. The natural frequency of the mode at 3048 Hz was found to steadily decrease with spindle speed. At 50 krpm, the difference in natural frequency was approximately 400 Hz. The magnitude of the mode at 3048 Hz was also found to decrease (relative to magnitude at 5 krpm) with spindle speed implying a stiffening effect.

Figure 4.27 shows the FRF magnitude along the machine y-direction. Once again, the natural frequency of the mode at 2959 Hz steadily decreases with spindle speed. Figure 4.28 shows the changes in the magnitude and frequency of the two most compliant modes of the FRF.

The carbide blank was mounted in the high speed spindle using a collet chuck. The dynamics of the system is highly sensitive to the connection stiffness at the collet. The repeatability of the measurement and the influence of connection stiffness and tightening torque on the dynamic response of the high speed spindle warrants further investigation.

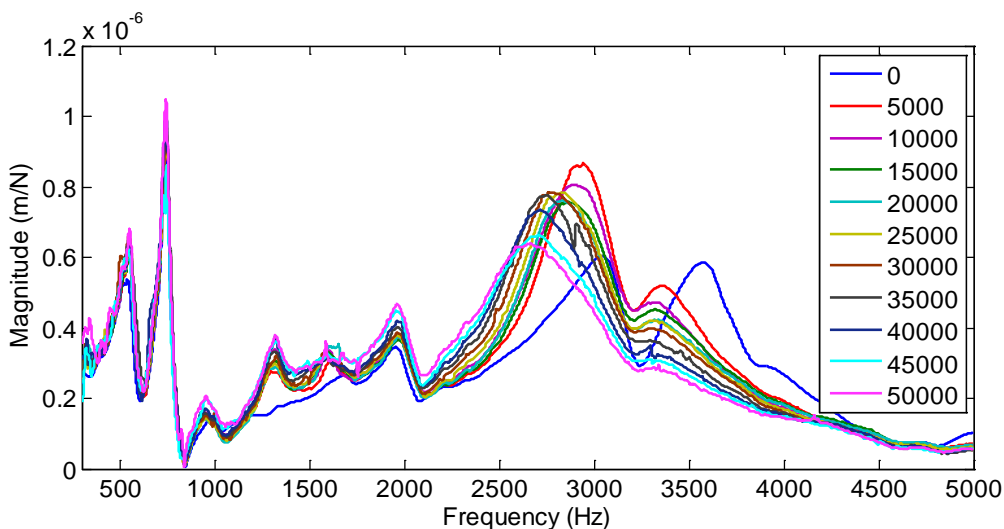


Figure 4.25: Speed-dependent FRF measurements on high speed spindle: x-direction.

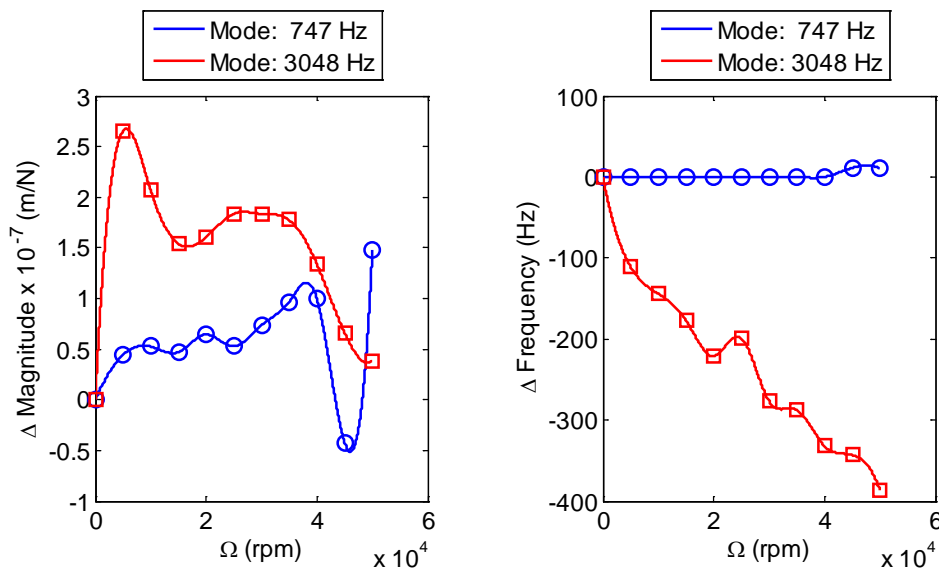


Figure 4.26: Changes in magnitude and frequency of two most compliant modes: x-direction.

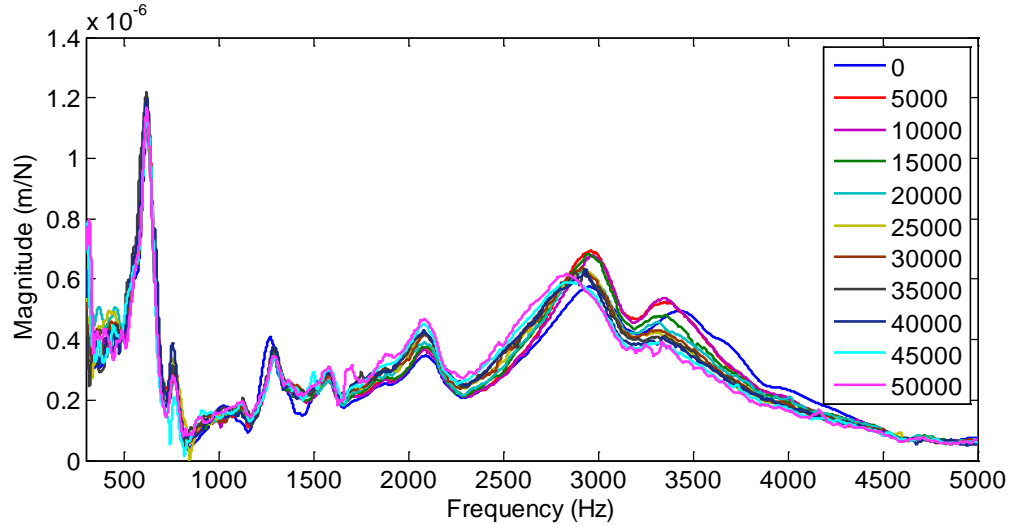


Figure 4.27: Speed-dependent FRF measurements on high speed spindle: y-direction.

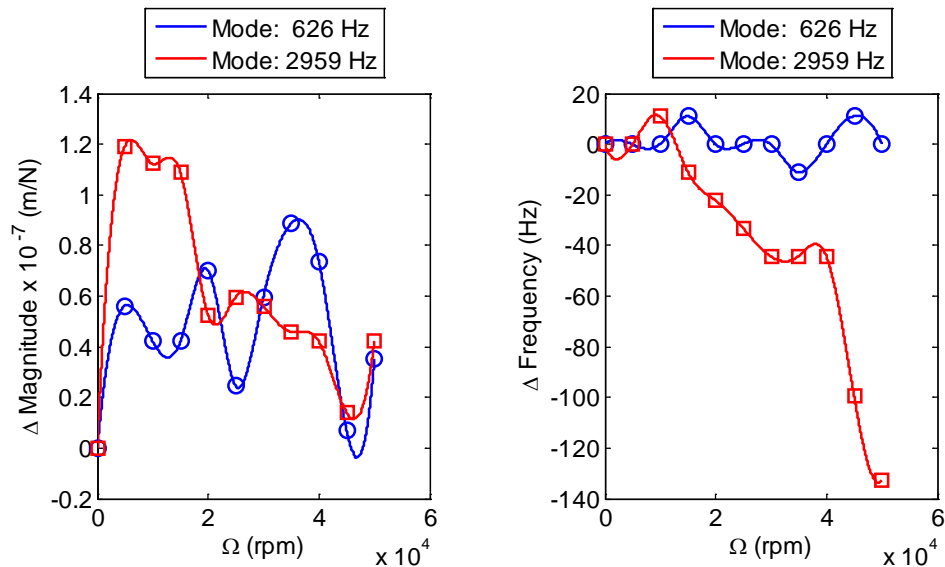


Figure 4.28: Changes in magnitude and frequency of two most compliant modes: y-direction.

4.2.2 SE Motions for NSK HES-500 High Speed Spindle

The SE motions and artifact form error were measured using the setup described in section 2.2.3. The LDV produced an output voltage proportional to the change in velocity. The velocity signal was integrated to produce displacement. The displacement data was high-pass filtered to eliminate the integration errors. In this study, data was collected for a total of 4500 spindle rotations at a range of spindle speeds: 0 rpm to 50

krpm in increments of 5 krpm). The data was then segmented into ten sections of 450 rotations, and the mean form and synchronous SE motions were estimated as described in section 3.2.2.1.

4.2.2.1 Artifact Form Error

Figure 4.29 shows a plot of the artifact form error for the ten spindle speeds, superimposed on each other. The maximum deviation in form error between the ten predictions was found to be 434 nm. The variation in the measured form error was attributed to the constraints imposed by the low sampling rate relative to the spindle speed and the integration errors. These errors may be remedied by using a higher sampling rate data acquisition system and a displacement sensor. The influence of sampling rate on the performance of the multi-probe error separation technique warrants further investigation.

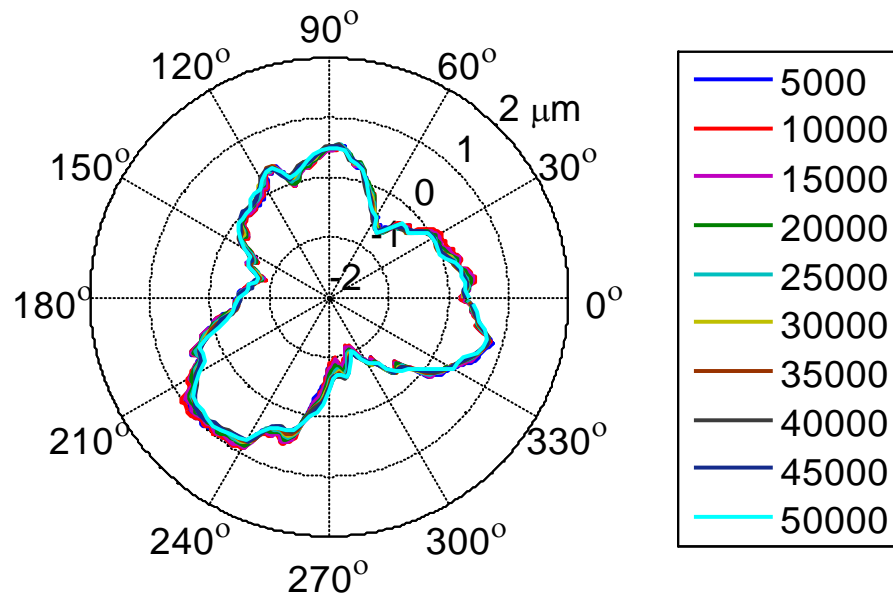


Figure 4.29: Comparison of artifact form error measured at different spindle speeds.

4.2.2.2 Synchronous SE Motions

Figure 4.31 shows the synchronous SE motions in the fixed sensitive x-direction (top), fixed sensitive y-direction (middle), and the rotating sensitive direction (bottom). The synchronous SE motions for the 10 different measurement speeds are superimposed on each other. In the case of the high speed spindle, the form of the synchronous SE motions was found to remain consistent over the entire speed range unlike for the Haas1 machine described earlier.

Figure 4.30 shows a plot of the peak-to-valley synchronous errors. The error bars indicate the $\pm 1 \sigma$ deviation in the estimate. The synchronous SE motions were found to decrease with increasing spindle speed. However, this may be due to the difficulty in estimating high angular frequency error content due to constraints in the sampling rate. As previously mentioned, the influence of sampling rate on SE motion estimation warrants further investigation.

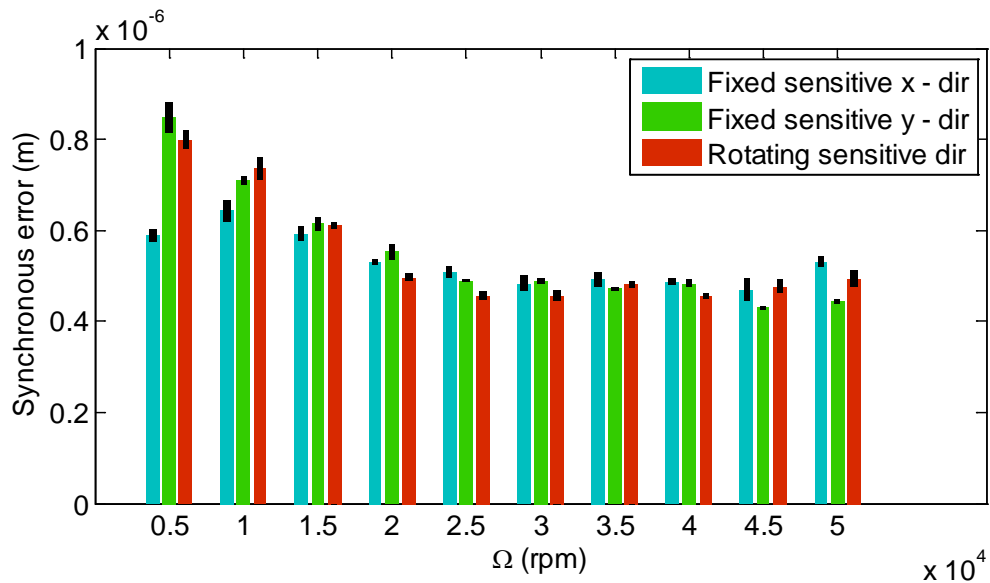


Figure 4.30: Peak-to-valley estimate of synchronous SE motions.

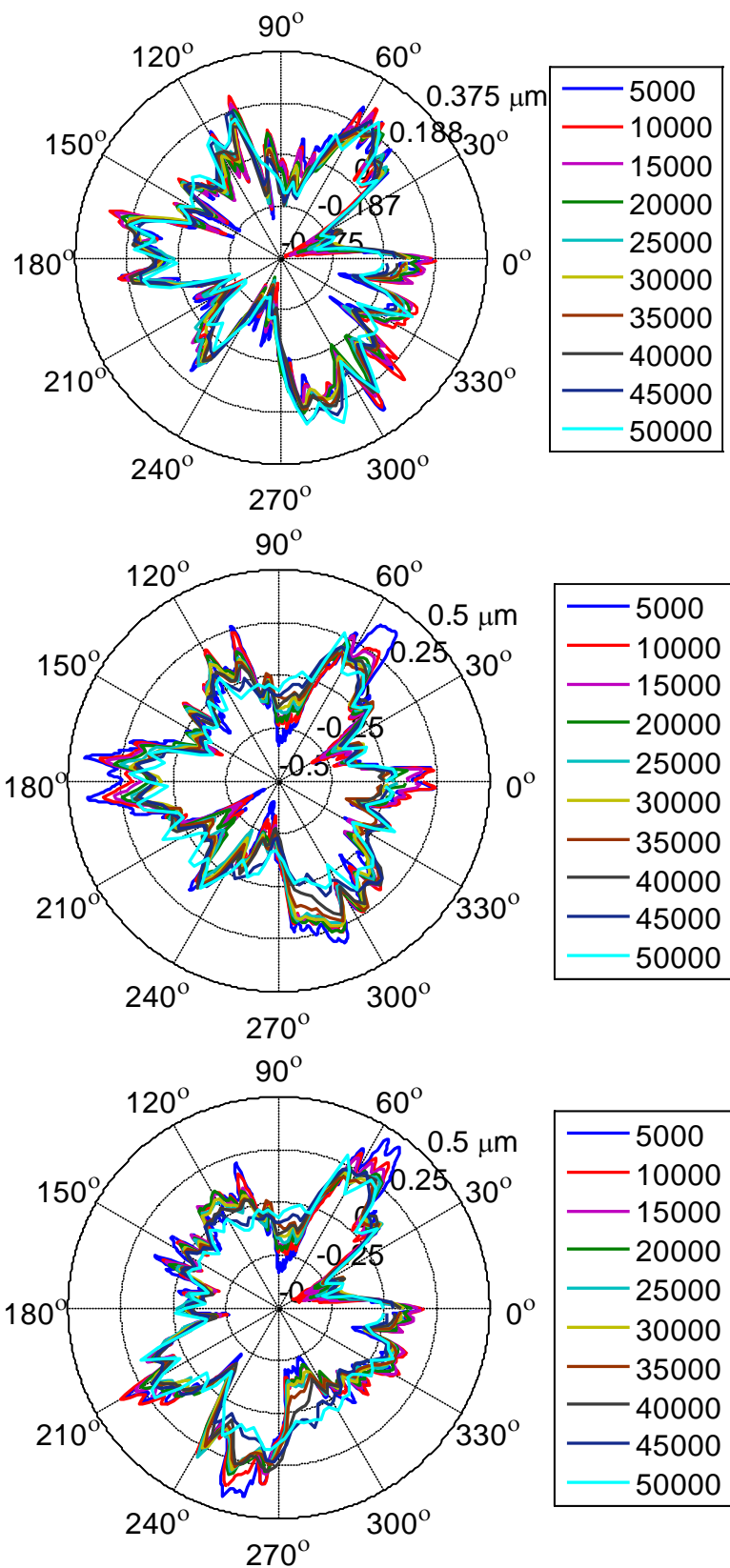


Figure 4.31: Synchronous SE: fixed sensitive x-direction (top), fixed sensitive y-direction (middle), rotating sensitive direction (bottom).

4.2.2.3 Asynchronous SE motions

Figure 4.33 shows polar plots of the 1σ standard deviations of the asynchronous SE motions as a function of spindle orientation in the fixed sensitive x-direction (top), the fixed sensitive y-direction (middle), and the rotating sensitive direction (bottom). The asynchronous error motions were found to increase with spindle speed. A strong directionality was observed in the polar plot of the asynchronous errors. The standard deviation of the asynchronous errors was found to be highest at spindle orientations between 30° and 60° . This was particularly true in the fixed sensitive y-direction and the rotating sensitive direction.

The maximum values of the 1σ standard deviations of the asynchronous error motions are plotted in Figure 4.32. The maximum asynchronous errors were observed at 45 krpm.

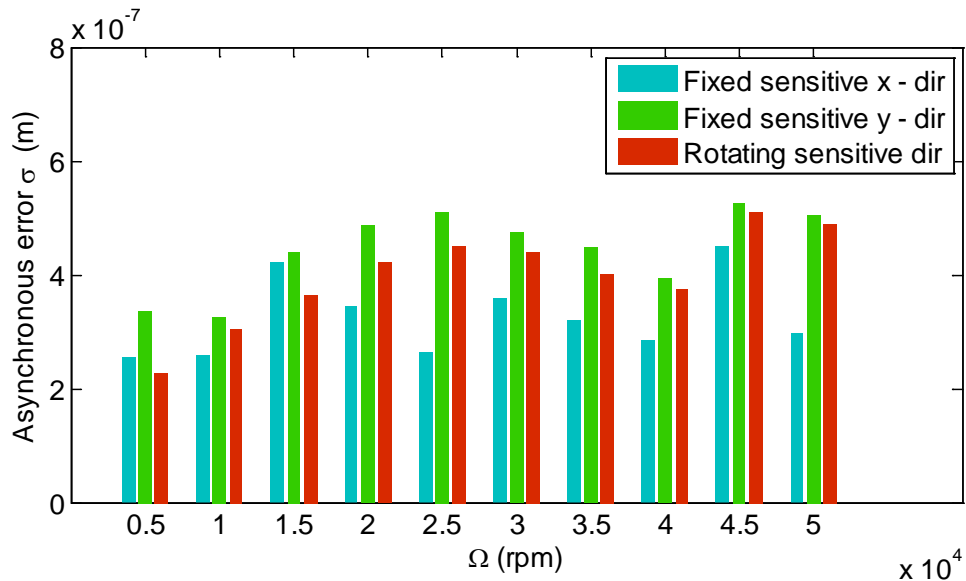


Figure 4.32: Maximum 1σ standard deviation of asynchronous SE motion.

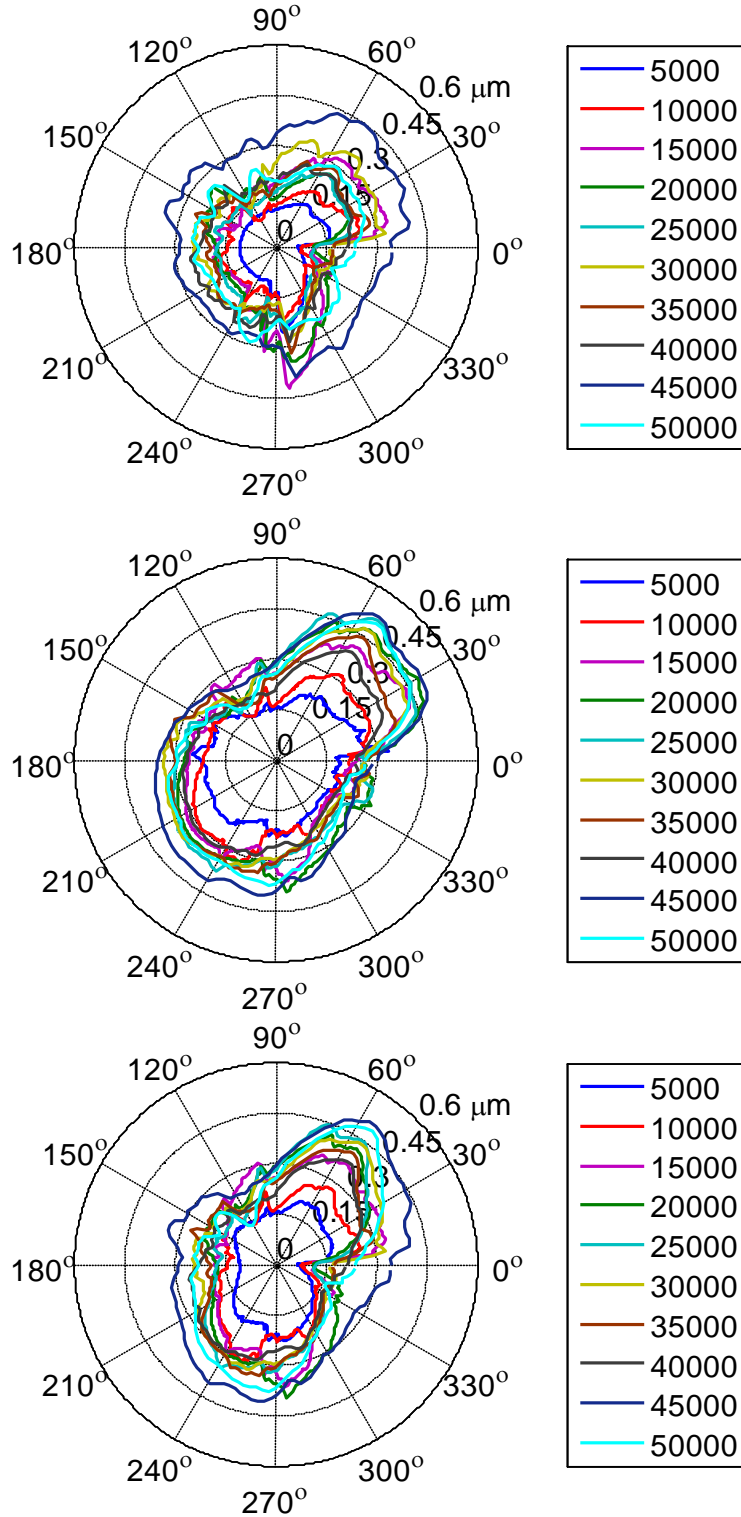


Figure 4.33: 1σ standard deviation of asynchronous SE motion: fixed sensitive x-direction (top); fixed sensitive y-direction (middle); rotating sensitive direction (bottom).

4.2.2.4 Frequency Content of SE Motions

Figure 4.34 to Figure 4.36 show the frequency content of the synchronous SE motions in the fixed sensitive x-direction, fixed sensitive y-direction, and the rotating sensitive direction, respectively. The horizontal axis is normalized by the spindle speed to denote undulations per revolution (UPR). Figure 4.37 to Figure 4.39 show the frequency content of the asynchronous SE motions in the fixed sensitive x-direction, fixed sensitive y-direction and the rotating sensitive direction respectively. In this case the horizontal axis represents frequency. An increase in the higher frequency content of the asynchronous errors was observed with increasing spindle speed. As the spindle speed increases, the frequency band influenced by unbalances in the spindle also increases.

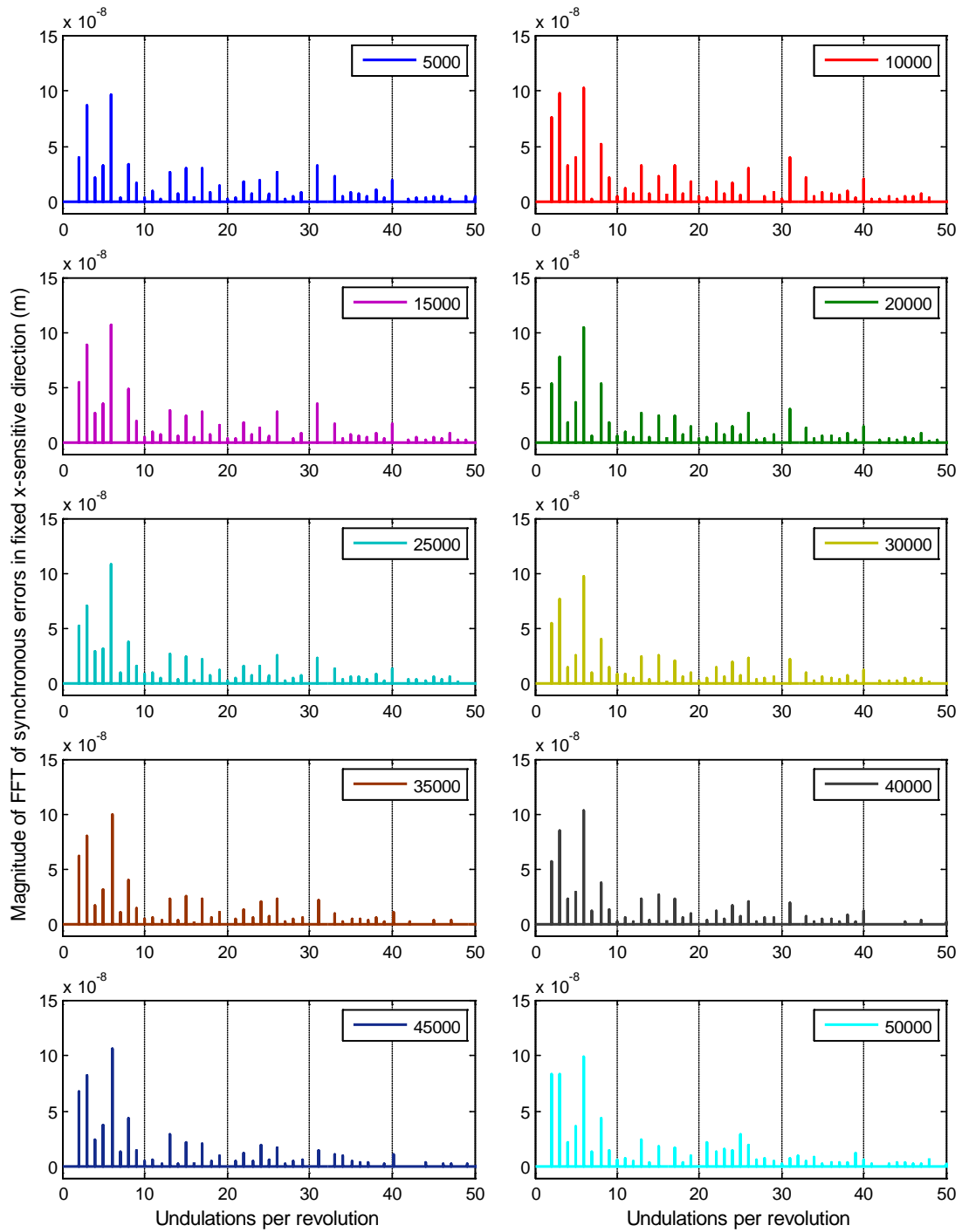


Figure 4.34: Magnitude of FFT of synchronous SE in fixed-sensitive x-direction.

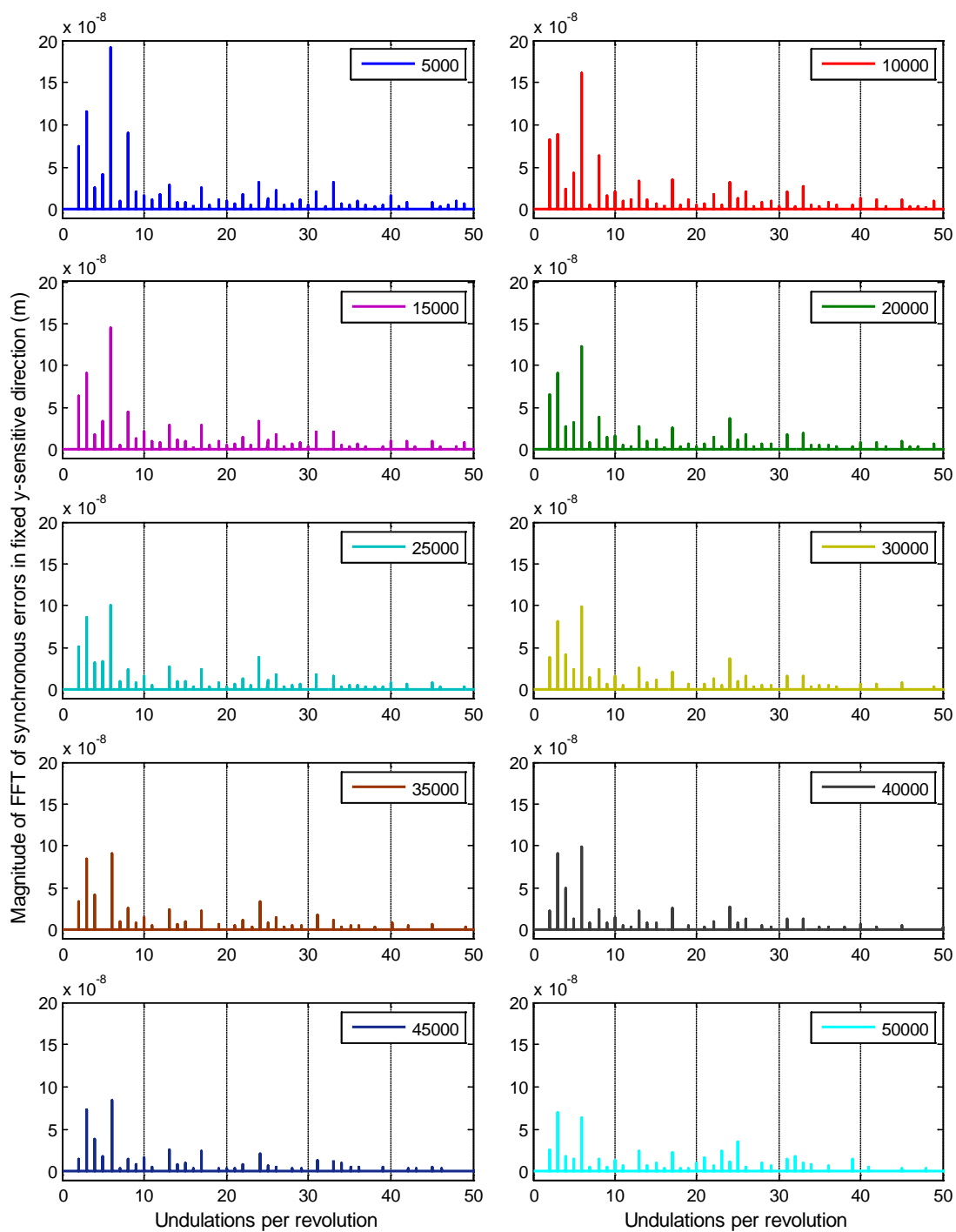


Figure 4.35: Magnitude of FFT of synchronous SE in fixed-sensitive y-direction.

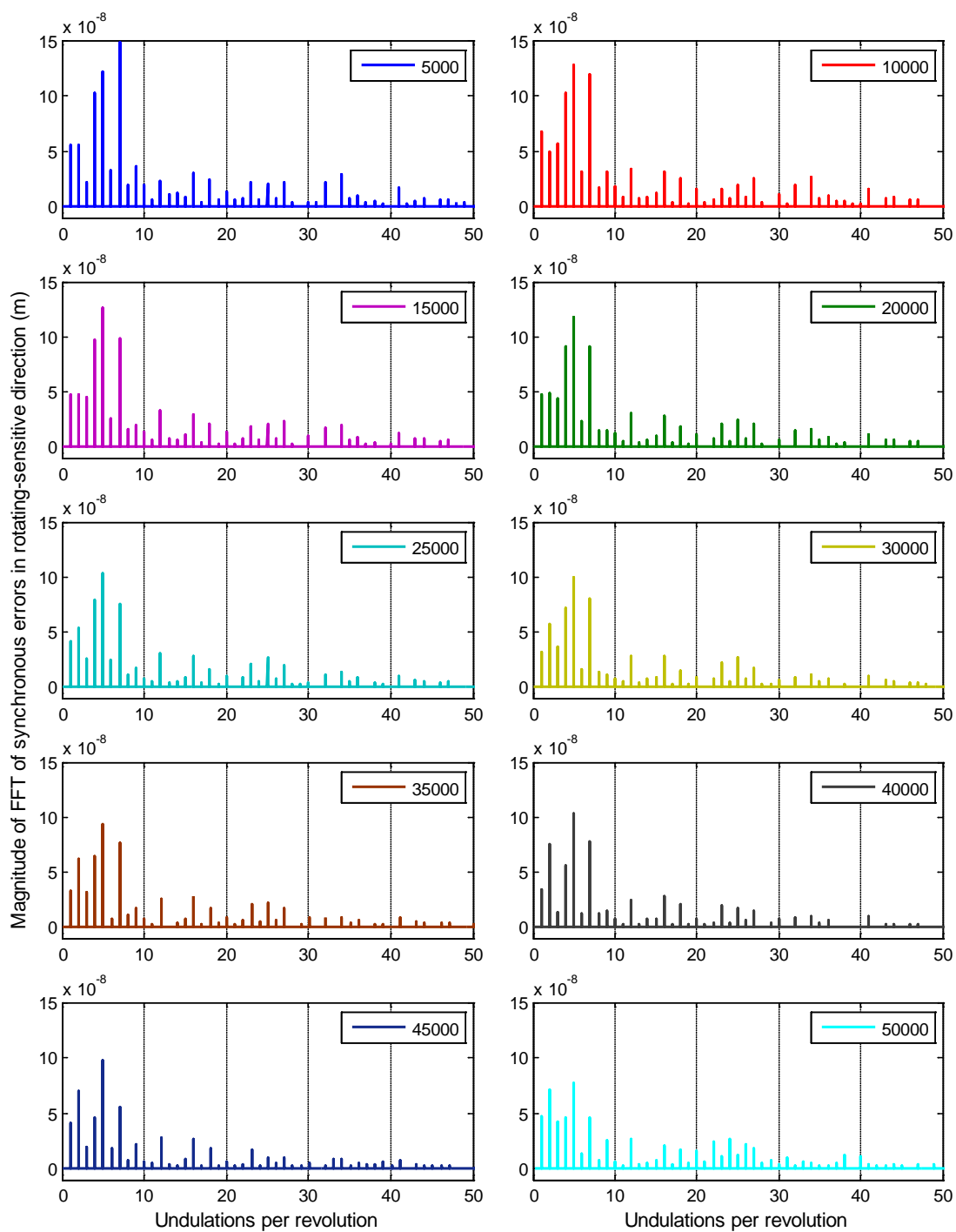


Figure 4.36: Magnitude of FFT of synchronous SE in rotating-sensitive direction.

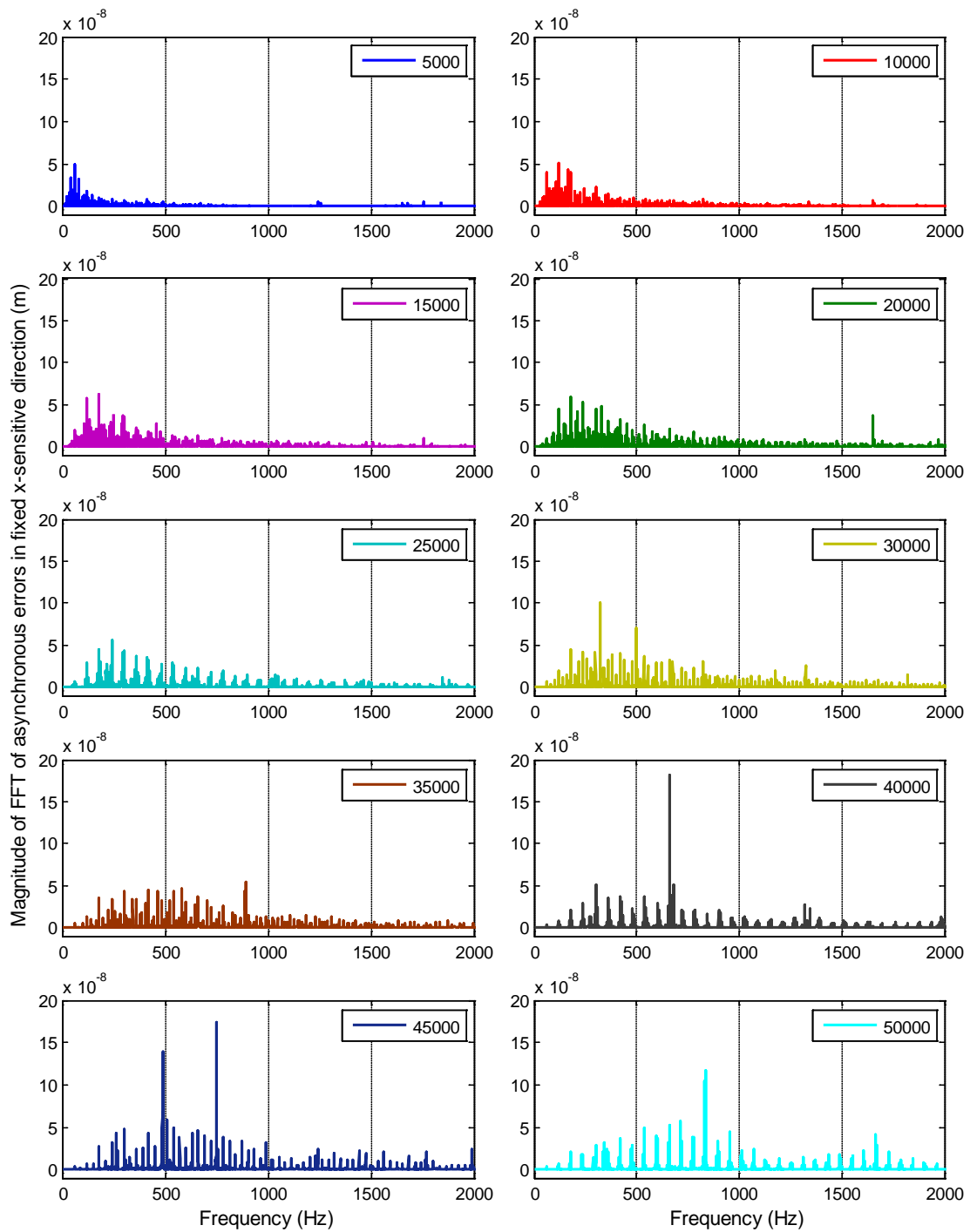


Figure 4.37: Magnitude of FFT of asynchronous SE in fixed-sensitive x-direction.

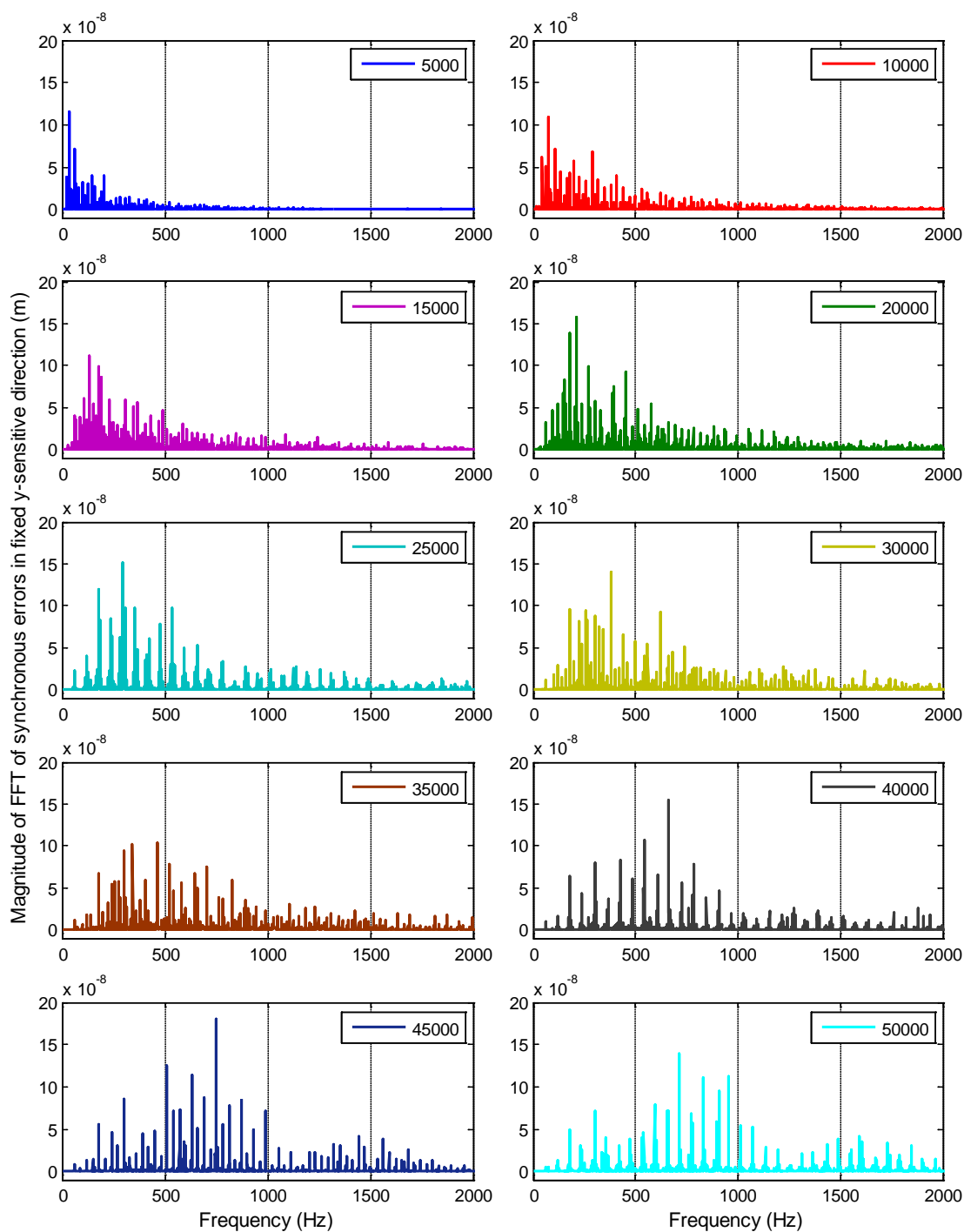


Figure 4.38: Magnitude of FFT of asynchronous SE in fixed-sensitive y-direction.

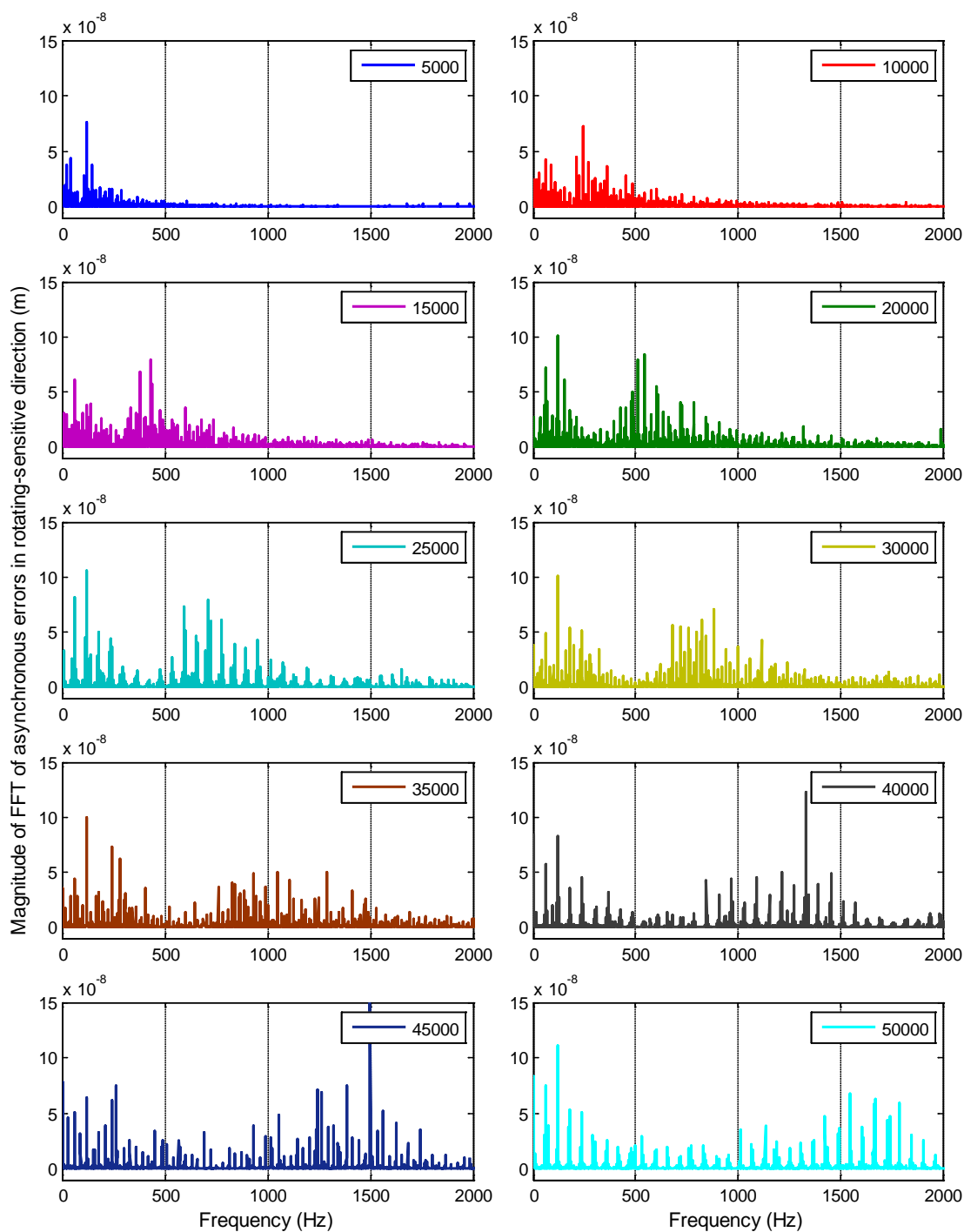


Figure 4.39: Magnitude of FFT of asynchronous SE in rotating-sensitive direction.

CHAPTER 5: RECEPTANCE COUPLING SUBSTRUCTURE ANALYSIS

Machining instability (chatter) leads to poor surface finish, high part rejection rates, rapid tool wear, and, potentially, spindle damage. Stable machining conditions may be identified using well-known milling process models [1]. This aids in pre-process parameter selection for optimal machining conditions. In order to identify stable machining conditions, the dynamics of the tool-holder-spindle-machine assembly as reflected at the tool tip is required. The FRF, which represents the structural dynamics, may be measured using modal techniques. In practice, a large number of different tool-holder combinations are available for a selected machining center. The cost of experimentally identifying the tool tip dynamics for each tool-holder combination may be prohibitively high in some cases. Receptance coupling substructure analysis (RCSA) provides a useful approach to predict the tool point response from a single measurement of the spindle-machine and models of the desired tool-holder combinations [1].

To complete the RCSA procedure, four spindle-machine receptances are required: displacement-to-force, displacement-to-couple, rotation-to-force, and rotation-to-couple. Only the former is convenient to measure. Therefore, in recent work [44], a procedure was described where each displacement-to-force mode in the measurement bandwidth was modeled as a fixed-free Euler-Bernoulli (EB) beam. Given an analytical description of each mode's fixed-free EB model, the other three receptances can also be described analytically [71] for that mode and no additional measurements are required. The sum of

the single mode fits are used to describe the four required spindle responses. This fitting procedure was manually completed mode-by-mode in the previous work. In this study, an optimization technique is implemented to automate the identification of the EB beam parameters for each mode.

5.1 RCSA Background

RCSA enables assembly dynamics to be predicted when the receptances of the individual components are known. The receptances of the individual components may be analytically modeled or measured. Conversely, the component receptances may be determined if the assembly receptances (as well as the other components receptances) are known, again through either models or measurements. This is referred to as inverse RCSA. For milling applications, the tool-holder-spindle-machine may be separated into two individual components: (I) the tool (endmill) and holder combination; and (II) the spindle-machine. In practice, many different tool-holder combinations are used in machining operations. The tool-holder receptances may be modeled as free-free Timoshenko beams. On the other hand, it is challenging to model the spindle-machine receptances. The spindle-machine receptances are also subject to change over the lifetime of the spindle. Therefore, it is generally more convenient to experimentally identify the spindle-machine receptance and archive it for each machine. Once the spindle-machine receptances are identified experimentally, they may be coupled with the modeled tool-holder receptances using RCSA to predict the tool point direct FRF.

In order to experimentally identify the spindle-machine receptances, a standard artifact with the appropriate taper geometry (e.g., CAT or HSK) is inserted in the spindle. Figure 5.1 provides a schematic of the setup, where $\{U_i\} = \{X_i \quad \Theta_i\}^T$ represents the

assembly generalized displacement coordinates and consists of a displacement, X_i , and a rotation, θ_i . $Q_i = \{F_i \quad M_i\}^T$ represents the assembly generalized forces and consists of a force, F_i , and a couple (or moment), M_i . The four assembly receptances are then defined as:

$$G_{ij} = \begin{bmatrix} H_{ij} & L_{ij} \\ N_{ij} & P_{ij} \end{bmatrix}, \quad (5.1)$$

where $\{U_i\} = [G_{ij}]\{Q_j\}$.

Similarly, $u_i = \{x_i \quad \theta_i\}^T$ represents the component generalized displacement coordinates and consists of a displacement, x_i , and a rotation, θ_i . $q_i = \{f_i \quad m_i\}^T$ represents the component generalized forces and consists of a force, f_i , and a couple (or moment), m_i . The component receptances are then defined as:

$$R_{ij} = \begin{bmatrix} h_{ij} & l_{ij} \\ n_{ij} & p_{ij} \end{bmatrix}, \quad (5.2)$$

where $\{u_i\} = [R_{ij}]\{q_j\}$.

The direct, displacement-to-force FRF at the free end of the artifact-spindle-machine, G_{11} , assembly is measured. The direct, R_{11} and R_{2a2a} , and cross, R_{12a} and R_{2a1} , receptance matrices for the portion of the standard artifact beyond the flange are described using free-free Timoshenko beam models. The spindle-machine receptances at the flange, R_{2b2b} , are unknown. The assembly receptance at the tip can be defined as [1, 44]:

$$G_{11} = R_{11} - R_{12a} (R_{2a2a} + R_{2b2b})^{-1} R_{2a1}, \quad (5.3)$$

where R_{2b2b} is the only unknown. It is obtained by rearranging Eq. (5.3).

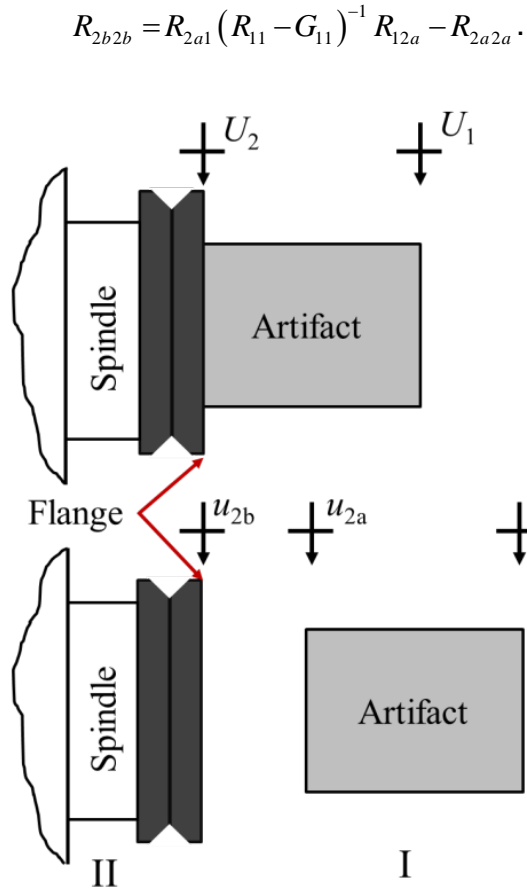


Figure 5.1: Schematic of the RCSA components.

As shown in Eq. (5.4), the receptances for the spindle-machine may be determined from the modeled direct and cross artifact receptances and the assembly receptances, G_{11} , where G_{11} consists of H_{11} , L_{11} , N_{11} , and P_{11} as previously described. $H_{11} = X_1/F_1$ can be measured using impact testing methods. Kumar and Schmitz [44] developed a method to fit the assembly response using multiple fixed-free EB beams. The number of EB beams corresponded to the number of modes within the measurement bandwidth. A manual, iterative approach was used to identify the individual beam geometries. Once the fixed-free EB beams were fit, the model parameters were used to compute L_{11} , N_{11} , and P_{11} [71] and fully populate the G_{11} matrix. The spindle-machine component receptances are

then identified using Eq. (5.4). These spindle receptances are coupled to modeled tool-holder receptances to predict the assembly tool point FRF.

Kumar and Schmitz [44] used the analytical, close-form EB beam receptances presented by Bishop and Johnson [71] to describe each measured displacement-to-force mode; see Eq. (5.5), where ω is the frequency (rad/s), d_j is the beam diameter, L_j is the beam length (m), ρ_j is the density (kg/m³), E_j is the elastic modulus (N/m²), η_j is the unitless solid damping factor, and f_{nj} is the natural frequency. The subscript j corresponds to the j^{th} mode.

$$H_{11}^j = \frac{\sin(\lambda_j L_j) \cosh(\lambda_j L_j) - \cos(\lambda_j L_j) \sinh(\lambda_j L_j)}{\lambda_j^3 E_j I_j (1 + i\eta_j) (\cos(\lambda_j L_j) \cosh(\lambda_j L_j) - 1)}, \quad (5.5)$$

where $\lambda_j^4 = \frac{\omega^2 \rho_j A_j}{E_j I_j (1 + i\eta_j)}$, $A_j = \frac{\pi d_j^2}{4}$, and $I_j = \frac{\pi d_j^4}{64}$.

For a given diameter, d_j , natural frequency, f_{nj} , density, ρ_j , and elastic modulus, E_j , the beam free length is obtained from a closed form expression for the natural frequency of a fixed-free cylindrical beam [72]; see Eq. (5.6). This free length of the beam is used in Eq. (5.5).

$$L_j = \left(\frac{1.87510407^2 d_j \left(\frac{E_j}{16\rho_j} \right)^{\frac{1}{2}}}{2\pi f_{nj}} \right)^{\frac{1}{2}} \quad (5.6)$$

All the beams were modeled assuming the material properties of steel ($\rho = 7800$ kg/m³ and $E = 200$ GPa). Then, for each mode within the measured bandwidth, a corresponding diameter, d_j , solid damping factor, η_j , and a natural frequency, f_{nj} , was identified by an iterative process such that the combined receptance for all modes accurately represents the fit displacement-to-force receptance, H_{11}^f ; see Eq. (5.7).

$$H_{11}^f = \sum_{j=1}^{\text{no. of modes}} H_{11}^j \quad (5.7)$$

In this study a simplex based Nelder-Mead optimization technique was applied to identify the fixed-free EB beam properties. This considerably reduces the difficulty in identifying the beam parameters in comparison with the manual, iterative fitting procedure. The FRF for each mode within the measured bandwidth may also be represented by an equivalent modal mass, M_j , damping ratio, ξ_j , and natural frequency, f_{nj} , as:

$$H_{11}^j = \frac{1}{-M_j \omega^2 + i \omega C_j + K_j}, \quad (5.8)$$

where $K_j = M_j (2\pi f_{nj})^2$ and $C_j = 2\xi_j \sqrt{M_j K_j}$. Eq (5.8) is computationally less expensive than Eq (5.5) and was therefore used in the optimization process to identify an equivalent modal mass, M_j , damping ratio, ξ_j , and natural frequency, f_{nj} , for each mode. Eq. (5.7) was used to sum the contributions of all the modes within the measured bandwidth. The optimization objective was to minimize the difference between the fit receptance and the measured receptance, H_{11}^m . For each mode within the measured bandwidth, an equivalent modal mass, M_j , damping ratio, ξ_j , and natural frequency, f_{nj} , was identified in order to minimize the error between H_{11}^f and H_{11}^m . The objective function, O , was defined as:

$$O = \sqrt{\left\{ \text{re}(H_{11}^m) - \text{re}(H_{11}^f) \right\}^2 + \left\{ \text{im}(H_{11}^m) - \text{im}(H_{11}^f) \right\}^2}, \quad (5.9)$$

where *re* indicates the real part and *im* indicates the imaginary part of the fit and measured receptances. The equivalent fixed-free EB beam diameter, d_j and solid damping factor, η_j , may then be estimated for each mode from the corresponding modal mass, M_j ,

and damping ratio, $\tilde{\zeta}_j$, by solving a set of non-linear optimization subroutines, one for each mode. The natural frequency, f_{nj} , used to compute the FRF is constant irrespective of whether the FRF is expressed in terms of modal parameters (M_j and $\tilde{\zeta}_j$), or in terms of fixed-free EB beam parameters (d_j and η_j).

The total number of variables for the optimization problem is three times the total number of modes identified within the measured bandwidth because there are three beam parameters (diameter, solid damping factor, and natural frequency) that must be identified for each mode. Once the equivalent beam geometries were identified using the optimization process, the other receptances of the G_{11} matrix were specified using Eqs. (5.10) - (5.12).

$$L_{11}^j = N_{11}^j = \frac{-\sin(\lambda_j L_j) \sinh(\lambda_j L_j)}{\lambda_j^2 E_j I_j (1 + i\eta_j) (\cos(\lambda_j L_j) \cosh(\lambda_j L_j) - 1)} \quad (5.10)$$

$$P_{11}^j = \frac{\sin(\lambda_j L_j) \cosh(\lambda_j L_j) + \cos(\lambda_j L_j) \sinh(\lambda_j L_j)}{\lambda_j E_j I_j (1 + i\eta_j) (\cos(\lambda_j L_j) \cosh(\lambda_j L_j) - 1)} \quad (5.11)$$

$$[L / N / P_{11}]^f = \sum_{j=1}^{\text{no. of modes}} [L / N / P_{11}]^j \quad (5.12)$$

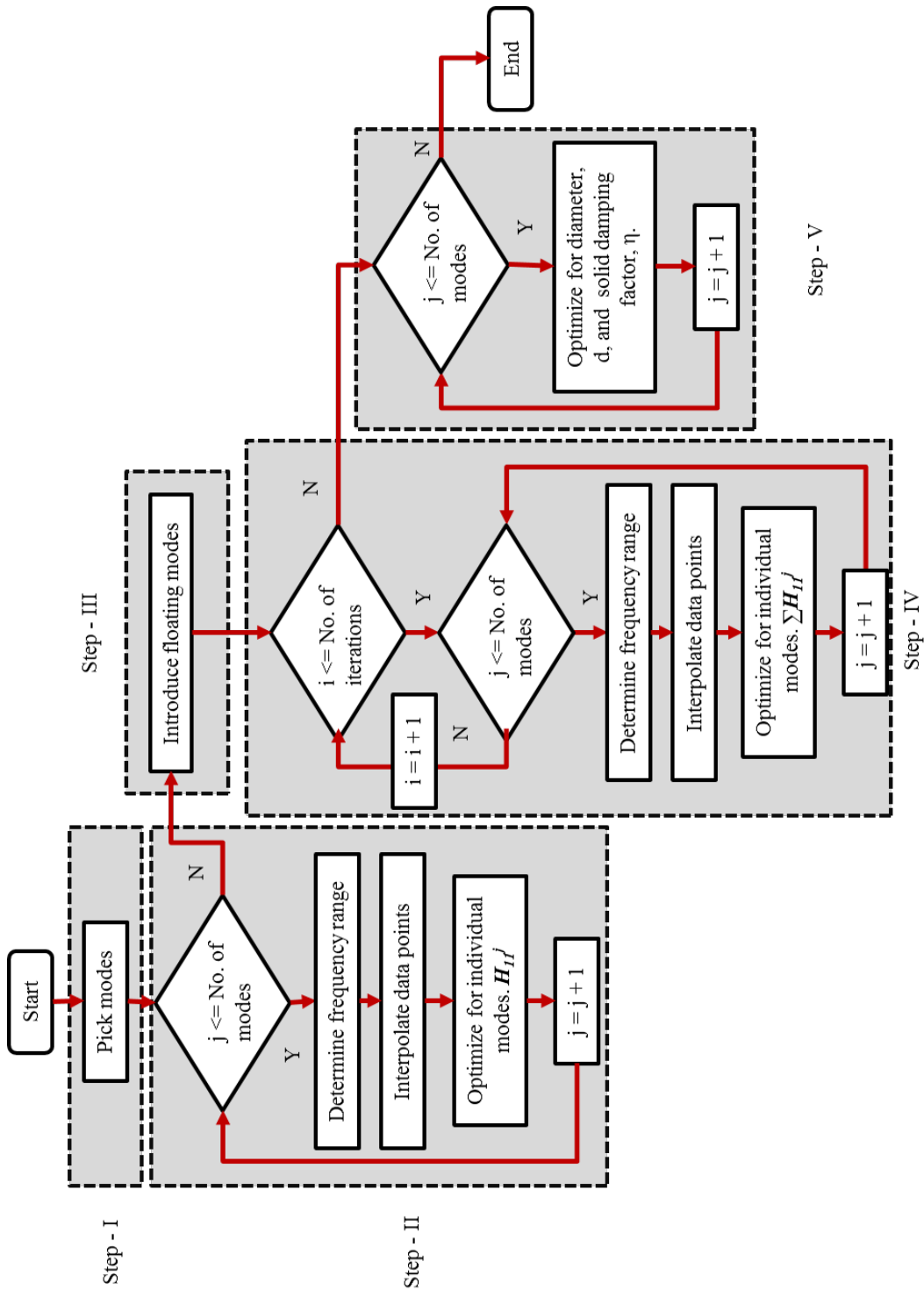


Figure 5.2: Optimization flow chart.

5.2 Simplex Based Nelder-Mead Optimization

In this section, the steps of the optimization algorithm are discussed in more detail. Figure 5.2 shows a flow chart of the optimization process.

5.2.1 Step 1: Individual Mode Identification

In this step, the different modes within the measured bandwidth are identified. For tool point direct FRFs (H_{11}^m), the imaginary part of the response is purely negative. Therefore, the natural frequencies of the different modes may be identified by searching for negative peaks in the imaginary part of the FRF. The mode identification algorithm compares each element within a vector with its neighboring elements and recognizes those which are less than both its neighboring elements, i.e., the search is for negative peaks. This method is highly susceptible to noisy response data. This is addressed by incorporating a moving average filter which smoothes the (potentially) noisy data. The number of points which defines the moving average filter is denoted as the horizontal sensitivity factor, H_{sens} . This value is defined by the optimizer through visual inspection of the real and imaginary parts of response function. A low H_{sens} value retains noise susceptibility, while a high value may miss closely-spaced modes along the frequency axis. A vertical sensitivity factor, V_{sens} , is also defined, which establishes a cutoff limit as a percentage of the magnitude of the imaginary part of the most flexible mode. All the modes with an imaginary part amplitude less than the cutoff limit (i.e., very stiff modes) are ignored.

Figure 5.3 shows the real and imaginary parts of a measured FRF. The selected peaks are identified by crosses. The effect of H_{sens} is demonstrated in Figure 5.4. The figure shows a magnified portion of the response. When $H_{sens} = 1$, six modes (circles) are

identified in this region, but when $H_{sens} = 20$, only two mode (cross) is recognized. The difference in the FRFs plotted in Figure 5.4 is due to the effect of the moving average filter. It should be noted here that, although the natural frequencies for the modes were identified in this step itself, they continued to remain as variables in the optimization process. This is not completely necessary, but it did provide some flexibility in the optimization process to account for any errors in the selected frequencies.

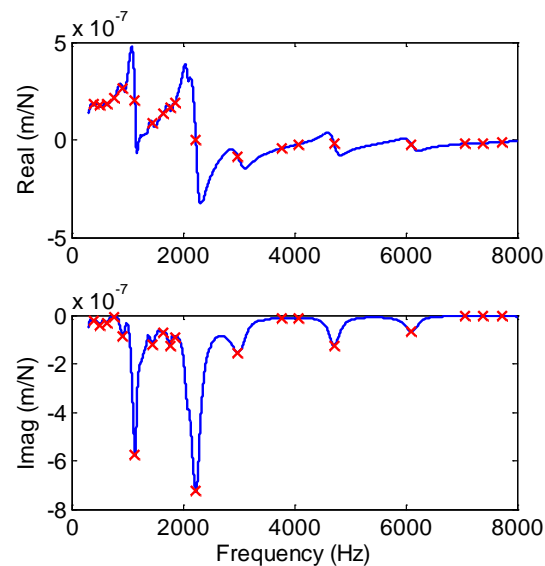


Figure 5.3: Measured direct FRF (H_{11}^m) with selected modes (crosses).

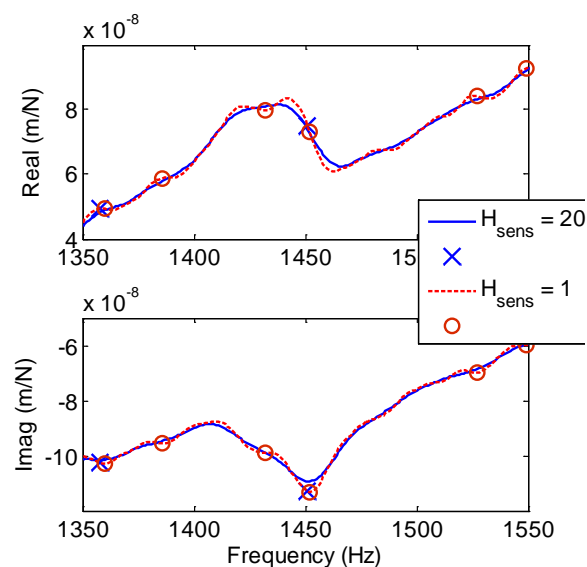


Figure 5.4: The effect of H_{sens} on peak identification ($H_{sens} = 1$: circles ; $H_{sens} = 20$: cross).

5.2.2 Step 2: Optimization for Individual Modes

Before optimizing for the combined response of all the modes together, Nelder-Mead optimization subroutines were executed over small frequency ranges to identify the modal mass, M_j , the damping ratio, ξ_j , and natural frequency, f_n , for each mode independently. These parameters were used to provide an initial estimate of the solution before optimizing for the combined response of all the modes together. This ensured faster convergence towards the optimal solution when optimizing for the combined FRF. The equation for H_{11}^f , Eq. (5.7), was modified to include only the mode under consideration. When optimizing for the individual modes, the objective function was also modified to include only the imaginary part of the FRF. The real part of the measured FRF in the frequency region of the mode under consideration is typically offset along the vertical axis due to effects of neighboring modes.

5.2.2.1 Step 2.1: Determining Frequency Range

When optimizing for the individual modes, only the data points of the FRF within a frequency range around the mode under consideration were considered. However, caution must be exercised when defining this frequency range. If the range is too small, there is not sufficient response data to find an optimal solution which accurately represents the contribution of the mode under consideration to the combined response. If the range selected is too large, the response data may be polluted by contributions of the neighboring modes, resulting in errors in the optimal beam parameter predictions for the mode under consideration.

A number of different constraints were established to identify the optimization frequency range for the individual modes. The lower and upper limits for the frequency

range for the j^{th} mode were defined as δf_{lower}^j and δf_{upper}^j , respectively. The natural frequency of the j^{th} mode identified in step one was defined as f_m^j . The constraints were then described as:

$$\begin{aligned}
 a) \quad & \delta f_{lower}^j < 0.4 (f_m^{j-1} - f_m^j) \quad f_m^0 = 0 \\
 & \delta f_{upper}^j < 0.4 (f_m^j - f_m^{j+1}) \quad f_m^{\text{no. of modes} + 1} = 10 \text{ kHz} \\
 b) \quad & \delta f_{lower}^j < 200 \text{ Hz} \\
 & \delta f_{upper}^j < 200 \text{ Hz} \\
 c) \quad & \delta f_{lower}^j / \delta f_{upper}^j < 3 \\
 & \delta f_{upper}^j / \delta f_{lower}^j < 3
 \end{aligned} \tag{5.13}$$

Constraint a) ensures that δf_{lower}^j and δf_{upper}^j were not greater than 40% the distance to the adjacent mode. Constraint b) ensures that δf_{lower}^j and δf_{upper}^j were not greater than 200 Hz from the natural frequency of the mode under consideration. Constraint c) ensures that the ratio of δf_{lower}^j to δf_{upper}^j was no more than three. The inverse was also held true. This ensured that the frequency range for optimization for a single mode was not unevenly distributed about the natural frequency for that mode. These constraints were developed on a trial and error basis, with continuous verification to ensure that they are robust for different FRFs. Figure 5.5 shows the influence of constraints a) and c) for a part of the FRF with closely spaced modes. Figure 5.6 shows the influence of constraint b) for a part of the FRF where the individual modes are well spread out.

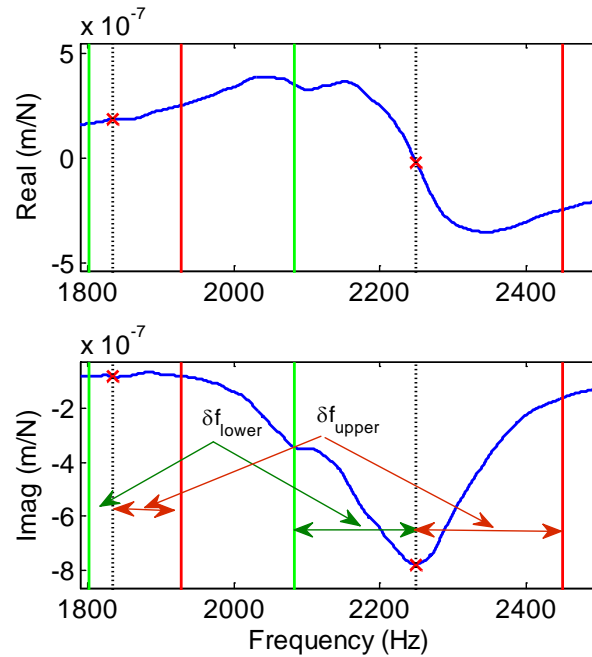


Figure 5.5: Selection of frequency range. Influence of constraints a) and c).

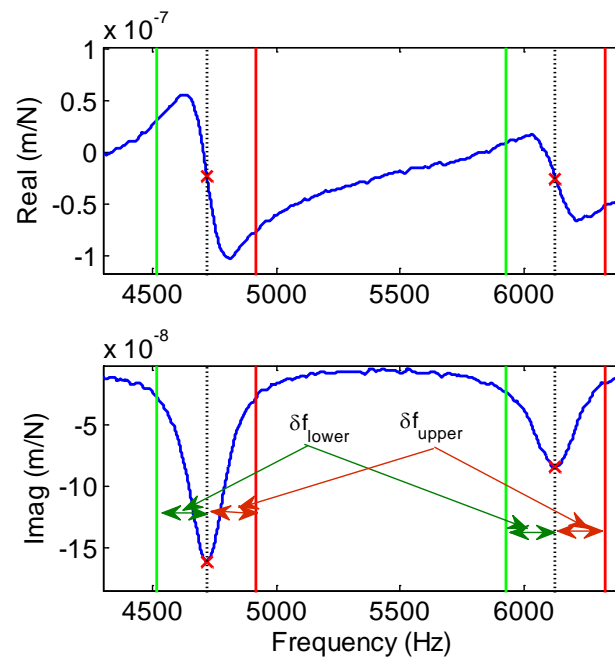


Figure 5.6: Selection of frequency range. Influence of constraint b).

5.2.2.2 Step 2.2: Optimization for Each Individual Mode

Once the frequency range for optimization for each individual mode was identified, a constrained simplex based Nelder-Mead algorithm was used to optimize for the

equivalent modal parameters as previously described [48]. The mode near 2254 Hz is used to demonstrate the process. Figure 5.7 shows the real and imaginary part of the measured response as well as of the simulated optimal solution at different iterations of the optimization process. As seen from the figure, the algorithm converges to the measured FRF.

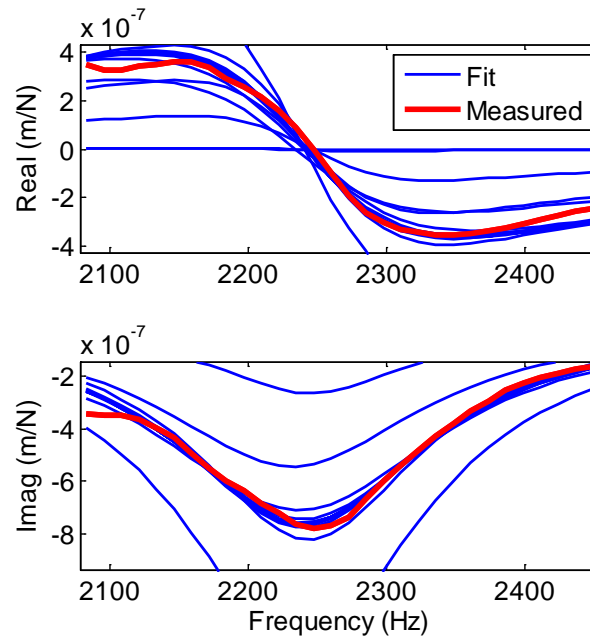


Figure 5.7: Optimal fit at different steps of the individual mode optimization process for mode at 2254 Hz.

5.2.3 Step 3: Floating modes

Here, the concept of floating modes is introduced. Often times, all the modes within the measured bandwidth may not be identified using the method defined in step 1 as there may be no negative peak in the imaginary part of the FRF to identify the modes. For example, in Figure 5.5, the mode near 2100 Hz is unidentified in step 1. Therefore, in this step, a number of “floating” modes were introduced into the solution. The modal mass, M_j , the damping ratio, ξ_j , and natural frequency, f_n , were randomly generated using the

rand function in MATLAB on the basis of some criterion. These criteria are defined below. First two ratios are defined as:

$$Rat_1 = \frac{Im_1}{Im_2}, \text{ and } Rat_2 = \frac{Im_1}{Im_3}, \quad (5.14)$$

where, Im_1 , Im_2 , and Im_3 correspond to the magnitude of the imaginary parts of the three modes selected in step 1 with highest absolute value of the imaginary part; see Figure 5.8. The floating modes were then distributed in three frequency ranges centered at the three corresponding frequencies f_1 , f_2 , and f_3 as shown in Figure 5.8.

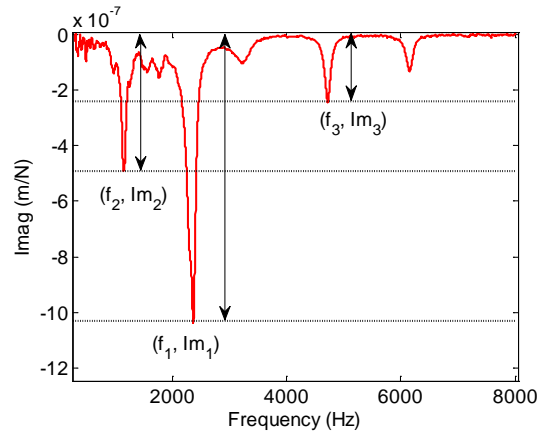


Figure 5.8: Identification of three modes with the largest absolute value of the imaginary part. The floating modes were distributed around these modes.

The number and distribution of the floating modes was then decided as follows,

$$i) \quad \text{if } Rat_1 > 2 \text{ and } Rat_2 > 2 \quad (5.15)$$

$$Float_{modes} = 60 ;$$

$$Modes_{range1} = 0.5 Float_{modes} ;$$

$$Modes_{range2} = 0.3 Float_{modes} ;$$

$$Modes_{range3} = 0.2 Float_{modes} .$$

$$ii) \quad \text{else if } Rat_1 < 2 \text{ and } Rat_2 > 2$$

$$FloatModes = 40 ;$$

$$Modes_{range1} = 0.6 Float_{modes};$$

$$Modes_{range2} = 0.4 Float_{modes};$$

$$Modes_{range3} = 0.$$

iii) *else*

$$FloatModes = 20;$$

$$Modes_{range1} = Float_{modes};$$

$$Modes_{range2} = 0;$$

$$Modes_{range3} = 0.$$

where $Modes_{range1}$, $Modes_{range2}$, and $Modes_{range3}$ were defined as the number of modes randomly distributed in the three frequency ranges, f_{range1} , f_{range2} , and f_{range3} respectively. Here, f_{range1} , f_{range2} , and f_{range3} are defined as $f_1 \pm 200$ Hz, $f_2 \pm 200$ Hz, and $f_3 \pm 200$ Hz respectively. The corresponding mass and damping properties for the floating modes were randomly generated from within a range of 0 to 3 and 0 to 0.03 respectively.

5.2.4 Step 4: Optimization for All Modes

Once the modal mass, M_j , damping ratio, ξ_j , and natural frequency, f_{nj} , were identified for all the different modes as described in step two, these optimized values were used provide an initial estimate for when optimizing for the combined effects of all modes simultaneously. Eq (5.9) was used to compute the value of the objective function. Unlike in step two, the contributions from the other modes were also considered. For each mode, the frequency range and interpolated data points were attained as described in step 2. Here, optimization sub-routines were performed for each individual mode to obtain an updated optimized equivalent modal mass, M_j , damping ratio, ξ_j , and natural frequency,

f_{nj} . The contributions from the other modes within the frequency range of interest were calculated based on the optimized values obtained from the previous optimization step.

Figure 5.9 shows an example of a single optimization sub-routine to optimize for the mode at 3000 Hz. The combined contribution from the other modes is also shown which remains constant.

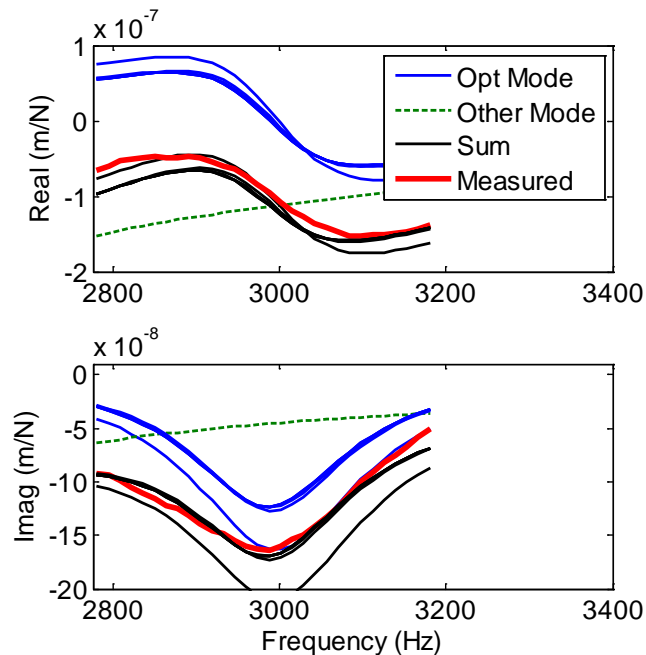


Figure 5.9: Optimization for individual mode with contributions of other modes taken into account.

Once the modal parameters for each mode were optimized, the process was repeated a few times to achieve convergence. It was found that convergence was achieved within 20 iterations. Figure 5.10 shows a plot of the optimized fit and the experimental data for the 20 iterations. The plot shows that the fit is in good agreement with the experimental measurement.

5.2.4.1 Mode Deletion

After 14 iterations, the modes that did not contribute to the solution were identified and deleted. These modes may be identified by examining the optimized the modal mass,

M_j , damping ratio, ξ_j , and natural frequency, f_{nj} values. If the optimal values equal the limits set on the variables in the constrained optimization problem, it may be concluded that these modes do not contribute to the solution. These modes were then removed from the solution space.

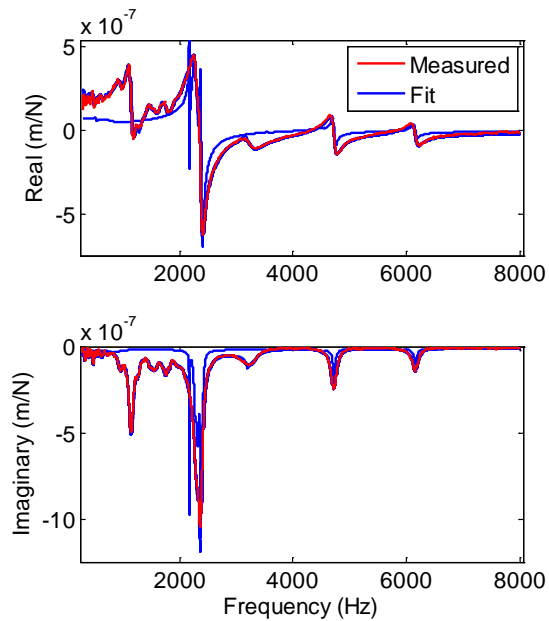


Figure 5.10: Comparison between optimized fit and experimental measurement. The fit for all 20 iterations are superimposed on the same plot.

5.2.5 Step 4: Mapping from Modal to Equivalent EB Beam Parameters

In this step, simplex based Nelder-Mead optimization subroutines were performed for each individual mode to map the optimized modal parameters (mass, M_j , and damping ratio, ξ_j) to the equivalent fixed-free EB beam parameters (diameter, d_j , and solid damping factor, η_j). The optimized natural frequency, f_{nj} , remained the same.

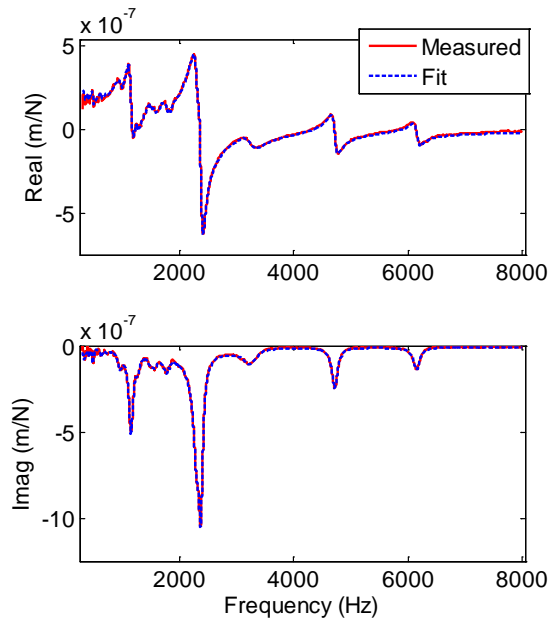


Figure 5.11: Comparison of fit and measured H_{11} direct FRF measured at tip of the spindle artifact.

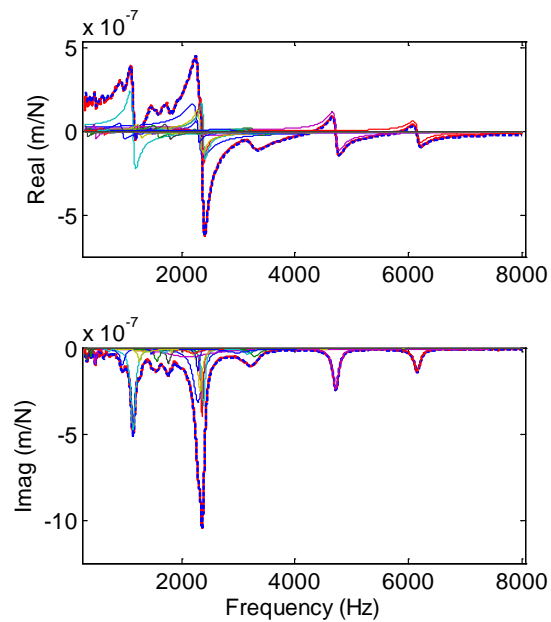


Figure 5.12: Individual H_{11}^j FRFs for the individual fixed-free EB beams.

Figure 5.11 shows the comparison of the measured FRF at the free end of the artifact mounted in the machined spindle and the optimal FRF obtained by fitting the equivalent fixed-free EB beams. Good agreement was found between the experimental and

optimized simulated FRFs. Figure 5.12 shows the real and imaginary parts of the individual FRFs for each of the optimized modes. In this example, after deletion, a total of 35 modes were used to best regenerate the measured FRF as a summation of the receptances of fixed-free EB beams. The assembly FRF was obtained by summing all the individual FRFs; see Eq. (5.7). Once the equivalent fixed-free EB beam parameters were identified, the other receptances, L_{11} , N_{11} , and P_{11} , were calculated using Eqs. (5.10) and (5.11). Combined, these receptances completely populate the G_{11} matrix. Figure 5.13 (left) shows L_{11} and N_{11} . Note that they are identical; see Eq. (5.10). The P_{11} receptance is displayed in Figure 5.13 (right).

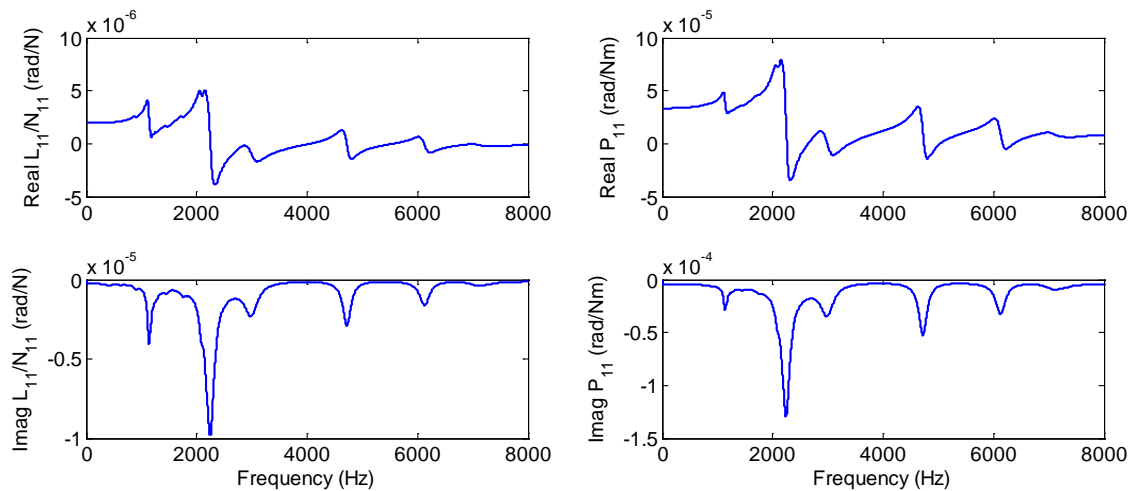


Figure 5.13: Simulated L_{11} and N_{11} (left) and P_{11} (right) receptances at the tip of the artifact.

The spindle receptances, R_{2b2b} , were computed by decoupling the modeled artifact receptances (for the portion of the artifact beyond the flange) using Eq. (5.4). The artifact was modeled as a free-free Timoshenko beam.

5.3 Equivalent Diameter Model of Fluted Endmill

In this study, a 12.7 mm diameter solid carbide tool with 76.2 mm overall length, 25.4 mm fluted length, and 30° helix angle was used. First, the fluted portion of the endmill

was modelled using Solidworks. A diamond dicing wheel was used to slice the end mill at a number of different sections. Slicing was performed on a Harig grinding machine. Then, a digital microscope (DinoCapture) was used to image the cut sections of the endmill. These images were imported into Solidworks and a 3D model of the end mill was generated. Figure 5.14 shows the images of the different sliced sections of the fluted portions as well as the generated 3D model.

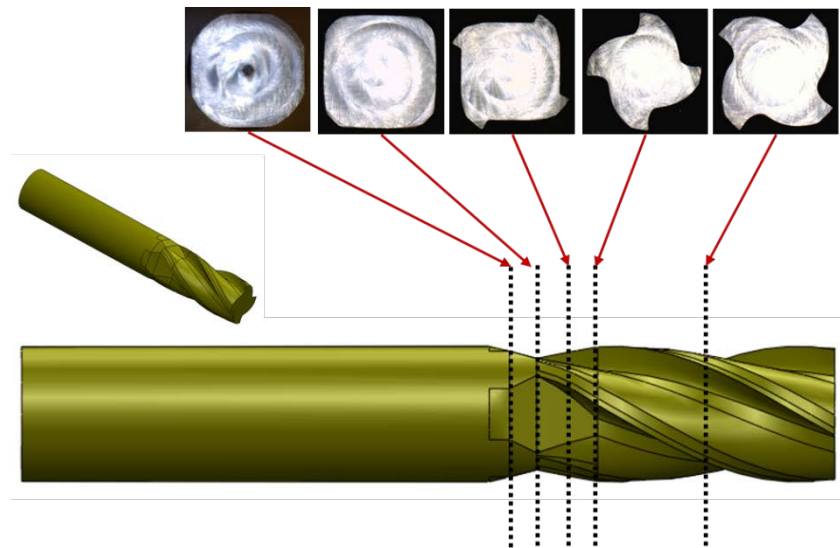


Figure 5.14: Solidworks model of fluted end mill.

A modal analysis of the tool was performed in ANSYS with free-free boundary conditions. The natural frequency of the first bending mode of the tool was identified as 10610.9 Hz. Figure 5.15 shows a plot of first bending mode shape obtained from ANSYS. An equivalent beam diameter approach was employed to model the fluted portion of the endmill. By modelling the fluted section as a cylinder, the receptances to be used in RCSA may then be computed using Timoshenko beam models. The equivalent diameter was identified as the diameter which produced the same natural frequency of the first bending modes when the frequency response was computed using Timoshenko beam theory. The length of the cylinder modelled using the equivalent diameter was the length

of the fluted portion plus half the diameter of the tool (31.75 mm). For this tool, with the defined geometry, the equivalent diameter was found to be 10.98 mm. Figure 5.16 shows the equivalent diameter depiction of the tool. Now, the two sections of the tool may be modelled using Timoshenko beam theory.

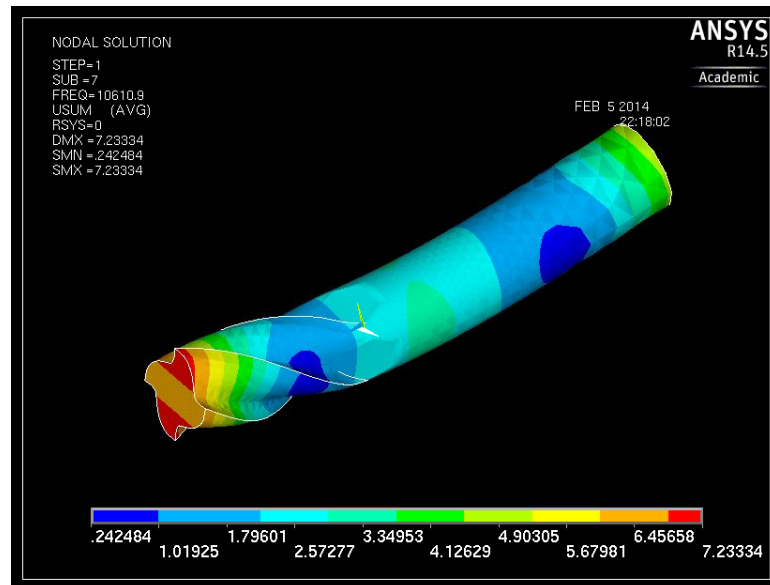


Figure 5.15: Modal analysis of endmill performed in ANSYS. First bending mode.

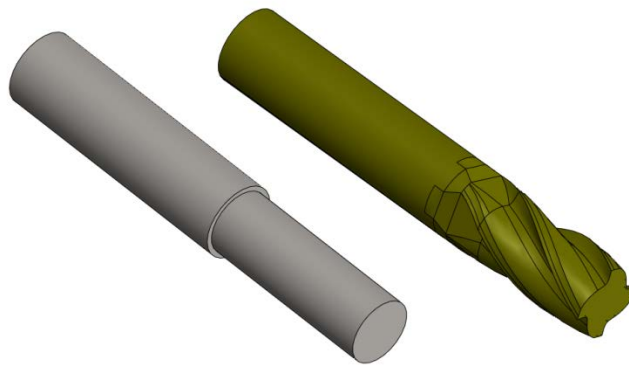


Figure 5.16: Equivalent diameter depiction of the fluted section.

5.4 Experimental Results

In this study, two different artifacts and the tool were modelled using Timoshenko beam theory. Both the artifact and the tool holder-tool combination were modeled as assemblies with tapered slices. The model receptances were estimated using FE methods

where the different slices of the artifact and holder-tool combination were modeled using conical (potentially) Timoshenko beam elements [37]. The assembly receptances were obtained by coupling the different slices using RCSA. Figure 5.17 shows the cross sectional views and identifies the different sections of the spindle artifact, the carbide blank, and the carbide endmill. The geometries and materials are defined in Table 5.1. All dimensions are defined in mm.

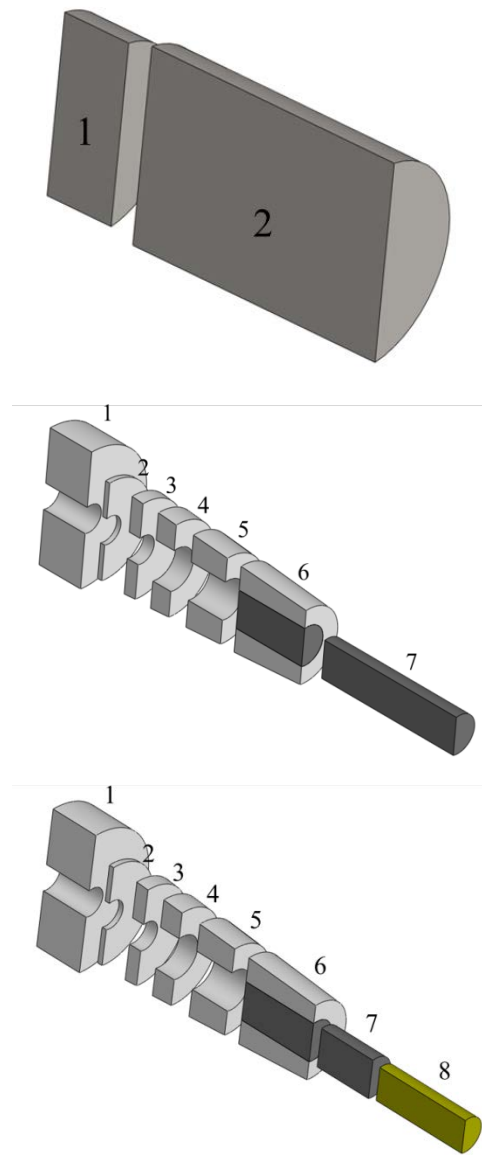


Figure 5.17: Models of the spindle artifact, blank-holder, and tool-holder assembly.

Table 5.1: Section geometries. All dimensions are in mm.

| Artifact section properties | | | | | | | | |
|---------------------------------|-------|-------|-------|-------|-------|---------|---------|---------|
| | 1 | 2 | | | | | | |
| d_{sout} | 44.00 | 47.70 | | | | | | |
| d_{ttout} | 44.00 | 47.70 | | | | | | |
| d_{in} | 0.00 | 0.00 | | | | | | |
| L | 17.5 | 66.2 | | | | | | |
| M_{out} | Steel | Steel | | | | | | |
| M_{in} | - | - | | | | | | |
| Blank-Holder section dimensions | | | | | | | | |
| | 1 | 2 | 3 | 4 | 5 | 6 | 7 | |
| d_{sout} | 44.46 | 31.76 | 31.76 | 31.08 | 30.98 | 28.04 | 12.70 | |
| d_{ttout} | 44.46 | 31.76 | 31.08 | 30.98 | 28.04 | 24.20 | 12.70 | |
| d_{in} | 9.00 | 9.00 | 9.00 | 13.56 | 12.70 | 12.70 | 0.00 | |
| L | 15.88 | 1.56 | 4.24 | 6.90 | 13.05 | 25.05 | 51.2 | |
| M_{out} | Steel | Steel | Steel | Steel | Steel | Steel | Carbide | |
| M_{in} | - | - | - | - | - | Carbide | Carbide | |
| Tool-Holder section dimensions | | | | | | | | |
| | 1 | 2 | 3 | 4 | 5 | 6 | 7 | 8 |
| d_{sout} | 44.46 | 31.76 | 31.76 | 31.08 | 30.98 | 28.04 | 12.70 | 10.99 |
| d_{ttout} | 44.46 | 31.76 | 31.08 | 30.98 | 28.04 | 24.20 | 12.70 | 10.99 |
| d_{in} | 9.00 | 9.00 | 9.00 | 13.56 | 12.70 | 12.70 | 0.00 | 0.00 |
| L | 15.88 | 1.56 | 4.24 | 6.90 | 13.05 | 25.05 | 19.05 | 15.88 |
| M_{out} | Steel | Steel | Steel | Steel | Steel | Steel | Carbide | Carbide |

| | | | | | | | | |
|----------|---|---|---|---|---|---------|---------|---------|
| M_{in} | - | - | - | - | - | Carbide | Carbide | Carbide |
|----------|---|---|---|---|---|---------|---------|---------|

Here, d_{sout} , is the outside diameter of the section at the end towards the spindle, d_{tout} , is the outside diameter of the section and the end towards the tool tip, d_{in} , is the inside diameter, L , is the length of the section. M_{out} and M_{in} define the materials. Note that the inside may be a different material than the outside. The material properties used are defined in Table 5.2.

Table 5.2: Material properties

| | Young's modulus E (GPa) | Poisson's ratio ν | Density ρ (Kg/m ³) | Solid damping η |
|---------|---------------------------------|-----------------------------|---|----------------------------|
| Steel | 200 | 0.29 | 7800 | 0.0015 |
| Carbide | 550 | 0.22 | 15000 | 0.0015 |

In this research, two different artifacts were used to predict the tool point FRF. Figure 5.18 and Figure 5.19 show the comparison between the measured tool point FRF, the FRF predicted using the standard cylindrical artifact receptances, and the FRF predicted using the blank receptances. In both cases, the prediction made using the blank artifact was found to be a closer match to the experimental measurements. This was attributed to the compliance in the shrink fit tool holder-tool interface. The RCSA prediction made using solid artifact receptances did not capture the compliance in the tool-holder interface. These compliances were better captured in the measurement performed on the carbide blank. Schmitz et al. [1] developed a method to incorporate the interface stiffness and damping in the RCSA model. Eq. (5.4) may be altered to include the interface stiffness: see Eq. (5.16).

$$G_{11} = R_{11} - R_{12a} (R_{2a2a} + K^{-1} + R_{2b2b})^{-1} R_{2a1}, \quad (5.16)$$

where,

$$K = \begin{bmatrix} k_{yf} + i\omega c_{yf} & k_{ym} + i\omega c_{ym} \\ k_{\theta f} + i\omega c_{\theta f} & k_{\theta m} + i\omega c_{\theta m} \end{bmatrix}. \quad (5.17)$$

Here, k_{ij} and c_{ij} represent stiffness and damping terms, respectively. The first subscript corresponds to the displacement coordinate, displacement (y)/ rotation (θ), and the second subscript corresponds to the applied force co-ordinate, force (f)/ moment (m). The incorporation of the interface compliance in the RCSA model would reduce the discrepancies between the simulated and measured tool point FRF.

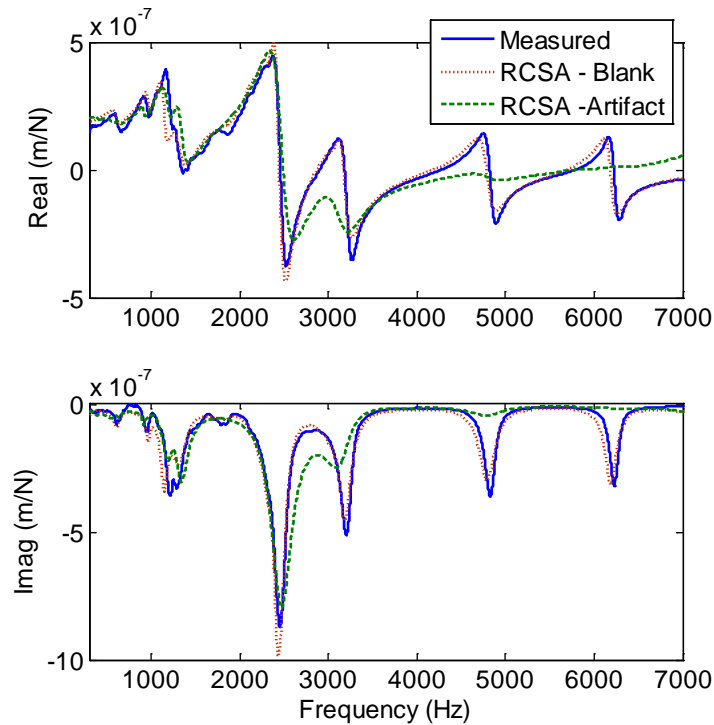


Figure 5.18: Comparison between predicted and measured tool tip FRF: x- direction.

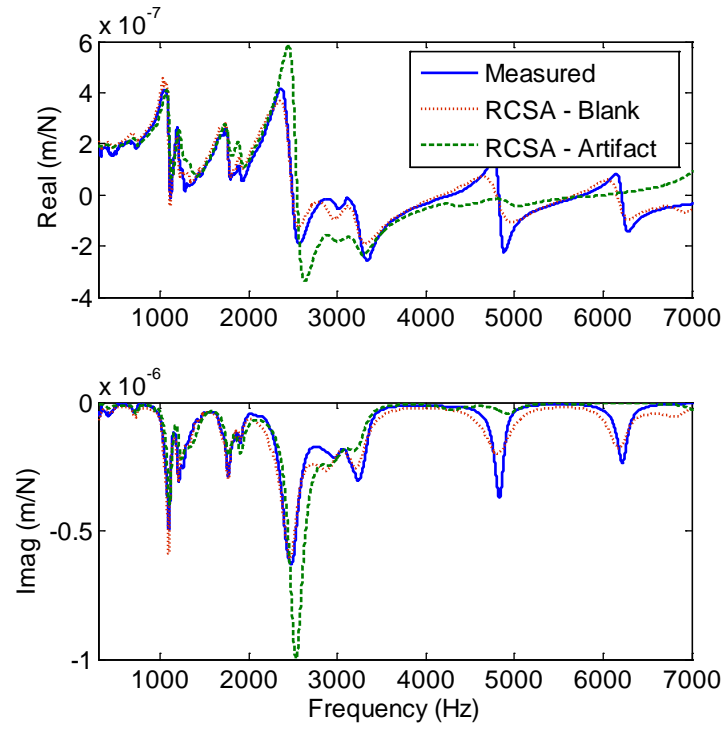


Figure 5.19: Comparison between predicted and measured tool tip FRF: y- direction.

CHAPTER 6: MACHINING STABILITY

In order to generate a SLD for a milling process, four parameters about the machining process must be identified:

- 1) the number of cutting teeth on the endmill,
- 2) the radial immersion,
- 3) the cutting force coefficients, and
- 4) the FRF at the tool tip in two orthogonal directions.

The number of cutting edges on the tool depends upon the selected tool and the radial immersion is commanded by the machinist. The cutting force coefficients and tool point FRF must be identified through experimentation or modeling.

6.1 Speed-dependent Cutting Force Coefficients

The cutting force coefficients provide a relationship between the chip area and the cutting forces. The cutting force coefficient may be represented by the specific cutting force, K_s , and the cutting angle, β , which relates the normal and tangential cutting forces [1]. In this study, the cutting force coefficients were measured at four different spindle speeds: 1000 rpm, 2000 rpm, 3000 rpm, and 4000 rpm. Figure 6.1 shows a plot of the specific cutting force coefficient, K_s , and the cutting force angle, β , as a function of spindle speed. The measured data points were interpolated using cubic interpolation to obtain an estimate of the cutting force coefficients at finer increments of spindle speed. These interpolated cutting force coefficients were used in the prediction of the speed-

dependent SLD to incorporate any dependence of spindle speed on the cutting force coefficients.

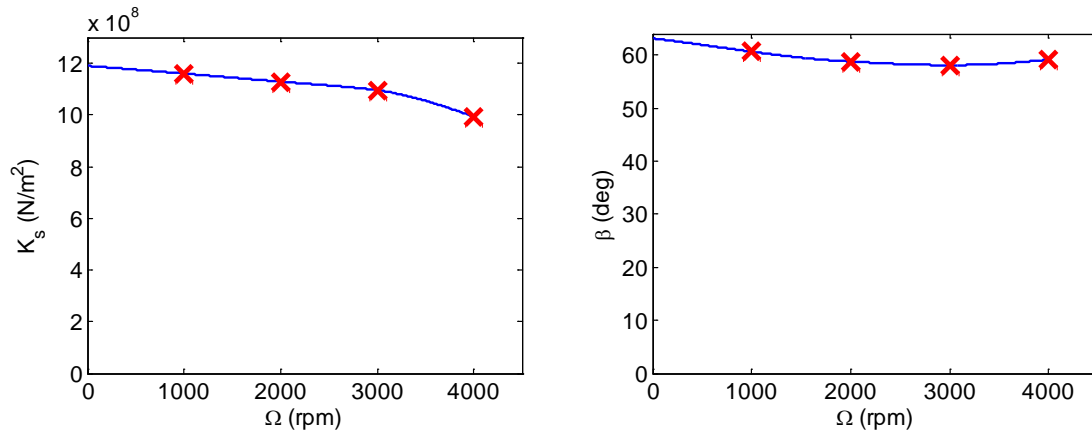


Figure 6.1: Speed-dependent specific cutting force coefficient, K_s (left), and cutting force angle, β (right).

6.2 Tool Tip FRF

Typically, the tool tip FRF may be measured directly by modal analysis. However, the objective of this study is to capture the changes spindle dynamics as a function of spindle speed and incorporate the influence of the changing dynamics into a speed-dependent SLD. Since it is not possible to measure the dynamics at the tool tip at speed, the dynamics were measured at the end of a cylindrical artifact which was impacted when the spindle was rotating. The RCSA method, described in the previous chapter, was then used to decouple the receptances of the artifact to isolate the spindle and then couple the receptances of the holder-tool subassembly to the spindle in order to predict the FRF at the tool tip. The artifact and holder-tool subassembly receptances were modeled using finite element theory. In this study, the speed-dependent dynamics were measured on two different artifacts.

6.2.1 Standard Cylindrical Artifact

Figure 6.2 shows a plot of the real and imaginary parts of the predicted tool point FRFs in the machine x-direction. The y-direction tool point FRF predictions are shown in Figure 6.3. These predictions were made using the dynamic measurements performed on the standard cylindrical artifact.

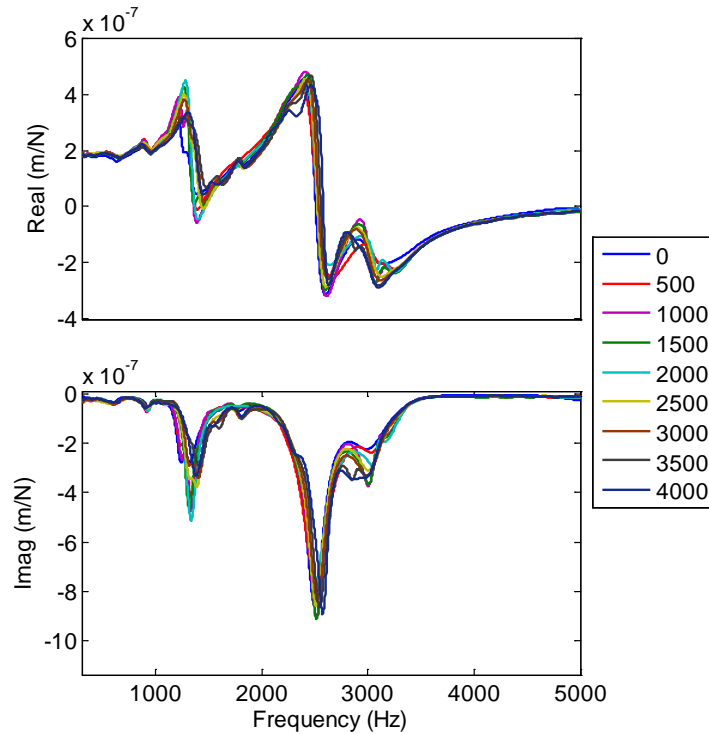


Figure 6.2: Tool tip FRF estimated using standard cylindrical artifact FRF measurements: x-direction.

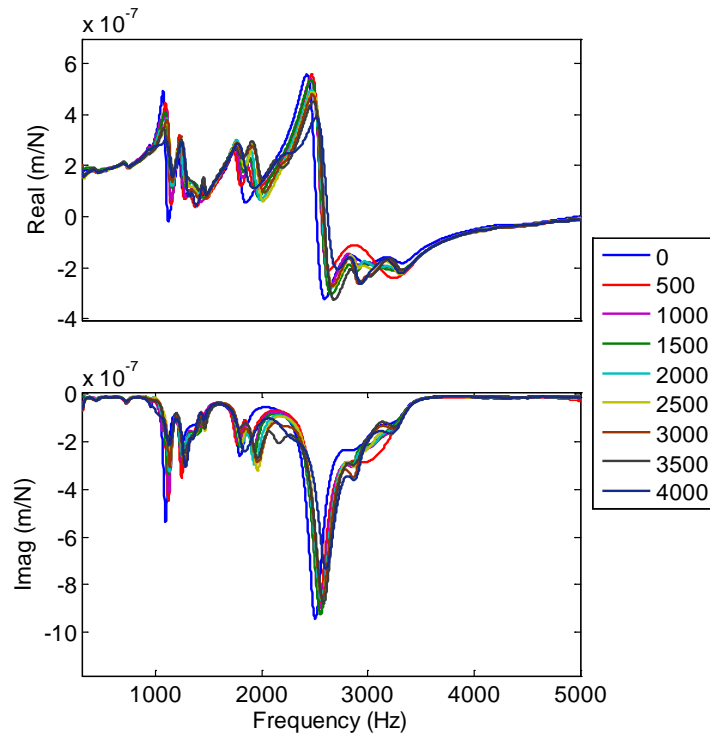


Figure 6.3: Tool tip FRF estimated using standard cylindrical artifact FRF measurements: y-direction.

6.2.2 Solid Carbide Blank

Figure 6.4 shows the real and imaginary parts of the predicted tool point FRFs in the machine x-direction. The y-direction tool point FRF predictions are shown in Figure 6.5. These predictions were made using the dynamic measurements performed on the solid carbide blank.

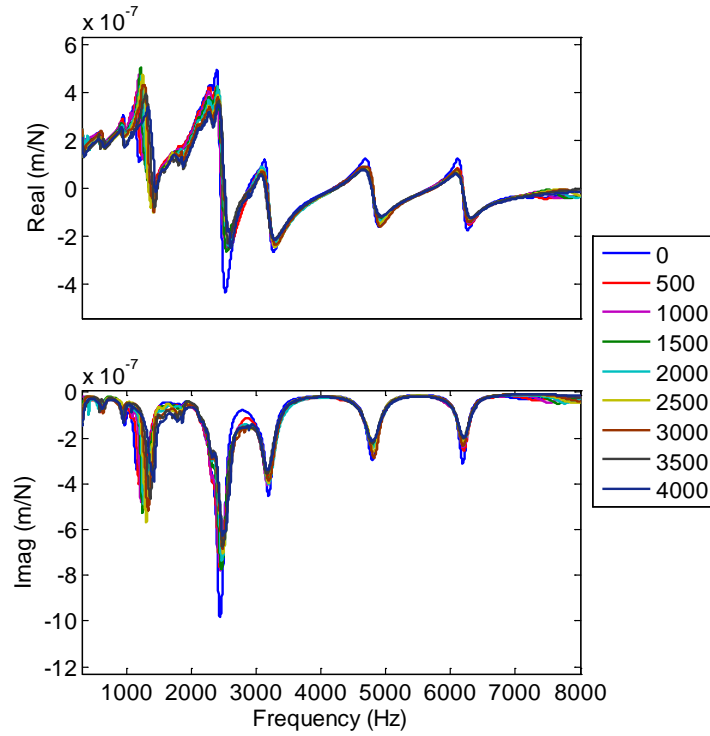


Figure 6.4: Tool tip FRF estimated using solid carbide blank FRF measurements: x – direction.

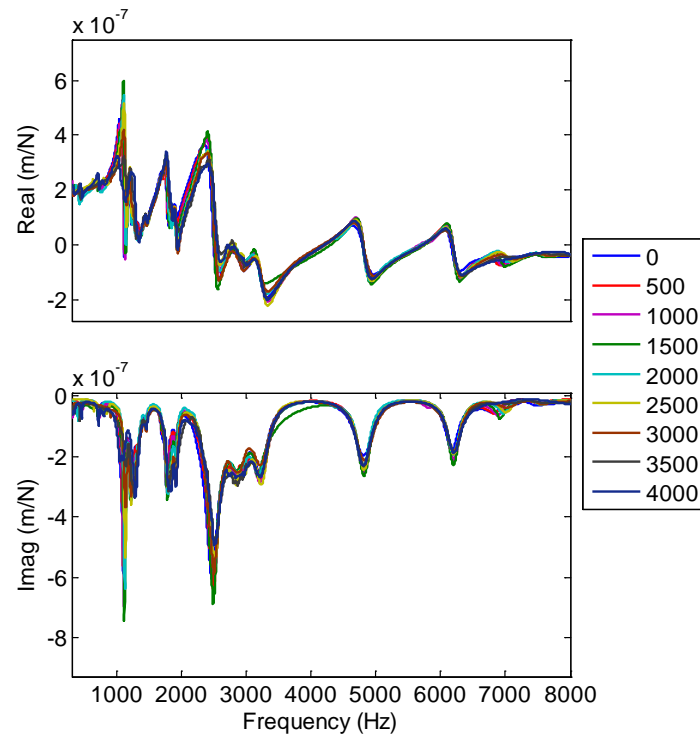


Figure 6.5: Tool tip FRF estimated using solid carbide blank FRF measurements: y – direction.

6.3 Speed-Dependent Stability Lobe Diagram

In order to develop a speed-dependent SLD, first, the tool point FRFs predicted using RCSA were interpolated using cubic interpolation to obtain a FRF in finer increments of spindle speed. Figure 6.6 shows a plot of the magnitude of the interpolated FRF. The interpolated FRFs were generated every 5 rpm. The tool point FRFs predicted using the carbide blank measurements are shown here. Secondly, the interpolated cutting force coefficients were identified. Then, for each spindle speed, the Altintas [5] stability model was used to identify the limiting stable depth of cut corresponding to that particular speed. In such a manner, the critical stability limit for every spindle speed was calculated and a speed-dependent SLD was developed.

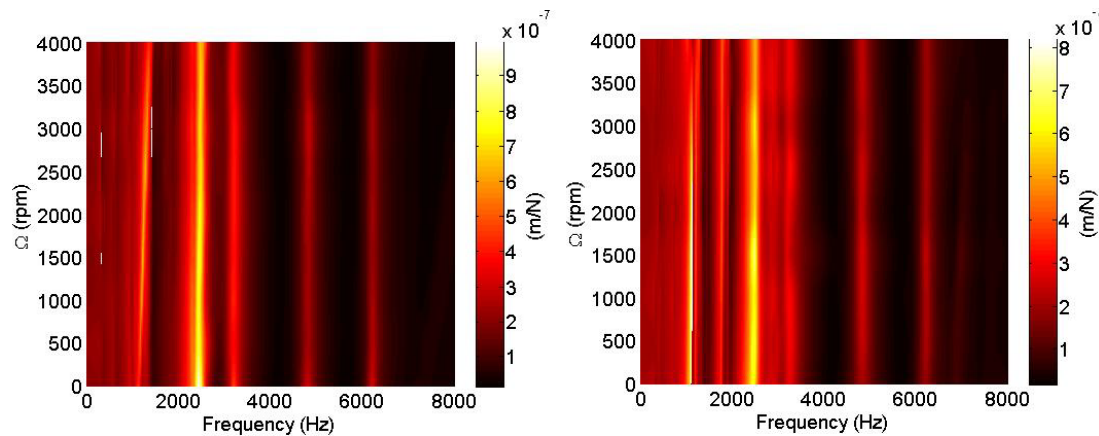


Figure 6.6: Magnitude of interpolated speed-dependent tool tip FRF: x-direction (left), y-direction (right).

In this study, machining trials were performed using a four-fluted, 12.7 mm diameter, 30° right handed helix, solid carbide endmill. Figure 6.7 shows the speed-dependent SLD for a 25% radial immersion upmilling cut at a cutting feed rate of 76.2 $\mu\text{m}/\text{tooth}$ (0.003 in/tooth) with the tool feeding along the machine x-direction. The SLD obtained using the standard artifact measurement, the SLD obtained from the solid carbide blank measurements, and the SLD obtained using the tool point FRF is plotted. The SLD

obtained using the tool point FRF corresponds to the stationary case stability limit as it does not incorporate the changes in dynamics with spindle speed. Note that in this case, all the three stability limits account for speed-dependent changes in cutting force coefficients.

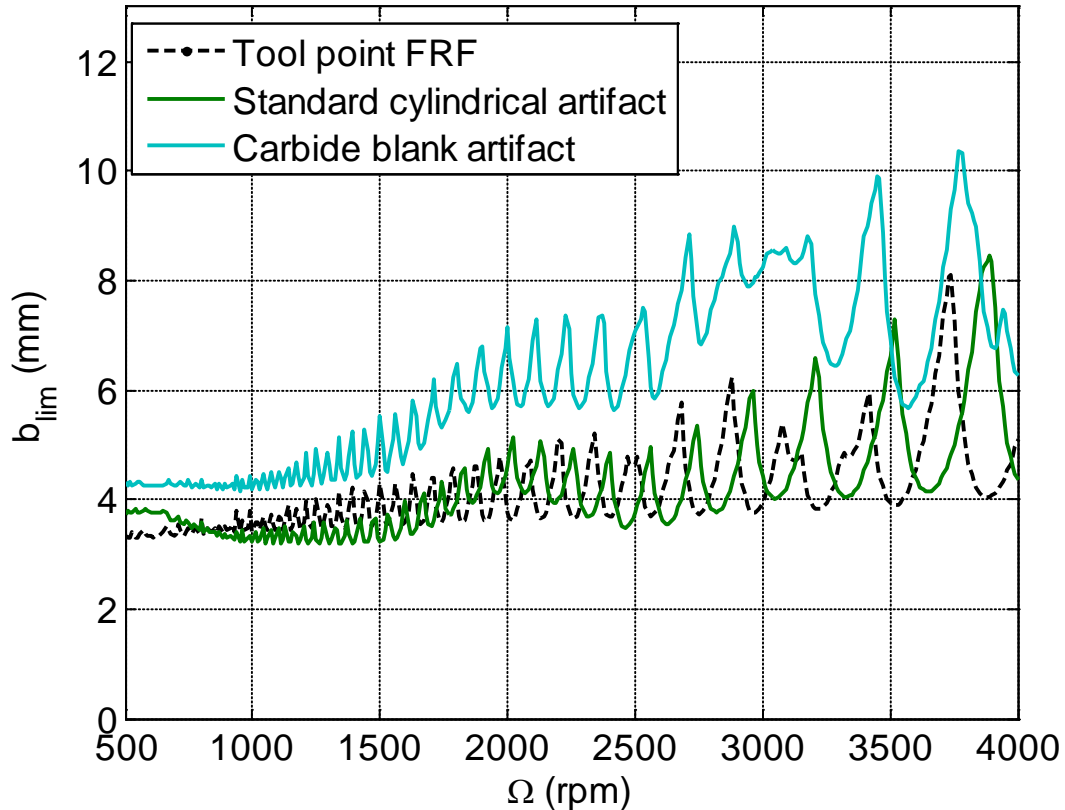


Figure 6.7: Speed-dependent stability lobe diagram comparison.

6.4 Machining Stability Trials

Figure 6.8 shows a picture of the machining setup used to evaluate the speed-dependent SLD. Two piezoelectric accelerometers (PCB 352 B10) were mounted on the stationary spindle housing along the orthogonal machine x- and y-directions. The two accelerometers produces time domain signals, $a_x(t)$, and $a_y(t)$. The two accelerometer signals were combined to obtain a metric to ascertain chatter.

$$|A(f)| = |A_x(f)| + |A_y(f)|, \quad (5.1)$$

where $|A_x(f)|$ and $|A_y(f)|$ correspond to the absolute values of the FFTs of the time domain acceleration signals $a_x(t)$, and $a_y(t)$, respectively.

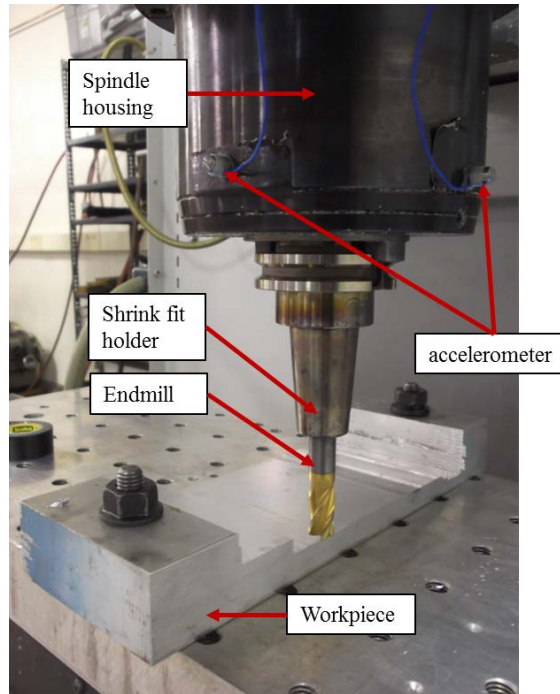


Figure 6.8: Experimental setup for machining stability trials.

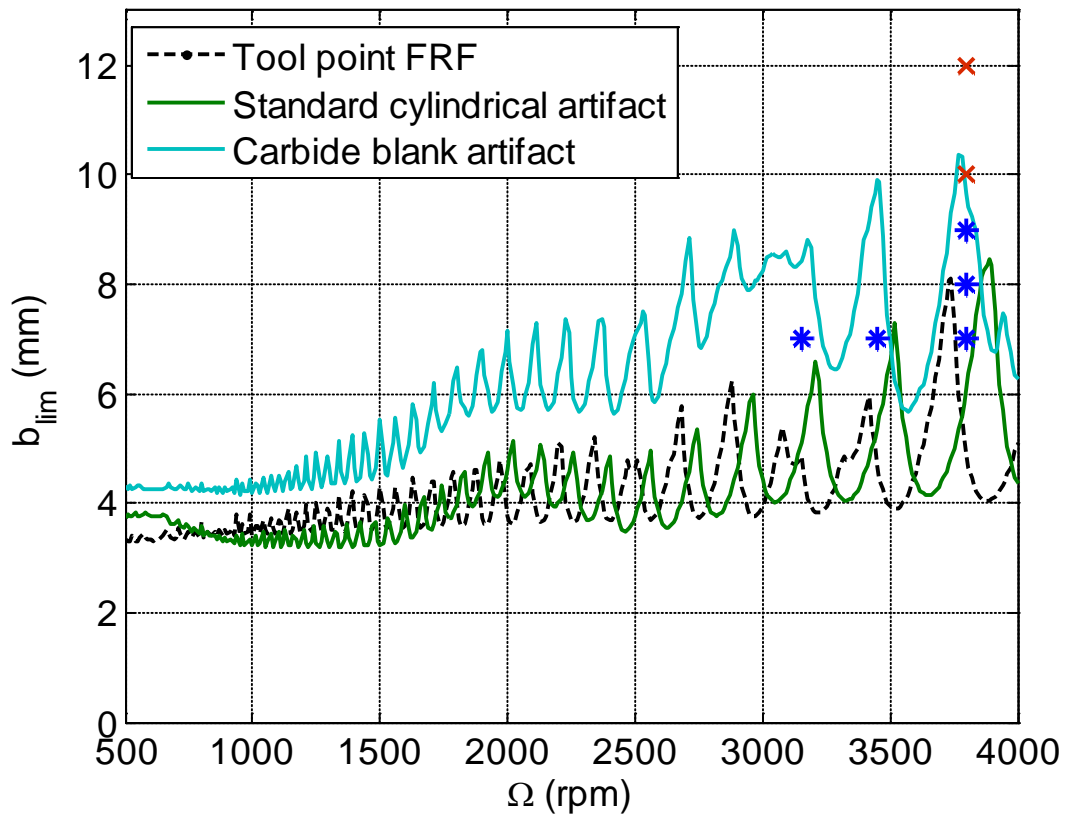


Figure 6.9: Machining stability trials: blue star indicates stable cut; red cross indicates unstable cut.

Figure 6.9 shows a plot of the three SLDs. The tested combinations are also plotted, where a red cross indicates chatter and the blue star indicates stable machining. Stable machining conditions were observed at combinations of spindle speed, Ω , and axial depth of cut, b , above the stationary tool point FRF stability limit. The SLD predicted using the carbide blank measurements were found to best predict machining stability. The SLD predicted using the standard cylindrical artifact measurements may be improved by incorporating the effects of the holder-tool connection stiffness. The holder-tool connection stiffness was captured in the speed-dependent FRF measurements performed on the carbide blank resulting in improved predictions of the speed-dependent tool point dynamics and, subsequently, improved prediction of chatter.

Figure 6.10 shows the plot of the acceleration metric, $|A(f)|$, used to identify chatter. Notice that the vertical axis was kept constant for all the subplots. Machining chatter conditions can be clearly identified by the peaks in the frequency content of the acceleration signal at 3200 Hz and 6400 Hz. Referring to Figure 6.4 and Figure 6.5, these frequencies correspond to the portion of the FRF where the magnitude of the real part is lowest.

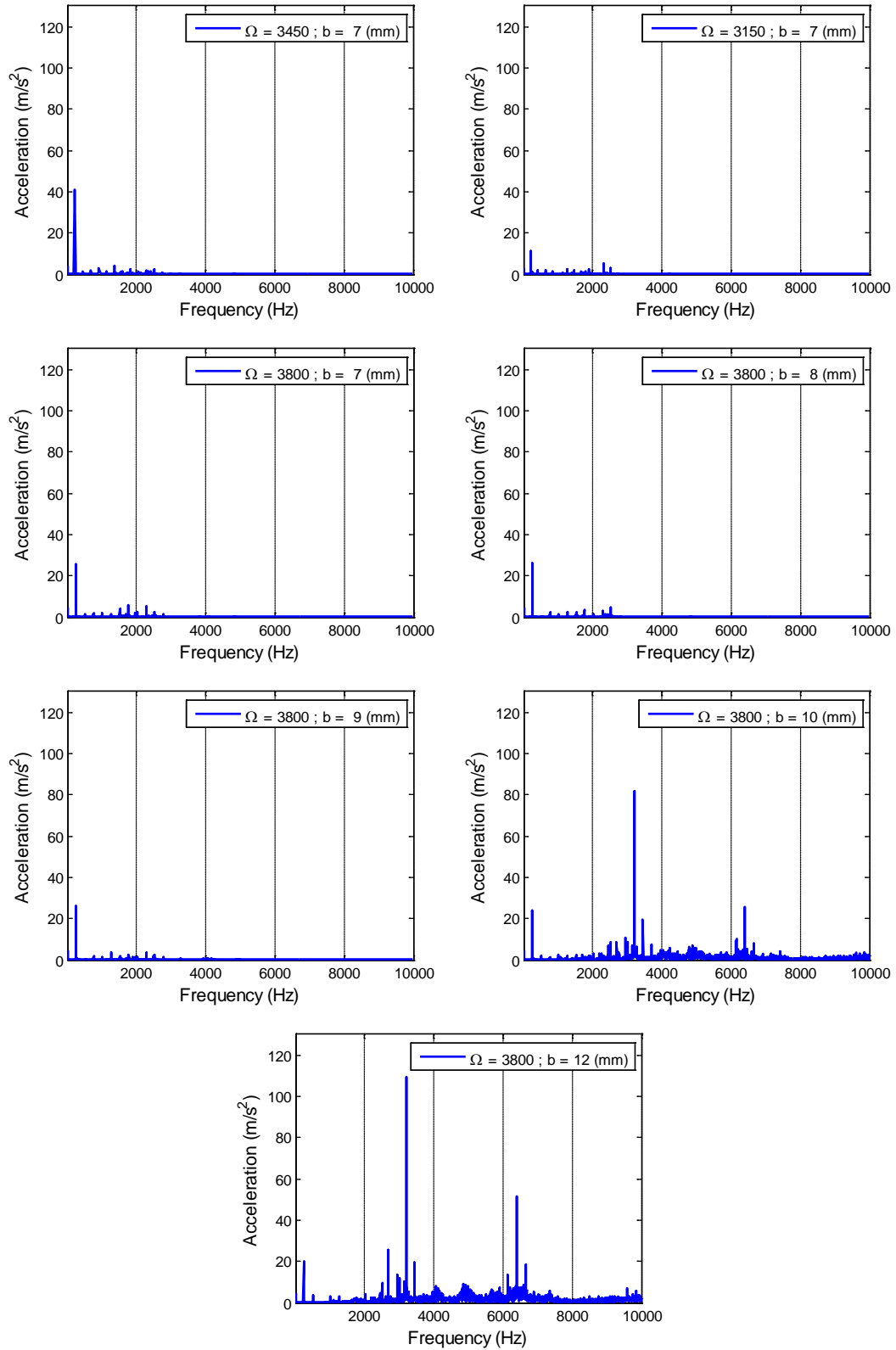


Figure 6.10: Magnitude of $|A(f)|$ at the different combinations of b_{lim} and Ω .

CHAPTER 7: CONCLUSIONS AND FUTURE WORK

7.1 Conclusions

First, a time domain simulation model was developed to investigate the influence of the dynamic properties of the impulse hammer and the target on contact forces and excited bandwidths. In this study, the model used to study the influence of hammer dynamics on excitation forces was enhanced to include the influence of the target dynamics. Hertzian contact theory was used to model the impact mechanics. The contact forces, excited bandwidth and response magnitude were studied from the perspective of modal testing. The excited bandwidth was found to have a strong relation with the target dynamics. Also, for constant hammer stiffness, the excited bandwidth was found to increase with a decrease in the mass of the impulse hammer. However, the magnitude of the target response was also found to decrease as the mass of the impulse hammer was reduced, making the FRF measurement more susceptible to sensor noise.

To account for the potentially different dynamics of the different targets studied here, two different setups were designed and constructed with different capabilities. The automated excitation setup enabled the ability to apply a consistent and controlled excitation impulse on the target.

Synchronization errors between the force and response signals result in frequency dependent phase errors in the calculated FRF. In this study, the time delay was measured for a Lion Precision capacitance gage sensors and a Polytec LDV sensor. A frequency

domain correction algorithm was used to rectify the measured FRF to account for synchronization errors.

In this study, speed-dependent FRF measurements were performed on a standard cylindrical artifact and on a solid carbide blank clamped in a shrink fit tool holder. The FRF measurements performed on the Haas TM1 CNC machines showed an increase in dynamic stiffness with increase in spindle speed. A multi-probe error separation technique was used to simultaneously identify the SE motions.

The dynamics of the NSK HES-500 high speed spindle were measured using a 3.175 mm carbide blank as the target. The dynamic stiffness of the spindle was found to increase with increasing spindle speed. The SE motions were measured using a multi-position error separation technique. The displacement data collected at the three angles was synchronized using a laser tachometer. The SE motion measurements of the high speed spindle were found to be constrained by the sampling capabilities. Note that for the high speed spindle, the dynamics and SE motions were measured independently using different setups.

To determine spindle receptances, a robust simplex based Nelder-Mead optimization algorithm was developed to automate the identification of equivalent fixed-free Euler Bernoulli beams for a direct force-to-displacement FRF measurement. The equivalent EB beam technique significantly reduces the experimental effort required to completely populate the receptance matrices. The method reduces the experimental noise associated with finite difference methods used to identify moment-to-rotation receptances. The optimization algorithm eliminates the previously employed iterative process used to identify the beam parameters, thereby streamlining the process.

The tool tip FRF predictions were made using RCSA. The speed-dependent spindle dynamics used in RCSA were identified using two different artifacts: a standard cylindrical artifact and a solid carbide blank clamped in a shrink fit tool holder. The predictions made using the carbide blank measurements were found to be a better match to the measured tool tip FRF. This was attributed to the connection stiffness in the shrink fit holder-tool connection. The connection stiffness was captured in the blank measurement but was unaccounted for in the cylindrical artifact predictions.

A speed-dependent SLD was developed which incorporated the spindle speed dependence of the tool point dynamics and the cutting force coefficients. The stability trials performed at seven different combinations of spindle speed and axial depth of cut indicated that the speed-dependent SLD provided a better estimate of machining stability.

7.2 Future Work

The maximum spindle speed for the Haas TM1 CNC machine is 4000 rpm. In the future, the measurement setup built in this work can be used to experimentally study the speed-dependent dynamics of other macro-milling machines with higher maximum spindle speed (greater than 15,000 rpm). The low mass excitation hammer setup can be used to characterize the speed-dependent dynamics of other miniature ultra-high speed spindles (greater than 100,000 rpm). The speed-dependent SLD developed here may then be applied and validated for micro-machining applications.

The time domain impact simulation provides the capability to simulate impact forces while accounting for the dynamics of the target. Further effort to validate the model for a variety of different combinations of geometries, material properties, and dynamics properties of the colliding bodies is warranted.

The time domain impact excitation model may be used to develop and optimize excitation systems to impart high bandwidth excitation for miniature structures which cannot be excited using commercially available impact hammers.

Further investigation of the influence of different holder/ tool geometries, types, and materials on holder-tool contact stiffness with the objective of improving RCSA predictions is necessary.

The speed-dependence of cutting force coefficients has been reported in this work. Theoretical models to capture these changes in cutting force coefficients with spindle speed may be developed.

The ability to measure SE motions was found to be impeded by constraints on the sampling rate. A study to examine the influence of sampling rate on measured SE motions is warranted.

REFERENCES

- [1] Schmitz TL, Smith KS. Machining dynamics: frequency response to improved productivity: Springer New York, 2009.
- [2] Tlustý J, Poláček M. The stability of machine tools against self excited vibrations in machining. International research in production engineering, ASME. 1963:465-74.
- [3] Tobias S, Fishwick W. Theory of regenerative machine tool chatter. The Engineer. 1958;205:199-203.
- [4] Merritt HE. Theory of self-excited machine-tool chatter: Contribution to machine-tool chatter research—1. Journal of Engineering for Industry. 1965;87:447.
- [5] Altıntaş Y, Budak E. Analytical prediction of stability lobes in milling. CIRP Annals-Manufacturing Technology. 1995;44:357-62.
- [6] Insperger T, Stépán G. Semi-discretization method for delayed systems. International Journal for numerical methods in engineering. 2002;55:503-18.
- [7] Sims N, Mann B, Huyanan S. Analytical prediction of chatter stability for variable pitch and variable helix milling tools. Journal of Sound and Vibration. 2008;317:664-86.
- [8] Quintana G, Ciurana J, Teixidor D. A new experimental methodology for identification of stability lobes diagram in milling operations. International Journal of Machine Tools and Manufacture. 2008;48:1637-45.
- [9] Jorgensen BR. Robust modeling of high-speed spindle-bearing dynamics under operating conditions. 1996.
- [10] Jorgensen BR, Shin YC. Dynamics of spindle-bearing systems at high speeds including cutting load effects. Journal of manufacturing science and engineering. 1998;120:387-94.
- [11] Bossmanns B, Tu JF. A thermal model for high speed motorized spindles. International Journal of Machine Tools and Manufacture. 1999;39:1345-66.
- [12] Lin C-W, Tu JF, Kamman J. An integrated thermo-mechanical-dynamic model to characterize motorized machine tool spindles during very high speed rotation. International Journal of Machine Tools and Manufacture. 2003;43:1035-50.
- [13] Li H, Shin YC. Analysis of bearing configuration effects on high speed spindles using an integrated dynamic thermo-mechanical spindle model. International Journal of Machine Tools and Manufacture. 2004;44:347-64.

- [14] Altintas Y, Cao Y. Virtual design and optimization of machine tool spindles. *CIRP Annals-Manufacturing Technology*. 2005;54:379-82.
- [15] Cao Y, Altintas Y. A general method for the modeling of spindle-bearing systems. *Journal of mechanical design*. 2004;126:1089.
- [16] Cao Y, Altintas Y. Modeling of spindle-bearing and machine tool systems for virtual simulation of milling operations. *International Journal of Machine Tools and Manufacture*. 2007;47:1342-50.
- [17] Holkup T, Cao H, Kolář P, Altintas Y, Zelený J. Thermo-mechanical model of spindles. *CIRP Annals-Manufacturing Technology*. 2010;59:365-8.
- [18] Movahhedy MR, Mosaddegh P. Prediction of chatter in high speed milling including gyroscopic effects. *International Journal of Machine Tools and Manufacture*. 2006;46:996-1001.
- [19] Gagnol V, Bouzgarrou B, Ray P, Barra C. Model-based chatter stability prediction for high-speed spindles. *International Journal of Machine Tools and Manufacture*. 2007;47:1176-86.
- [20] Mañé I, Gagnol V, Bouzgarrou BC, Ray P. Stability-based spindle speed control during flexible workpiece high-speed milling. *International Journal of Machine Tools and Manufacture*. 2008;48:184-94.
- [21] Cao H, Li B, He Z. Chatter stability of milling with speed-varying dynamics of spindles. *International Journal of Machine Tools and Manufacture*. 2012;52:50-8.
- [22] Alfares MA, Elsharkawy AA. Effects of axial preloading of angular contact ball bearings on the dynamics of a grinding machine spindle system. *Journal of Materials Processing Technology*. 2003;136:48-59.
- [23] Ozturk E, Kumar U, Turner S, Schmitz T. Investigation of spindle bearing preload on dynamics and stability limit in milling. *CIRP Annals-Manufacturing Technology*. 2012;61:343-6.
- [24] Smith S, Jacobs T, Halley J. The effect of drawbar force on metal removal rate in milling. *CIRP Annals-Manufacturing Technology*. 1999;48:293-6.
- [25] Cheng C-H, Schmitz TL, Scott Duncan G. Rotating tool point frequency response prediction using RCSA. *Machining Science and Technology*. 2007;11:433-46.
- [26] Schmitz T, Davies M, Medicus K, Snyder J. Improving high-speed machining material removal rates by rapid dynamic analysis. *CIRP Annals-Manufacturing Technology*. 2001;50:263-8.

- [27] Schmitz TL, Davies MA, Kennedy MD. Tool point frequency response prediction for high-speed machining by RCSA. *Journal of manufacturing science and engineering*. 2001;123:700-7.
- [28] Schmitz TL, Donalson R. Predicting high-speed machining dynamics by substructure analysis. *CIRP Annals-Manufacturing Technology*. 2000;49:303-8.
- [29] Park SS, Altintas Y, Movahhedy M. Receptance coupling for end mills. *International Journal of Machine Tools and Manufacture*. 2003;43:889-96.
- [30] Schmitz TL, Duncan GS. Three-component receptance coupling substructure analysis for tool point dynamics prediction. *Journal of manufacturing science and engineering*. 2005;127:781-90.
- [31] Duncan GS, Tummond M, Schmitz TL. An investigation of the dynamic absorber effect in high-speed machining. *International Journal of Machine Tools and Manufacture*. 2005;45:497-507.
- [32] Ertürk A, Özgüven H, Budak E. Analytical modeling of spindle-tool dynamics on machine tools using Timoshenko beam model and receptance coupling for the prediction of tool point FRF. *International Journal of Machine Tools and Manufacture*. 2006;46:1901-12.
- [33] Schmitz TL. Torsional and axial frequency response prediction by RCSA. *Precision Engineering*. 2010;34:345-56.
- [34] Timoshenko S. *Vibration problems in engineering*. 1974.
- [35] Yokoyama T. Vibrations of a hanging Timoshenko beam under gravity. *Journal of Sound and Vibration*. 1990;141:245-58.
- [36] Nelson H. A finite rotating shaft element using Timoshenko beam theory. *Journal of mechanical design*. 1980;102:793.
- [37] Greenhill L, Bickford W, Nelson H. A conical beam finite element for rotor dynamics analysis. *ASME, Transactions, Journal of Vibration, Acoustics, Stress, and Reliability in Design*. 1985;107:421-30.
- [38] Hutchinson J. Shear coefficients for Timoshenko beam theory. *Journal of Applied Mechanics*. 2001;68:87-92.
- [39] Bediz B, Kumar U, Schmitz TL, Burak Ozdoganlar O. Modeling and experimentation for three-dimensional dynamics of endmills. *International Journal of Machine Tools and Manufacture*. 2012;53:39-50.

- [40] Filiz S, Cheng C-H, Powell K, Schmitz T, Ozdoganlar O. An improved tool-holder model for RCSA tool-point frequency response prediction. *Precision Engineering*. 2009;33:26-36.
- [41] Yagci B, Filiz S, Romero LL, Ozdoganlar OB. A spectral-Tchebychev technique for solving linear and nonlinear beam equations. *Journal of Sound and Vibration*. 2009;321:375-404.
- [42] Kivanc E, Budak E. Structural modeling of end mills for form error and stability analysis. *International Journal of Machine Tools and Manufacture*. 2004;44:1151-61.
- [43] Kops L, Vo D. Determination of the equivalent diameter of an end mill based on its compliance. *CIRP Annals-Manufacturing Technology*. 1990;39:93-6.
- [44] Kumar UV, Schmitz TL. Spindle dynamics identification for Receptance Coupling Substructure Analysis. *Precision Engineering*. 2012;36:435-43.
- [45] **Ganguly V**, Schmitz TL. Spindle dynamics identification using particle swarm optimization. *Journal of Manufacturing Processes*. 2013;15:444-51.
- [46] Lagarias JC, Reeds JA, Wright MH, Wright PE. Convergence properties of the Nelder--Mead simplex method in low dimensions. *SIAM Journal on Optimization*. 1998;9:112-47.
- [47] Nelder JA, Mead R. A simplex method for function minimization. *The computer journal*. 1965;7:308-13.
- [48] D'Errico J. fminsearchbnd, fminsearchcon. MATLAB Central File Exchange. 2012.
- [49] Box M. A comparison of several current optimization methods, and the use of transformations in constrained problems. *The Computer Journal*. 1966;9:67-77.
- [50] Schmitz TL, Powell K, Won D, Scott Duncan G, Gregory Sawyer W, Ziegert JC. Shrink fit tool holder connection stiffness/damping modeling for frequency response prediction in milling. *International Journal of Machine Tools and Manufacture*. 2007;47:1368-80.
- [51] Ertürk A, Özgüven H, Budak E. Effect analysis of bearing and interface dynamics on tool point FRF for chatter stability in machine tools by using a new analytical model for spindle-tool assemblies. *International Journal of Machine Tools and Manufacture*. 2007;47:23-32.
- [52] Özşahin O, Ertürk A, Özgüven HN, Budak E. A closed-form approach for identification of dynamical contact parameters in spindle-holder-tool assemblies. *International Journal of Machine Tools and Manufacture*. 2009;49:25-35.

- [53] Wang E, Wu B, Hu Y, Yang S, Cheng Y. Dynamic parameter identification of tool-spindle interface based on RCSA and Particle Swarm Optimization. *Shock and Vibration*. 2013;20:69-78.
- [54] Evans CJ, Hocken RJ, Estler WT. Self-calibration: reversal, redundancy, error separation, and 'absolute testing'. *CIRP Annals-Manufacturing Technology*. 1996;45:617-34.
- [55] Donaldson R. Simple method for separating spindle error from test ball roundness error. California Univ., Livermore. Lawrence Livermore Lab., 1972.
- [56] Grejda R, Marsh E, Vallance R. Techniques for calibrating spindles with nanometer error motion. *Precision Engineering*. 2005;29:113-23.
- [57] Whitehouse D. Some theoretical aspects of error separation techniques in surface metrology. *Journal of Physics E: Scientific Instruments*. 1976;9:531.
- [58] Marsh ER. Precision spindle metrology: DEStech Publications, Inc, 2010.
- [59] Marsh ER, Arneson DA, Martin DL. A comparison of reversal and multiprobe error separation. *Precision Engineering*. 2010;34:85-91.
- [60] Ewins DJ. Modal testing: theory, practice and application: Research studies press Baldock, 2000.
- [61] Bediz B, Korkmaz E, Ozdoganlar OB. An Impact Excitation System for Repeatable, High-Bandwidth Modal Testing of Miniature Structures. *Topics in Modal Analysis, Volume 7*: Springer, 2014. p. 249-57.
- [62] Gilardi G, Sharf I. Literature survey of contact dynamics modelling. *Mechanism and machine theory*. 2002;37:1213-39.
- [63] Lankarani HM, Nikravesh PE. Continuous contact force models for impact analysis in multibody systems. *Nonlinear Dynamics*. 1994;5:193-207.
- [64] Puttock MJ, Thwaite EG. Elastic compression of spheres and cylinders at point and line contact: Commonwealth Scientific and Industrial Research Organization Melbourne, VIC, Australia, 1969.
- [65] Stronge WJ. Impact mechanics: Cambridge university press, 2004.
- [66] Lion Precision. TechNote LT03-0031 EliteSeries Amplitude/Phase Frequency Response. 2011.
- [67] Polytec OFV - 5000 Vibrometer Controller - User Manual.

- [68] **Ganguly V**, Schmitz TL. Phase correction for frequency response function measurements. *Precision Engineering*. 2013.
- [69] Anandan KP, Ozdoganlar OB. An LDV-based methodology for measuring axial and radial error motions when using miniature ultra-high-speed (UHS) micromachining spindles. *Precision Engineering*. 2012.
- [70] Rahman AGA, Chao OZ, Ismail Z. Effectiveness of impact-synchronous time averaging in determination of dynamic characteristics of a rotor dynamic system. *Measurement*. 2011;44:34-45.
- [71] Bishop RED, Johnson DC. *The mechanics of vibration*: Cambridge University Press, 2011.
- [72] Blevins RD. *Formulas for natural frequency and mode shape*. 1979.

APPENDIX A: FRF MEASUREMENTS

A.1: Speed-Dependent FRF : Haas2

A.1.1: Standard Cylindrical Artifact

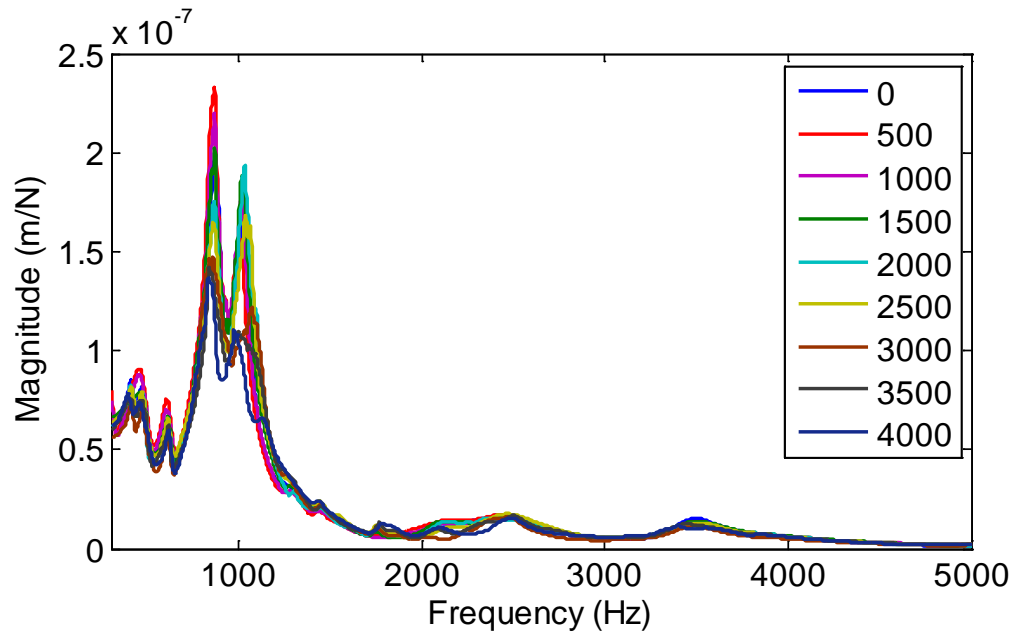


Figure A.1: Standard cylindrical artifact FRF (Haas2): x-direction.

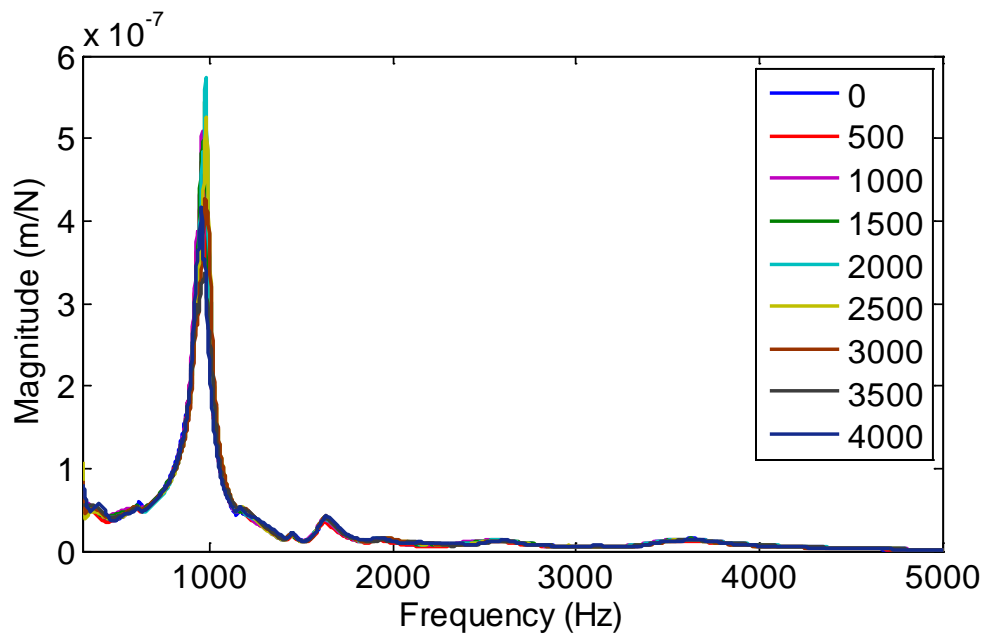


Figure A.2: Standard cylindrical artifact FRF (Haas2): y-direction.

A.1.2: Solid Carbide Blank

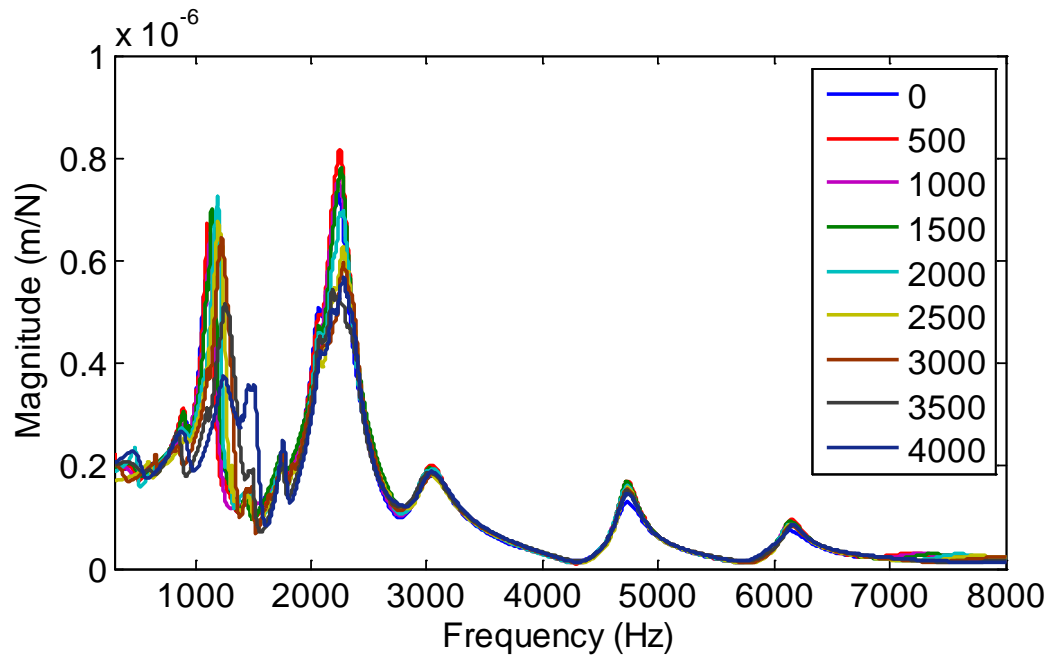


Figure A.3: Solid carbide blank FRF (Haas2): x-direction.

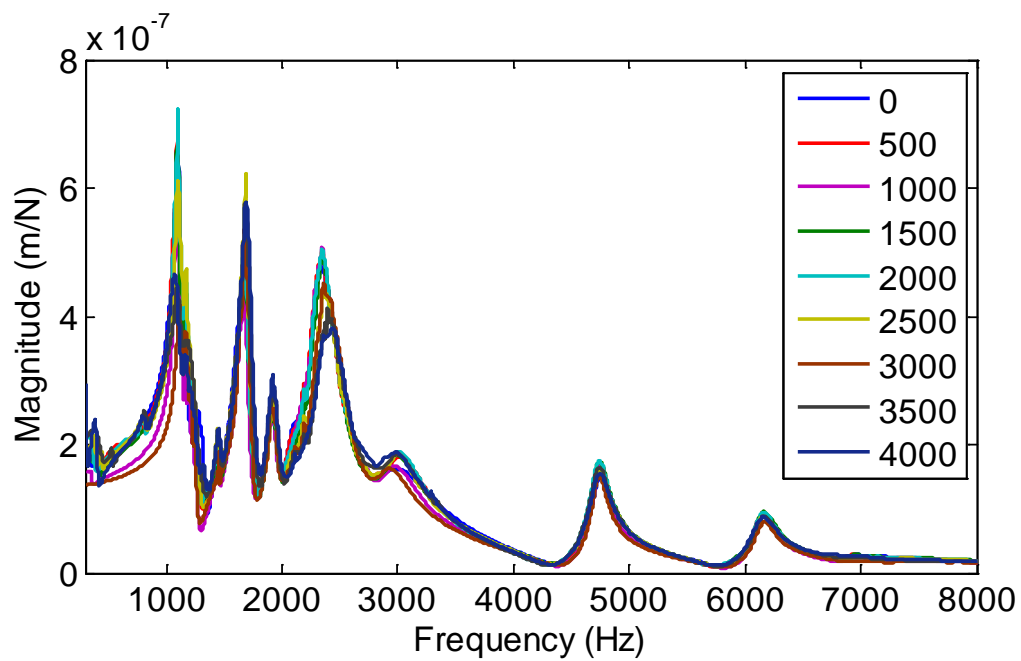


Figure A.4: Solid carbide blank FRF (Haas2): y-direction.

A.2: Speed-Dependent FRF : Haas3

A.2.1: Standard Cylindrical Artifact

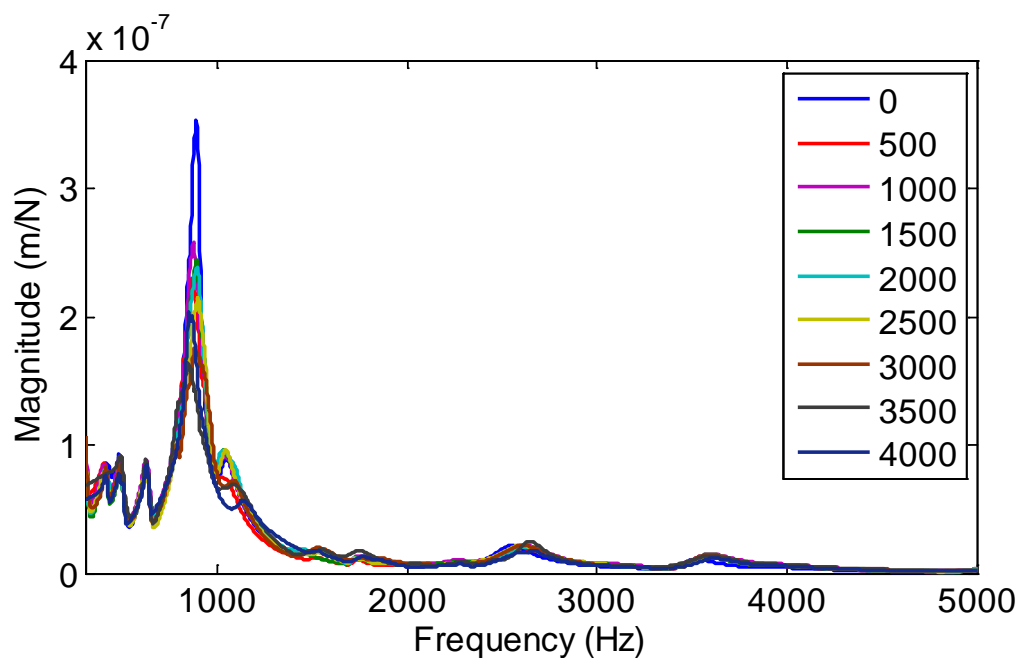


Figure A.5: Standard cylindrical artifact FRF (Haas3): x-direction.

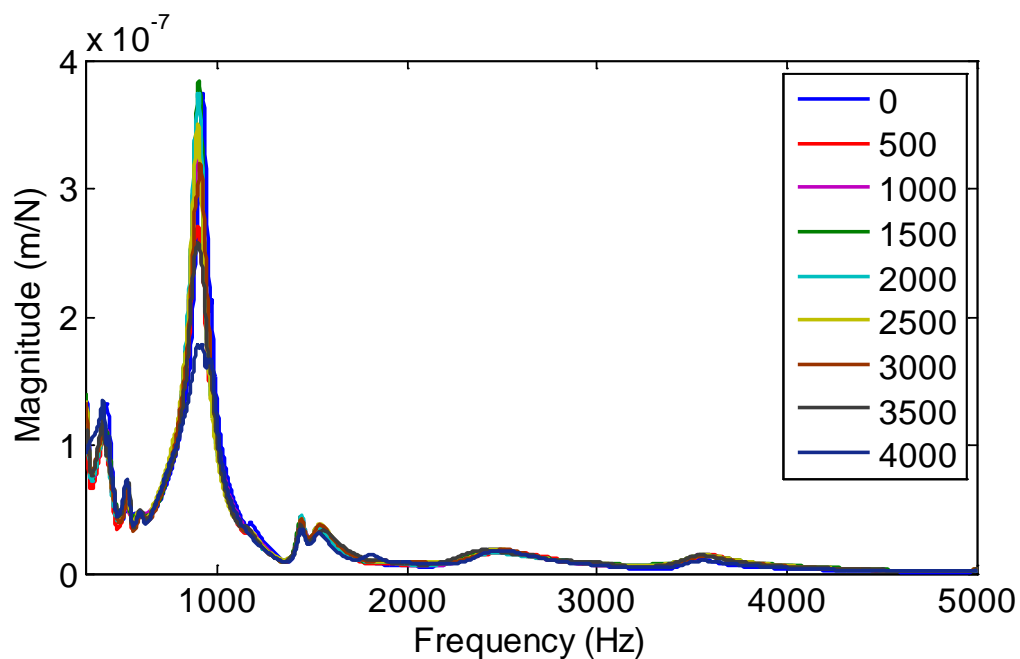


Figure A.6: Standard cylindrical artifact FRF (Haas3): y-direction.

A.2.2: Solid Carbide Blank

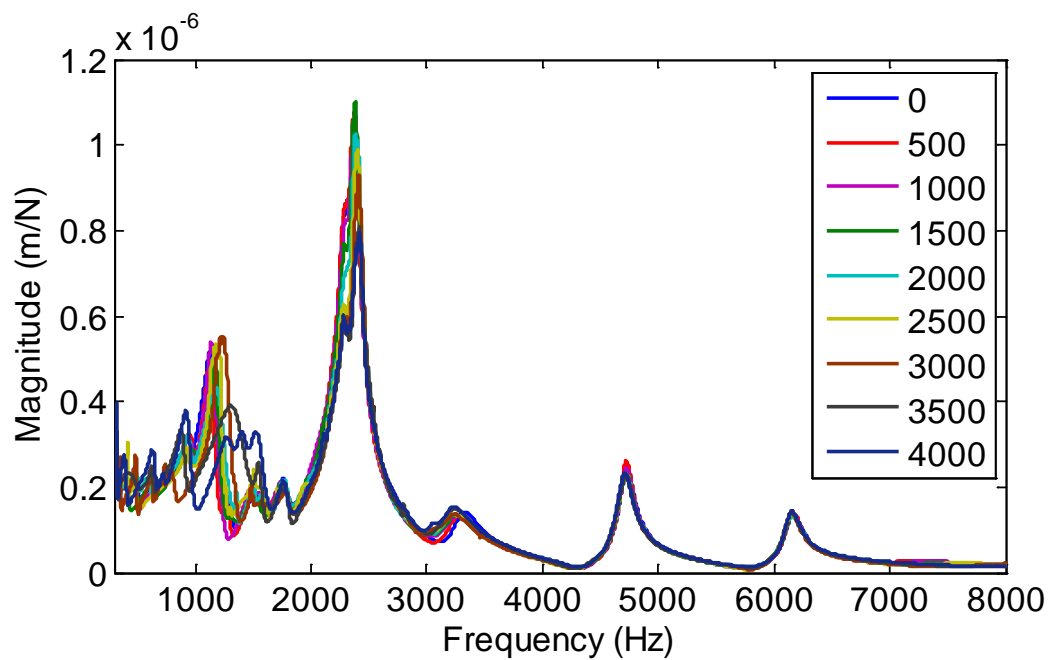


Figure A.7: Solid carbide blank FRF (Haas3): x-direction.

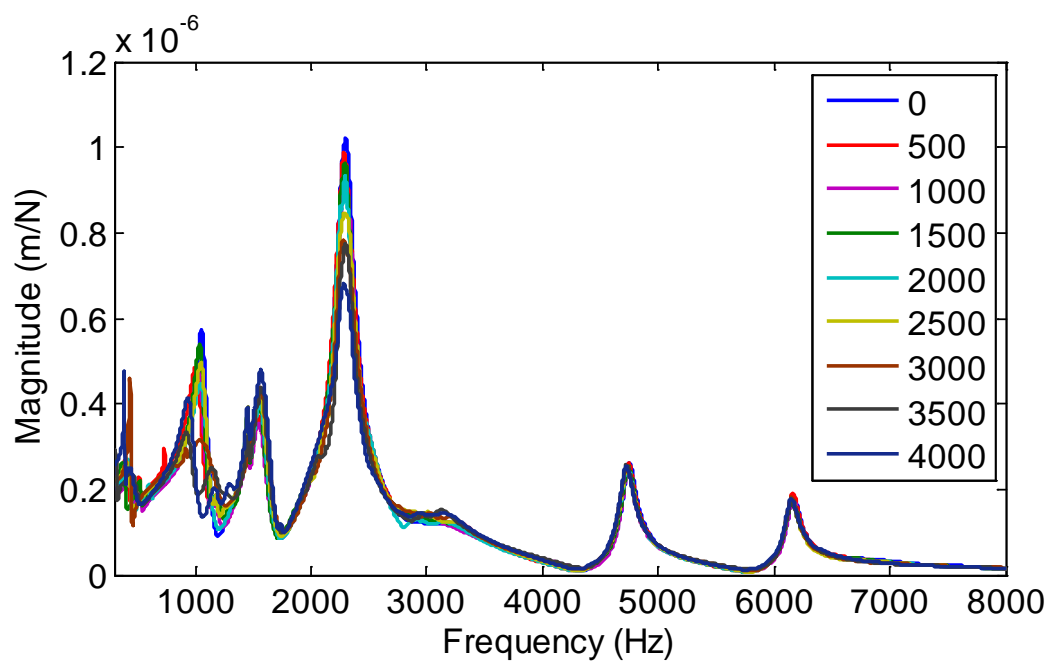


Figure A.8: Solid carbide blank FRF (Haas3): y-direction.

APPENDIX B: SE MOTION MEASUREMENTS

B.1: SE Measurements : Haas2

B.1.1: Synchronous SE Motions

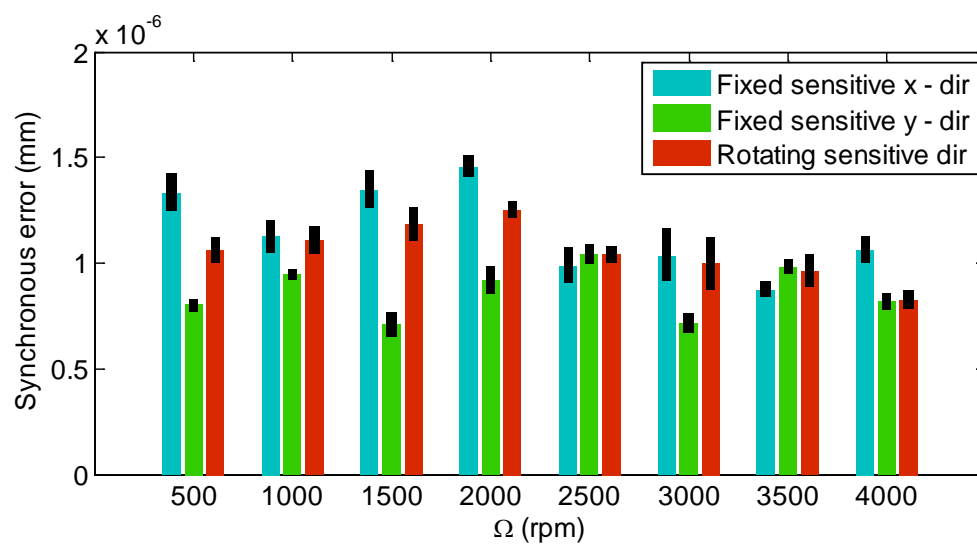


Figure B.1: Peak-to-valley estimate of synchronous SE motions.

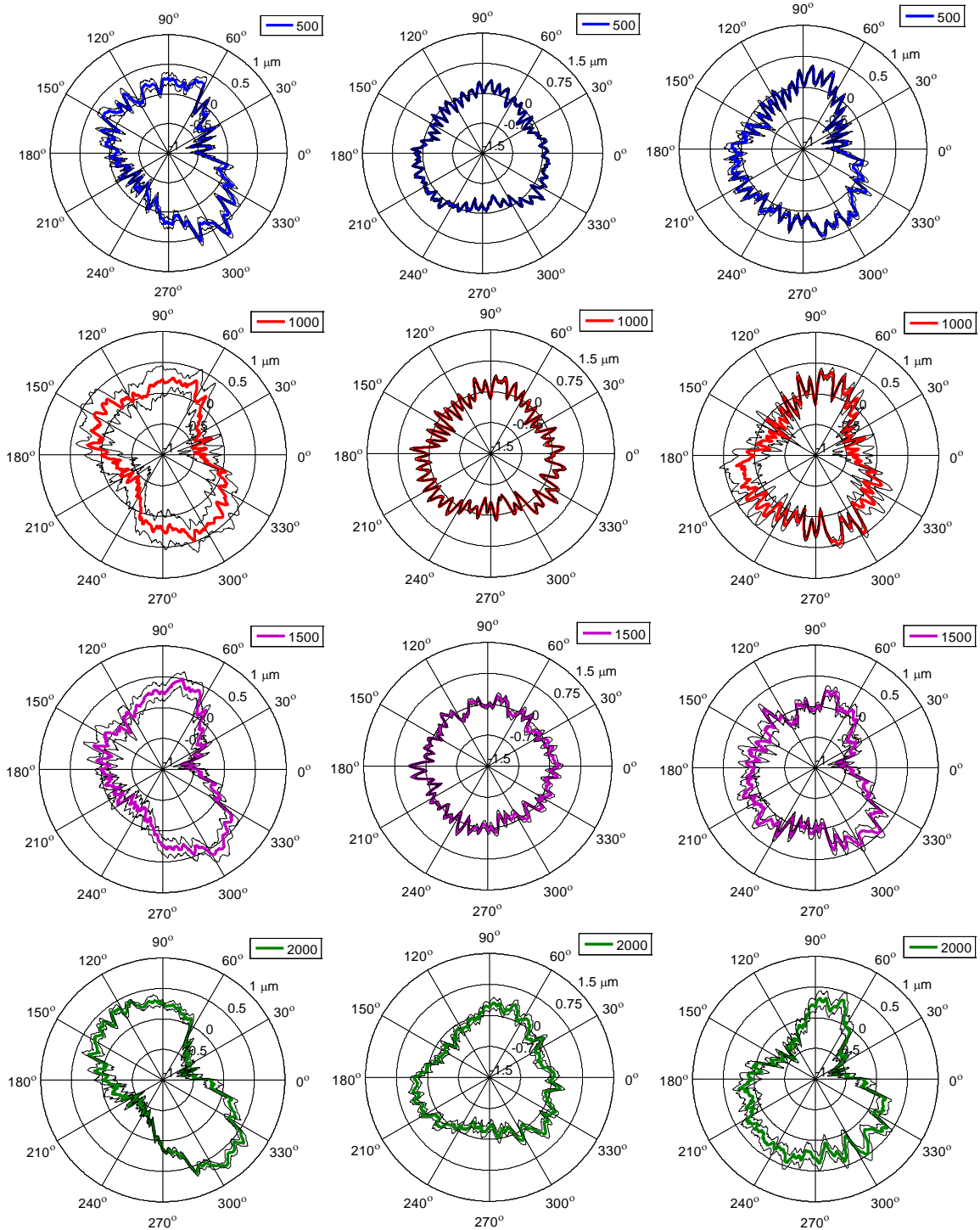


Figure B.2: Synchronous SE motion: fixed sensitive x-direction (left); fixed sensitive y-direction (middle); rotating sensitive direction (right). Spindle speeds: 500 rpm, 1000 rpm, 1500 rpm, 2000 rpm.

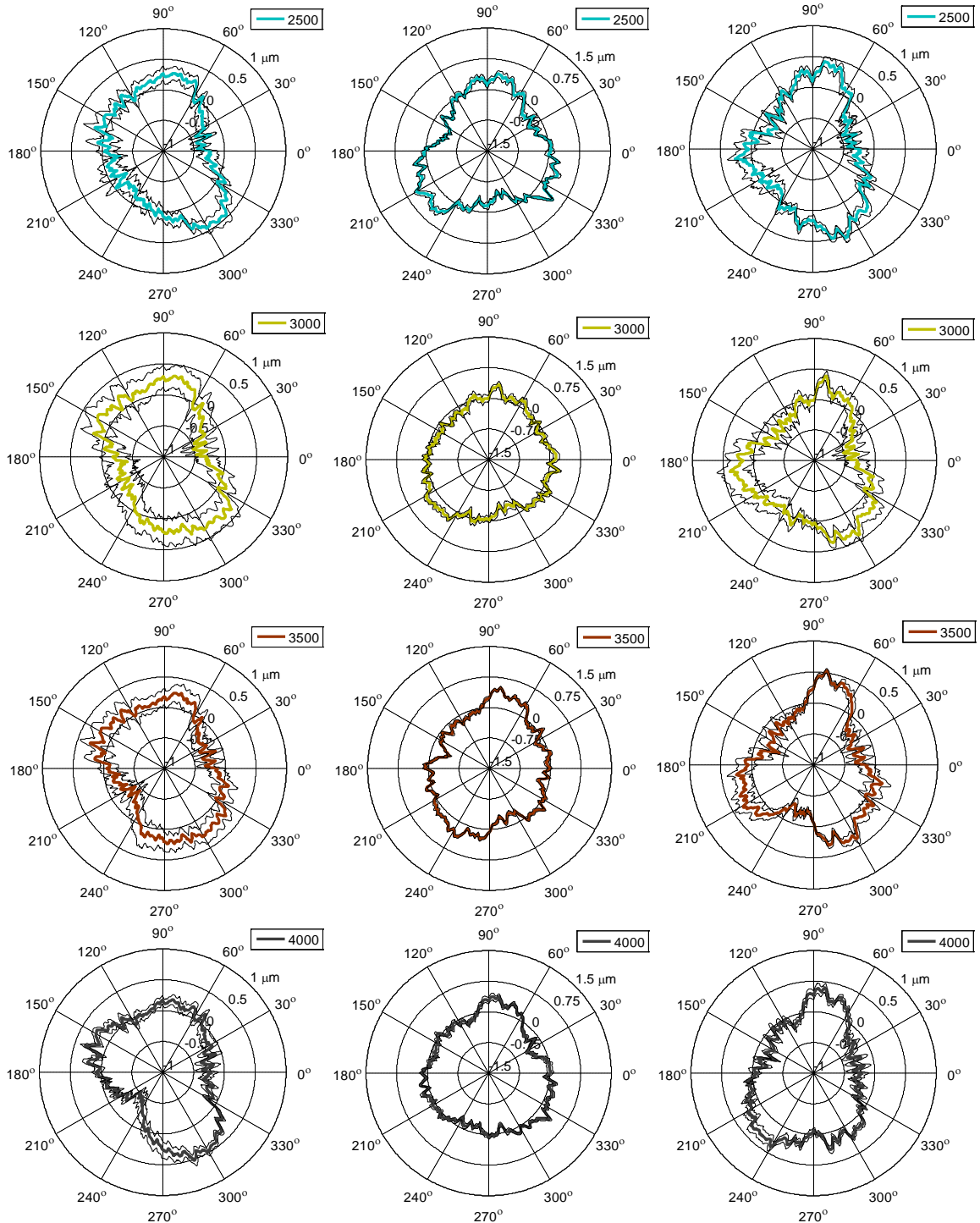


Figure B.3: Synchronous SE motion: fixed sensitive x-direction (left); fixed sensitive y-direction (middle); rotating sensitive direction (right). Spindle speeds: 2500 rpm, 3000 rpm, 3500 rpm, 4000 rpm.

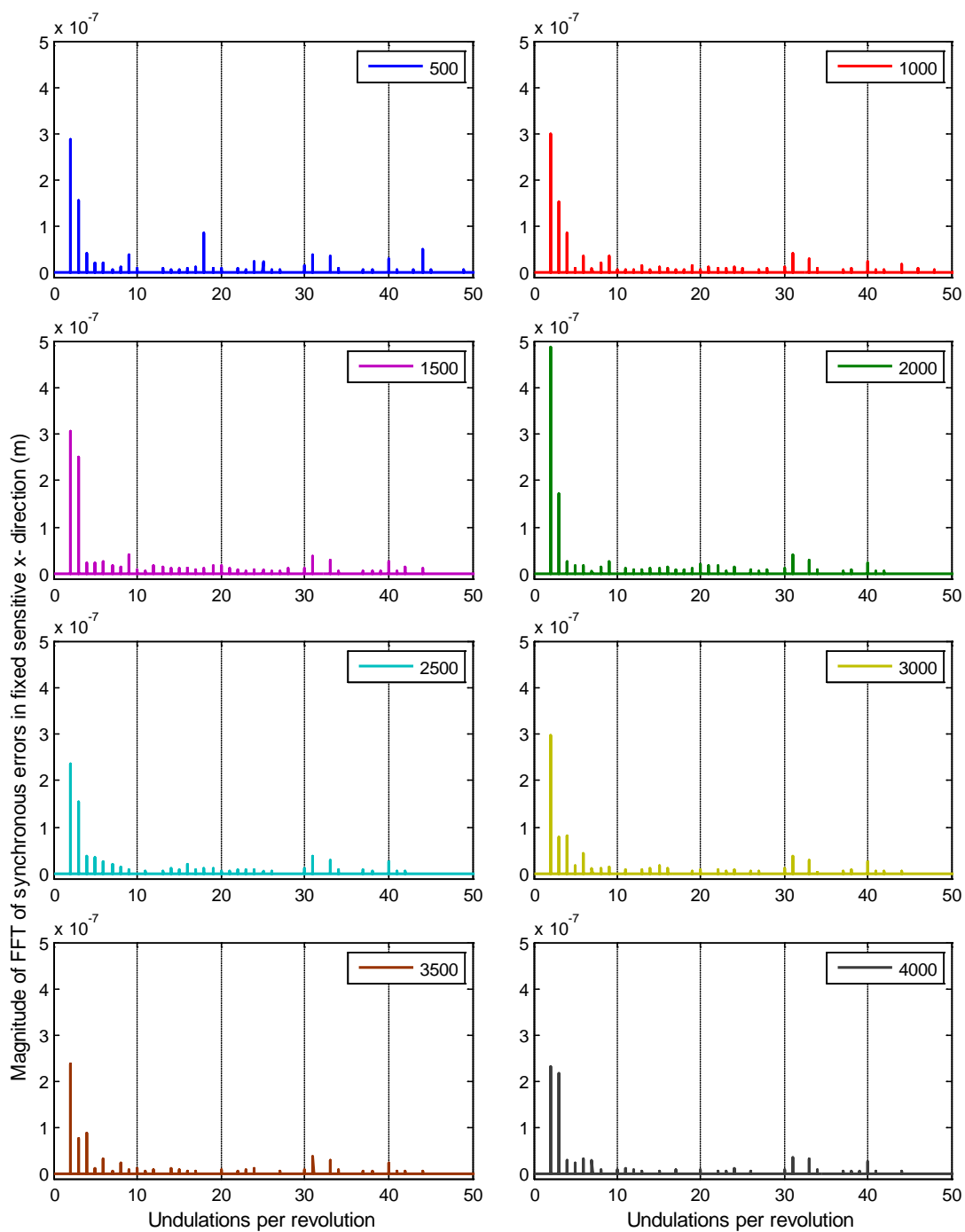


Figure B.4: Magnitude of FFT of synchronous SE in fixed sensitive x-direction.

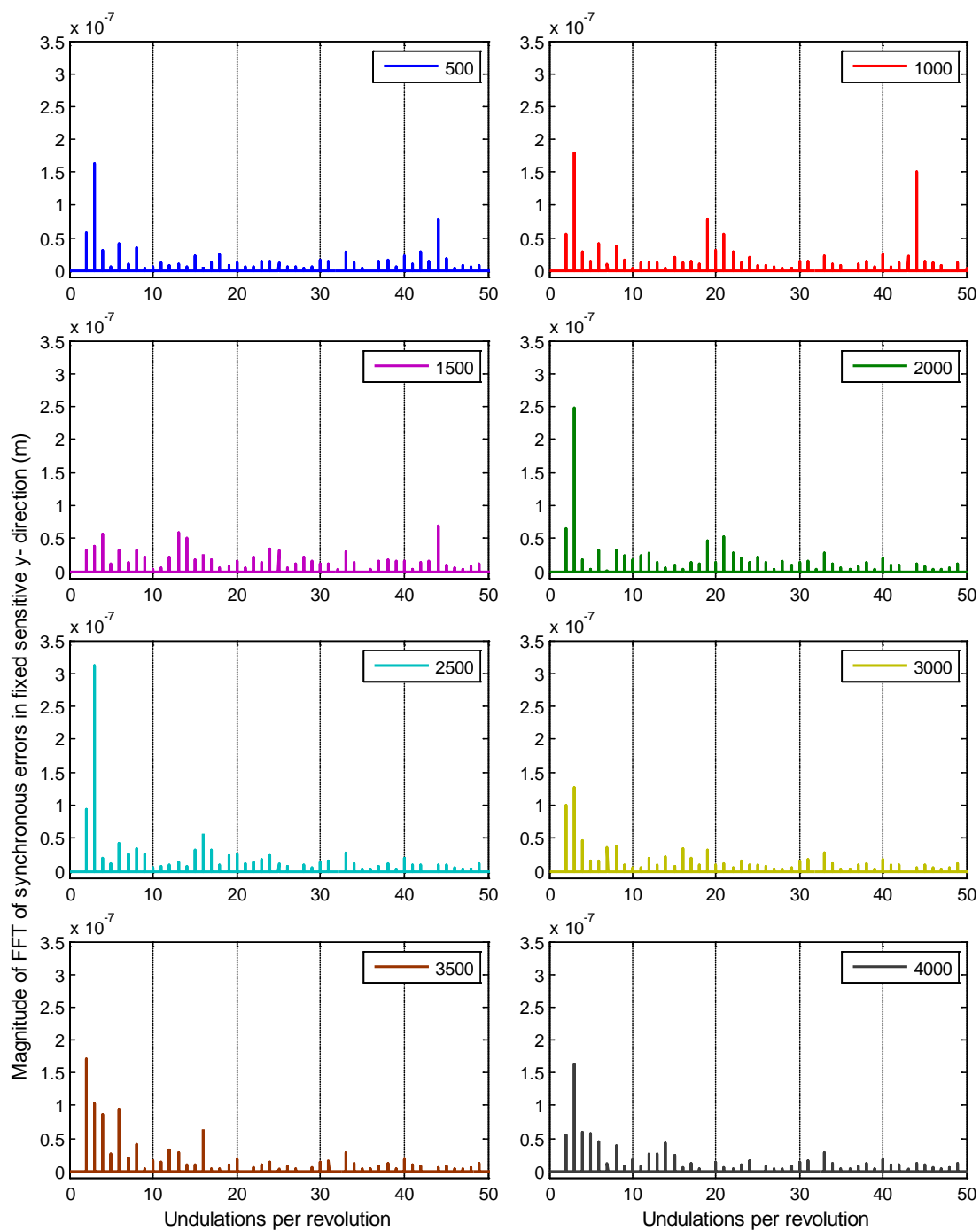


Figure B.5: Magnitude of FFT of synchronous SE in fixed sensitive y-direction.

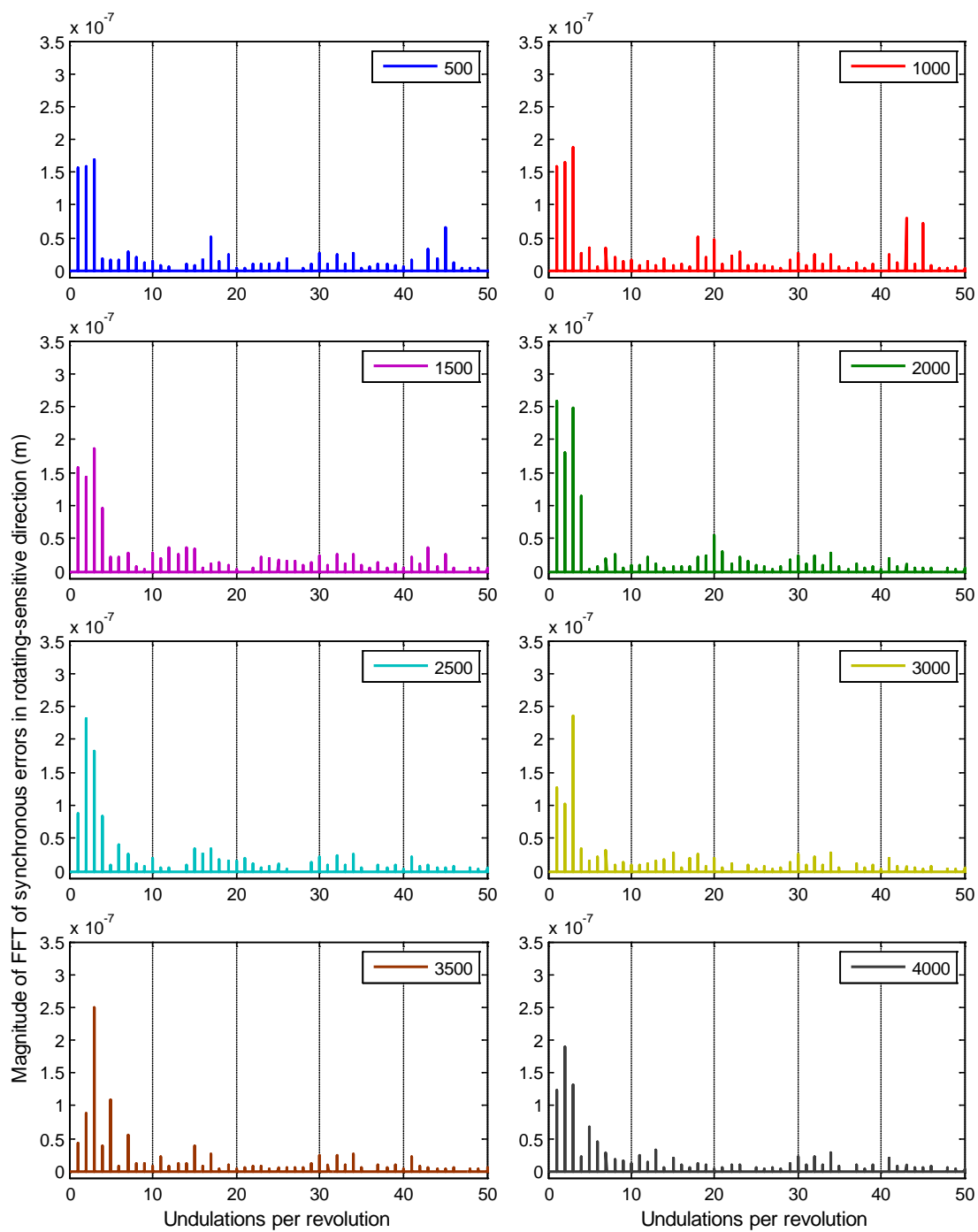
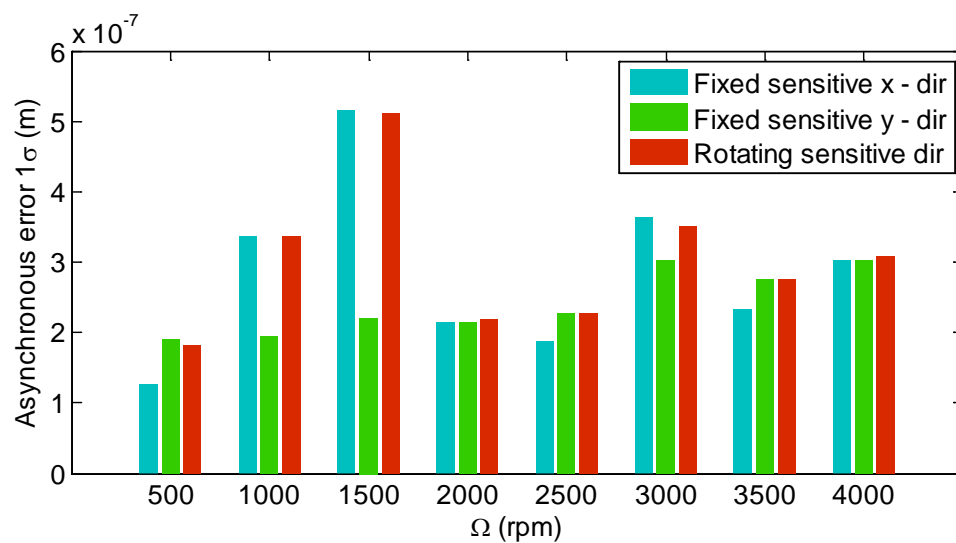


Figure B.6: Magnitude of FFT of synchronous SE in rotating-sensitive direction.

B.1.2: Asynchronous SE Motions

Figure B.7: Maximum 1σ standard deviation of asynchronous SE motion.

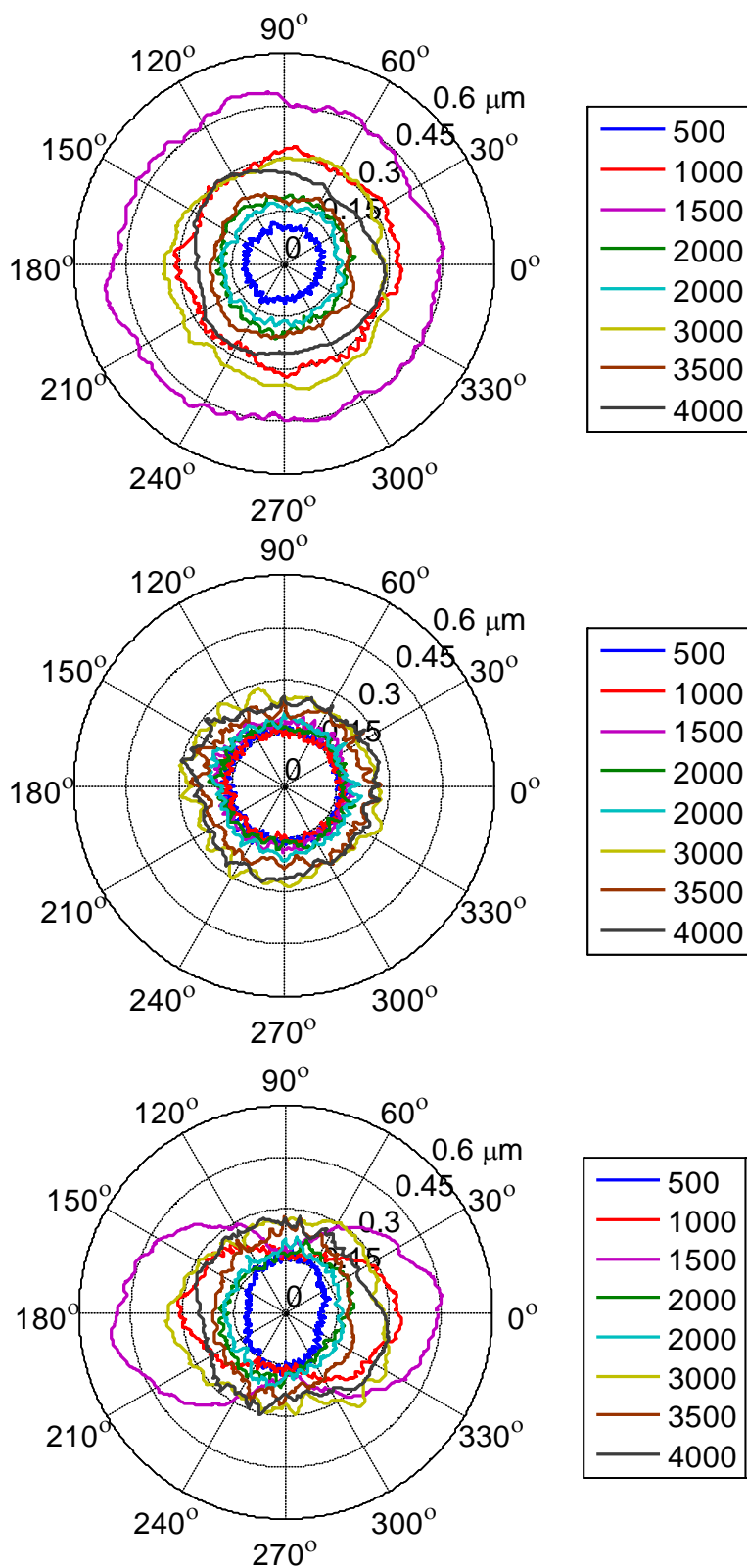


Figure B.8: 1σ standard deviation of asynchronous SE motion: fixed sensitive x-direction (top); fixed sensitive y-direction (middle); rotating sensitive direction (bottom).

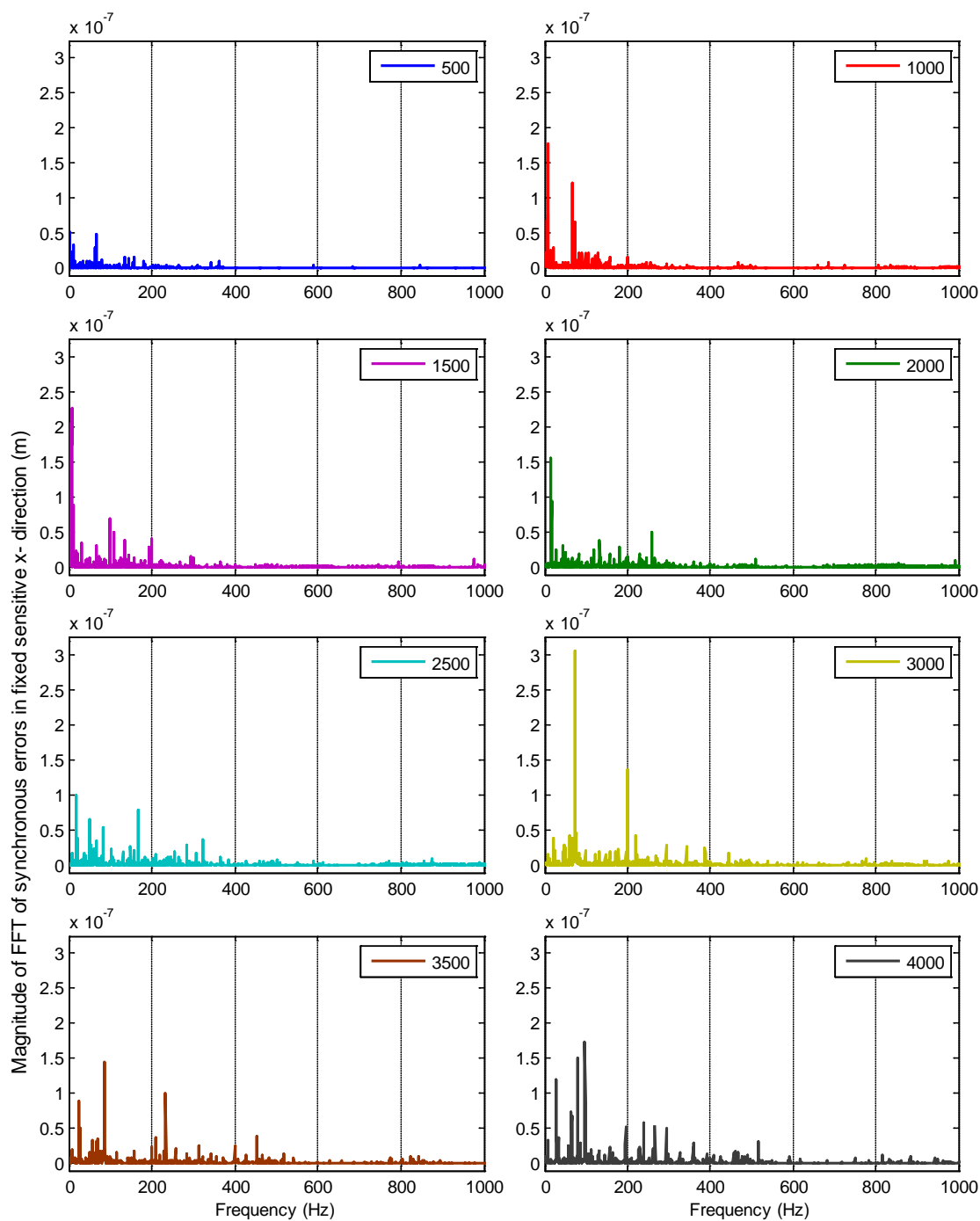


Figure B.9: Magnitude of FFT of asynchronous SE in fixed sensitive x-direction.

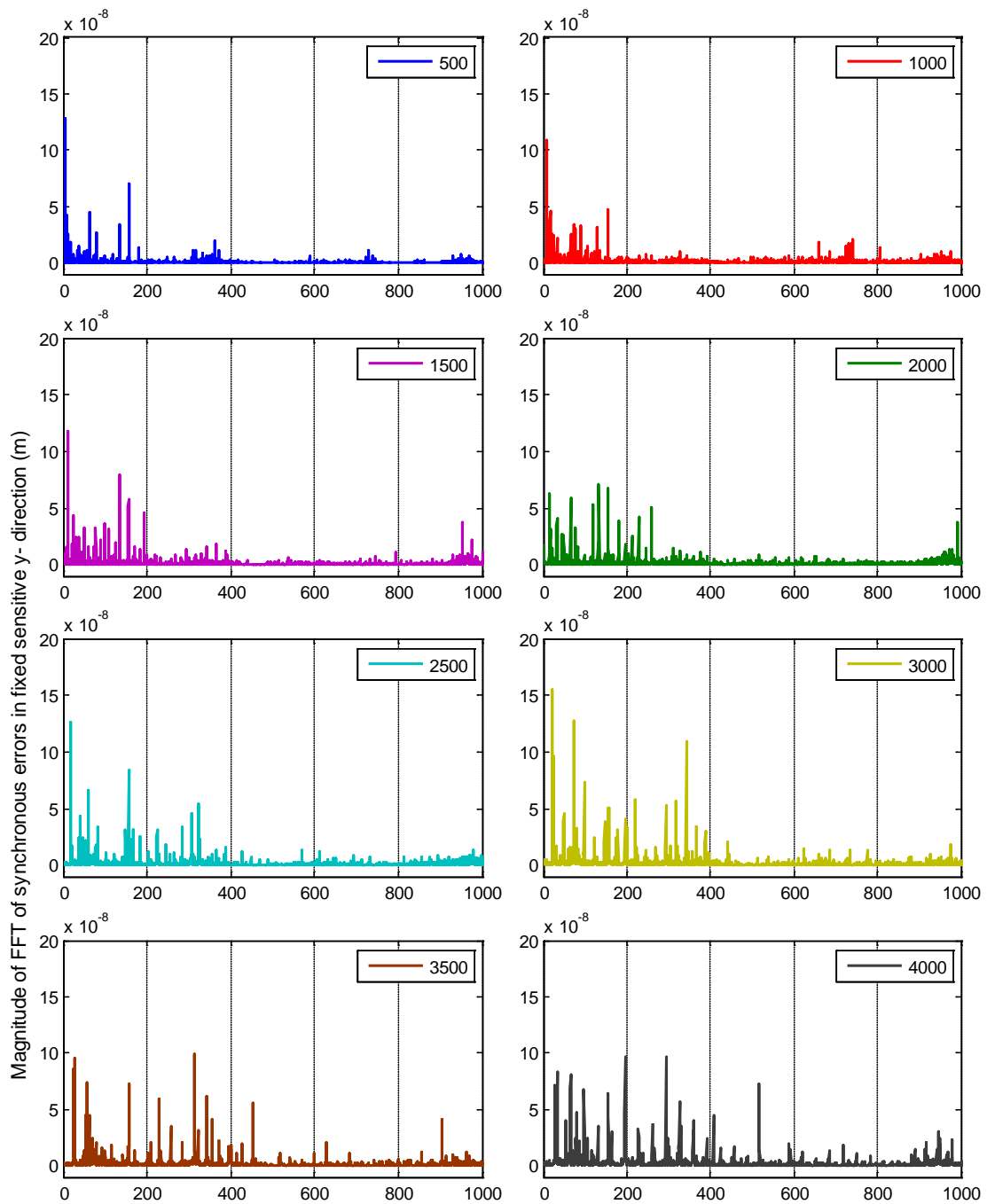


Figure B.10: Magnitude of FFT of asynchronous SE in fixed sensitive y-direction.

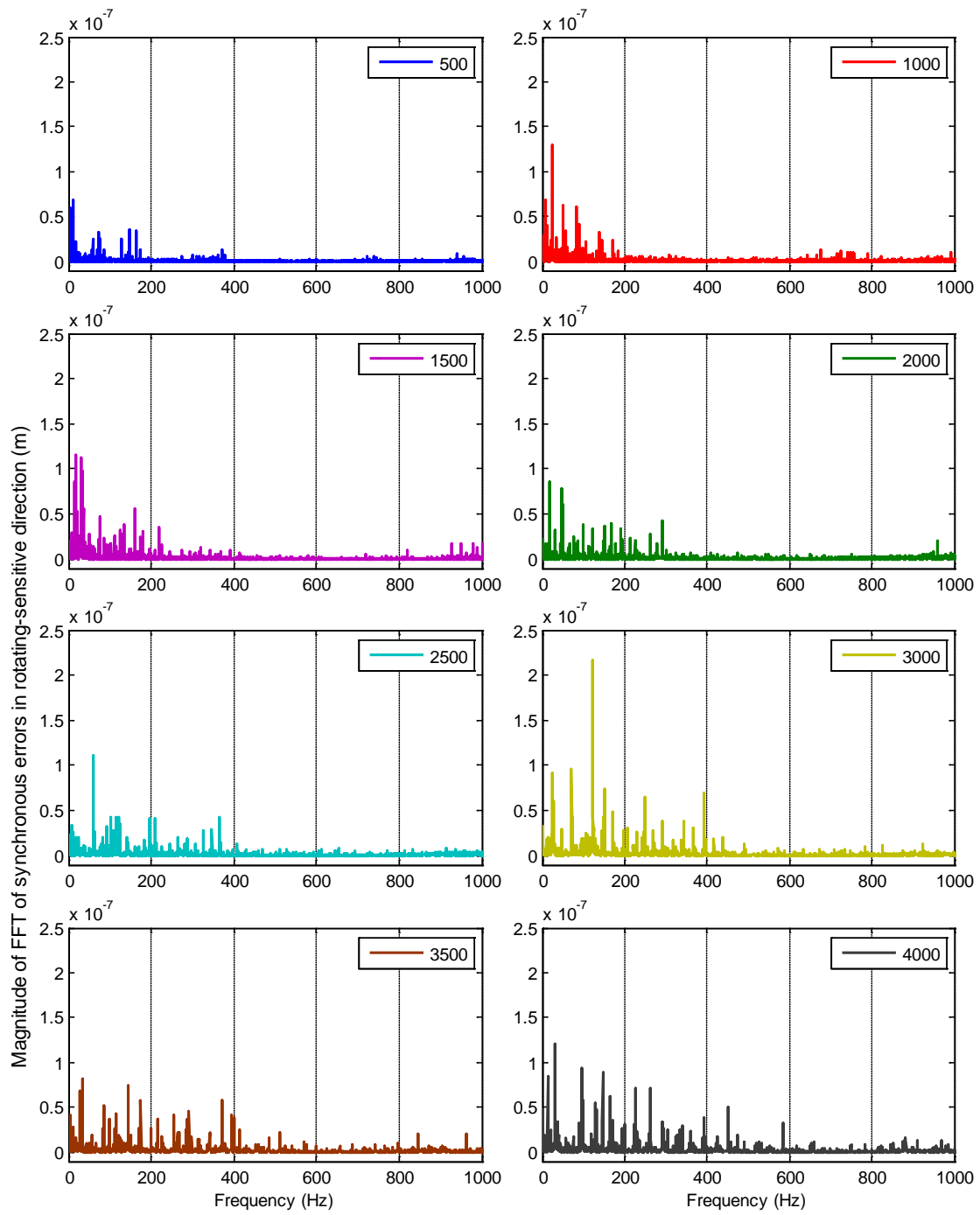


Figure B.11: Magnitude of FFT of asynchronous SE in rotating sensitive direction.

B.2: SE Measurements : Haas3

B.2.1: Synchronous SE Motions

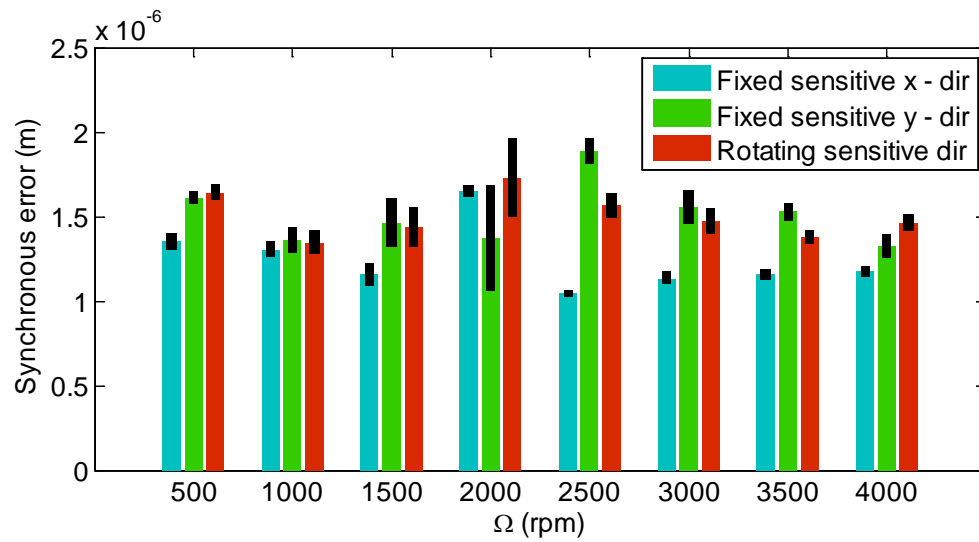


Figure B.12: Peak-to-valley estimate of synchronous SE motions.

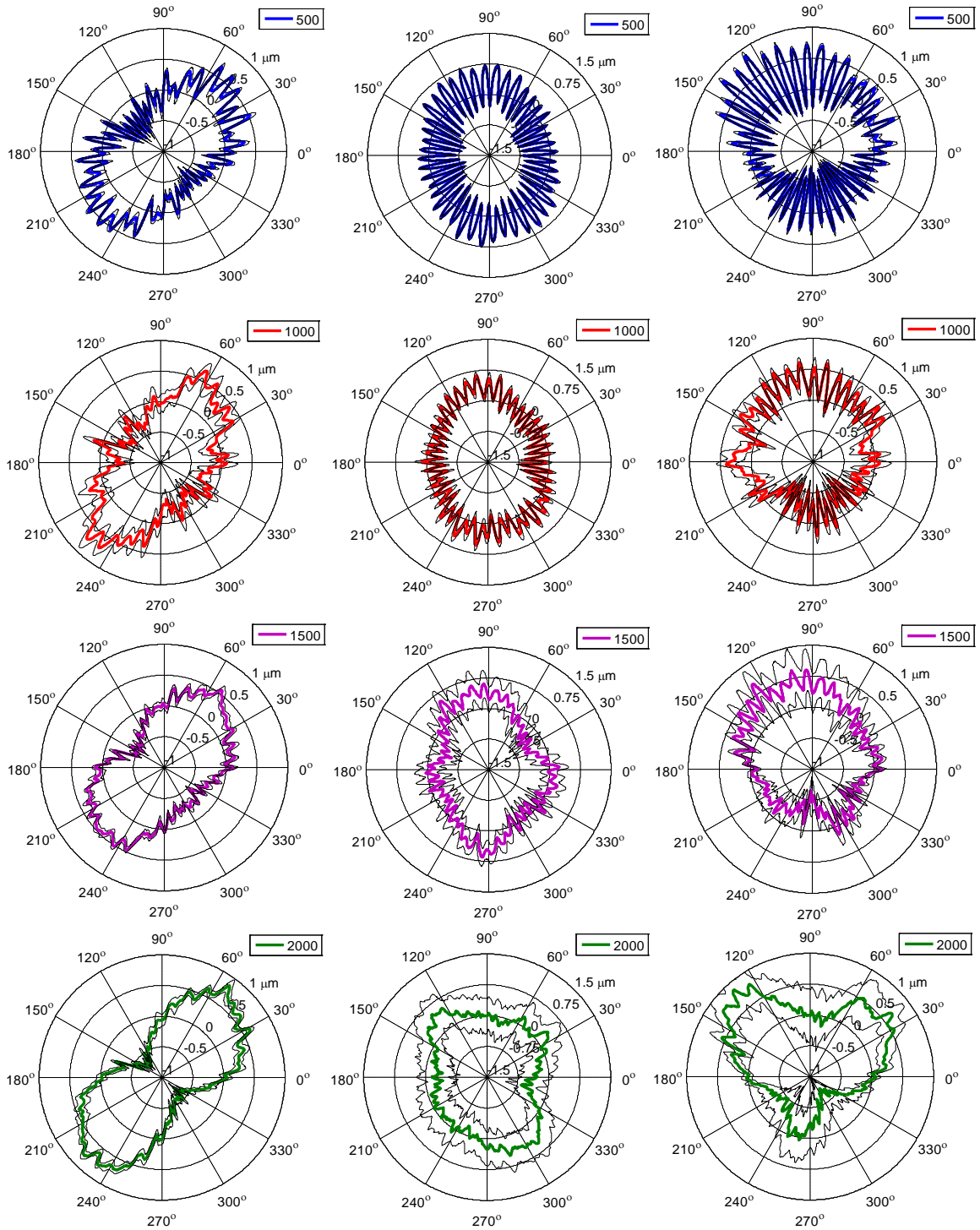


Figure B.13: Synchronous SE motion: fixed sensitive x-direction (left); fixed sensitive y-direction (middle); rotating sensitive direction (right). Spindle speeds: 500 rpm, 1000 rpm, 1500 rpm, 2000 rpm.

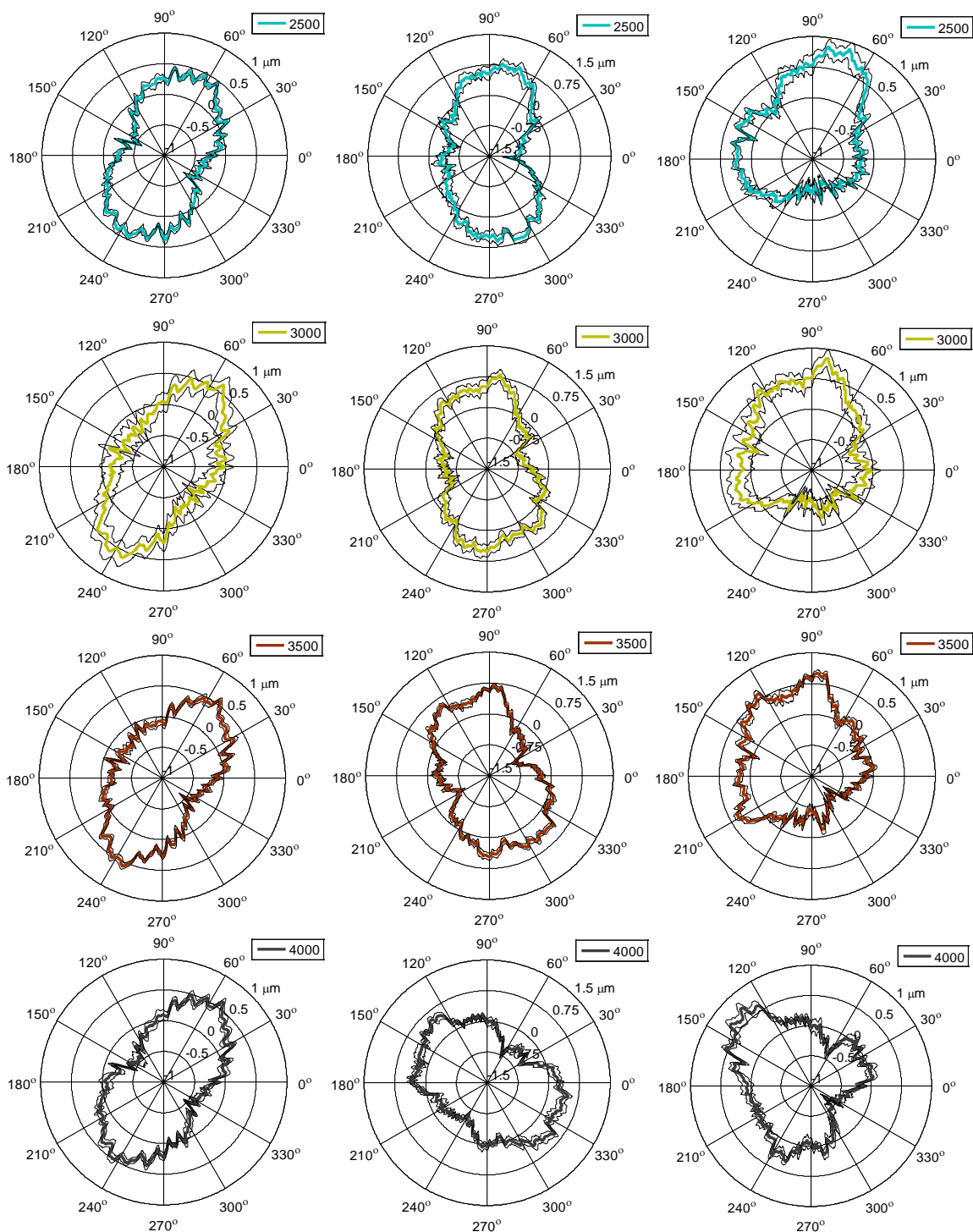


Figure B.14: Synchronous SE motion: fixed sensitive x-direction (left); fixed sensitive y-direction (middle); rotating sensitive direction (right). Spindle speeds: 500 rpm, 1000 rpm, 1500 rpm, 2000 rpm.

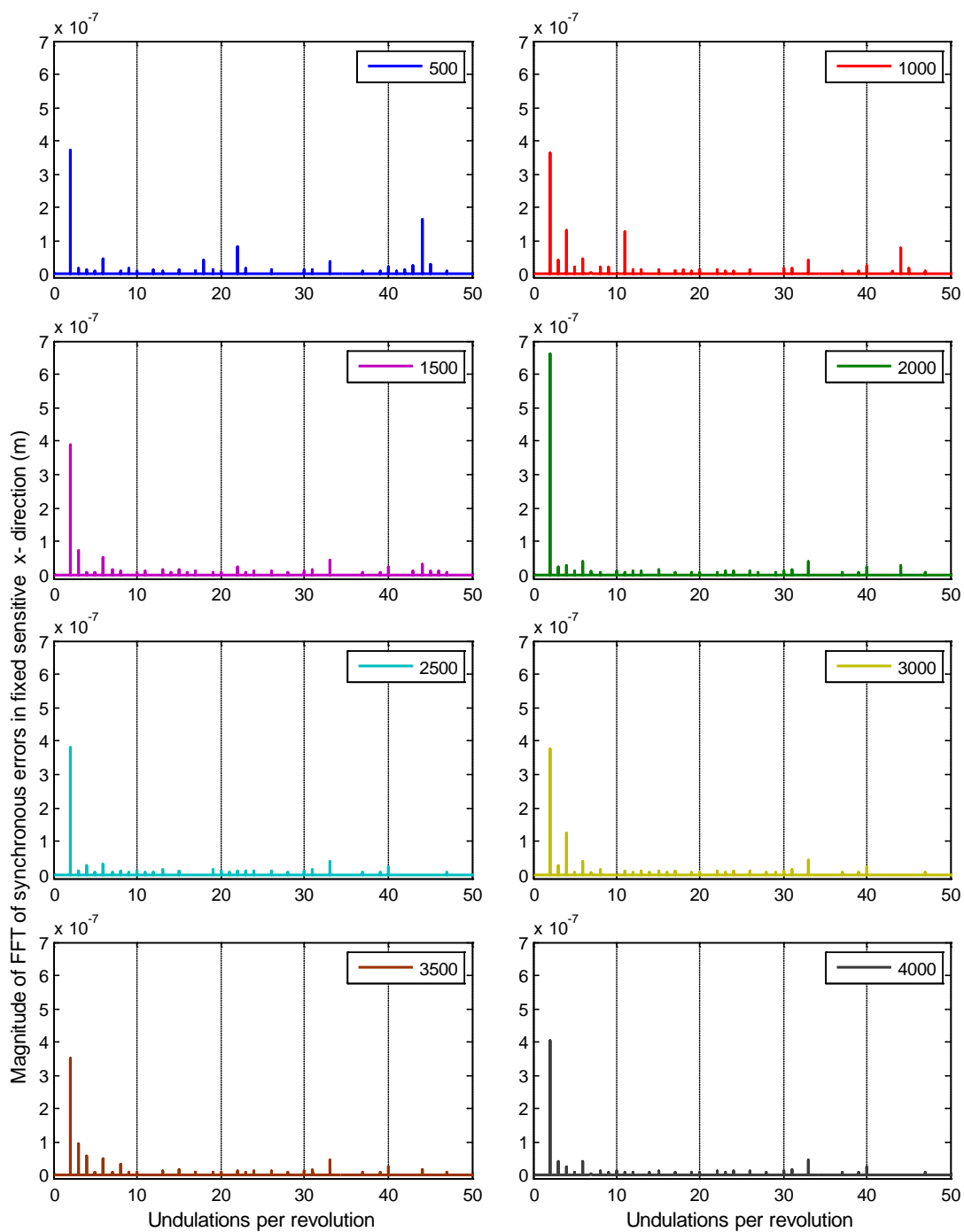


Figure B.15: Magnitude of FFT of synchronous SE in fixed sensitive x-direction.

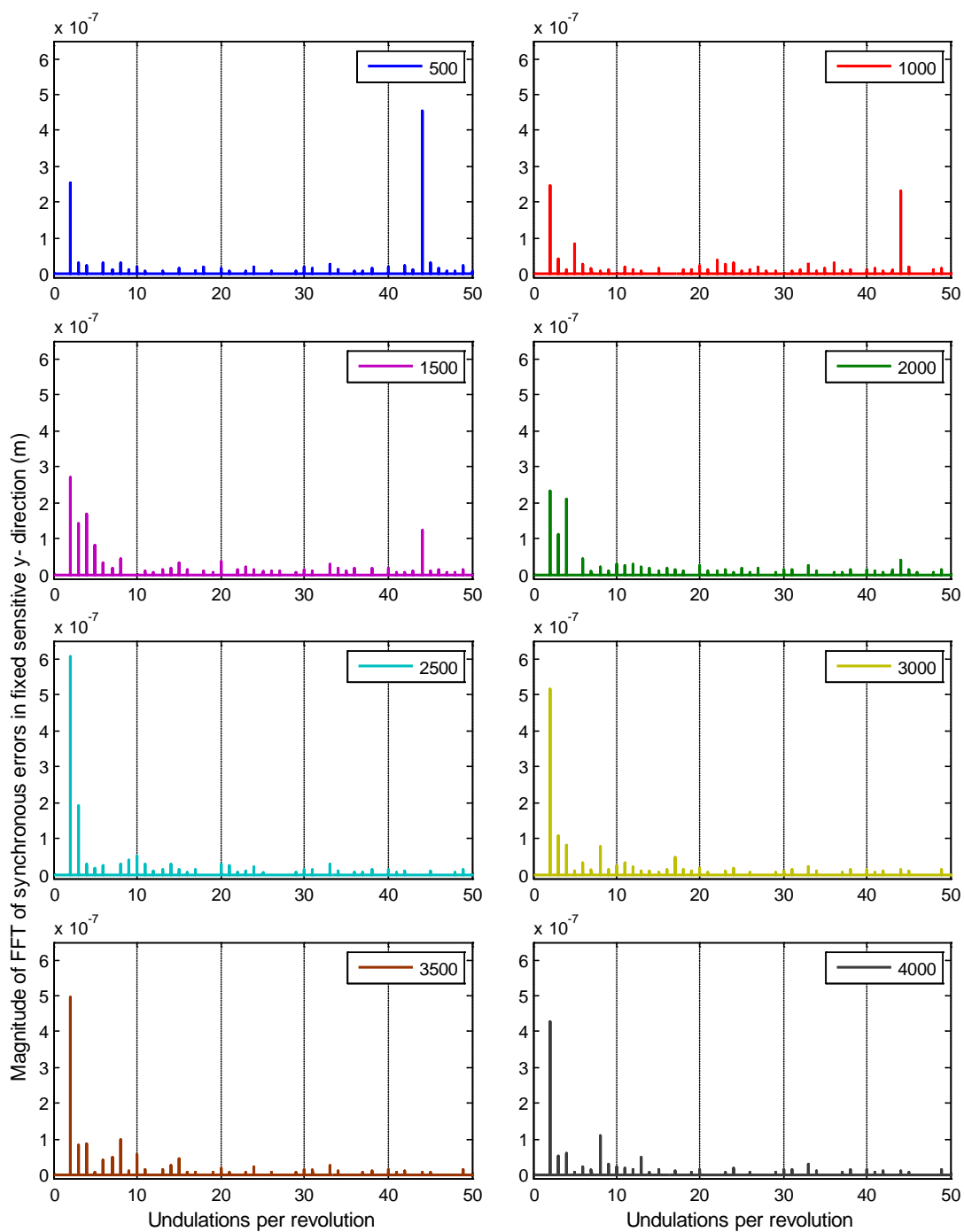


Figure B.16: Magnitude of FFT of synchronous SE in fixed sensitive y-direction.

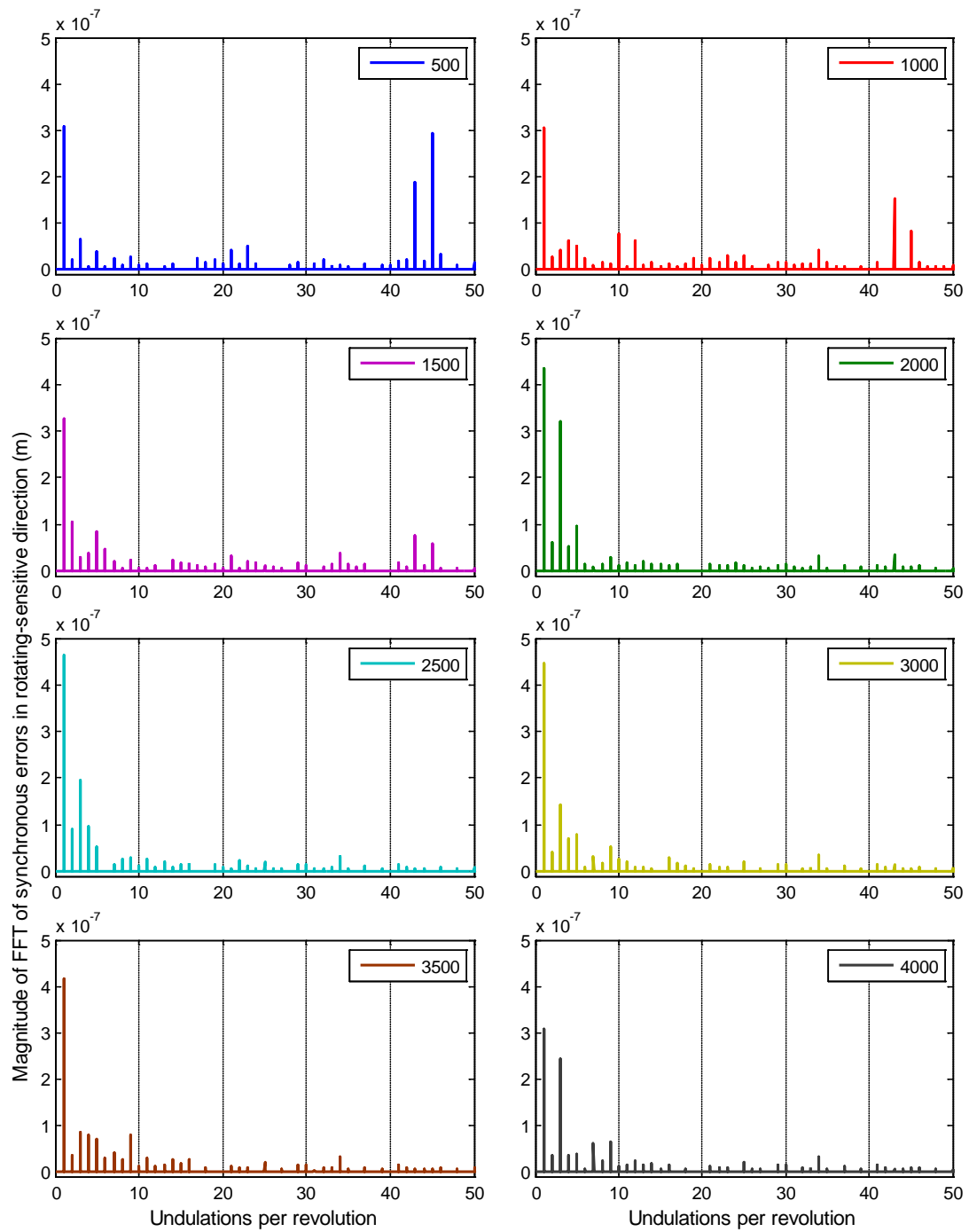
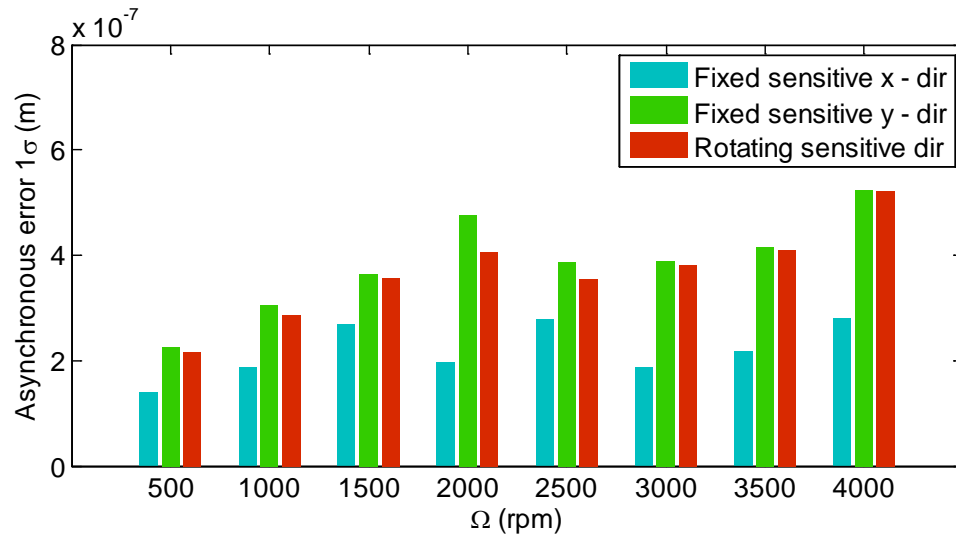


Figure B.17: Magnitude of FFT of synchronous SE in rotating sensitive direction.

B.2.2: Asynchronous SE Motions

Figure B.18: Maximum 1σ standard deviation of asynchronous SE motion.

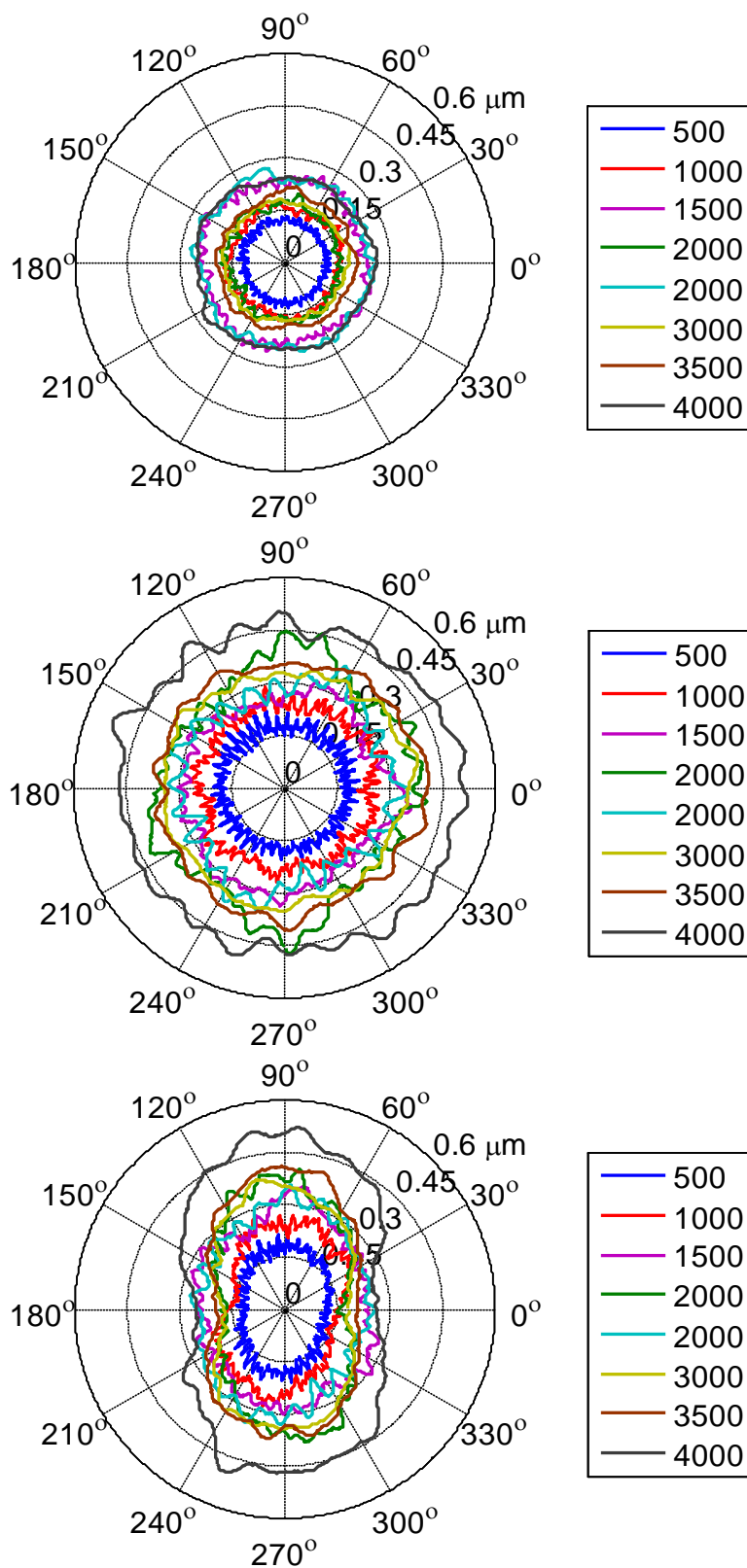


Figure B.19: 1σ standard deviation of asynchronous SE motion: fixed sensitive x-direction (top); fixed sensitive y-direction (middle); rotating sensitive direction (bottom).

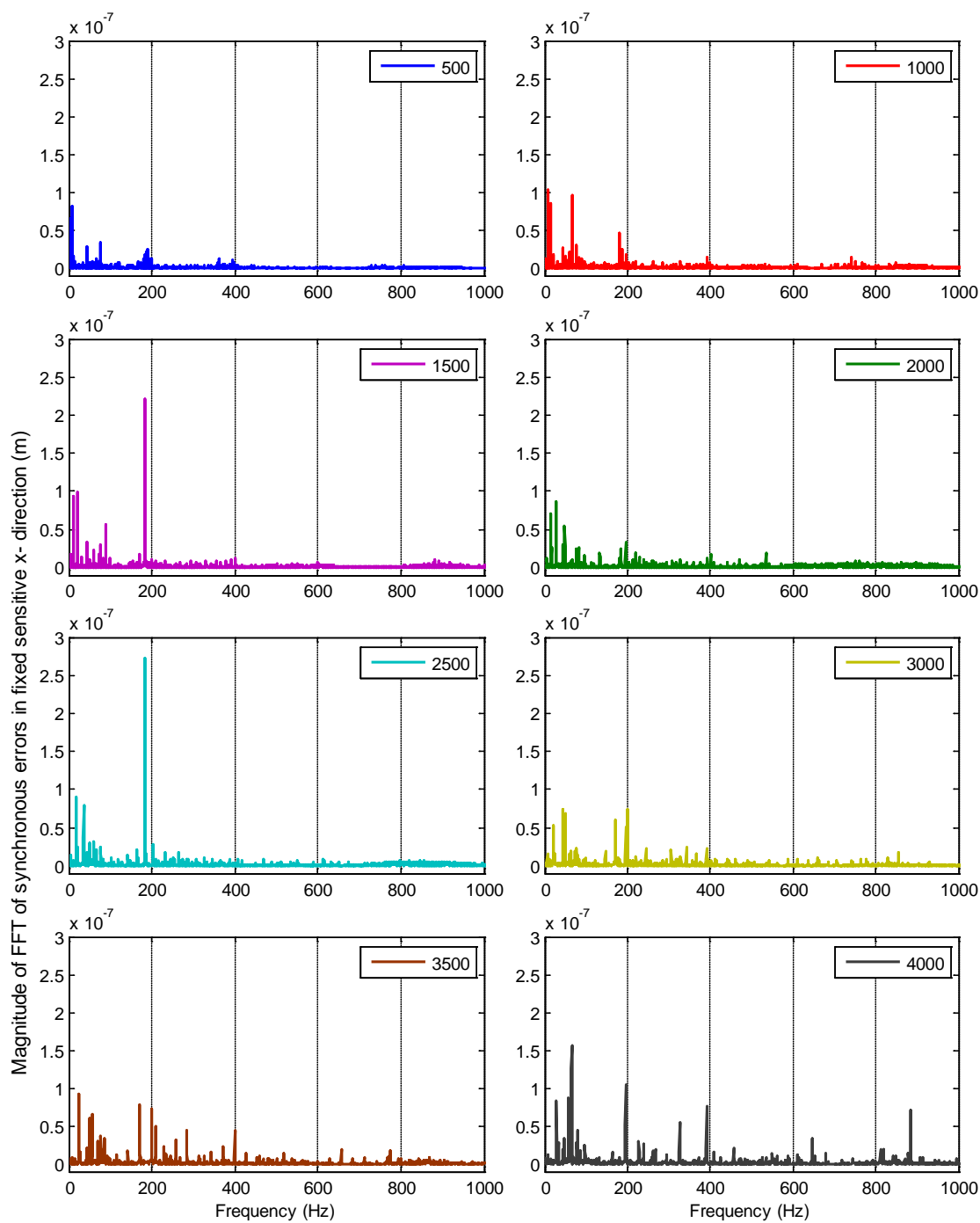


Figure B.20: Magnitude of FFT of asynchronous SE in fixed sensitive x-direction.

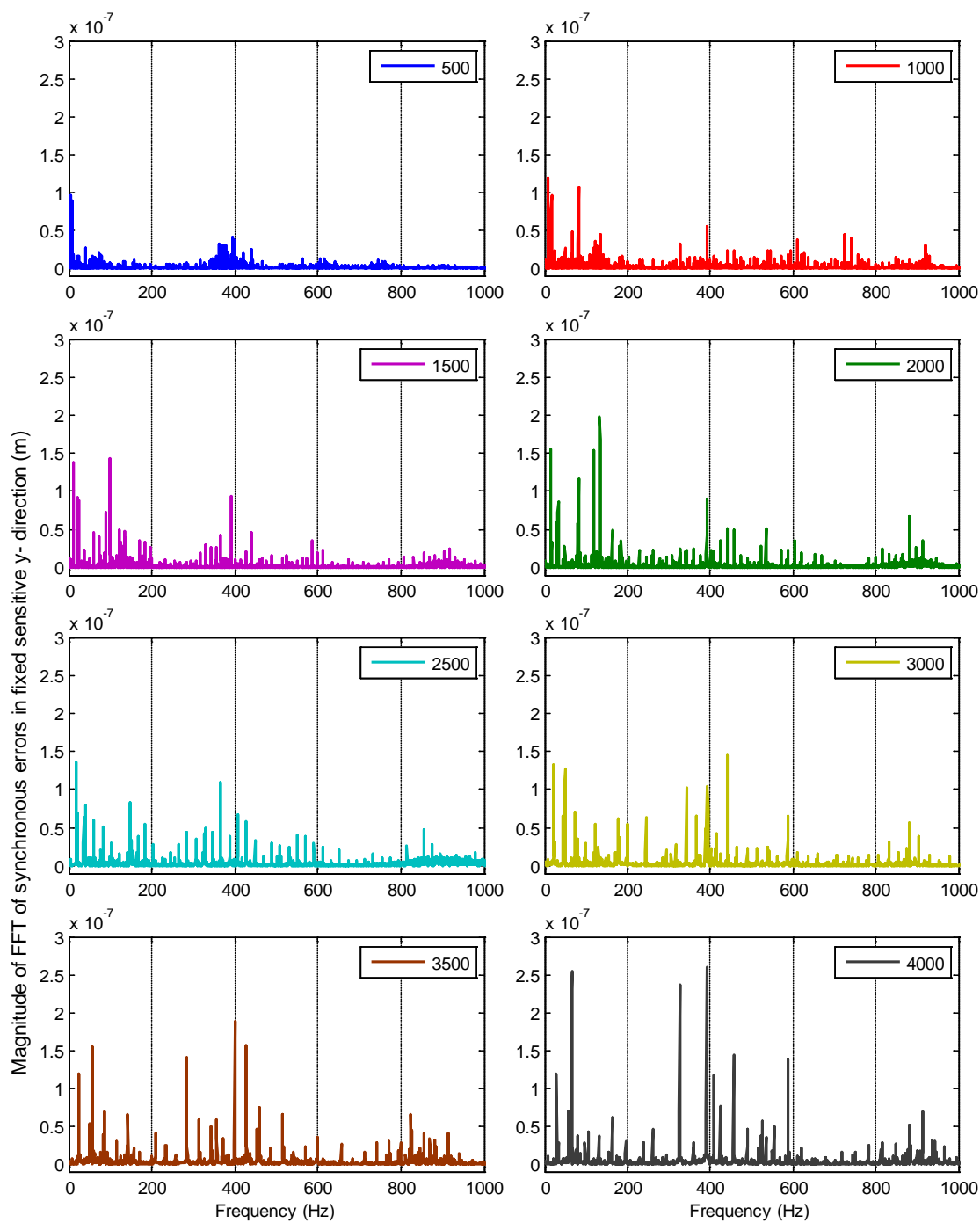


Figure B.21: Magnitude of FFT of asynchronous SE in fixed sensitive y-direction.

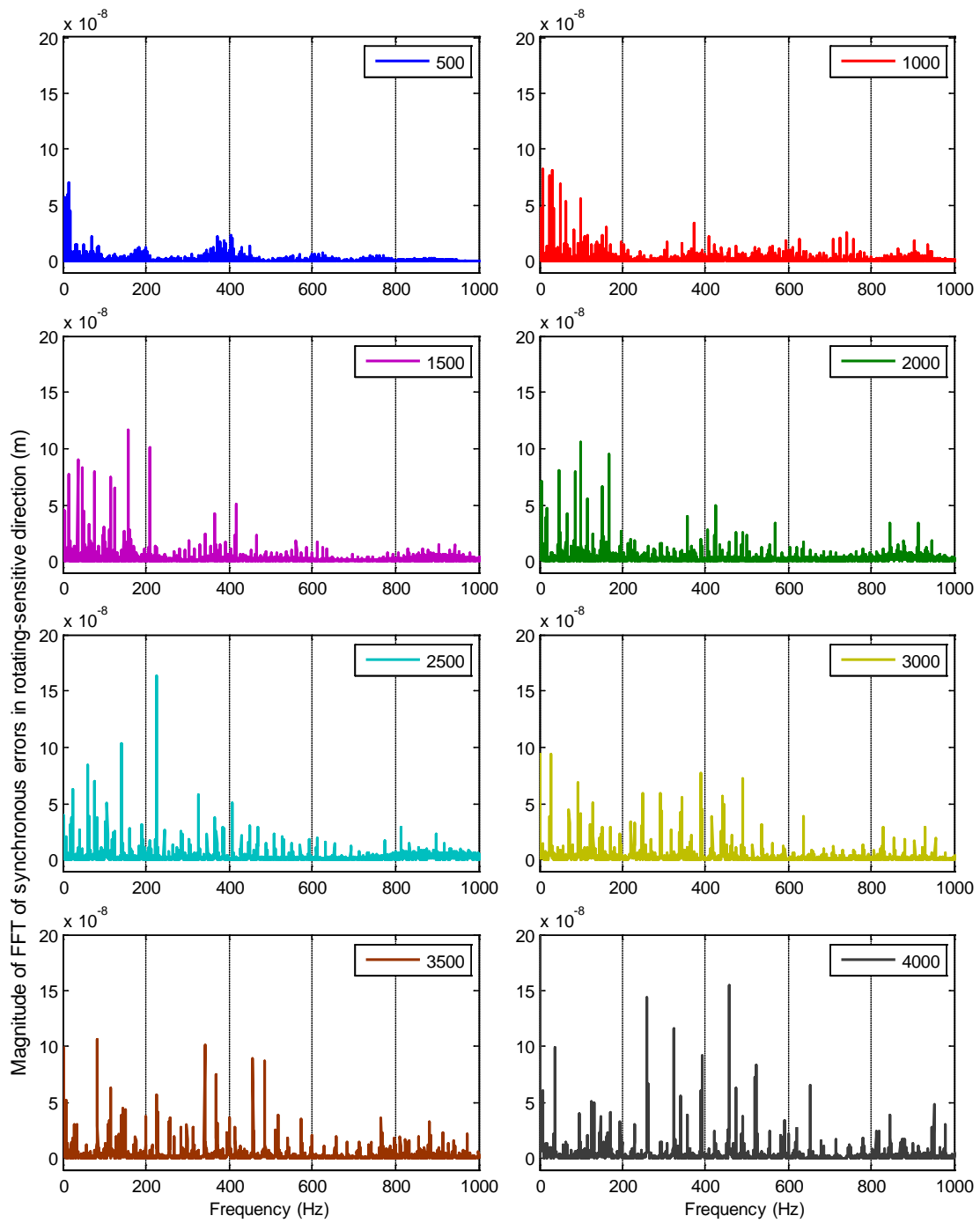


Figure B.22: Magnitude of FFT of asynchronous SE in rotating-sensitive direction.

APPENDIX C: RCSA COMPARISONS

C.1: RCSA Comparison : Haas2

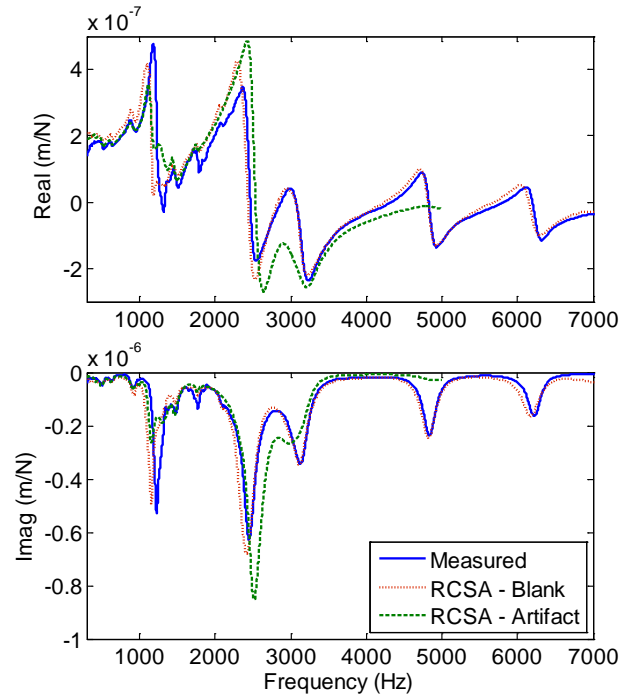


Figure C. 1: Comparison between predicted and measured tool tip FRF: x- direction.

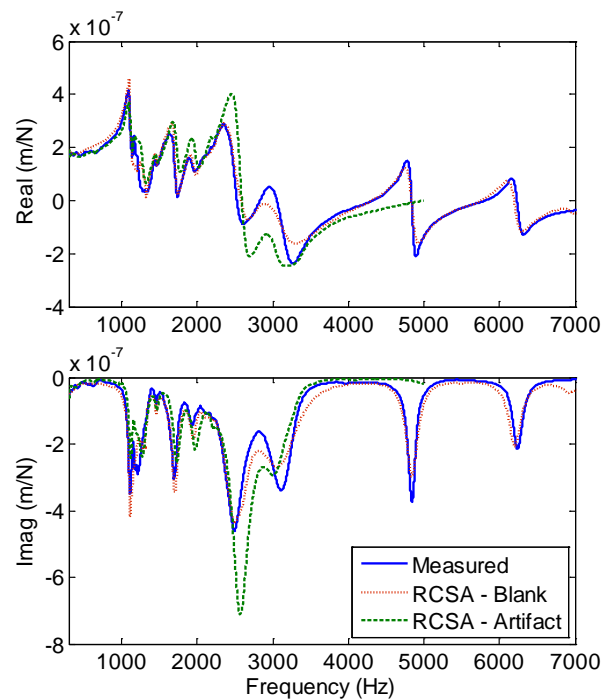


Figure C. 2: Comparison between predicted and measured tool tip FRF: y- direction.

C.2: RCSA Comparison : Haas3

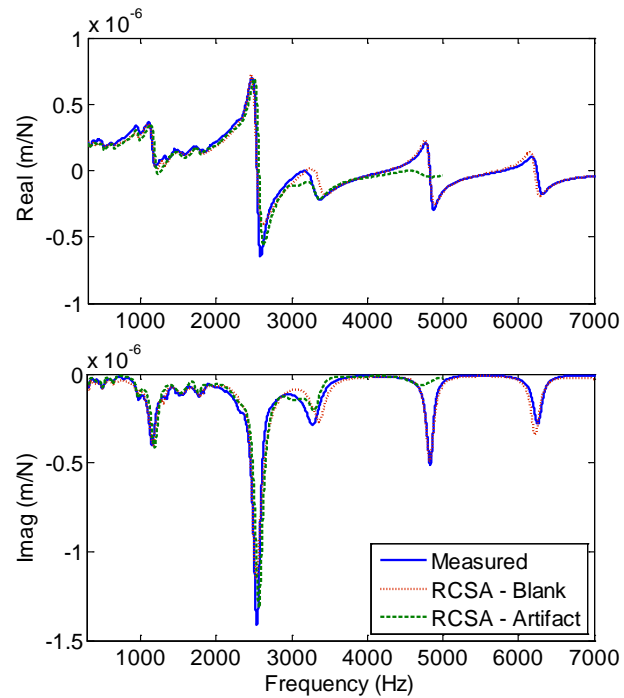


Figure C. 3: Comparison between predicted and measured tool tip FRF: x- direction.

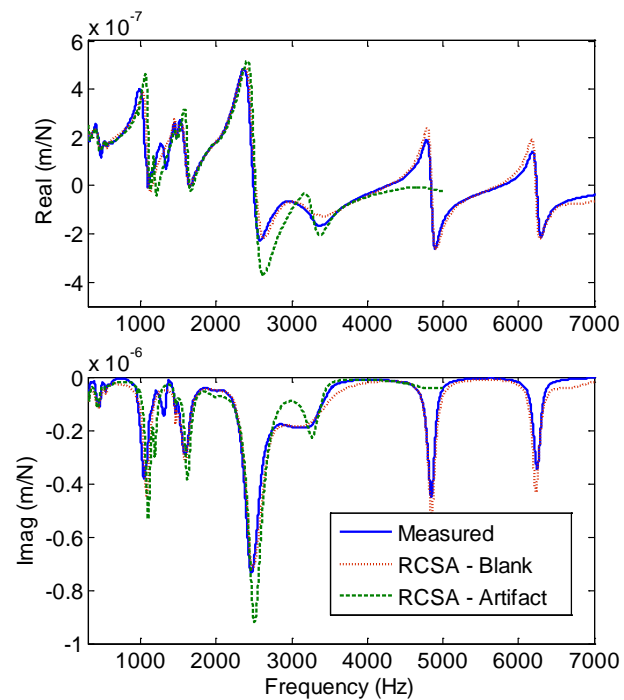


Figure C. 4: Comparison between predicted and measured tool tip FRF: y- direction.